Technische Universiteit Delft

Thermodynamic Modeling of High Temperature Heat Pump Systems

Decarbonizing Industrial Heat

S. Vermani

TU Delft

Thermodynamic Modeling of High Temperature Heat Pump Systems

Decarbonizing Industrial Heat

by

S. Vermani

to obtain the degree of Master of Science in Aerospace Engineering

at the Delft University of Technology,

to be defended publicly on October 10, 2022.

Student number: 4657764

Project duration: February 3, 2022 – October 10, 2022

Thesis committee:

Prof. dr. ir. P. (Piero) Colonna,	TU Delft, Chair
Dr. ir. C. M. de Servi,	TU Delft, Supervisor
Dr. ir. M. (Matteo) Pini,	TU Delft, Examiner
Dr. ir. R. Pecnik,	TU Delft, Examiner
Prof. dr. P. Stathopoulos	DLR, Examiner

An electronic version of this thesis is available at http://repository.tudelft.nl/.

Source of the cover image https://bit.ly/3PkwvFX.

TU Delft

Preface

This thesis report marks the end of my five years as a student at TU Delft, starting with my Bachelor's degree in Aerospace Engineering. Every day of this thesis project was a new learning opportunity, and I will cherish this experience.

This exciting yet challenging journey would not have been possible without the guidance and support from my supervisor Dr. Carlo de Servi. I am very grateful for his continued support throughout the project. From introducing me to the thesis topic to all the technical discussions and providing critical comments to improve my final report, I am really thankful for his time. He motivated me to push my boundaries and broaden my perspective. I want to thank Dr. Matteo Pini for his valuable inputs on the turbomachinery design. I want to thank Ir. Andrea Giuffré for taking the time to introduce me to the *TurboSim* tool and helping me troubleshoot the problems I encountered with the tool. I am also thankful to Ir. Federica Ascione and Ir. Matteo Majer for their suggestions on the model methodology.

Finally, I would like to thank my parents and my brother, without whom my dream of graduating with an MSc in Aerospace Engineering would not have been possible. Thank you for always being there and looking out for me despite being on different continents. I want to thank all my friends for their constant support and company; this journey would have been much more challenging without all of you.

S. Vermani
Delft, October 2022

Contents

List of Figures

List of Tables

Nomenclature

Acronyms

EU	European Union
CS	Climate Protection Scenario
$\mathrm{COP_h}$	Coefficient of performance for a Heat Pump
HP	Heat Pump
GWP	Global Warming Potential
ODP	Ozone Depletion Potential
VCC	Vapor Compression Cycle
TRL	Technology Readiness Level
ECN	Energieonderzoek Centrum Nederland
MHP	Magnetocaloric Heat Pump
MCM	Magnetocaloric Material
AMR	Active Magnetic Regeneration
TEHP	Thermoelectric Heat Pump
CFD	Computational Fluid Dynamics
HEX	Heat Exchanger
EOS	Equation of State
LB	Lower Bound
UB	Upper Bound
OR	Operating Range

Symbols

T	Temperature [^{o}C]
P	Pressure [bar]
s	Specific Entropy [$\mathrm{J/kgK}$]
h	Specific Enthalpy [$\mathrm{J/kg}$]
β_{total}	Total pressure ratio of the cycle [-]
ΔP	Pressure drop in Heat Exchanger [bar]
ΔT_{min}	Minimum Approach Temperature in Heat Exchangers [^{o}C]
ΔT_{sink}	Temperature drop in Sink Heat Exchanger [^{o}C]
$\eta_{\mathrm{is,\ c}}$	Compressor isentropic efficiency (total-to-total) [-]
$\eta_{\mathrm{is,\ t}}$	Turbine isentropic efficiency (total-to-total) [-]

η_m	Mechanical efficiency [-]
η_{motor}	Electric Motor efficiency [-]
η_{gen}	Electric Generator efficiency [-]
X	Mass fraction of the working fluid [kg/kg]
x	Vapor quality [-]
$\dot{Q}_{\text{sink}}$	Thermal power exchanged at the sink heat exchanger [W]
$\dot{Q}_{\text{source}}$	Thermal power exchanged at the source heat exchanger [W]
W_{comp}	Compressor Work Input [W]
W_{turb}	Turbine Work Output [W]
$\dot{m}$	Mass flow rate of the working fluid [$\mathrm{kg/s}$]

Subscripts

source	Thermal source of the heat pump/ Evaporator
sink	Thermal sink of the heat pump/ Condenser
low	Minimum pressure level in cycle
intm	Intermediate pressure level in cycle
high	Maximum pressure level in cycle
des	Related to design point conditions

Molecules

$\mathrm{H_2O}$	Water
$\mathrm{CO_2}$	Carbon dioxide
$\mathrm{N_2}$	Nitrogen
$\mathrm{R152a}$	Difluoroethane

1 Introduction

1.1. Background and Motivation

Industrial processes are estimated to be responsible for about 20 % of the total greenhouse gas emissions within the European Union (EU) [1]. On a global scale also, greenhouse gas emission reduction potential in the industrial sector has been identified as the second largest, after the energy sector, estimated to be a total of 5.4 GtCO_2eq in 2030 [2]. As per Eurostat, the total energy consumption for the industrial sector in European Union countries (EU-28) alone was 2950 TWh/year for the year 2019 [3]. The industrial sector mainly utilizes energy in two forms: thermal energy and electricity. As shown in Figure 1.1, derived from [1], the majority of the demand is in the form of thermal energy, which accounts for roughly 81% of the total energy requirement. This required thermal energy is categorized into four broad categories based on end-use applications. Among these categories, process heating accounts for 66 % of the total thermal energy demand. Around 78% of this energy demand is currently met by using fossil fuels, with natural gas and coal being the most used. Due to this high dependence on fossil fuels, the estimated CO_2 emissions, only to satisfy the required process heating demands of the industrial processes, were found to be around 552 Mt/a for the year 2019. This clearly indicates the need to make radical changes to achieve net-zero CO_2 emissions in the industrial sectors while still achieving the required energy demand.

In this regard, the utilization of waste thermal energy from industrial processes has been identified as a key element of the industrial energy supply‘s decarbonization strategy [1][4]. A definition of waste thermal energy as a resource is defined by Bendig et al. [5] as, “exergy that unavoidably leaves a process or is lost within it, independent of the technological choices made within the process”. Effective recovery of the waste thermal energy has been estimated to provide savings in energy demand ranging from 5 to 30 %, depending on the specific industry [4][6]. To exploit the potential of the waste thermal energy, which is otherwise rejected from a process, electrically driven heat pump technology has been identified as one of the promising technologies in recent times [7][8]. In its simplest form, a heat pump system has a similar thermodynamic cycle as a household refrigerator. It supplies the thermal energy at higher temperature levels while using the energy available at lower temperature levels. Thus, essentially “pumping” the thermal energy from a low temperature to a high temperature (hence the word heat pump) while using electrical energy as the input. The type of work input is not restricted to electrical energy and can differ significantly based on the type of the system used [9]. An example of the implementation of a simple heat pump integrated process is shown in Figure 1.2. The amount of the thermal energy demand met by the heat pump will vary based on the process characteristics and the type of heat pump used. Apart from improving the overall energy efficiency of the processes, the use of heat pumps also reduces fossil fuel consumption and thus reduces the associated greenhouse gas emissions. Heat pump systems driven by electrical power can also lead to a net carbon zero technology as a higher share of renewable electricity is expected in the near future [10][11].

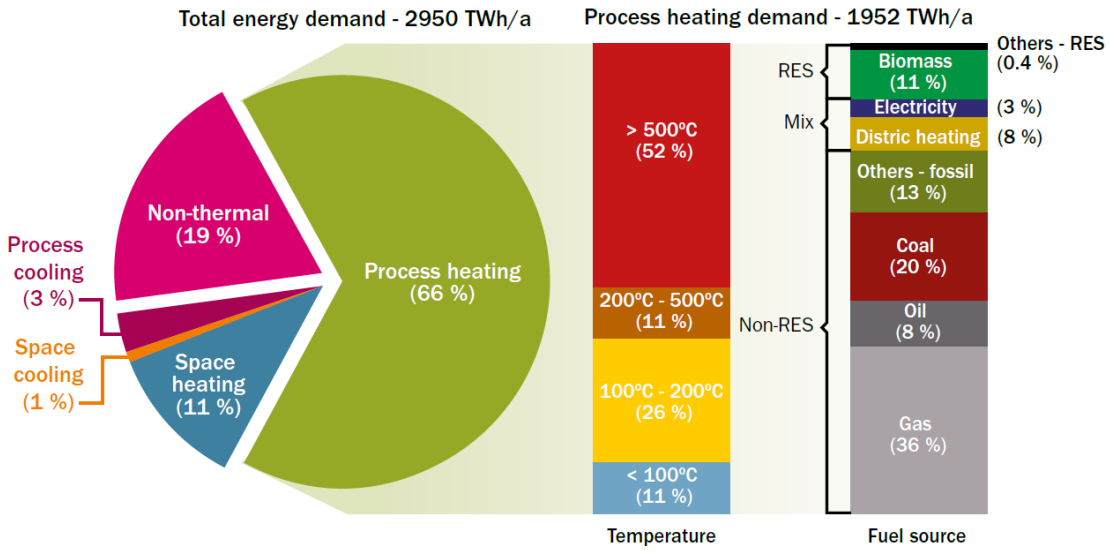

Figure 1.1: Breakdown of the total energy demand by the EU industries [1]

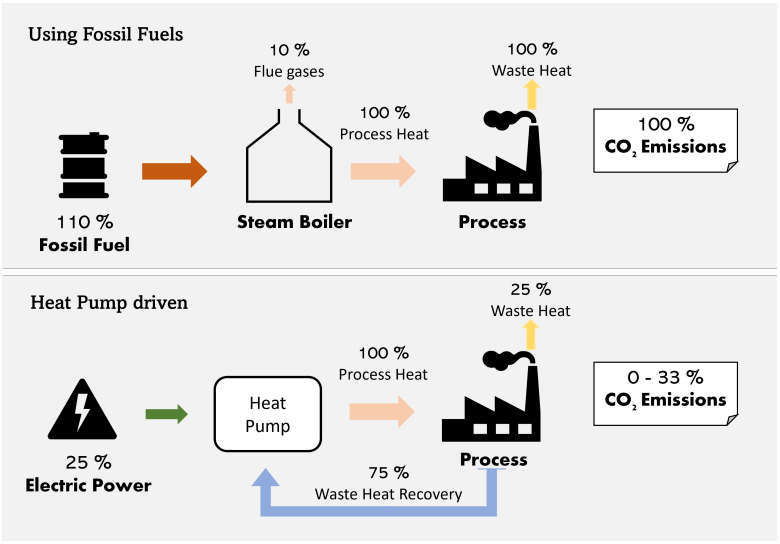

Figure 1.2: Simplified illustration of heat pump integrated thermal energy supply. Adapted from [1]

To assess the potential use of heat pumps in a specific industrial sector, two main factors need to be considered: the amount of available waste thermal energy and the associated temperature levels, as well as the required energy demand and the corresponding temperature level. Estimating available waste thermal energy potential in different industrial sectors is complicated because it is highly dependent on the specific process setup. Thus, the waste thermal energy source characteristics vary significantly in terms of temperature level, continuous availability, or composition. As a result, quantifying the related potential on a global scale or even on an industrial scale is challenging [12].

Several recent reports estimate the potential of waste thermal energy in industry, focusing on policy and energy efficiency aspects [6][13]. All of these reports aim to quantify the available waste thermal energy that can be reused in the process through different technical solutions. The focus of these reports differ in terms of geographical area coverage, for e.g. United Kingdom [14], Germany [15], EU wide [16][17][18].

One of these studies, [17], tried to estimate the waste thermal energy potential by investigating different

temperature levels within different industrial sectors. As per this study, the primary energy consumers within the temperature interval of 100°-200°C are food, paper, and non-mineral industries, and they account for roughly 2/3 of the total energy consumption. Assuming a constant COP value, this study estimated the possible energy demand coverage by heat pumps for different industrial sectors. Figure 1.3 shows the obtained results, considering the available waste thermal energy in the temperature interval 100°-200°C. As can be observed from the figure, there is a high potential for high temperature (100°C or higher) heat pumps to reduce the energy consumption demand. Non-metallic mineral, paper/pulp, and food industries were found to be the most promising, considering the absolute magnitude of the process heating demand covered. However, the non-ferrous metal industry was the most promising in terms of percentage coverage. Based on this study, the total potential of heat pumps for the EU industries was estimated to be around 102 PJ. However, in this study, only aggregated values for process heating demand and waste thermal energy availability per sector and temperature range are provided. This makes it impossible to identify the specific process conditions which exhibit maximum potential for heat pump technology.

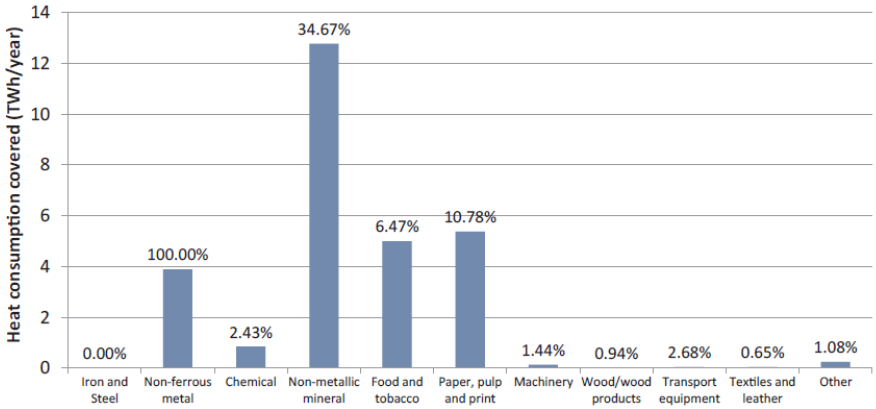

Figure 1.3: Estimated process heating consumption coverage by the heat pump systems, per industrial sector within EU, for the temperature interval 100-200 °C [17].

Another study [18] provided a similar estimate for the heat pump potential, but in this case, using the actual process data rather than estimating the overall cumulative values, thus, following a so-called "bottom-up" approach. This approach is more accurate as it can provide direct information about heat pump integration into the most promising processes while highlighting the overall potential of a certain sector. A drawback of this approach is that only a subset of all the processes was considered within each industry. The results obtained using this approach for the waste thermal energy and the process heating demand are provided in Figure 1.4. Similar to the previous study's findings, a high amount of waste thermal energy potential for the paper and food industries is observed. Further, using the individual process information, the integration of heat pumps into the processes and the corresponding savings were also estimated in this study. The results of the estimated potential coverage are also shown in Figure 1.4. The highest coverage is observed for both the chemical and paper industries. The potential for the refinery industries is very low despite a large amount of waste thermal energy. This is mainly because the required temperature level of the processes is usually greater than 500°C, which is infeasible to reach for heat pump technology. Further, this study also estimated the required thermal power capacities of the heat pump systems needed to cover the estimated demand. Figure 1.5 shows this distribution of required capacities. The majority of the heat pump systems (around 88 %) were found to be in the capacity range of less than 10 MW.

Both of these studies ([17], [18]) also highlight the potential of high-temperature heat pumps (> 100°C) in terms of energy demand coverage and greenhouse gas emission reductions. Similar conclusions are also supported by another study [1], which highlights that for temperature levels up to 100 °C, heat pump technology can provide coverage up to 11% of the total process heating demand in EU industries (equivalent to about 222 TWh/a) for a potential reduction in CO_2 of about 51 Mt/a. However, if the temperature ranges up to 200°C is also included, the coverage potential increases to 37% of the total heating demand (equivalent to about 730 TWh/a). This corresponds to a possible reduction of

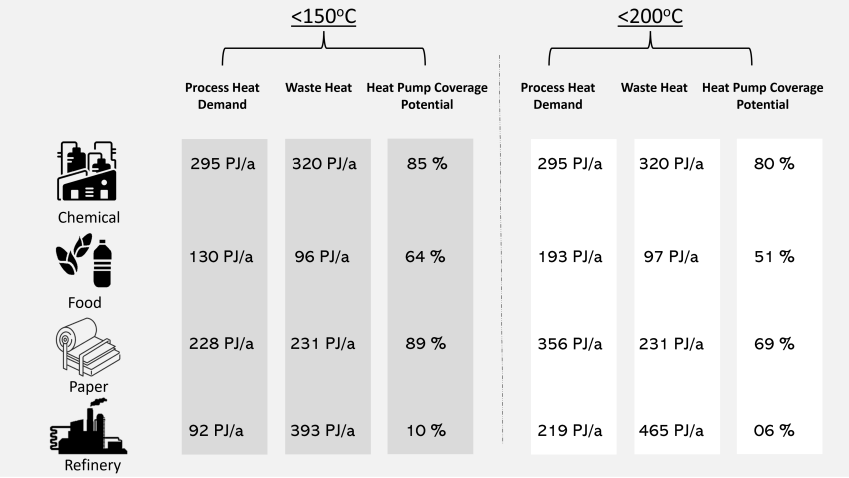

Figure 1.4: Industrial heat pump market potential for EU industries. Based on data from [18]

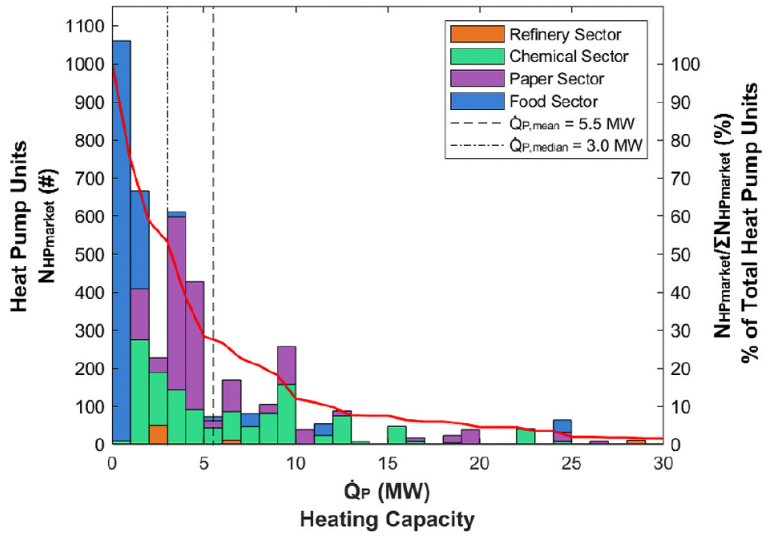

Figure 1.5: Estimated distribution of the required heating capacity for the heat pump systems [18].

CO_2 emissions of about 146 Mt/a. The most promising sectors, in this case, become the paper and pulp, chemical, and food industries.

Another recent study [19] highlighted the potential of heat pump technology for the industrial thermal energy supply in Germany to comply with the climate goals set by the EU. The findings of the study are shown in Figure 1.6, where the trend of CO_2 reduction along with the required energy drivers (renewable energy and energy efficiency) are highlighted. The two dotted lines indicate the required target level based on different climate protection scenarios [19]. The findings presented show the vital role of heat pump technology in the coming years to achieve the net-zero targets, aligning with the results of the previously mentioned studies.

As per the current state of the art, the heat pump technology can effectively operate up to a temperature range of 100 °C [20][21][8], with a few demonstrated applications in the range of 120°-160°C [8]. However, different studies are being conducted to increase the operating range and improve the achievable temperature lift [22][23][24][25]. Most of these investigations are research projects to develop specific technological components for high-temperature feasibility. However, only a limited number of studies are focused on assessing the feasibility of different cycle designs for the high-temperature range (>150°C) [26]. Such studies are vital to understand which cycle configurations and refrigerant choices

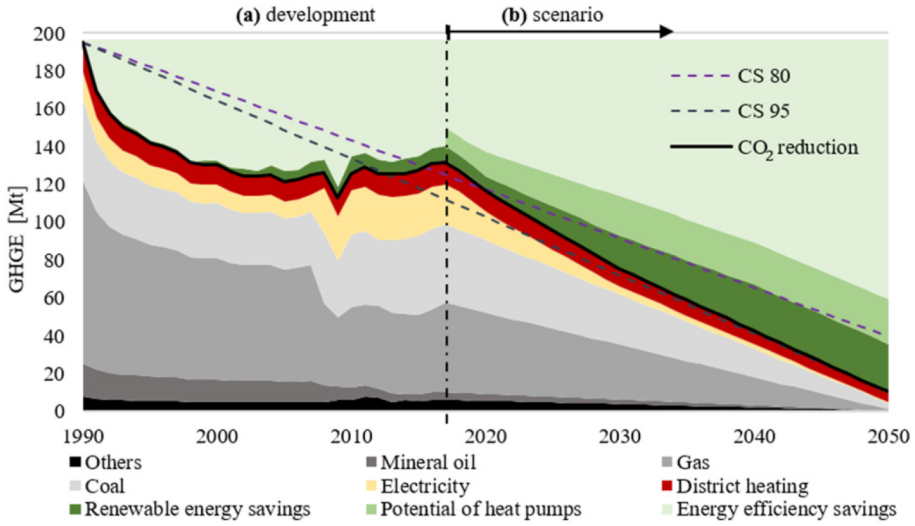

Figure 1.6: (a) Trend of greenhouse gas emissions by German industries, highlighting the causes and improvement drivers (b) Different strategic scenarios based on climate protection scenario 80 & 95 (CS 80 & 95) [19].

can provide the best solution for the considered metric of interest.

Motivated by this research gap, the current project aims to provide details about the characteristics of different heat pump configurations for different temperature levels (>150 °C). The focus of the investigation is to highlight the difference among different configurations in terms of maximum thermodynamic performance and the design requirements for the different sub-components. The results obtained from this study are expected to provide relevant information about which heat pump configurations can be considered for high-temperature applications (>150°C) and what are the associated challenges.

1.2. Project Overview

Figure 1.7 provides an overview of the different steps followed to define the project scope and the main research objectives based on the research gap found. Firstly, a literature review is conducted regarding the different possible heat pump categories. As a part of this review, the feasibility of different configurations at high-temperature conditions (> 150°C) is also assessed. Based on the findings of the literature exploration, the two most promising categories were selected, and the main research questions for the project were established. The details of all these steps leading up to the project scope and objectives are provided in Chapter 2. The remaining chapters provide details of the steps followed to answer the derived research questions. An overview of these steps, defining the structure of this report (from Chapter 2 onward), is also provided in Chapter 2.

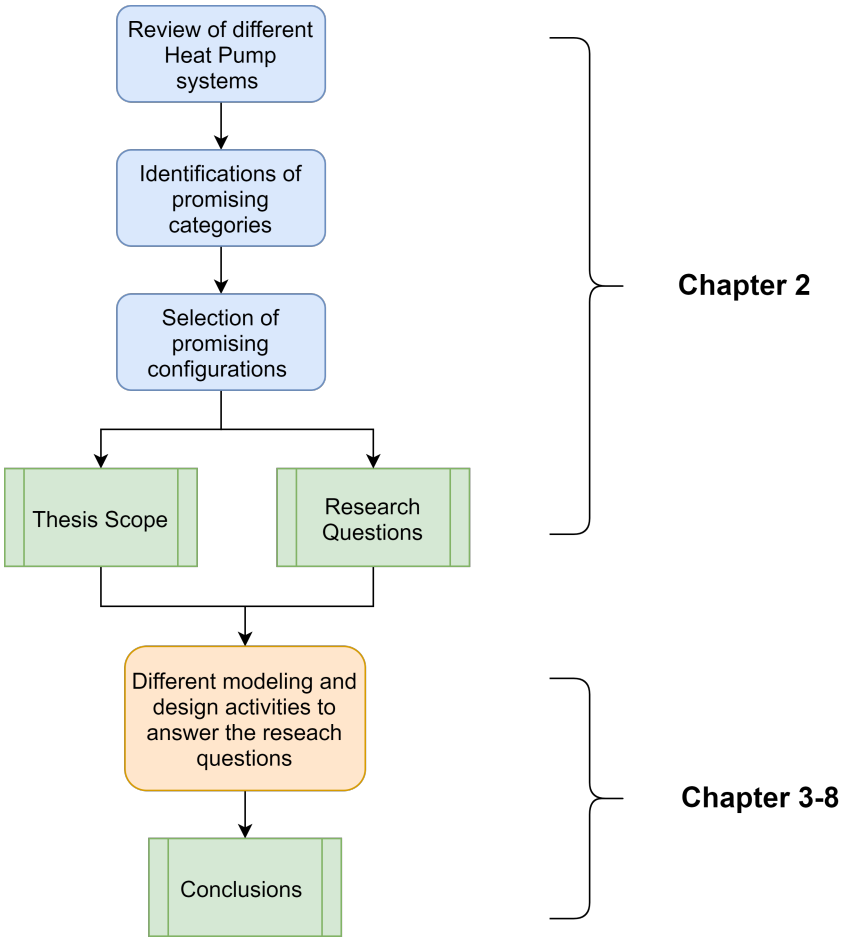

Figure 1.7: Project overview flow-diagram.

2

Potential High-Temperature Heat Pump Technologies - Literature Review

The literature review's main focus was on exploring and comparing possible heat pump technologies for high-temperature operating conditions. The definition of this "high-temperature" varies across the literature, depending upon the application. For the current study, the focus is on the heat pump (HP) systems capable of utilizing the low-temperature source (around 100°C) to achieve sink temperatures greater than 150°C.

2.1. Thermodynamic Performance Indicator

In terms of performance evaluation, the coefficient of performance ($\mathrm{COP_h}$) is a parameter widely used to indicate the thermodynamic performance of a specific heat pump system [27]. $\mathrm{COP_h}$ indicates the amount of thermal energy provided at the sink with respect to the provided work input. Thus, a high value of the $\mathrm{COP_h}$ for a specific HP system indicates better profitability and techno-economic competitiveness under the given operating conditions. The quantification of this parameter is shown inEquation (2.1). For the current study as well, $\mathrm{COP_h}$ is used as the primary indicator to quantify the thermodynamic performance of a specific heat pump system.

$$\mathrm{COP_h} = \frac{\text{Amount of useful thermal energy supplied at sink}}{\text{Amount of work input required}} = \frac{\dot{Q}_{\text{sink}}}{W} \tag{2.1}$$

2.2. Overview of Different Technologies

In literature, there are many heat pump configurations and design options that can achieve the desired operating conditions and provide the required temperature lift. This section provides detail about the different types of heat pump technologies explored in this study.

As a first step, the different heat pump options were categorized. The type of categorization can vary based on the operating cycle, use of refrigerant, heat-driven vs. electrically driven, etc. However, for the current study, the categorization shown in Table 2.1 is used.

Table 2.1 provides a generic overview of the different types of heat pump design options available in the literature. This implies that within each category, there are numerous configurations/design options available. The following sections provide a detailed overview of the studied literature with respect to

these categories, along with a general explanation of the working principle of each category.

Table 2.1: Categorization of heat pumps used for this study.

Category	Description
Reverse Rankine cycle based Heat Pumps	These configurations require the use of a refrigerant, which undergoes phase change during the operation.
Reverse Brayton cycle based Heat Pumps	These configurations require the use of a refrigerant, which remains in the vapor phase at all times during the operation.
Solid State Heat Pumps	This category includes the heat pumps that do not require mechanical compression [1] and instead are based on energy exchange due to electrocaloric, or magnetocaloric effect.
Thermally driven Heat Pumps	This category includes the heat pumps based on absorption/adsorption phenomenon.

2.3. Reverse Rankine cycle based Heat Pumps

Heat pumps based on the reverse Rankine cycle are one of the most commonly used types of heat pumps [28]. Based on the type of application and operating conditions, there are many different types of configurations possible within this category. For the simple cycle configuration, the heat pump has essentially four main components: an evaporator, condenser, compressor, and expansion valve. The corresponding thermodynamic cycle is shown in Figure 2.1. This is also known as the vapor compression cycle (VCC).

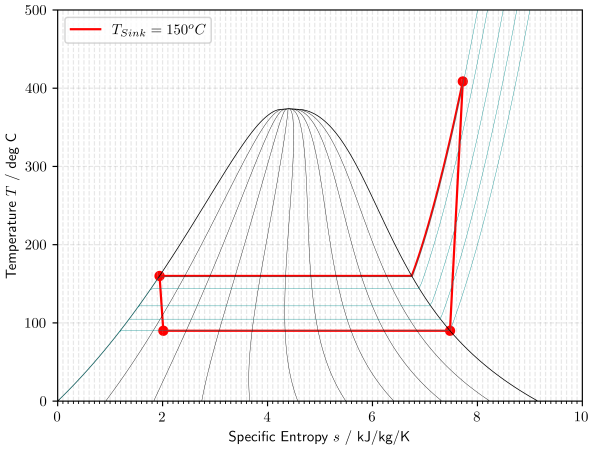

Figure 2.1: Simple vapor compression cycle (single stage, no superheating/subcooling and using H_2O).

As can be observed from the figure, there are four main processes in this type of heat pump, namely, evaporation, compression, condensation, and expansion. Firstly, the energy is taken by the refrigerant from the heat source, which then evaporates. The vapor is then compressed to increase its temperature and pressure by providing external work to the system. Next, the compressed vapor enters the condenser, where the fluid undergoes condensation. Further, this saturated liquid is expanded through an expansion valve to reduce its temperature and pressure. Finally, the expanded fluid enters the evaporator, closing the cycle.

[1] Some of the possible system configurations do use a heat transfer fluid instead to implement regeneration, which requires a pumping system.

The above-shown cycle is the most straightforward theoretical cycle for this type of heat pump. To increase the efficiency of the reverse Rankine cycle technology, a wide variety of options are available, ranging from changing refrigerant and type of components to the overall cycle configuration itself. Focusing mainly on the high-temperature applications, Table 2.2 shows the different vapor compression heat pumps available in the market.

Table 2.2: Reverse Rankine cycle based high-temperature heat pump systems available in the market (Compiled using data from [8]).

Company	Heat Pump ID	Type of Refrigerant	Maximum Sink Temperature [°C]	Maximum Capacity [kW]	Compressor Type	Reference
Kobe Steel	SGH 165 SGH 120	R134a/R245fa R245fa	165 120	660 370	Twin screw	[29], [30]
Vicking Heating Engines AS	HeatBooster S4	R1336mzz(Z)/R245fa	150	188	Piston	[31]
Ochsner	IWWDSS R2R3b IWWDS ER3b	R134a R245fa	130 130	750 750	Screw	[32],[33]
Hybrid Energy	Hybrid Heat Pump	R717/R718	120	2500	Piston	[34]
Mayekawa	Eco Sirocco Eco Cute Unimo	R744 R744	120 90	90 110	Screw	[35],[30]
Combitherm	HWW 245fa HWW R1234ze	R245fa R1234ze(E)	120 95	252 1301	Piston	[36],[37]
Durr thermea	Thermeco2	R744	110	2200	Piston	[35]
Friotherm	Unitop 22	R1234ze(E)	95	3600	Two stage Turbo	[38],[39]
Star Refrigeration	Neatpump	R717	90	15000	Screw	[40]

As can be observed in the table, most of the heat pump systems have a maximum sink temperature well below the desired temperature for the current study (200 °C). As per one report from Energieonderzoek Centrum Nederland (ECN) [41], for reverse Rankine cycle based heat pumps, the technology readiness level (TRL) is 9 up to 90 °C. However, for temperatures above 160 °C, the TRL is 5. This explains why no one reaches high temperature levels in the market products listed above. Nonetheless, it is interesting to look at the $\mathrm{COP_h}$ values of these heat pumps as a function of temperature lift (difference between sink and source temperature, denoted by ΔT_{lift}). This is shown in Figure 2.2, as derived from [8].

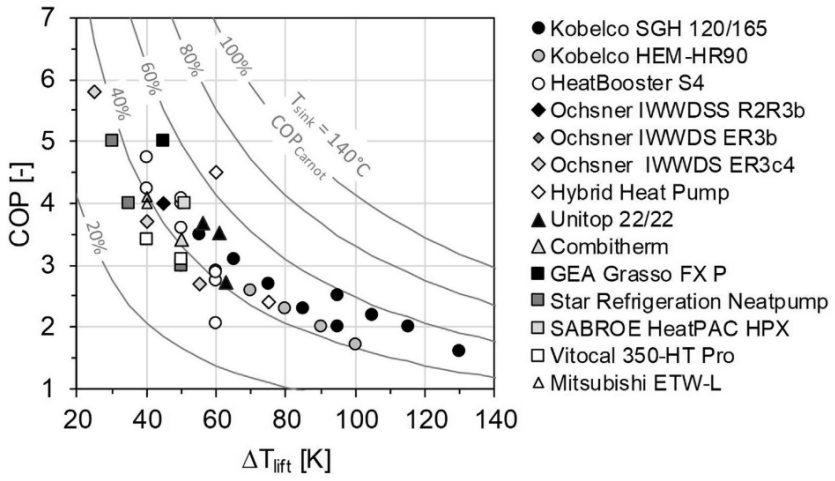

Figure 2.2: $\mathrm{COP_h}$ variation as a function of temperature lift for various industrial high-temperature heat pumps [8].

As can be observed from the figure, with an increase in ΔT_{lift}, there is a sharp decrease in the performance parameter of the heat pump. This also indicates the issue related to high-temperature applications, like those studied in this project, where the range of ΔT_{lift} considered is around 100-150 K. Based on Figure 2.2, it is clear that with the current state-of-the-art products, achieving such high-temperature lifts would lead to very low $\mathrm{COP_h}$ values and thus high input power requirements.

However, in recent years, many ongoing research projects have focused on improving vapor compression-

based systems to have higher performance values at high-temperature conditions. These projects involve innovative modifications of conventional vapor compression systems. Some of such projects are summarized in Table A.2. Based on the findings of these research projects, it is clear that there is a wide range of options to achieve a better performance value for vapor compression cycle-based heat pumps at high-temperature conditions. Qualitatively, based on the data shown in the Table A.2, for high sink temperatures around 160 °C and ΔT_{lift} of about 70 K, COP_{h} is in the range 2.5-3.

2.4. Reverse Brayton cycle based Heat Pumps

The working principle of the reverse Brayton cycle-based heat pump is similar to that of vapor compression cycles. The main difference lies in the fact that the heat transfer at both the source and sink sides does not occur at a constant temperature. The working fluid for this cycle configuration, thus, always remains in the vapor state. Because of this reason, during expansion, a certain amount of work can be recovered using the turbine to increase the cycle performance. Figure 2.3 shows a schematic of a simple single-stage reverse Brayton cycle based heat pump system, using CO_2 as working fluid.

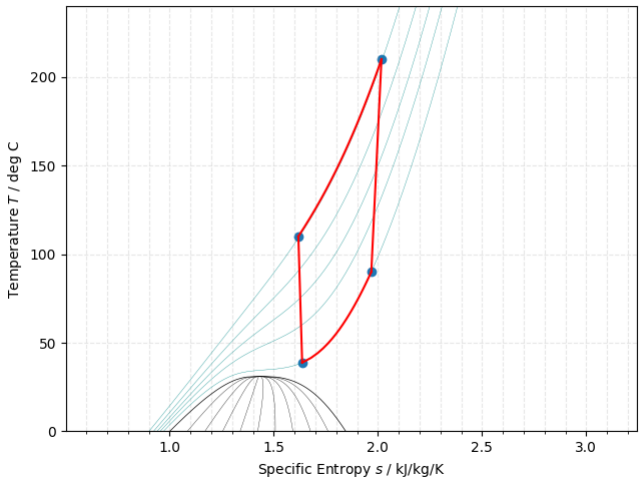

Figure 2.3: Single stage heat pump system based on reverse Brayton cycle (using CO_2).

In the past, the use of reverse Brayton cycle based configurations has always been very limited for both cooling and heating purposes because the thermodynamic performance for these cycles is found to be inherently lower than the reverse Rankine cycle based configurations [42]. For reverse Brayton cycle based configurations, the amount of turbomachinery work per unit of heat output is higher than the one obtained for the reverse Rankine cycle based configurations, which results in lower thermodynamic performance for reverse Brayton cycle based heat pump [42]. Due to the condensation of the working fluid in reverse Rankine cycle based configurations, low values of specific volume are obtained, which results in lower turbomachinery work requirements per unit of heat output. For the case of the reverse Brayton cycle, lower specific volumes can also be achieved by compressing the fluid close to the critical region. When operating the cycle under such conditions, the thermodynamic performance is found to be comparable to that of reverse Rankine cycle based configurations [26][43]. Therefore, high COP_{h} is achieved only when the operating conditions cover a particular region of the state diagram. With recent developments in the design of turbomachinery components, high-pressure near-critical region conditions are feasible for different working fluids, which makes the reverse Brayton cycle based systems very promising.

Similar to the case of the reverse Rankine cycle, the performance values of Brayton-type heat pump systems reported in the literature (both commercial and theoretical) for high-temperature levels were gathered, and they are reported in Table 2.3. In the table, the value of temperature lift is defined as

the difference between the maximum thermal source and minimum thermal sink temperatures. Very limited studies were found for high-temperature conditions. Most of them focused on low-temperature applications like water cooling, space heating, and cryo-cooling [44][45][46][47]. For high-temperature conditions, no experimental/commercial data was found. Thus all the values reported in Table 2.3 are the outcome of numerical studies. For the Brayton-type heat pump systems, higher sink temperature values were found, as these are not feasible for the reverse Rankine cycle due to the high-pressure ratio that they would entail. Defining a maximum feasible pressure limit is critical for the reverse Brayton cycle based systems due to the high values of minimum pressure level. Different studies have highlighted different feasible limits for this maximum operating pressure, ranging from 140 to 300 bar [48][49][50], depending on the selected techno-economic constraints.

Table 2.3: Overview of the studies related to reverse Brayton cycle based high-temperature heat pump.

Author	Type of System	Refrigerant	Maximum Sink Temperature [°C]	Temperature lift [°C]	COP	Reference
Huang R. et. al. (2022)	Two stage with refrigerant injection	CO_2	157.1	87.1	2.85	[46]
Mahdi Z. et. al. (2022)	Single stage	N_2	560	175	1.8	[51]
Kousidis V. et. al. (2019)	Single stage with recuperator	CO_2	360	-	1.43	[52]
Zuhlsdorf B. et. al. (2019)	Single stage with recuperator	CO_2	290	187.5	1.72	[26]
Kousidis V. et. al. (2019)	Single stage with recuperator	CO_2	300	-	1.5	[52]
Farres-Antunez P. et. al. (2019)	Single stage with recuperator	N_2	565	165	1.58	[53]
Zuhlsdorf B. et. al. (2019)	Single stage with recuperator	CO_2	217.5	175.2	1.61	[26]

2.5. Solid State Heat Pumps

The second category of explored heat pump technologies includes electrocaloric and magnetocaloric heat pumps. In this case, the work supplied to the system is used to initiate/amplify the temperature variation in the material due to the electrocaloric or magnetocaloric effects. In recent years, these heat pumps have been explored further, mainly because they do not require any moving parts or harmful refrigerants and can significantly decrease the global warming potential (GWP) or ozone depletion potential (ODP) [9]. Their initial exploration was for home heating/cooling applications, as these generally involve a small temperature difference between the source and sink temperature. However, with the immediate need for emission reduction, these technologies are also being explored for high-temperature applications [54].

Based on the underlying working phenomenon, it is possible to distinguish between two main types of heat pumps:

1. Magnetocaloric Heat Pumps
2. Thermoelectric Heat Pumps

The basic principles of both these technologies and the current research for high-temperature applications are presented in the following sub-sections.

2.5.1. Magnetocaloric Heat Pumps

The magnetocaloric Heat Pumps (MHP) are based on the magnetocaloric effect, namely the ability of a solid substance to get heated up when it is magnetized and cool down when the external magnetic field is removed. This interesting property has been used extensively in the industry, especially for

cryogenics, since its discovery in 1997. In an analogy with conventional VCC, this ability of the material to undergo a temperature change as a result of magnetic field change can be compared with the compression/expansion of the refrigerant in conventional VCC.

From a thermodynamic point of view, this effect is directly related to the entropy changes of the magnetocaloric material used in the system. The entropy of a ferromagnetic material can be written as shown in Equation (2.2) (at constant pressure). In Equation (2.2), $S_{\mathrm{m}}(T,H)$, $S_{\mathrm{lat}}(T)$ and $S_{\mathrm{el}}(T)$ describe the contribution of magnetic (due to magnetization of material), lattice (due to lattice vibration) and electronic (due to presence of free electrons) entropy to the total entropy of the material, respectively. As can be observed, the magnetic contribution depends on both the applied magnetic field and the temperature, while the others are only a function of temperature.

$$S(T,H) = S_{\mathrm{m}}(T,H) + S_{\mathrm{lat}}(T) + S_{\mathrm{el}}(T) \tag{2.2}$$

When the magnetic field is applied to the ferromagnetic material under adiabatic conditions, the $S_{\mathrm{m}}(T,H)$ contribution decreases as the magnetic spin system tries to align with the externally applied field. However, since the total entropy remains constant, the other two contributions must increase to compensate. As a result of this, a temperature increase is experienced. This temperature increase is called the adiabatic temperature change (ΔT_{ad}). When the magnetic field is removed, the opposite is experienced: the magnetic spin system tends to return to the initial arrangement by capturing the energy from lattice vibrations. As a result, the thermal entropy is reduced, and the material returns to its initial temperature. This working principle is also sketched in Figure 2.4.

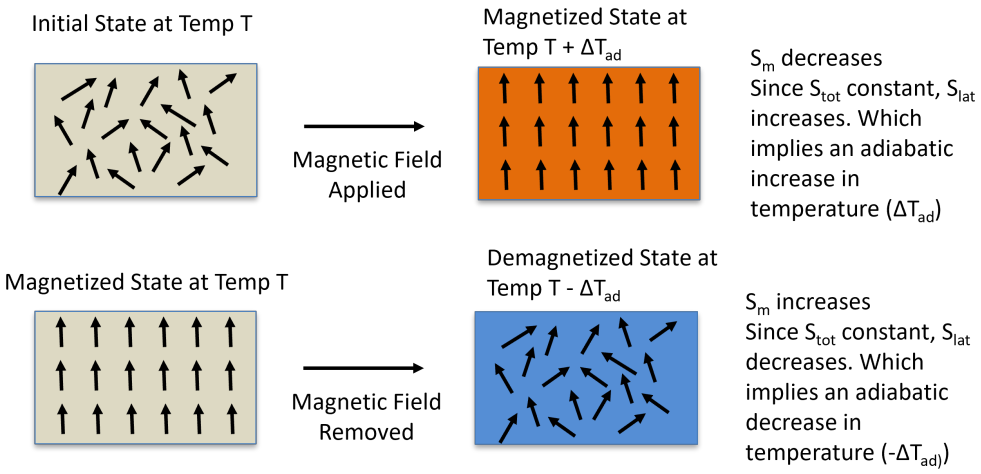

Figure 2.4: Visualization of the magnetocaloric effect.

The behavior described above is valid for the case of the adiabatic application of an external magnetic field. If the magnetic field is applied at isothermal conditions, the total entropy would no longer be a constant and would decrease. Thus, since the temperature is kept constant, the lattice and electronic entropy contributions would no longer be able to change to compensate for the decrease in magnetic entropy contribution.

Both of the above-discussed transformations can be used in a thermodynamic cycle to pump energy from a low temperature level to a high temperature one. Three main cycles are usually considered for magnetic heat pumps. These are shown in Figure 2.5 (derived from [55]) and are briefly discussed in the following. All the cycles shown in Figure 2.5 are ideal cycles and thus do not reflect the effect of any system loss.

Figure 2.5a represents an ideal Carnot cycle based MHP. In this cycle, the process between states 1 and 2 corresponds to adiabatic magnetization. This process needs to be quick to avoid a large amount of thermal energy being lost in the surroundings through conduction [55]. From states 2 to

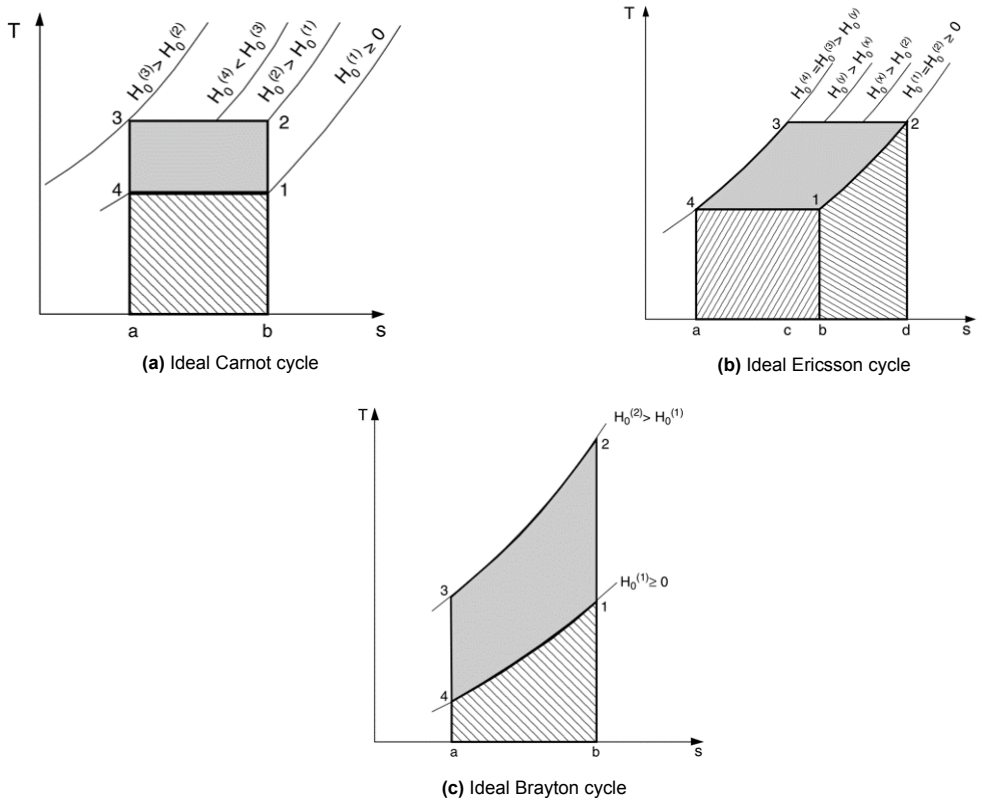

(a) Ideal Carnot cycle

(b) Ideal Ericsson cycle

(c) Ideal Brayton cycle

Figure 2.5: Different thermodynamic cycles used for magnetic heat pump [55].

3, further magnetization occurs at a constant temperature. The thermal energy is transferred as heat into the sink during this process. After this, from states 3 to 4, demagnetization occurs under adiabatic conditions. Finally, from states 4 to 1, further demagnetization occurs. However, during this process, thermal energy is absorbed from the source, thus maintaining constant temperature conditions.

Figure 2.5b depicts an ideal Ericsson cycle based MHP. This cycle is a regenerative cycle, implying that a heat transfer fluid circuit is present, which helps to recover thermal energy from later steps of the cycle is utilized back into the cycle. From states 2 to 3, isothermal magnetization occurs. Here, thermal energy is released (to sink) simultaneously with magnetization, thus ensuring isothermal conditions. From states 3 to 4, the regenerative fluid absorbs excess thermal energy, decreasing the temperature of the magnetocaloric material (MCM) further. This process occurs at a constant magnetic field. Further, from states 4 to 1, demagnetization occurs. During this process, heat transfer co-occurs with demagnetization, maintaining isothermal conditions. Finally, from states 1 to 2, the thermal energy from the regenerative fluid is released, at a constant magnetic field, bringing the temperature back to the initial state and closing the cycle.

Figure 2.5c represents an ideal Brayton cycle-based MHP. In this cycle, the transformation from state 1 to 2 corresponds to adiabatic magnetization. As a result, an adiabatic temperature increase is experienced by the MCM. From states 2 to 3, thermal energy is released to sink at a constant magnetic field. Further, from states 3 to 4, the external magnetic field is removed at adiabatic conditions, leading to an adiabatic decrease in temperature. From states 4 to 1, the thermal energy is absorbed from the source under a constant magnetic field, thus completing the cycle.

To better understand the performance of the different cycles, the performance of the ideal Ericsson cycle and ideal Brayton cycle were analyzed using simplified first-principles mathematical models available in the literature. For both cycles, Gadolinium (Gd) is used as the MCM. The details of the conducted analysis and results are discussed in the following.

Ideal Ericsson Cycle Based MHP (with regeneration)

The overall process of this cycle is already shown in Figure 2.5b. To model this cycle, perfect regeneration was assumed. Thus, it was assumed that the regenerator had no heat transfer losses. As shown by Figure 2.5b, the thermal energy addition/release happens under isothermal conditions. Thus, the thermal energy involved in this isothermal process can be estimated as shown in Equation (2.3), where $\frac{\partial S_m}{\partial H}$ represents the change in magnetic entropy due to change in the magnetic field and ΔH represents the change in the magnetic field.

$$Q = T\Delta S_{m|T} = T\left(\frac{\partial S_m}{\partial H}\right)_T \Delta H \tag{2.3}$$

Further, to model this change in magnetic entropy, the modeling methodology used in [56] was used. This methodology is based on the Curie-Weiss Law to model the change in entropy of the material. According to this law, the change in magnetic entropy with variation in the magnetic field can be written as shown in Equation (2.4). The explanation of the different parameters used in this equation and their respective values are provided in Table A.1.

$$\begin{gathered}\left(\frac{\partial S_m}{\partial H}\right)_T = -C\,(H + H_{ext}) \cdot [T - \Gamma]^{-2} \\ \Gamma = \frac{12CkT_C J_A^2\,(J_A+1)^2}{N_m N_S\,(N_S+1)\,\mu_B^2\,[3J_A\,(J_A+1) + N_S\,(N_S+1) - J_O\,(J_O+1)]^2}\end{gathered} \tag{2.4}$$

Using this notation, combined with Equation (2.3), the amount of reversible thermal energy released at the sink (Q_h) and the amount of reversible thermal energy absorbed at the source (Q_c) can be written as shown in Equation (2.5).

$$\begin{aligned}Q_h &= T_h\,(S_2 - S_1) = -C\frac{T_h}{(T_h - \Gamma)^2}\,(H_1 - H_0) \\ Q_c &= T_{\text{cold}}\,(S_4 - S_3) = C\frac{T_{\text{cold}}}{(T_{\text{cold}} - \Gamma)^2}\,(H_1 - H_0)\end{aligned} \tag{2.5}$$

Thus, the $\mathrm{COP_h}$ of the cycle can be calculated as shown in Equation (2.6), where the amount of work input is equal to Q_h - Q_c.

$$\mathrm{COP_h} = \frac{1}{\frac{T_{cold}}{T_h}\left(\frac{T_h - \Gamma}{T_{\text{cold}} - \Gamma}\right)^2 + 1} \tag{2.6}$$

Using the above-given formulations, the $\mathrm{COP_h}$ of a Gadolinium (Gd) based cycle, one of the most common types of MHP, was estimated as a function of the total MCM mass, which is proportional to the number of atoms in the system (N_m in the Equation (2.4)) [57] [58]. Further, a source and sink temperature of 100°C and 250°C, respectively, were assumed. Note that the MCM mass or N_m is the only degree of freedom for optimizing the $\mathrm{COP_h}$ once the temperature levels are fixed. The $\mathrm{COP_h}$ trend is illustrated in Figure 2.6.

As can be observed from the figure, the $\mathrm{COP_h}$ values reach an asymptote with increasing mass of the MCM. Further, the achieved $\mathrm{COP_h}$ values for this high-temperature range are very low compared to the results obtained for VCC. The regeneration heat losses would further decrease the $\mathrm{COP_h}$. Note also

that the methodology used for this analysis approximates the actual thermodynamic process. Significant deviations from experimental results may occur for high-temperature applications. Nevertheless, these simple calculations help assess the expected performance of an MHP [56].

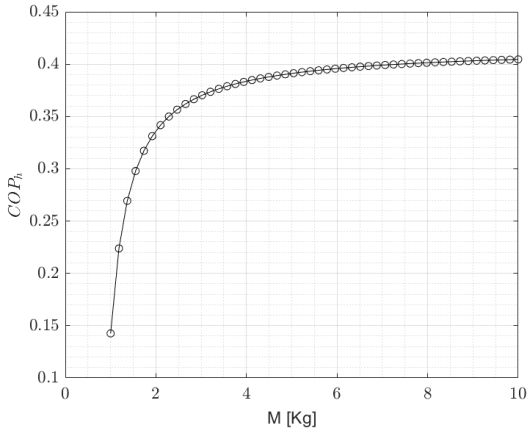

Figure 2.6: $\mathrm{COP_h}$ Results obtained for ideal Ericsson cycle based MHP as a function of the total mass of magnetocaloric material (Gadolinium).

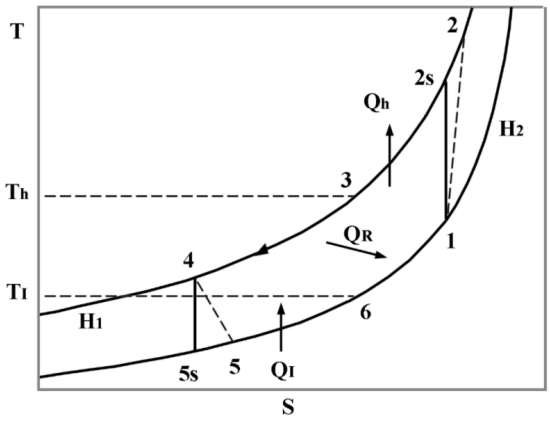

Figure 2.7: Ideal Brayton cycle based MHP, with regeneration [56].

Ideal Brayton Cycle Based MHP (with regeneration)

The second cycle chosen for analysis is the ideal Brayton cycle with regeneration. The ideal Brayton cycle sketched earlier in Figure 2.5c does not feature any regeneration. An ideal Brayton cycle-based MHP with regeneration is shown in Figure 2.7 (derived from [56]). To model this cycle, similar to the previous case, no thermal losses are assumed during regeneration. Compared to the Ericsson cycle, evaluating reversible thermal energy released/absorbed becomes difficult as the temperature is not constant (adiabatic process).

To estimate the amount of thermal energy released/absorbed for this cycle type, the model provided in [56] is used. This model is based on Helmholtz's free energy equation, using statistical mechanics principles to get an estimate for the solution. Based on this approach, the specific heat at a constant magnetic field C_H, can be written as shown in Equation (2.7), where C is the Curie constant, H is the magnetic field, and T is the temperature.

$$C_H = \frac{CH^2}{T^2} \tag{2.7}$$

Using this equation, the amount of reversible thermal energy released/absorbed (Q_h/Q_c) can be written as shown in Equation (2.8), where β is the ratio of the magnetic fields (H_2/H_1), with $H_2 > H_1$. Further, the convention of state numbering is consistent with the one shown in Figure 2.7.

$$\begin{aligned} Q_h &= CH_2^2\beta^2\left(T_h^{-1} - T_2^{-1}\right) \\ Q_c &= CH_2^2\left(T_5^{-1} - T_l^{-1}\right) \end{aligned} \tag{2.8}$$

As can be observed from Equation (2.8), this expression involves the intermediate temperatures T_2 and T_5, which are not available at this preliminary stage. To further simplify the expression, the definition of isentropic efficiency of the adiabatic processes (η_e/η_c) and degree of regeneration (α) are introduced, see Equation (2.9).

$$\eta_e = \frac{T_4 - T_5}{T_4 - T_{5s}} \quad ; \quad \eta_c = \frac{T_{2s} - T_1}{T_2 - T_1}$$
$$\alpha = \frac{T_1}{T_h} \tag{2.9}$$

Using these expressions, the amount of reversible thermal energy released/absorbed can be written as shown in Equation (2.10).

$$Q_h = CH_2^2 \left\{ \frac{\tau\beta^2 \left[\alpha \left(\beta + \eta_c - 1\right) - \eta_c\right]}{\alpha T_l \left(\beta + \eta_c - 1\right)} \right\}$$
$$Q_c = CH_2^2 \left[\frac{\alpha + \left(\alpha\beta^2 - 1\right)\tau - \alpha\beta \left(\eta_e - \beta\eta_e + \beta\right)}{\alpha\beta T_l \left(\eta_e - \beta\eta_e + \beta\right)} \right] \tag{2.10}$$

Thus, the $\mathrm{COP_h}$ of the cycle can be estimated by Equation (2.11), where the amount of work input is computed as Q_h - Q_c. Thus, the electric work associated with the magnetic field is estimated using only thermodynamic considerations, and the electric losses are neglected.

$$\mathrm{COP}_h = \frac{Q_h}{Q_h - Q_c} \tag{2.11}$$

As can be observed from Equation (2.10) and Equation (2.11), several unknown parameters are needed to compute the $\mathrm{COP_h}$ value for this system. Since no specific data is available for these parameters, it was decided to treat them as a variable and analyze the effect of each parameter separately by only varying one parameter at a time.

First, the effect of β is analyzed, see Figure 2.8. The figure also reports the value of the other parameters kept constant. As can be observed from the figure, the COP value becomes highest for a specific β value, called β_m. When $\beta > \beta_m$, the effective $\mathrm{COP_h}$ starts to decrease rapidly.

Next, the effect of α is analyzed. In this case, the value of β is equal to β_m. The value of α is varied between T_h/T_c and 1, which correspond to the case of no regeneration and maximum regeneration, respectively. The results are shown in Figure 2.9. As can be observed from the figure, with an increasing degree of regeneration, the effective $\mathrm{COP_h}$ increases, which is in line with expectations, as the amount of “wasted” thermal energy is reduced as the value of α is increased.

The definition of α also has an impact on the value of βm, as shown in Figure 2.10. Notably, the required magnetization level decreases with an increasing degree of regeneration. This is expected since less thermal energy is wasted with a higher degree of regeneration.

Further, the effect of isentropic efficiency on $\mathrm{COP_h}$ is evaluated, see Figure 2.11. With increasing isentropic efficiency, the effective $\mathrm{COP_h}$ increases. This is mainly because as the isentropic efficiency increases, the irreversibility of the adiabatic process is lowered, which leads to higher performance of the system.

The typical $\mathrm{COP_h}$ range for MC heat pumps can be estimated from all the results presented above. For the high temperature lift considered, this is between 1.2-1.6. However, notice that these values are for very high values of process efficiency and that thermal losses during regeneration are neglected. Thus, the $\mathrm{COP_h}$ values obtained using this cycle are higher than the ones obtained for Ericsson cycle-based MHP but still are lower than those obtained for VCC-based heat pumps.

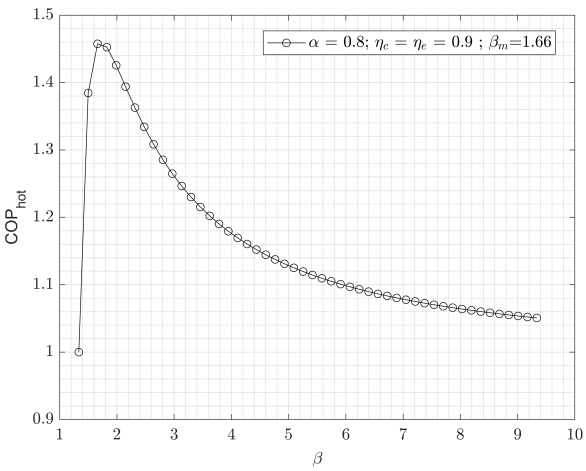

Figure 2.8: Effect of β on $\mathrm{COP_h}$ for Ideal Brayton cycle based MHP (with regeneration).

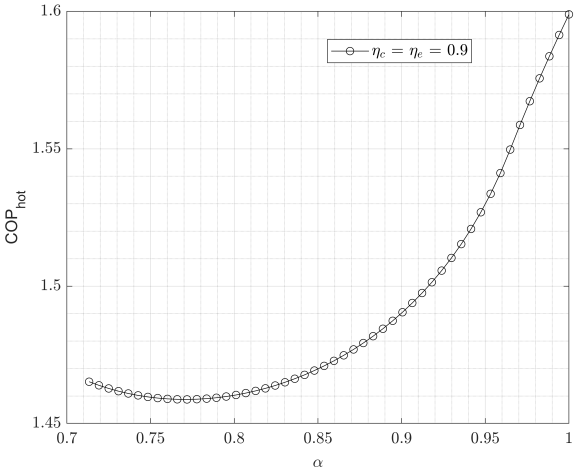

Figure 2.9: Effect of degree of regeneration (α) on $\mathrm{COP_h}$ for Ideal Brayton cycle based MHP (with regeneration).

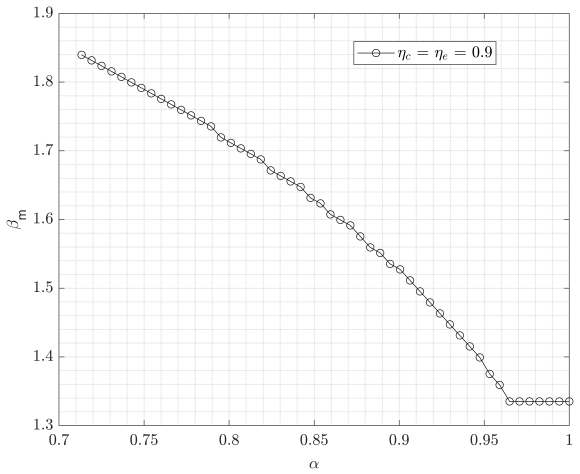

Figure 2.10: Effect of α on β_m for Ideal Brayton cycle based MHP (with regeneration).

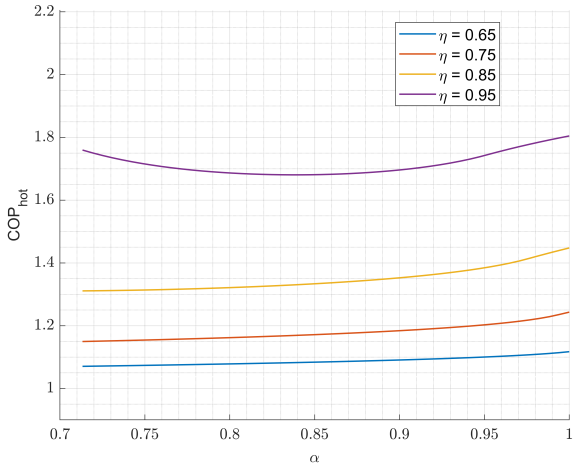

Figure 2.11: Effect of isentropic efficiency of adiabatic processes on $\mathrm{COP_h}$ for Ideal Brayton cycle based MHP (with regeneration).

Recent Advancements and Conclusion for High-Temperature Application

As can be observed from the above analysis, the conventional MHP cycles have generally very low $\mathrm{COP_h}$ for a high-temperature lift. Therefore, new cycle concepts have been investigated over the years, such as active magnetic regeneration (AMR). This cycle configuration allows a higher ΔT_{lift} than that commonly achieved by magnetocaloric effect only. Thus, most of the current research related to MHP is focused on AMR [57] [58] [59]. One possible implementation of the AMR concept is shown in Figure 2.12 [58]. The MCM generally has a porous structure that allows for the circulation of a heat transfer fluid [58]. Thus, the MCM performs both the role of the element, which realizes part of the temperature lift as well as of the regenerator for the heat transfer fluid. The latter does not need to undergo a phase change and is used to transfer the thermal energy from the thermal source to the sink.

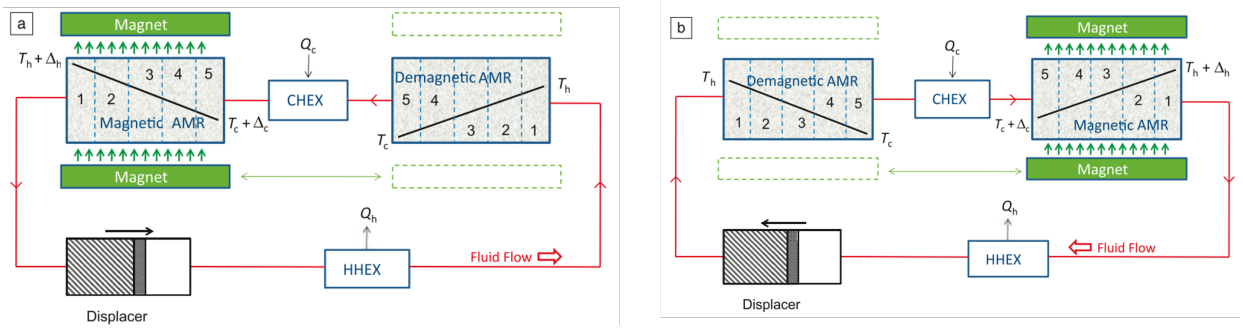

Figure 2.12: A representation of the AMR cycle working principle for MHP [58].

As mentioned, MHPs were initially (and are still) investigated for residential applications involving relatively low temperature ranges and temperature lifts. At about room temperatures and for temperature lifts less than 9 K, the $\mathrm{COP_h}$ of MHP ranges between 5-25, depending on the characteristics of the MCM used as well as of the adopted cycle configuration [57] [60]. However, there are a few studies that investigated the performance of this kind of heat pump for high temperature levels. The reason thereof is the stringent magnetic field requirements. To achieve a temperature lift from 0.5° to 2°C, a change in the magnetic field of around 1 Tesla is required [9]. A couple of studies have shown an exponential decrease in the $\mathrm{COP_h}$ values as the temperature of the hot sink is increased for a constant cold source temperature [57] [61]. Thus, for MHP, it can be concluded that the temperature range is still relatively very low compared to the ones in industrial applications. Nonetheless, the $\mathrm{COP_h}$ values achieved at low temperatures are very promising. Based on the current research findings, it is expected that MHP technology will become applicable also to high temperatures applications, but the research is still at preliminary stages [57] [61]. Based on the studied literature, the conventional VCC seems, in any case, more suitable than MHP to satisfy the process heating demand of the industry.

2.5.2. Thermoelectric Heat Pumps

The thermoelectric heat pumps (TEHP) exploit the so-called thermoelectric effect, also known as the "Peltier effect", namely the ability of a material to undergo a temperature change when a voltage difference is applied. As a result of this effect, thermal energy can be transported from low to high temperatures without needing any moving parts. To have an effective energy transfer, the choice of the material is critical as this needs to satisfy a few properties. In general, the material needs to have high electrical conductivity while having a low thermal conductivity. This makes semiconductor materials the only suitable option [9].

The extent of the Peltier effect is directly related to the applied voltage. The amount of thermal power generated from this effect is given by Equation (2.12), where π is the Peltier coefficient and is a function of temperature; I is the current going through the material.

$$\dot{Q}_P(T) = I\ \pi(T) \tag{2.12}$$

The magnitude of the heat flux per unit of current that can be achieved depends on the material's properties, specifically the energy density spectrum, which is usually modeled by π. Doped semiconductors have been found to have the highest value for this coefficient and thus are promising for cooling or heating applications [62].

To compare the thermoelectric potential of different materials, ZT is usually used as the figure of merit [9] [63]. ZT is a dimensionless quantity based on material properties such as electric and thermal conductivity. It reflects the potential of a material to exhibit the thermoelectric effect. The definition of ZT is given in Equation (2.13), where γ is electrical conductivity, α is the Seebeck coefficient, and κ is the Thomson coefficient. A high value of $ZT$is desired as it implies that a more efficient energy

conversion (electric to thermal energy) can be achieved.

$$ZT = \frac{\gamma \alpha^2}{\kappa} T \tag{2.13}$$

Using the value of ZT, an approximate theoretical maximum performance value of TEHP can also be calculated. The required formulation is shown in Equation (2.14) [9], where the first term is essentially the Carnot efficiency term and the second term accounts for the material efficiency. Observing the formulation, it can be deduced that ZT should roughly be at least 2 to have the performance of TEHP comparable with conventional VCC. This formulation also shows the severe negative effect of high-temperature lift on performance. This is also observed in a few studies, where the value of $\mathrm{COP_h}$ decreases rapidly as the temperature increases [63] [64] [65].

$$\mathrm{COP_{h,max}} = \frac{T_{\text{sink}}}{T_{\text{sink}} - T_{\text{source}}} \cdot \frac{\sqrt{1 + Z\overline{T}} - \frac{T_{\text{source}}}{T_{\text{sink}}}}{\sqrt{1 + Z\overline{T}} + 1} \quad \text{, where} \quad \overline{T} = \frac{T_{\text{sink}} + T_{\text{source}}}{2} \tag{2.14}$$

The variation of $\mathrm{COP_h}$ with ZT, for the temperature range 100°C - 250°C is shown in Figure 2.13. As can be observed from the figure, the $\mathrm{COP_h}$ range of such systems is well below the conventional VCC, for typical semiconductors, at the given temperature range.

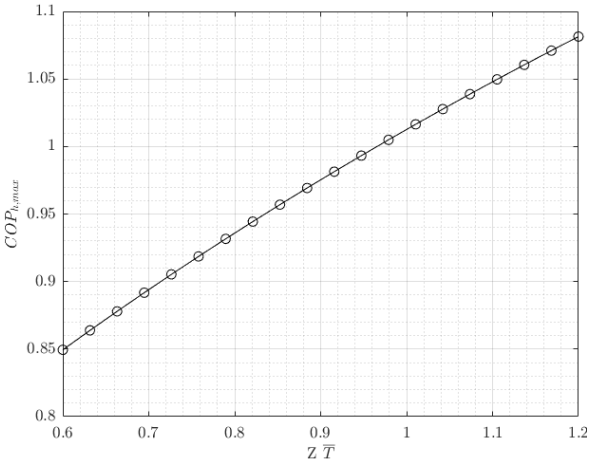

Figure 2.13: Variation of theoretical maximum $\mathrm{COP_h}$ of TEHP with figure of merit of material (T_{source} = 100°C ; T_{sink} = 250°C).

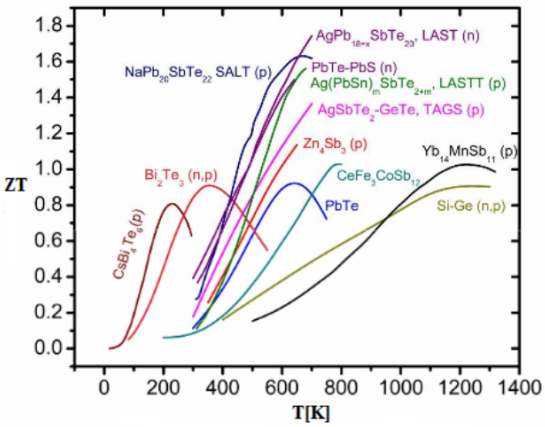

Figure 2.14: Variation of the figure of merit with temperature for different materials [66].

In recent years extensive research has been done to find materials having high ZT values [66]. ZT values commonly found are shown in Figure 2.14, as a function of the operating temperature [66]. As can be observed from the figures, the values of ZT are below 2 for all the materials, and the ZT value is also highly dependent on the operating temperature.

Based on the obtained results, it can be concluded that the TEHP has many advantages in terms of reliability, as it does not require any moving parts. However, the achievable temperature lift is relatively small and more suitable for domestic applications. For the case of high-temperature applications, those investigated in the present project, the performance gain is no longer present as the efficiency value drops significantly.

2.6. Thermally driven Heat Pumps

As the name suggests, this category of heat pumps directly utilizes the thermal energy available rather than requiring mechanical energy for compression, as is the case for the VCC-based heat pumps. The general efficiency of this category of heat pumps is usually found to be lower than that of conventional VCC-based heat pumps [9]. Nevertheless, these systems are promising for some industrial applications as only a few energy-conversion steps are involved with almost no moving parts [67]. Within this category, there are two main types of systems, namely

1. Absorption-based Heat Pumps
2. Adsorption-based Heat Pumps

The principles of each of these technologies and the current research for their potential use in the high-temperature applications are summarized in the following sub-sections.

2.6.1. Absorption Heat Pumps

The working principle of absorption heat pumps is similar to that of VCC-based heat pumps. The main difference is that mechanical compression is replaced by a kind of ”thermal” compression in the case of absorption heat pumps. Here, the thermal energy is directly supplied to the liquid solution present in the desorber ($\dot{Q}_{\text{desorb}}$). The absorber of the system acts as a replacement for the suction phase of the mechanical compressor of VCC and the desorber as a substitute for the discharge phase. A schematic of a general absorption heat pump is shown in Figure 2.15 (derived from [9]).

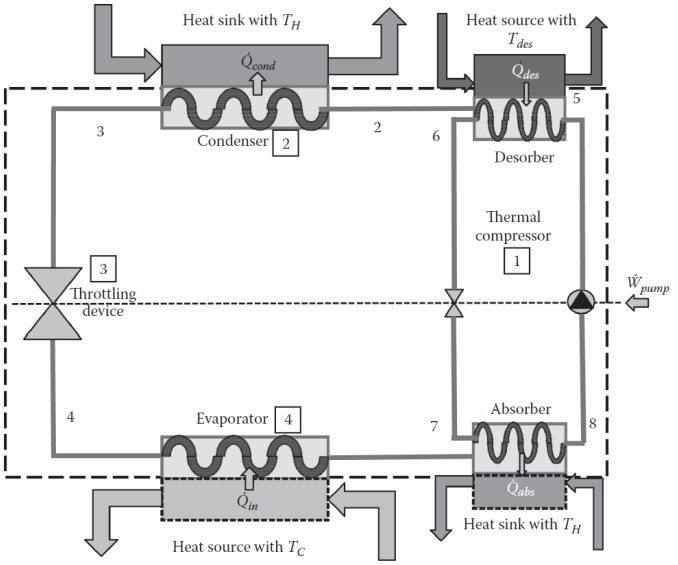

Figure 2.15: A general schematic of absorption heat pump [9]

As can be observed from the figure, except for the compression phase, the rest of the components and processes are similar to those observed in conventional VCC-based heat pumps. However, for absorption heat pumps, the required pump work (W_{pump}) is relatively small as compared to the one needed for VCC systems. This is because the working fluid is pressurized in the liquid phase. Further, the thermal energy is delivered at both condenser ($\dot{Q}_{\text{conden}}$) and the absorber ($\dot{Q}_{\text{absorb}}$) and therefore, both needs to be accounted when considering the total performance. Thus, the general $\mathrm{COP_h}$ for these kinds of systems can hebe computed as shown in Equation (2.15).

$$\mathrm{COP_h} = \frac{\dot{Q}_{\mathrm{absorb}} + \dot{Q}_{\mathrm{conden}}}{\dot{Q}_{\mathrm{desorb}} + W_{\mathrm{pump}}} \tag{2.15}$$

With respect to conventional VCC, these systems tend to have lower efficiency due to the presence of thermodynamic losses in different processes, which play a significant role during operation [56] [67]. However, to compare the two, the actual primary energy consumption associated to the electric power delivered of the VCC system should be accounted in the $\mathrm{COP_h}$ calculation. The performance and feasible operating range of these absorption systems are significantly dependent on the choice of the refrigerant-absorbent mixture. Most commonly used combinations are water-ammonia (H_2O-NH_3) and water-Lithium Bromide (H_2O-LiBr) [68].

These systems offer a wide range of operating temperatures, depending on the selected combination of refrigerant/absorbent and cycle configuration. Based on the few studies found in the literature, focusing on the temperature range of 100 °C or higher, the $\mathrm{COP_h}$ range for these kinds of systems was found to be around 0.8-1.3, depending on cycle configuration and refrigerant/absorbent combination [67] [68] [69]. Thus, the $\mathrm{COP_h}$ range of these kinds of systems (based on conventional cycles) is lower than the conventional VCC for the high-temperature range.

2.6.2. Adsorption Heat Pumps

The adsorption heat pump is the second type of thermal heat pump. These systems allow to directly use the thermal energy available and thus are very promising from emissions and energy-saving viewpoint. An illustration of the working principle is shown in Figure 2.16 [9]. The functionality of both condenser and evaporator is similar to the one observed for absorption-based systems. However, the process of ”compression” is different. Two beds are present in the thermal compressor. These beds contain the adsorbent and the external fluid flows through them.

The working fluid undergoes a phase change during the desorption process, leading to an increase in the pressure in the desorption volume. This increase in pressure is continued until the pressure is high enough to actuate a controlling valve placed between the bed and the condenser [9]. The vapor is then condensed in the condenser, maintaining a constant pressure. During the process of the adsorption, the pressure in adsorpent bed decreases until it is low enough to actuate the controlling valve placed between the bed and the evaporator. The vapor from the evaporator then enters the adsorpent bed. In this way, during the adsorption, a constant pressure is maintained at the evaporator. At a certain point, the adsorpent bed gets saturated with the working fluid. Therefore, the required regeneration is provided by the desoprtion process. To achieve a continuous cycle, the working fluid flow is switched between the two beds. During the adsorption process (exothermic process), the flow which needs to be heated flows the adsorpent bed, whereas the opposite is true for the desorption bed.

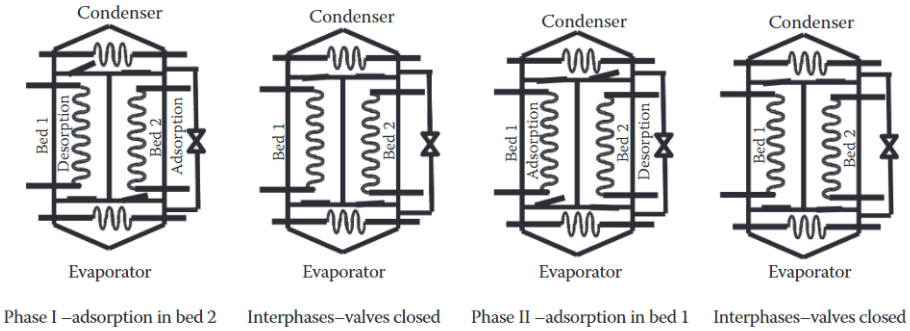

Figure 2.16: A general schematic of absorption heat pump [9]

The most commonly used combinations of working fluid (or refrigerant) and adsorbent are water-silica,

ammonia-carbon(activated), and water-zeolite [70]. These type of systems allows for a broad operational spectrum in terms of temperature, as the used adsorbent beds are always solid [56] [70]. Further, based on the type of adsorbent, two different types can be identified: physical adsorption and chemical adsorption. The main difference between the two is related to the change in state/composition of the adsorbent during the cycle. In the case of physical adsorption, intermolecular forces are generated between the two compounds, while in the case of chemical adsorption a chemical reaction occurs.

Despite the advantages of no moving parts, no harmful refrigerants, and direct use of thermal energy, these systems have a very low $\mathrm{COP_h}$ [71] [72]. This is mainly related to the irreversibilities occurring during adsorption/ desorption [72]. Further, limited specific cooling power (SCP) is also one of the significant factors for these kinds of systems [9]. In cooling mode, the most common application for adsorption heat pumps, the COP lies in the range of 0.3-0.6 for a temperature lift around 50-60 K [70] [72] [73]. The expected COP range for heating applications would be then around 1.3-1.6 but for a temperature range lower than that investigated in this work. For higher temperature lifts and high operating temperatures, this is expected to decrease further [70] [73].

2.7. Selected Configurations

Based on the conducted literature study, heat pump systems based on the reverse Rankine cycle and reverse Brayton cycle were found to be the most promising for high temperature industrial applications, considering both the thermodynamic performance and feasibility. Thus, these two technologies were further studied in the project. For each of this heat pump concepts, different possible configurations were identified [74][75][76]. The reference studies used for the selection of the configurations were mainly for low-temperature applications. These identified configurations only represent a subset of all the different possible combinations which can be made to match the needs of a specific process. To limit the scope of the current project, these selected configurations were deemed sufficient.

2.7.1. Reverse Rankine cycle based Heat Pumps

Figure 2.17 shows all the selected configurations for reverse Rankine cycle based heat pump systems. The first one is the simple single-stage configuration (Figure 2.17a), which was described earlier in Section 2.3. The second configuration (Figure 2.17b) is the two-stage configuration i.e. two compression stages are present. In this configuration, the superheated vapor at the exit of the first compressor is mixed with the low temperature condensate (referred to as secondary stream), before it enters the second compressor. As a result, the inlet temperature of the fluid in the second compressor is reduced, leading to a decreased in the compression power and a higher performance value for the system. This secondary stream is taken from the exit of the condenser by splitting the main stream into two sub-streams with different mass flow rates. The secondary sub-stream is first expanded to further reduce the temperature and match the pressure of the vapor leaving the first compression stage.

The third configuration (Figure 2.17c) also features two compression stages. In this case, the secondary stream used to cool down the vapor leaving the first compressor is taken from a flash-tank and thus, is in a saturated vapor state. The other output stream of the flash-tank is a saturated liquid, which is further expanded till the evaporator pressure level. The fourth configuration (Figure 2.17d) is similar to the third one. However, in this case, a saturator is used in place of the flash tank. The saturator is essentially a flash-tank with an intercooler. The output stream of the first compressor enters the saturator in this case, along with the expanded condensate coming form a first expansion valve. Therefore, a two-phase flow stream and a superheated vapor stream enters the saturator. The streams leaving the saturator are a saturated vapor and a saturated liquid stream. Saturated vapor, thus, enters the second compressor, similarly to the first compressor (assuming no superheating). The final configuration (Figure 2.17e) is also a two-stage configuration but uses an internal heat exchanger in place of the saturator or the flash tank. The stream leaving the condenser is further subcooled by using this internal heat exchanger and thus heating the secondary stream to be mixed with the output stream of the first compressor.

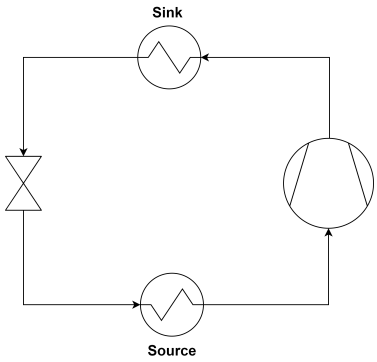

(a) Single Stage

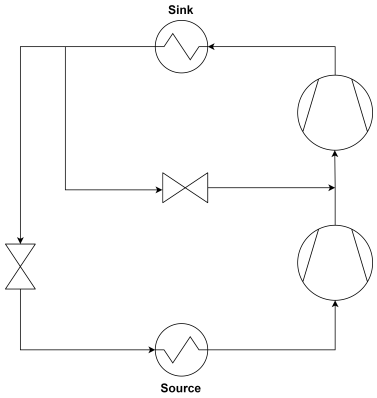

(b) Two stage with direct injection

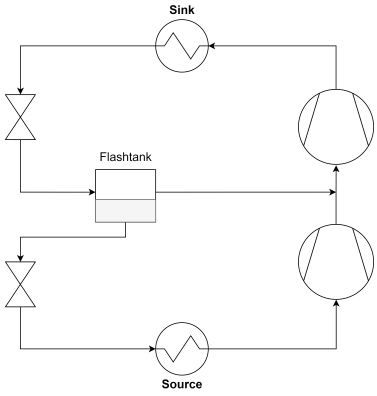

(c) Two stage with flash-tank

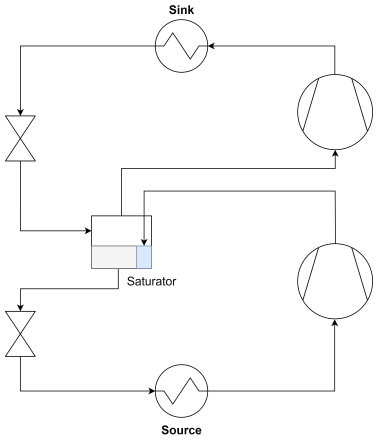

(d) Two stage with saturator

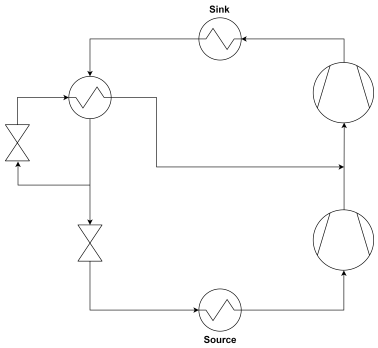

(e) Two stage with internal heat exchanger

Figure 2.17: Selected configurations for reverse Rankine cycle based heat pump systems.

2.7.2. Reverse Brayton cycle based Heat Pumps

Figure 2.18 shows the selected configurations for the reverse Brayton cycle based configurations. The first configuration (Figure 2.18a) is a simple single-stage configuration, comprising four basic components: low-temperature low-pressure heat exchanger (source), a compressor, a high-temperature high-pressure heat exchanger (sink), and a turbine. Second configuration (Figure 2.18b) is an extension of the first one. Here, an internal heat exchanger (called a recuperator) is included in the system. Due to the addition of this recuperator, the working fluid is further cooled before it is expanded through the turbine and the compressor inlet temperature also increases, positively impacting the thermodynamic performance of the system.

The next configuration features a two-stage compression (Figure 2.18c). Two sink heat exchangers are also present in this configuration to allow for inter-stage cooling. The working fluid is first compressed up to an intermediate pressure level and then the thermal energy is exchanged with the required process stream in the first heat sink. The stream from the exit of this heat exchanger is then compressed to the maximum pressure level of the system. Afterwards, the thermal energy is transferred to the second sink. Similar to the second configuration, a recuperator is also included in this configuration to increase the compressor inlet temperature. The last configuration also features two compressors (Figure 2.18d) and is similar to the two-stage configuration with inter-cooling. The difference lies in an additional internal heat exchanger. After the exit of the high-pressure sink, the working fluid is split into two streams. One of the streams (secondary stream) is expanded to an intermediate pressure value and its temperature is increased using the additional internal heat exchanger before it is mixed with the stream coming from the outlet of the first sink of the system. The other stream (high pressure) is used to heat up the stream sent to the second compressor before being delivered to the low pressure part of the working fluid loop.

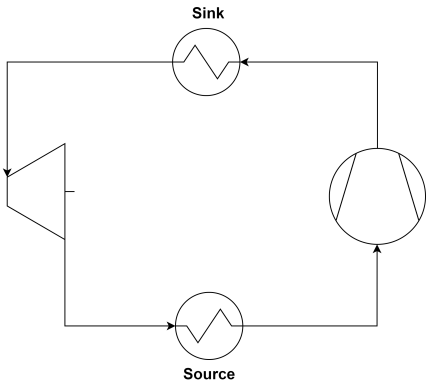

(a) Single Stage

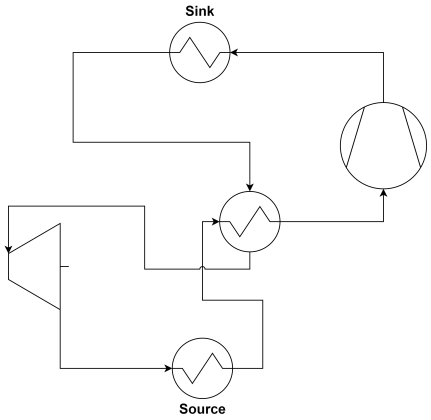

(b) Single stage with Internal Recuperation

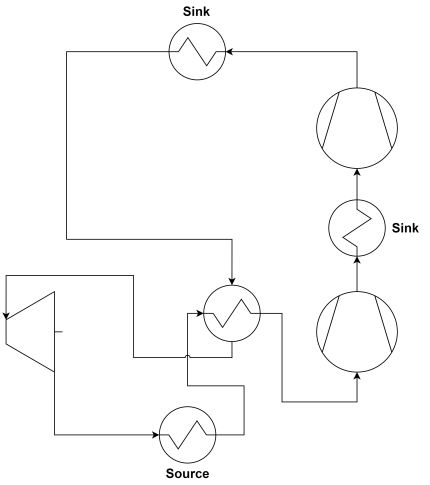

(c) Two stage with Intercooling

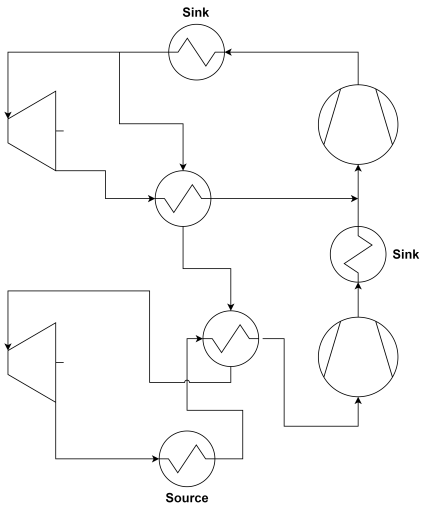

(d) Two stage with Internal heat exchanger and Intercooling

Figure 2.18: Selected configurations for reverse Brayton cycle based heat pump systems.

2.8. Research Objectives

As per the findings of the literature study, the main focus of the project was decided to be on the comparison between the reverse Rankine cycle and reverse Brayton cycle-based heat pump technologies.

To limit the scope of the thesis, only three working fluids were considered: H_2O for reverse Rankine cycle-based systems and Air and CO_2 for the reverse Brayton cycle-based configurations. Thus, the main research objective of the thesis is:

> "Compare reverse Brayton and Rankine cycle based heat pump systems for high temperature applications, in terms of performance, design feasibility of the key components, and ease of integration with industrial processes."

The above research objective has the following sub-goals:

- Development of a steady-state numerical model of different cycle concepts (Reverse Brayton and Rankine cycle) operating with different refrigerants (H_2O, air, and CO_2) for high-temperature heat pump system.
- Parametric analysis of different cycle configurations to identify the best performing one(s) and the corresponding design parameters.
- Development of a design optimization framework allowing for the design of turbomachinery components for a given high-temperature heat pump cycle type and refrigerant.
- Analysis of an industrial test case to assess the performance of the different cycle concepts when integrated into an industrial process.

2.8.1. Research Questions

The main research questions have been provided below, along with the derived sub-questions.

1. What are the effects of the cycle parameters and refrigerant choice on the thermodynamic performance of reverse Brayton cycle and reverse Rankine cycle-based high-temperature heat pump systems, for a given temperature lift/industrial process?
   (a) How does the thermodynamic performance of the system change?
   (b) What is the effect on the design requirements of sub-components?
   (c) What is the difference in the thermodynamic performance between the reverse Rankine cycle and reverse Brayton cycle based heat pumps?
2. What are the technological challenges associated with the development of reverse Rankine cycle and reverse Brayton cycle based heat pumps and with their integration in an actual industrial process?
   (a) What are the challenges associated with the turbomachinery design for the two cycle types?
   (b) What are the practical limitations identified for each cycle type, when a specific industrial process is considered?

2.9. Thesis Outline

To answer the above research questions, the research work consisted of two main tasks, which in turn can be split in multiple subtasks as summarized in Figure 2.19. This work structure is reflected also in the organization of the thesis chapters. The adopted modeling methodology, along with turbomachinery design methods, is discussed in Chapter 3. The verification of these models is discussed in Chapter 4. Chapter 5 discusses the results of the thermodynamic cycle analysis of different heat pump concepts. The case studies and the related results are analyzed in Chapter 6. The main outcomes

of the case studies treated in Chapter 6 are discussed in Chapter 7. Finally, the conclusions and the recommendations for future research activities are summarized in Chapter 8.

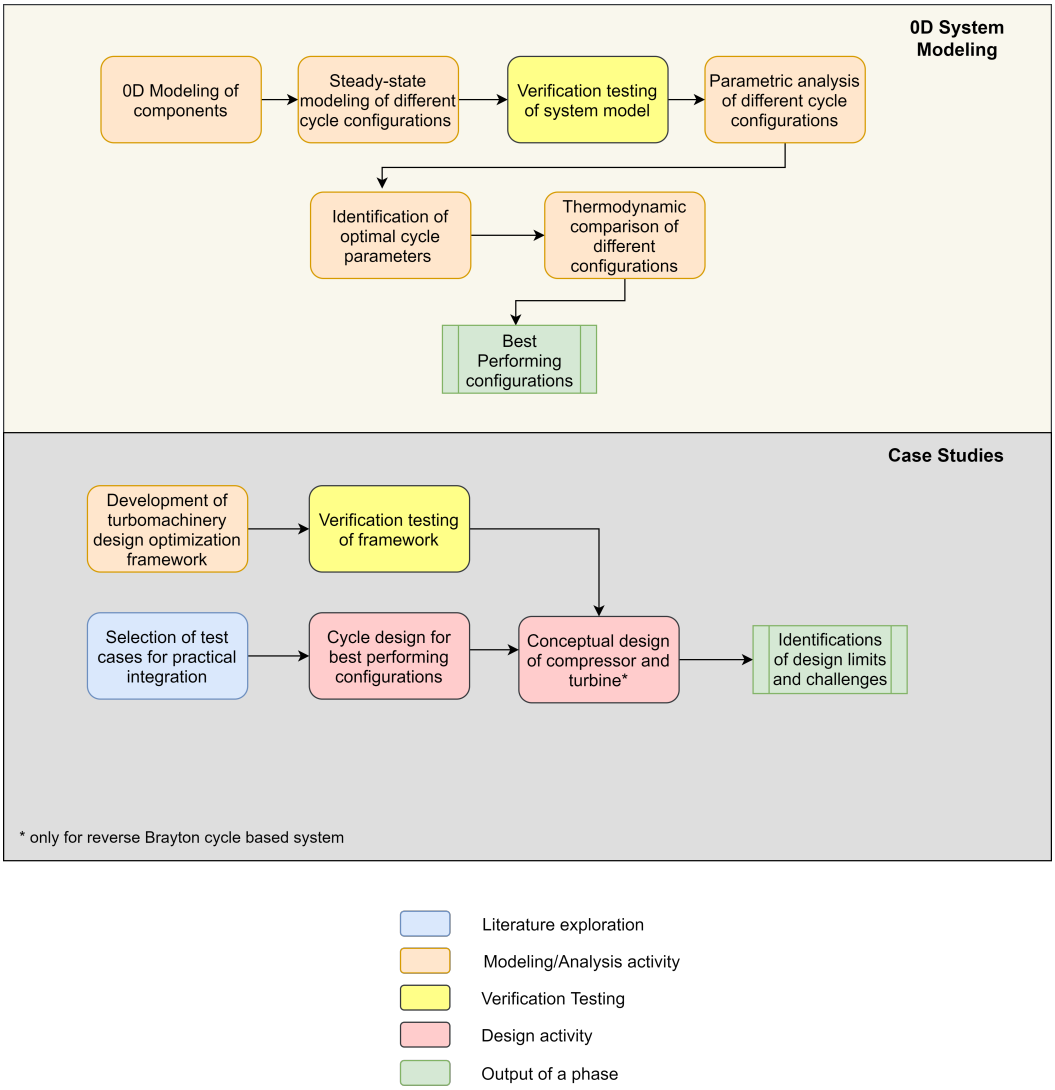

Figure 2.19: Project overview

3

Model Development

This chapter aims to provide the details of the methods used for the 0D modeling of the different heat pump configurations and the conceptual design of the turbomachinery components. The structure of the chapter is as follows, first, the general modeling methodology adopted for the thermodynamic cycle analysis is presented in Section 3.1. Afterward, the modeling assumptions related to the component performance in the thermodynamic cycle analysis are discussed in Section 3.2. Next, the details of the working fluid modeling are provided in Section 3.3. The specific details about the reverse Rankine cycle-based heat pump configurations are provided in Section 3.4, followed by the details of reverse Brayton cycle-based configurations in Section 3.5. Finally, the details about the compressor and turbine design methodology is provided in Section 3.6 and Section 3.7 respectively.

3.1. System Modeling Methodology

This section provides detail about the high-level modeling methodology adopted for the thermodynamic cycle analysis. To develop the required system models the 9 step modeling method is followed. This methodology is suitable for the development of both dynamic and steady-state models, for more details see [77]. The nine fundamental steps included in this procedure are listed below:

1. Definition of Model Purpose.
2. Choice of System boundaries and variables.
3. Listing Relevant Phenomenon.
4. Formulation of Hypotheses and/or Assumptions.
5. Deriviation of required Sub Models.
6. Writing of Conservation Laws and Constitutive Equations.
7. Simplifications.
8. Implementation.
9. Simulation, Verification, Documentation, and Application.

The 9-step method is iterative, namely after the execution of all the steps the modeler verifies whether the given purpose is achieved or not. If not, revaluation of the considered phenomenon, hypothesis,

and assumptions is done until the desired purpose is met. The following subsections provide details about steps 1 to 5. Appendix B give details about steps 6 and 7. Chapter 5 describes the results obtained using the models (steps 8 and 9) and Chapter 4 provides detail about the model verification (step 9).

3.1.1. Model Purpose

Before proceeding towards the modeling of different system configurations and individual components, it is important to define the main objective of the model, the type of problem to be solved and the requirements to be followed by the modeling exercise. For the case at hand, the system model shall allow for an evaluation of required work input and the available thermal energy at the sink, so that the thermodynamic performance of different cycles can be compared, as per Equation (2.1). The purpose of the system model, along with its requirements is summarized in Table 3.1. Following the mentioned criteria, the models were built in *Modelica* language using *Dymola* as interface.

Table 3.1: Modeling criteria

Criteria	Definition
Model Objective	The system model will be used to obtain the thermodynamic performance of the heat pump configuration and the design requirements of the individual system components, at the given operating conditions.
Type of Problem	Steady State Modeling
Model Requirements	1. The system model shall be implemented following the lumped parameters approach. 2. The system model shall be based on the modularity principle. 3. The system model shall allow for assessing the effect of individual component design parameters on the overall system performance.

3.1.2. System Boundaries and Variables

The selected system boundary defines the imaginary line separating the modeled system from the surrounding environment. As a general guideline, the boundary is often placed where the inputs are known, where certain environmental disturbances are present, where a control input is applied or where the output is desired [77]. Figure 3.1 shows the selected boundary for a simple single-stage heat pump system, for an arbitrary process. For the different heat pump system models described later in Section 3.4 and Section 3.5, this boundary remains valid. Only the heat pump configuration is different.

Once the system boundaries are well defined, the model‘s input and output variables are defined. The selected input variables describe the surrounding environment on the system model, and vice versa for the output variables. The input variables of the system model are listed below.

- Pressure, mass flow rate, and temperature of the incoming waste heat source stream.
- Pressure, mass flow rate, and temperature of stream to be heated at the heat pump sink.
- Pressure, mass flow rate, and temperature of both the waste heat source stream and the stream at the sink.

In the thermodynamic cycle analysis (Chapter 4 and Chapter 5), only the working fluid side of both the thermal sink and source is modeled. Thus no process variables are crossing the model border there. This is further explained in Section 3.4 and Section 3.5.

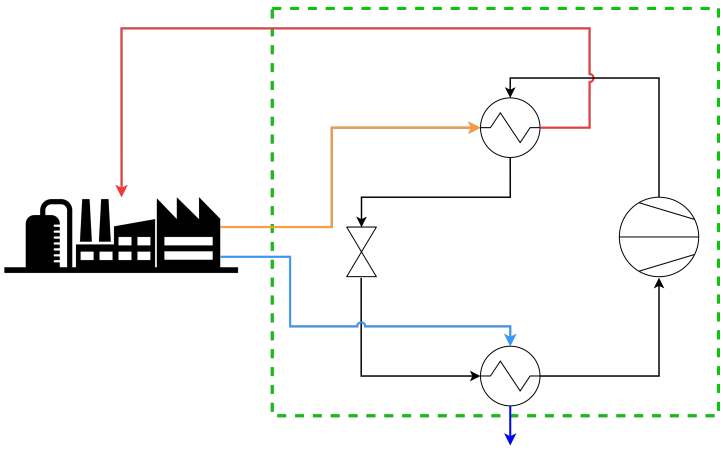

Figure 3.1: Selected system boundary (highlighted in green), illustrating an arbitrary process and a general single-stage heat pump configuration.

The output variables of the system model are as follows:

- Required compressor power (W_{comp}).
- Thermal energy exchange at the source side (source thermal capacity $\dot{Q}_{\text{source}}$).
- Thermal energy exchange at the sink side (sink thermal capacity $\dot{Q}_{\text{sink}}$).
- For the case of reverse Brayton cycle-based systems, turbine power output (W_{turb}).

3.1.3. Relevant Phenomena

As a next step, all the relevant phenomena to be accounted by the model were listed. For this step, the principle of parsimony was followed which states that the "*whenever we have different explanations of the observed data, the simplest one is preferable*" [78]. The relevant phenomena for the general system model are listed below. The relevant phenomena for each of the subsystem models are given in Appendix B.

- Conversion of mechanical energy supplied to the compressor into a pressure and temperature increase of the working fluid.
- Thermal energy exchange between the working fluid and external stream in both the heat pump sink and source.
- Expansion of the working fluid in a turbine/expansion valve and a corresponding drop in temperature and pressure.
- For the case of vapor compression cycle-based systems, evaporation of the working fluid in the heat exchanger corresponding to the heat pump thermal source.
- For the case of vapor compression cycle-based systems, condensation of the working fluid in the heat exchanger corresponding to the heat pump thermal sink.
- Pressure losses in all components due to friction.
- Conversion of the electrical energy supplied to the motor into mechanical energy.
- For the case of reverse Brayton cycle-based systems, conversion of mechanical energy into electrical energy via the generator connected to the turbine(s).

3.1.4. Hypotheses and Assumptions

To simplify the model complexity, several assumptions were made. The assumptions specific to the different component models are presented in Appendix B.

- The variation of potential and kinetic energy across all the components is negligible.
- All the components are thermally insulated,thus the system can be considered adiabatic. This allows one to simplify the conservation equations.
- The compressor operation is always in the stable region by using adequate flow control systems. Thus, the flow instabilities (occurring near the stall, surge operating lines) inside the compressor can be neglected for the system model.
- The friction forces in the connecting lines are negligible and thus can be neglected.

3.1.5. Subsystem Models

As mentioned in the model requirements, the system model is to be developed following a modular approach. The system is thus decomposed into different component models, where each component has an independent set of conservation and constitutive equations. As a result of using this approach, the component models can be re-used to easily implement different system configurations. For this project, the component models of the Modelica *DeSimECS* library, developed by the Propulsion and Power group, were used. The 9 steps related to the development of the component models used in this project are provided in Appendix B.

Once the different subsystem models are developed, they must be connected systematically and consistently to ensure that no numerical issues arise when trying to solve the system model. The different kinds of connectors used for the system model are summarized in Table 3.2.

Table 3.2: Different types of connectors used and the associated bilateral coupled variables.

Connector Type	Potential Variable	Flow Variable	Additional
Fluid	Pressure (P)	Mass flow rate (f)	Specific enthalpy (h) and composition (X)
Thermal	Temperature (T)	Energy flux ($\dot{Q}$)	-
Mechanical	Angular velocity (ω)	Torque (τ)	-
Electrical	Electric potential (V)	Electric current (I)	-

3.2. Boundary Conditions

The system model developed is a steady-state model, as for the purpose of the model. In other words, the model developed is an *"on-design"* static model, which allows for performance evaluation at the design conditions and also provides the required design specifications of the individual system components. It is important to ensure that the system of equations associated with the overall system model is well-posed [79]. To ensure this, the design specifications of the system level must be specified as discussed in Section 3.4 and Section 3.5.

Table 3.3 shows the reference operating conditions of the heat pump system considered in the thermodynamic cycle analysis. The selected source temperature is characteristic of high temperature heat pumps according to the literature explored. Concerning the thermal sink temperature, three temperature levels were selected.

For the heat exchanger components, the pressure drop was assumed to be negligible in this modeling phase. This was done to simplify the system model as the pressure drop depends on the actual geom-

etry of the heat exchangers. To allow for a feasible heat exchanger size, a finite minimum temperature difference between the two streams (hot and cold) was imposed (ΔT_{min}). Equation (3.1) shows the importance of this parameter, where U and A represent the overall heat transfer coefficient (with units W/m^2K) and the total heat exchange area. Typical value of ΔT_{min} vary in the range 5-20 K, depending on the type of fluid and the required techno-economic constraints [80][81][82]. A value of 10 K was selected as a conservative estimate for the current analysis [81].

$$\dot{Q}_{\text{HEX}} = U\ A\ \Delta T \tag{3.1}$$

The values for the isentropic efficiency of the turbomachinery components have been taken from the literature for representative cases [83][84]. These literature cases are for different operating conditions than those studied in this work. Nevertheless, they were chosen to get a good initial estimate for the system simulations. More representative values were obtained in the second phase of the project as the conceptual design of turbomachinery components was performed.

Table 3.3: Selected operating conditions

Boundary Condition	Value	Unit
Temperature of the thermal Source (T_{source})	100	°C
Temperature of the thermal Sink (T_{sink})	$150, 200, 250$	°C
Working fluid Mass flow rate ($\dot{m}$)	1	kg/s
Minimum Temperature difference in heat exchangers (ΔT_{min})	10	K
Pressure drop in heat exchangers (ΔP)	0	bar
Compressor Isentropic Efficiency ($\eta_{\text{is, c}}$)	0.75	-
Turbine Isentropic Efficiency ($\eta_{\text{is, t}}$)	0.85	-
Mechanical Efficiency (η_m)	0.95	-
Electrical Motor Efficiency (η_{motor})	0.95	-
Electrical Generator Efficiency (η_{gen})	0.95	-
Working fluid	H_2O (for reverse Rankine cycle) CO_2 and Dry Air (for reverse Brayton cycle)	-

Often, $\dot{m}$ is computed from the energy balance associated with the sink heat exchanger, see Equation (3.2), as the desired thermal load of the heat pump is often known. In Equation (3.2), $\dot{Q}_{\text{sink}}$ represents the thermal power transferred to the sink and Δh_{sink} indicates the change in the specific enthalpy of the working fluid over the heat exchanger corresponding to the system sink. However, as the primary focus of the numerical study was on the comparison of the maximum achievable thermodynamic performance and cycle characteristics of the considered heat pump technologies, a constant value of $\dot{m}$ was selected. On the contrary, in the simulations aimed at studying the integration of a high temperature heat pump in actual industrial processes, actual process information was used to determine $\dot{m}$ (Chapter 6).

$$\dot{m} = \frac{\dot{Q}_{\text{sink}}}{\Delta h_{\text{sink}}} \tag{3.2}$$

3.3. Working Fluid Modeling

To model the working fluid properties, the *COOLPROP* tool was used, which is an open-source C++ based fluid property database [85]. It uses reduced Helmholtz energy equation of state (EOS) models. This type of formulation provides an advantage in terms of accuracy as all the desired thermodynamic properties can be directly obtained using the partial derivatives of Helmholtz energy. The details of the EOS models used for different fluids are provided in [85].

Using this formulation, the Helmholtz energy of the fluid, in non-dimensional form, can be represented

as shown in Equation (3.3), where α^0 represents the ideal gas contribution and α^r is the residual contribution which accounts for the non-ideal behavior of a certain fluid.

$$\alpha = \alpha^0 + \alpha^r \tag{3.3}$$

The EOS inputs are two non-dimensional parameters δ and τ. The respective definition of these terms is shown in Equation (3.4), where ρ_c and T_c represent the critical density and temperature respectively. The exact formulation of the terms α^0 and α^r is fluid dependent [85].

$$\begin{aligned} \delta &= \rho/\rho_c \\ \tau &= T_c/T \end{aligned} \tag{3.4}$$

Once the exact formulation of Helmholtz energy terms is obtained, all the desired thermodynamic properties can be obtained using the derivatives of the energy terms. As an example, the required formulation for pressure (p), specific internal energy (u) and specific enthalpy (h) are shown in Equation (3.5).

$$\begin{aligned} p &= \rho RT\left[1 + \delta\left(\frac{\partial \alpha^r}{\partial \delta}\right)_\tau\right] \\ \frac{u}{RT} &= \tau\left[\left(\frac{\partial \alpha^0}{\partial \tau}\right)_\delta + \left(\frac{\partial \alpha^r}{\partial \tau}\right)_\delta\right] \\ \frac{h}{RT} &= \tau\left[\left(\frac{\partial \alpha^0}{\partial \tau}\right)_\delta + \left(\frac{\partial \alpha^r}{\partial \tau}\right)_\delta\right] + \delta\left(\frac{\partial \alpha^r}{\partial \delta}\right)_\tau + 1 \end{aligned} \tag{3.5}$$

For the reverse Rankine cycle-based heat pump, the saturation state properties and the properties of the working fluid in the two-phase region are also required. To compute such properties, the program uses the known ancillary equations for pure fluids (for density of saturated liquid and vapor), often derived as a function of temperature and are given by the first and second order derivative of density respectively [85]. Thus, an initial guess for the saturated vapor and liquid density can be obtained using the density derivatives for a given temperature. Further details are provided in [85].

3.4. Model Setup: Reverse Rankine Cycles

The following subsections describes how the system models for the different configurations selected for the reverse Rankine cycle-based heat pump system (Section 2.7) were built.

3.4.1. Single Stage

Figure 3.2 shows the schematic of the model developed for a single-stage heat pump system, based on the reverse Rankine cycle. It is one of the most basic configurations, where the working fluid is evaporated, given the thermal input from the system source, and is compressed further. This high-temperature high-pressure fluid is condensed at the desired sink temperature. Then, the working fluid is expanded to decrease both its pressure and temperature, before it enters the evaporator again, completing the cycle.

Table 3.4 shows the imposed design specifications and constraints at different state points in the model, to have a well-posed system of equations. In Table 3.4, X refers to the mass fractions of the working fluid, and $\mathrm{X}_{\mathrm{ref}}$ indicates the reference value of the mass fractions for the working fluid. For the current project, since all the working fluids are pure fluids, this value is always equal to one. The symbol x indicates the vapor quality of the working fluid at the specified state point. ΔT refers to the minimum temperature difference in the heat exchangers (minimum approach temperature).

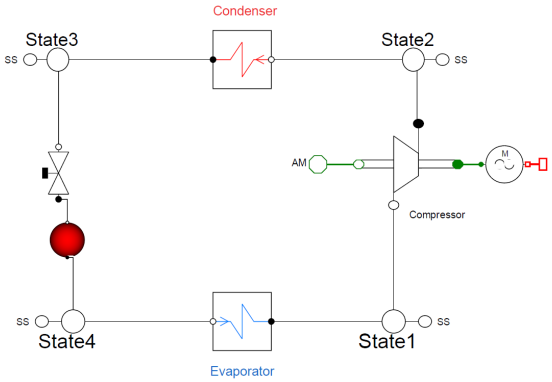

Figure 3.2: Schematic of single-stage heat pump system model based on reverse Rankine cycle

Table 3.4: Selected design specifications and constraints for single stage heat pump based on reverse Rankine cycle

State/Component	Imposed Constraints
1	$x = 1, T = T_{source} - \Delta T,\ \dot{m} = 1\ kg/s$
2	None
3	$T = T_{sink} + \Delta T,\ x = 0$
4	$X = X_{ref}$
Compressor	$\eta_{is,\,c}$, η_{m} , η_{motor}

In this case, saturated conditions are imposed at both evaporator and condenser exit. Thus, the pressure value becomes a redundant variable, since both the vapor quality and the temperature value are prescribed. As a result, there are no degrees of freedom for this cycle configuration, once the temperature levels at the source and the sink side are fixed.

3.4.2. Two Stage with Direct Injection

Figure 3.3 shows the schematic of the model developed for a two-stage HP system with direct injection, based on the reverse Rankine cycle. This is a two-stage cycle configuration implying that there are three different pressure levels present in the cycle: low, intermediate, and high. Table 3.5 shows the imposed constraints at the different state points in the model, to have a well-posed system of equations. In Table 3.5, the degrees of freedom of the system are highlighted in red and a similar convention is followed for all the other system models. In this case, an additional vapor quality constraint is present at State 3. By making this choice, the required mass flow rate of the secondary stream to be mixed with the high-temperature working fluid becomes fixed.

Both the compressors have saturated vapor at their inlet. However, for the second compressor (high-pressure side), the inlet pressure is not fixed. This is because the overall pressure ratio of the system is fixed but the pressure ratio split between the two compression stages is a design parameter. Therefore, in this case, there is one degree of freedom, p_{intm}, for a given source temperature and temperature lift.

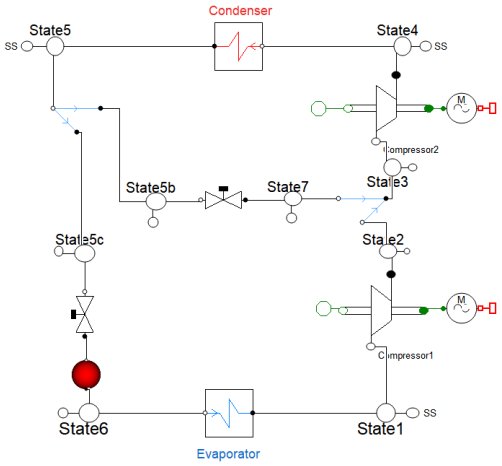

Figure 3.3: Schematic of a two-stage heat pump with direct injection, based on reverse Rankine cycle

Table 3.5: Selected design specifications and constraints for two-stage heat pump with direct injection, based on reverse Rankine cycle

State/Components	Imposed Constraints
1	$x = 1, T = T_{source} - \Delta T$
2	$p_2 = p_{intm}$
3	$x = 1, \dot{m} = 1 kg/s$
4	None
5	$T = T_{sink} + \Delta T, x = 0$
6	$X = X_{ref}$
7	$p_7 = p_{intm}$
Compressor	$\eta_{is,\,c}$, η_{m} , η_{motor}

3.4.3. Two Stage with Flash-tank

Figure 3.4 shows the schematic of the model developed for a two-stage heat pump system with a flash-tank, based on the reverse Rankine cycle. Table 3.6 shows the imposed constraints at different state points in the model, to have a well-posed system of equations. In this case, no additional constraint is imposed at the inlet of the second compressor because, by definition, the vapor leaving the flash-tank is at saturated vapor condition. The remaining constraints are similar to those considered for the two-stage configuration with direct injection. There is only one degree of freedom, namely, p_{intm}.

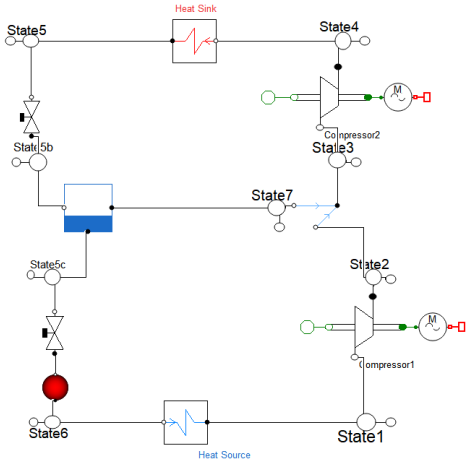

Figure 3.4: Schematic of a two-stage heat pump with flash-tank, based on reverse Rankine cycle

Table 3.6: Selected design specifications and constraints for two-stage heat pump with flash-tank, based on reverse Rankine cycle

State/Components	Imposed Constraints
1	$\mathrm{x} = 1, \mathrm{T} = \mathrm{T}_{\text{source}} - \Delta\mathrm{T}$
2	$p_2 = p_{\text{intm}}$
3	$\dot{m} = 1\mathrm{kg/s}$
4	None
5	$\mathrm{T} = \mathrm{T}_{\text{sink}} + \Delta\mathrm{T}, \mathrm{x} = 0$
6	$\mathrm{X} = \mathrm{X}_{\text{ref}}$
7	$p_7 = p_{\text{intm}}$
Compressor	$\eta_{\text{is, c}}$, η_{m} , η_{motor}

3.4.4. Two Stage with Saturator

Figure 3.5 shows the schematic of the model developed for a two-stage heat pump system with a saturator, based on the reverse Rankine cycle. Table 3.7 shows the imposed constraints at different state points in the model, to have a well-posed system of equations. For this case, additional constraints of X_{ref} and p_{intm} were applied at State 5b and State 3 respectively. This was done because the subsystem model developed for the saturator did not include the pressure balance and mass fraction balance equations. Also for this configuration, one degree of freedom was obtained, namely, p_{intm}.

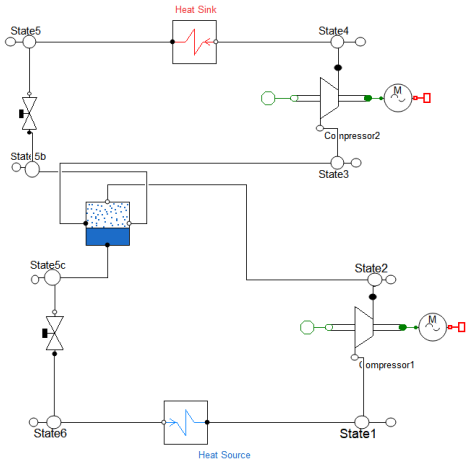

Figure 3.5: Schematic of a two-stage heat pump with saturator, based on reverse Rankine cycle

Table 3.7: Selected design specifications and constraints for two-stage heat pump with saturator, based on reverse Rankine cycle

State/Components	Imposed Constraints
1	$\mathrm{x} = 1, \mathrm{T} = \mathrm{T}_{\text{source}} - \Delta\mathrm{T}$
2	$p_2 = p_{\text{intm}}$
3	$p_3 = p_{\text{intm}}, \dot{m} = 1\mathrm{kg/s}$
4	None
5	$\mathrm{T} = \mathrm{T}_{\text{sink}} + \Delta\mathrm{T}, \mathrm{x} = 0$
5b	$\mathrm{X} = \mathrm{X}_{\text{ref}}$
6	$\mathrm{X} = \mathrm{X}_{\text{ref}}$
Compressor	$\eta_{\text{is, c}}$, η_{m} , η_{motor}

3.4.5. Two Stage with Internal Heat Exchanger

Figure 3.6 shows the schematic of the model developed for a two-stage HP system with an internal heat exchanger and working fluid injection. Table 3.8 shows the imposed constraints at different state points in the model. In this case, an additional constraint is imposed on the temperature of the State 5b. This constraint reflects the maximum feasible thermal energy exchange in the internal heat exchanger, for a given ΔT value.

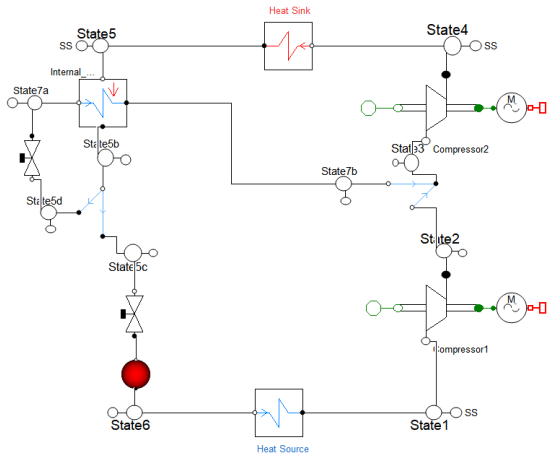

Figure 3.6: Schematic of a two-stage heat pump with internal heat exchanger, based on reverse Rankine cycle

Table 3.8: Selected design specifications and constraints for two-stage heat pump with internal heat exchanger, based on reverse Rankine cycle

State/Components	Imposed Constraints
1	$\mathrm{x} = 1, \mathrm{T} = \mathrm{T}_{\mathrm{source}} - \Delta\mathrm{T}$
2	$p_2 = p_{\mathrm{intm}}$
3	$\dot{m} = 1\mathrm{kg/s}, \mathrm{x} = 1$
4	None
5	$\mathrm{T} = \mathrm{T}_{\mathrm{sink}} + \Delta\mathrm{T}, \mathrm{x} = 0$
5b	$\mathrm{T}_5 = \mathrm{T}_{7b} + \Delta\mathrm{T}$
6	$\mathrm{X} = \mathrm{X}_{\mathrm{ref}}$
7 b	$p_{7\mathrm{b}} = p_{\mathrm{intm}}$
Compressor	$\eta_{\mathrm{is,\,c}}$, η_{m} , η_{motor}

Like all the other two-stage configurations, for this configuration as well, there is only one degree of freedom to optimize the cycle performance.

3.5. Model Setup: Reverse Brayton Cycles

This section reports the constraints applied to the different system models for the reverse Brayton cycle heat pumps. Notice that the same model setup was used for both the working fluids considered i.e. CO_2 and Air.

Contrary to what was done in the thermodynamic cycle analysis of the reverse Rankine cycle-based systems (in Section 3.4), the reverse Brayton cycle-based heat pump performance was evaluated for two different scenarios or set of specifications. In the first scenario (referred to as “Baseline case”), the system constraints were similar to that of reverse Rankine cycle-based systems i.e. temperature and pressure (in place of x, as the working fluid is always in vapor phase) are specified at the outlet of the heat exchangers corresponding to the sink and source of the heat pump.

However, it was hypothesized that this approach would have led to lower thermodynamic performance values for the reverse Brayton cycle-based systems since the heat transfer in the sink (also in the source) occurs under a large temperature difference rather at constant temperature as applicable for the case of reverse Rankine cycle based systems. This implies that the maximum temperature at sink inlet is much higher as compared to the reverse Rankine cycle based systems. Therefore, to take into account this effect, in the second scenario (referred to as the “Sensible Heat Sink Case”), the maximum temperature of the working fluid is prescribed at the sink inlet rather than the outlet, and set equal to the condensing temperature of the inverse Rankine cycle systems. This implies that a finite temperature drop over the sink is assumed for the stream to be heated up by the heat pump. In the following subsections, the constraints of both scenarios are shown for each of the cycle configurations.

3.5.1. Single Stage

Figure 3.7 shows the schematic of the model developed for a single-stage heat pump system based on the reverse Brayton cycle. Table 3.9 shows the imposed constraints at the different state points in the model, for the two considered scenarios.

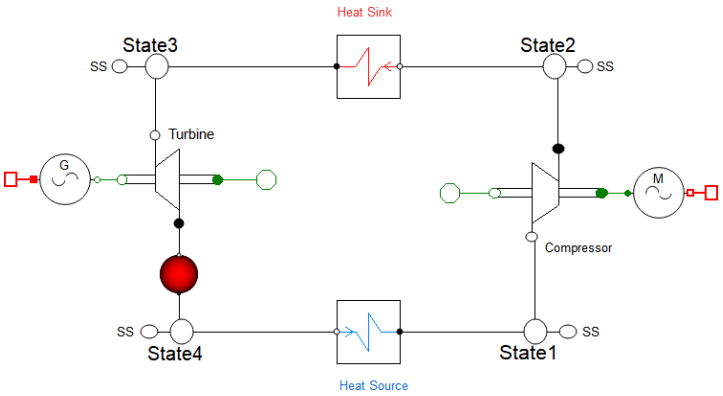

Figure 3.7: Schematic of single-stage heat pump based on reverse Brayton cycle

In the baseline scenario, the thermodynamic cycle has two degrees of freedom: p_{high} and p_{low} i.e. the pressure values at the sink and source respectively. This is different from the case of reverse Rankine cycle-based systems because there is no phase change. Therefore in addition to the temperature value, the pressure value also needs to be specified.

Table 3.9: Selected design specifications and constraints for single stage heat pump based on reverse Brayton cycle

State/Components	**Imposed Constraints** (*Baseline Case*)	**Imposed Constraints** (*Sensible Heat Sink Case*)
1	$T_1 = T_{\text{source}} - \Delta\text{T}, \dot{m} = 1\text{kg/s}$	$T_1 = T_{\text{source}} - \Delta\text{T}, \dot{m} = 1\text{kg/s}$
2	None	$T_2 = T_{\text{sink}} + \Delta\text{T}$
3	$\text{T}_3 = \text{T}_{\text{sink}} + \Delta\text{T},\ p_3 = p_{\text{high}}$	$\text{T}_3 = \text{T}_{\text{sink}} + \Delta\text{T} - \Delta\text{T}_{\text{sink}}$
4	$p_4 = p_{\text{low}}, \text{X} = \text{X}_{\text{ref}}$	$p_4 = p_{\text{low}}, \text{X} = \text{X}_{\text{ref}}$
Compressor	$\eta_{\text{is, c}}, \eta_{\text{m}}$	$\eta_{\text{is, c}}, \eta_m$
Turbine	$\eta_{\text{is, t}}, \eta_{\text{m}}$	$\eta_{\text{is, t}}, \eta_{\text{m}}$

In the sensible heat sink case, it is not necessary to specify the pressure value in the sink as the temperature at the compressor outlet is also imposed. The temperature drop of the working fluid over the sink heat exchanger ($\Delta\text{T}_{\text{sink}}$) becomes the design parameter in place of p_{high}. As a result, there are two degrees of freedom in this case as well.

3.5.2. Single Stage with Recuperator

Figure 3.8 shows the schematic of the model developed for a single-stage heat pump system with a recuperator, based on the reverse Brayton cycle. Table 3.10 shows the imposed constraints at different state points in the model, for the two different scenarios.

In this heat pump configuration, an additional constraint is imposed at State 2 to prescribe a minimum approach temperature in the recuperator. The value taken for this variable is the same as the one used for other heat exchangers. Similarly to the previous single stage configuration, the thermodynamic cycle has two degrees of freedom i.e. p_{high} and p_{low}.

For the sensible heat sink scenario, only the specifications in State 3 and State 4 are changed with respect to the baseline case. Two degrees of freedom are also present in this case, namely, ΔT_{sink} and p_{low}. However, the value of ΔT_{sink} and ΔT have to be chosen carefully, as there are combinations that can lead to an unfeasible temperature profile in the recuperator.

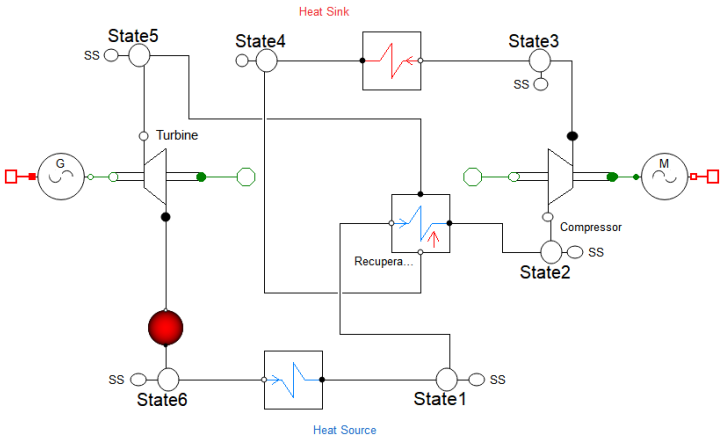

Figure 3.8: Schematic of a single-stage heat pump with recuperator, based on reverse Brayton cycle

Table 3.10: Selected design specifications and constraints for single stage heat pump with recuperator, based on reverse Brayton cycle

State/Components	**Imposed Constraints** (*Baseline Case*)	**Imposed Constraints** (*Sensible Heat Sink Case*)
1	$T_1 = T_{source} - \Delta T, \dot{m} = 1 kg/s$	$T_1 = T_{source} - \Delta T, \dot{m} = 1 kg/s$
2	$T_2 = T_4 - \Delta T$	$T_2 = T_4 - \Delta T$
3	None	$T_2 = T_{sink} + \Delta T$
4	$T_4 = T_{sink} + \Delta T,\ p_4 = p_{high}$	$T_4 = T_{sink} + \Delta T - \Delta T_{sink}$
5	None	None
6	$p_6 = p_{low}, X = X_{ref}$	$p_6 = p_{low}, X = X_{ref}$
Compressor	$\eta_{is,c}, \eta_m, \eta_{motor}$	$\eta_{is,c}, \eta_m, \eta_{motor}$
Turbine	$\eta_{is,t}, \eta_m, \eta_{gen}$	$\eta_{is,t}, \eta_m, \eta_{gen}$

3.5.3. Two Stage with Intercooling

Figure 3.9 shows the schematic of the model developed for a two-stage heat pump system with an intercooler between the two compressors. Table 3.11 shows the imposed constraints at different state points in the model, for the two different scenarios.

In this cycle configuration, two sink heat exchangers are present. Therefore, similar constraints are applied to both the heat exchangers. The internal recuperator is constrained similarly to the previous case of the single stage heat pump with internal recuperation. An additional degree of freedom is present for the baseline case, namely, the intermediate pressure level (p_{intm}). Thus, in the baseline scenario, three degrees of freedom are available for this cycle configuration.

The value for p_{intm} becomes redundant for the sensible heat sink scenario, as the temperatures at the inlet and outlet of the intercooler (the additional heat sink) are fixed. Thus, the thermodynamic cycle has only two degrees of freedom in the sensible heat sink scenario: ΔT_{sink} and p_{low}.

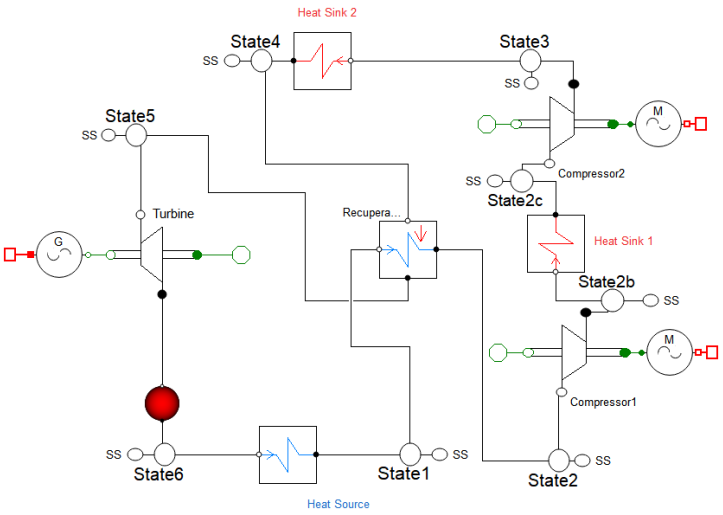

Figure 3.9: Schematic of a two-stage heat pump with an intercooler, based on reverse Brayton cycle

Table 3.11: Selected design specifications and constraints for two-stage heat pump with an intercooler, based on reverse Brayton cycle

State/Components	**Imposed Constraints** (*Baseline Case*)	**Imposed Constraints** (*Sensible Heat Sink Case*)
1	$T_1 = T_{\text{source}} - \Delta T, \dot{m} = 1\text{kg/s}$	$T_1 = T_{\text{source}} - \Delta T, \dot{m} = 1\text{kg/s}$
2	$T_2 = T_4 - \Delta T$	$T_2 = T_4 - \Delta T$
2b	$p_{2b} = p_{\text{intm}}$	$T_{2b} = T_{\text{sink}} + \Delta T$
2c	$T_{2c} = T_{\text{sink}} + \Delta T$	$T_{2c} = T_{\text{sink}} + \Delta T - \Delta T_{\text{sink}}$
3	None	$T_3 = T_{\text{sink}} + \Delta T$
4	$T_4 = T_{\text{sink}} + \Delta T,\ p_4 = p_{\text{high}}$	$T_4 = T_{\text{sink}} + \Delta T - \Delta T_{\text{sink}}$
5	None	None
6	$p_6 = p_{\text{low}}, X = X_{\text{ref}}$	$p_6 = p_{\text{low}}, X = X_{\text{ref}}$
Compressor	$\eta_{\text{is, c}}, \eta_{\text{m}}, \eta_{\text{motor}}$	$\eta_{\text{is, c}}, \eta_{\text{m}}, \eta_{\text{motor}}$
Turbine	$\eta_{\text{is, t}}, \eta_{\text{m}}, \eta_{\text{gen}}$	$\eta_{\text{is, t}}, \eta_{\text{m}}, \eta_{\text{gen}}$

3.5.4. Two Stage with Intercooling and Vapor Injection

Figure 3.10 shows the schematic of the model developed for a two-stage heat pump system with an intercooler and vapor injection. Table 3.12 shows the imposed constraints at different state points in the model, for the two different scenarios.

In this cycle configuration, two internal heat exchangers are present along with two heat exchangers representing the heat pump sink. The value of temperature at State 2 was selected in accordance to the minimum ΔT deemed feasible for both heat exchangers. Similar to the previous two-stage configuration, two degrees of freedom are present for this cycle configuration in the baseline scenario (Table 3.12).

For the sensible heat sink scenario, the cycle specifications are similar to those of the baseline scenario. However, in this case, ΔT_{sink} corresponding to the second heat pump sink has to be limited to prevent a too low temperature in the low-pressure recuperator. Two degrees of freedom are available in this cycle configuration or the sensible heat sink scenario (Table 3.12).

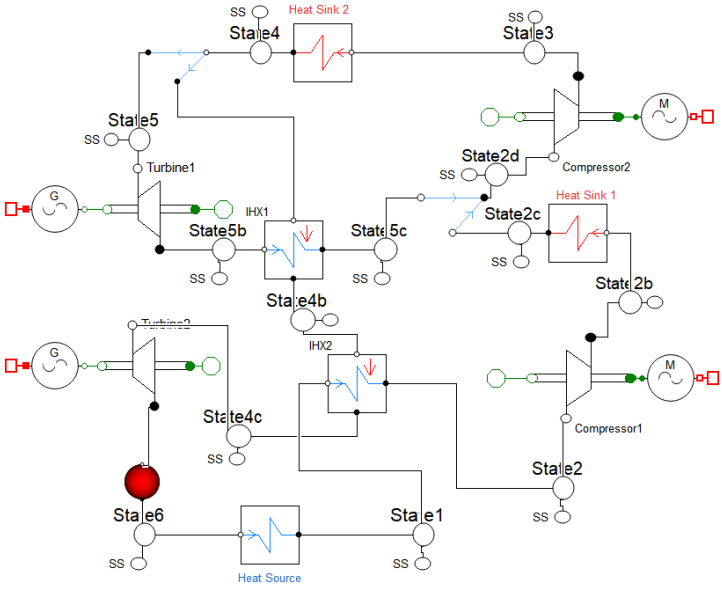

Figure 3.10: Schematic of a two-stage heat pump with an intercooler and vapor injection, based on reverse Brayton cycle

Table 3.12: Selected design specifications and constraints for two-stage heat pump with an intercooler and vapor injection, based on reverse Brayton cycle

State/Components	**Imposed Constraints** (*Baseline Case*)	**Imposed Constraints** (*Sensible Heat Sink Case*)
1	$T_1 = T_{\text{source}} - \Delta T$	$T_1 = T_{\text{source}} - \Delta T$
2	$T_2 = T_4 - 3 \cdot \Delta T$	$T_2 = T_4 - 3 \cdot \Delta T$
2b	$p_{2b} = p_{\text{intm}}$	$T_{2b} = T_{\text{sink}} + \Delta T$
2c	$T_{2c} = T_{\text{sink}} + \Delta T$	$T_{2c} = T_{\text{sink}} + \Delta T - \Delta T_{\text{sink}}$
2d	$\dot{m} = 1\text{kg/s}$	$\dot{m} = 1\text{kg/s}$
3	None	$T_3 = T_{\text{sink}} + \Delta T$
4	$T_4 = T_{\text{sink}} + \Delta T,\ p_4 = p_{\text{high}}$	$T_4 = T_{\text{sink}} + \Delta T - \Delta T_{\text{sink}}$
5	None	None
5b	$p_{5b} = p_{\text{intm}}$	$p_{5b} = p_{2b}$
5c	$T_{5c} = T_4 - \Delta T$	$T_{5c} = T_4 - \Delta T$
4b	$T_{4b} = T_2 + \Delta T$	$T_{4b} = T_2 + \Delta T$
6	$p_6 = p_{\text{low}}$, $X = X_{\text{ref}}$	$p_6 = p_{\text{low}}$, $X = X_{\text{ref}}$
Compressor	$\eta_{\text{is, c}}$, η_m , η_{motor}	$\eta_{\text{is, c}}$, η_m , η_{motor}
Turbine	$\eta_{\text{is, t}}$, η_m , η_{gen}	$\eta_{\text{is, t}}$, η_m , η_{gen}

3.6. Compressor Conceptual Design

In the final phase of the project, a conceptual design of the required turbomachinery components was made, as mentioned earlier in Section 2.9. This section provides details regarding the method adopted for the conceptual design of the compressor. First, the general design methodology is explained, which is followed by a description of the procedure adopted for design optimization.

3.6.1. General Design Method

Radial compressors are widely used for heat pump applications, as they allow for high pressure ratios with a few stages and for relatively low working fluid mass flow rates [86]. In the current project as well, only radial compressors were considered. Figure 3.11 shows the general schematic of a single stage radial compressor, highlighting the different sections [87]. The incoming flow is turned by the impeller, leading to a pressure increase, due to the combined effect of centrifugal forces and the flow turning. The flow is further decelerated in a diffuser, recovering part of the kinetic energy from the flow. To study

the conceptual design of a radial compressor, the turbomachinery design suite called *TurboSim* was used. This tool is developed by the Power and Propulsion research group of the Delft University of Technology [87]. The general methodology used by the program is provided below, based on [87][88].

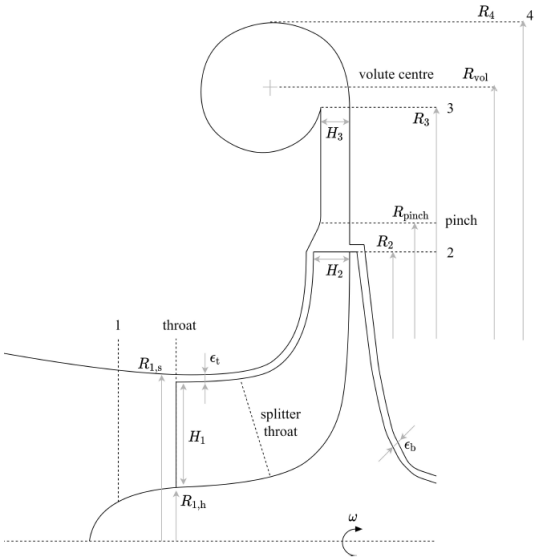

Figure 3.11: Meridional view of a generic radial compressor stage, with an overhung volute and vaneless diffuser [87].

The conceptual design of the compressor is obtained using a reduced-order model. Using the similarity rules, the characteristics of a single stage radial compressor, represented by vector $\boldsymbol{y}$, can be expressed as a function of different parameters, as shown in Equation (3.6). The design characteristics contained in $\boldsymbol{y}$ include, but are not limited to, rotational speed, values of different efficiencies, operating range, radii information, etc.

$$\boldsymbol{y} = f\left(\phi_{t1}, \psi, \alpha_2, \beta, \overline{\gamma_{Pv}}, \mathrm{Re}, \boldsymbol{\sigma}\right) \tag{3.6}$$

The impeller flow angles are fixed, once the non-dimensional duty coefficients such as the flow coefficient (ϕ), the work coefficient (ψ), and the degree of reaction (χ) are selected. For the case of radial compressors, often in practice, the flow coefficient is replaced by the swallowing capacity ($\phi_{t,1}$), and the absolute flow angle at the inlet of the diffuser (α_2) replaces the degree of reaction. The latter parameter (α_2) also directly affects the diffuser stability. The vector $\boldsymbol{\sigma}$ in Equation (3.6), represents the group of non-dimensional geometric design parameters. The information related to the impact of viscous effects is obtained via the average value of Reynolds number (Re) within different sections of the compressor. The other two parameters in Equation (3.6), β and $\overline{\gamma_{Pv}}$ represent the required pressure ratio and the average value of the isentropic pressure-volume exponent. The amount of specific work delivered by the impeller is a function of these two parameters.[87]

The required physical properties of the working fluid are computed using an external thermodynamic library, developed by NIST [89]. The reduced order model used is derived following a lumped parameter approach. The dimensions of the stage and the different required flow quantities are evaluated at different stations along the meridional channel, as shown by Figure 3.11. It is assumed that the incoming flow is axial, as no inlet guide vanes are present. Using the given value of swallowing capacity (as specified by the user), the inlet velocity triangle is determined by minimizing the relative Mach number at the inducer shroud, as per the design guidelines given in [90]. To capture the effect of changes in centrifugal potential and free-vortex flow distribution, five different span-wise computational points are considered at the inducer section. After computing the inlet state, an initial guess for the outlet velocity triangle is obtained using the given values for α_2 and isentropic work coefficient ψ_{is}. Once this initial guess is obtained, the effect of slip and other losses is taken into account to update the flow quantities. An iteration is then carried out over the value of ψ until the achieved pressure ratio by the stage matches

the required target. The impact of losses and slip is evaluated via the means of semi-empirical relations, where some of the factors need to be tuned based on the type of impeller considered. Further details about the different models used are provided in [87]. If the calculated throat length is found to be lower than a given threshold value, the use of splitter blades is considered iteratively, until a feasible impeller design is obtained. In terms of diffuser design, no diffuser vanes are considered. The flow distribution through the diffuser is obtained via integration of a system of differential equations (a two-dimensional system), as derived in [91]. Lastly, to obtain a preliminary design of the volute, a set of conservation equations are used. However, to simplify the design procedure, the assumption of no friction and no pressure gradient in the circumferential direction is made.

The general design methodology implemented in *TurboSim* estimates the whole operating range of the machine, rather than only evaluating compressor performance at a single design point. Therefore, the performance computation at off-design conditions and the calculations of the maximum operating range of the machine is also included. To this purpose, the mass flow rate through the stage is increased successively, starting from the design point mass flow rate value. The choking point of the compressor stage is determined by evaluating the meridional Mach number at the exducer outlet and the relative Mach number at the throat section of the blade passage. This second parameter is computed at five span-wise locations, by solving one-dimensional isentropic flow equations at the respective location. Once the outlet meridional Mach number becomes equal to one or the relative Mach number at the throat is one at all the span-wise locations, the stage is considered as choked. The minimum mass flow rate depends instead on two phenomena, surge and rotating stall. For the estimation of the surge, the slope of pressure ratio and mass flow rate curve is analyzed. As this slope becomes zero ($d\beta/d\dot{m}$ = 0), the initiation of surge is expected [92]. For the rotating stall, a semi-empirical correlation, provided in [93], is used, as the associated flow phenomenon with rotating stall inception is very complex and as a result, time-dependent 3D CFD analysis is required for accurate prediction [94]. This correlation provides a critical value for the absolute flow angle at the inlet of the diffuser ($\alpha_{2,c}$), for a given design. So, to estimate the minimum mass flow rate, the mass flow rate value through the stage is continuously reduced until, either the surge limit ($d\beta/d\dot{m}$ = 0) or the rotating stall inception limit ($\alpha_2 > \alpha_{2,c}$) is obtained.

The above description is related to the design of the single-stage machine. However, for this project, a twin-stage configuration was also explored, as the single-stage configuration was found to be infeasible in some cases. The twin stage configuration considered in this project, which is implemented in *TurboSim*, is a back-to-back configuration, see Figure 3.12. Both the stages are placed on the same shaft and have individual overhung-type volutes. Compared to the methodology explained above, there are two additional points to consider when looking into the conceptual design of the twin-stage machine. Firstly, as both the stages are on the same shaft, the rotational speed is constrained for the second stage, as it results from the design of the first stage. Therefore, for a fixed first stage design, the value of the flow coefficient of the second stage determines the work coefficient for the second stage. Secondly, the maximum axial thrust exerted by the two stages may be critical for the bearings. In the current project, no constraints on the axial thrust were considered as the bearing technology is unknown at this stage of the research. There are also some additional constraints related to the twin-stage configuration, such as the electric motor cooling and the amount of bleed mass flow rate required for cooling. All of these features are implemented in *TurboSim*, but for the current project, these aspects were not considered, given the preliminary character of the investigation. Thus, for the sake of simplifying the compressor design, no motor cooling via the working fluid was considered. Nevertheless, a qualitative investigation of the electric motor feasibility was conducted based on data in the the literature. The conceptual design model for the compressor has also been validated against experimental data. The details about the validation and verification of *TurboSim* are provided in [87][88].

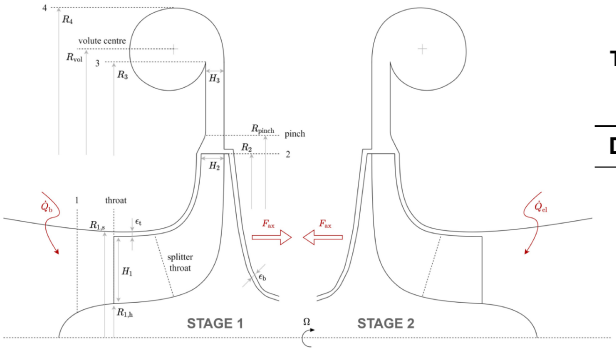

Figure 3.12: Meridional view of a twin stage radial compressor in a back-to-back configuration [88].

Table 3.13: Selected bounds of the design variables for compressor design optimization.

Design Variable	Lower Bound	Upper Bound
κ_{s}	0.5	2
ϕ_{t1}	0.02	0.2
ψ_{is}	0.6	1.0
α_2	60^o	75^o
k	0.65	0.97
N_{b}	12	26
R_3/R_2	1.3	2
$R_{\mathrm{r,\,pinch}}$	0	1
$H_{\mathrm{r,\,pinch}}$	0	1

3.6.2. Design Optimization

Using the conceptual design model of the radial compressor, a design optimization was also carried out. Two objectives were considered in the optimization problem (which need to be maximized), total-to-total efficiency and operating range (OR). The value of the efficiency used as the objective function is determined as the weighted average of the total-to-efficiency value over the design speed line. The definition of OR is given in Equation (3.7), where $\dot{m}_{\mathrm{des}}$ represents the mass flow rate value at design point. The value of $\dot{m}_{\mathrm{max}}$ and $\dot{m}_{\mathrm{min}}$ were estimated considering the choking and stall/surge limits, discussed above. The design optimization problem is thus a multi-objective problem, resulting in a set of design solutions, instead of a single optimal design. These design solutions form the so-called "Pareto front" of the problem. The selection of the design point from the "Pareto front" is then governed by the application requirements.

$$OR = \frac{(\dot{m}_{\mathrm{max}} - \dot{m}_{\mathrm{min}})}{\dot{m}_{\mathrm{des}}} \tag{3.7}$$

The mathematical formulation of the design optimization problem is shown below, where M and U represent the Mach number and peripheral speed respectively. All the constraint functions ($g(\boldsymbol{x})$) represent inequality constraints, where the sign is adjusted such that for feasible designs all $g(\boldsymbol{x}) < 0$. The actual values of the constraints depend on the specific case. The imposed inequality constraints are set to ensure the mechanical and manufacturing feasibility of a design solution. The upper and lower bounds of the different design variables are instead shown in Table 3.13. The values listed in this table were used for both stages. All the design variables are treated as float points except for the number of blades variable (N), which is treated as an integer.

This design optimization framework is also available in the *TurboSim* package. To reduce the computational cost of an individual function evaluation during optimization, only the design speed line is considered for the evaluation of both objective functions and constraints. *Python* library Pymoo [95] is used for implementation of this multi-objective optimization problem and the selected optimization method is the NSGA-II algorithm [96]. The selection of an evolutionary algorithm for the optimization was motivated by the characteristics of the problem and the objectives functions. Further details related to the problem characteristics and the motivation behind the selection of this algorithm are provided in Appendix D.

$$\text{Minimize} \quad f_1(\bar{\boldsymbol{x}}) = 1 - \eta_{tt,\text{avg}} \,, \quad f_2(\bar{\boldsymbol{x}}) = 1 - OR \,,$$

$$\text{with respect to} \quad \bar{\boldsymbol{x}} = [\kappa_s, \phi_{t1,\,1s}, \psi_{is,\,1s}, \alpha_{2,\,1s}, k_{1s}, N_{1s}, \left(\frac{R_3}{R_2}\right)_{1s}, \mathrm{R}_{r,\,\text{pinch, 1s}}, \mathrm{H}_{\text{r, pinch, 1s}},$$
$$\phi_{t1,\,2s}, \psi_{is,\,2s}, \alpha_{2,\,2s}, k_{1s}, N_{2s}, \left(\frac{R_3}{R_2}\right)_{2s}, \mathrm{R}_{\text{r, pinch, 2s}}, \mathrm{H}_{\text{r, pinch, 2s}}] \,,$$

$$\text{subject to} \quad g_1(\bar{\boldsymbol{x}}) = \beta_2 + \beta_{2,\text{max}}$$
$$g_2(\bar{\boldsymbol{x}}) = U_2 - U_{2,\text{max}}$$
$$g_3(\bar{\boldsymbol{x}}) = M_3 - M_{3,\text{max}}$$
$$g_4(\bar{\boldsymbol{x}}) = AR_{\text{volute}} - AR_{\text{volute, max}}$$
$$g_5(\bar{\boldsymbol{x}}) = AR_{\text{volute, min}} - AR_{\text{volute}}$$
$$g_6(\bar{\boldsymbol{x}}) = RPM - RPM_{\text{max}}$$
$$g_7(\bar{x}) = \dot{m}_{\text{des}} - \text{Max choke margin} \cdot \dot{m}_{\text{choke}}$$
$$g_8(\bar{\boldsymbol{x}}) = \beta_{tt} - (1 + \text{Max deviation}) \cdot \beta_{tt\ \text{target}}$$
$$g_9(\bar{\boldsymbol{x}}) = (1 - \text{Max deviation}) \cdot \beta_{tt,target} - \beta_{tt}$$
$$g_{10}(\bar{\boldsymbol{x}}) = W_{input} - \text{Max Power} \,,$$

3.7. Turbine Conceptual Design

For the case of reverse Brayton cycle-based configurations, the conceptual design of the turbine was also considered. This section provides detail of the methodology used for the conceptual design of this component.

For this project, a radial turbine was considered. The radial turbines exhibit high-pressure ratios with a single stage and are often characterized by a lower rotational speed than axial turbines for the same inlet conditions [97]. Similar to the case of radial compressors, a positive contribution from the centrifugal effect is achieved for these machines as well. Figure 3.13 shows a simplified schematic of a radial turbine machine, highlighting the different sections [98]. In this case, the flow enters the stator vanes via an overhung volute. After getting accelerated and deflected via the stator vanes (also called nozzles), the flow enters the rotor. Through the rotor, the flow is turned. The combination of aerodynamic forces on the blades generated by the flow and Coriolis force effects due to change in radius results in a net work output. After the rotor, flow enters a diffusing channel, to achieve a higher total-to-static efficiency, via the means of kinetic energy recovery. For the conceptual design of the radial turbine, given the system requirements, again *TurboSim* was used.

Similar to the compression design methodology, a reduced order model was used. Applying the similarity rule to the radial turbine machine, the design characteristics can be written as a function of duty coefficients, required expansion ratio, non-dimensional geometrical design parameters, flow conditions, and the working fluid characteristics. The resulting equation would be the same as Equation (3.6). Expanding further, the shape of the velocity triangles for the case of radial turbines is fully defined when the flow coefficient at station 3 (ϕ_3) is also known. Therefore, ϕ_3 is a function of flow coefficient at station 2 (ϕ_2) i.e. $\phi_3 = \mathrm{f}(\phi_2)$. However, the ratio of flow coefficients can also be substituted by the ratio of the radii of the machine, as shown by Equation (3.8). As a result, by fixing the duty coefficients and the non-dimensional radius ratio, the velocity triangles are fully defined. Thus, the similarity equation for radial turbines can be written as shown in Equation (3.9).

$$\frac{\phi_3}{\phi_2} = \frac{U_2}{U_3}\frac{v_{3m}}{v_{2m}} = \frac{R_2}{R_3}\frac{v_{3m}}{v_{2m}} \propto \frac{R_2}{R_3}\frac{A_3}{A_2} \tag{3.8}$$

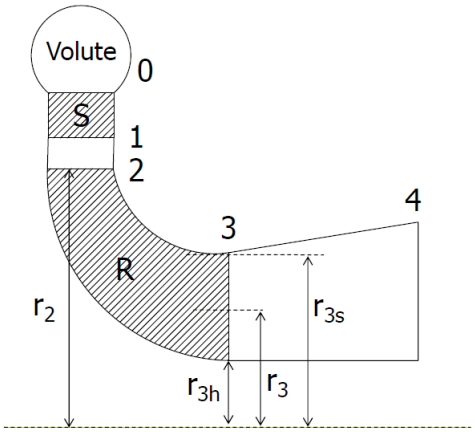

Figure 3.13: Meridional view of a generic radial turbine stage, with an overhung volute and vaned stator [98].

$$\boldsymbol{y} = f\left(\phi_2, \psi, \chi, \beta, Re_m, \frac{R_2}{R_3}, \boldsymbol{\sigma}, \text{ fluid }\right) \tag{3.9}$$

The flow at the inlet of the rotor is considered purely radial and the flow at the exit of the rotor is considered purely axial. In the case of radial turbines, slip also plays an important role, but at the inlet. The presence of slip reduces the amount of work achievable by increasing the tangential component of velocity at the inlet. To cope with this, highly negative incidence angles are generally adopted in radial turbines. As a result, the degree of reaction thus becomes a redundant parameter, because the angle at the inlet of the rotor blade is set. The required physical properties of the working fluid are computed using an external thermodynamic library developed by NIST [89], as for the compressor design method.

The reduced order model used for the turbine design is also derived following a lumped parameter approach. The dimensions of the stage and the different required flow quantities are evaluated at different stations in the meridional channel, as shown in Figure 3.13. Once the values of duty coefficients (flow coefficient (ϕ) and isentropic work coefficient (ψ)) and the non-dimensional radius ratio are selected, the ideal velocity triangles are computed. After this initial guess is obtained, the effect of slip and other losses is taken into account to update the flow quantities. An iteration is then carried out over the value of ψ until the achieved expansion ratio by the stage matches the required target. The impact of losses and slip is evaluated via the means of semi-empirical relations [99]. For the design of the diffuser, the required parameters such as cant angle, divergence angle, and the area ratio are provided as inputs. Based on these input values, a diffuser design is computed using the conservation equations. Finally, the diffuser losses are calculated and the final stage efficiency value is updated. For the case of the turbine, the volute design was not included. However, the general design procedure is similar to the one for compressor [100].

For the conceptual design of the radial turbine, only design point calculations were performed. In terms of optimization, only non-dimensional duty coefficients (ϕ and ψ) were used as optimization variables. The objective was to maximize the total-to-total efficiency of the machine. The values of the other design variables, such as radius ratios and diffuser geometry, that are not optimized, were selected based on reference designs available in the literature for similar operating conditions. Due to the relatively simple optimization problem (as compared to compressor design optimization), the gradient-based algorithm ($\mathrm{NelderMead}$) [101] was deemed sufficient for this case.

4

Model Verification

All the system models were verified before proceeding with the thermodynamic cycle analysis. The individual subsystem models used for the system model were already verified, as they were developed as a part of the *DeSimECS* library, a modeling library developed by the Power and Propulsion research group of Delft University of Technology. The following approach was used to verify the system models developed as a part of this project. Firstly, different system-level tests were conducted to ensure the proper functioning of the system model. An example of such a test is that the sum of source thermal power and the compressor power should be equal to the sink thermal power, as per the total energy balance. In the case of the reverse Brayton cycle-based models, the overall energy balance includes the work output of the turbine. The results of further tests are provided in Appendix B. As a final system test, reference cases from the literature for similar heat pump cycle configurations were reproduced, and the values of $\mathrm{COP_h}$ provided in the literature sources were compared with the values obtained using the system models. This section provides the results of this verification tests.

For the reverse Rankine cycle-based heat pump configurations, the reference case was taken from [74] . The paper investigated the use of a heat pump to produce hot water that is then used to preheat crude oil, using the available cold water as the thermal energy source. The details of this case are provided in Table 4.1.

Table 4.1: Data of the test case used to verify the reverse Rankine cycle-based models.

Boundary Condition	Value	Unit
Evaporation temperature	25-35	°C
Condensation temperature	98	°C
Degree of superheating after evaporator	3	°C
Degree of subcooling after condenser	5	°C
Pinch Point temperature in evaporator	5	°C
Intermediate Pressure	$\sqrt{p_{\text{low}} \cdot p_{\text{high}}}$	MPa
Working fluid	R152a	-

The temperature of the working fluid in the condenser (sink) is fixed, while the evaporator temperature is varied in the range 25°-35°C. As shown by Table 4.1, the reference thermodynamic cycles consider working fluid superheating and subcooling which were, instead, neglected in the system models discussed earlier in Section 3.4 and Section 3.5. Therefore, additional heat exchangers (using one medium) were added for this verification case to account for the superheating and subcooling of the working fluid. Figure 4.1 shows an example of the modified system configuration for the two-stage heat pump with direct injection.

Figure 4.2 shows the obtained values of $\mathrm{COP_h}$ for different evaporation temperatures and different heat pump configurations, along with the results derived from [74]. The solid lines represent the data given

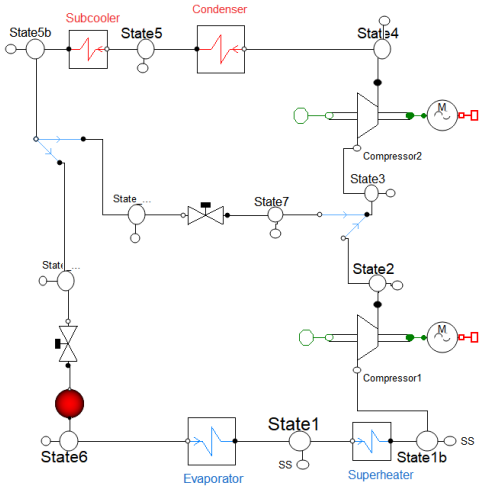

Figure 4.1: Modified two-stage configuration with direct injection after addition of superheating and subcooling.

in [74], while the dashed lines indicate the simulation results. All the system models showed a similar variation of $\mathrm{COP_h}$ with the evaporation temperature, in accordance with the results in [74]. However, in terms of magnitude, the values of $\mathrm{COP_h}$ obtained in the simulations are lower than the reference values. Nevertheless, the relative error in $\mathrm{COP_h}$ is less than 3 % for all the system models, as shown by Figure 4.3.

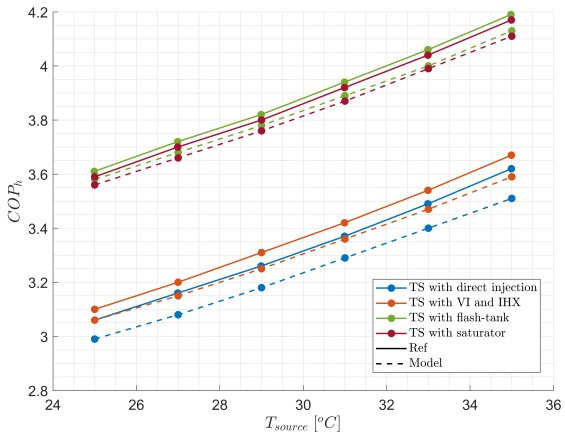

Figure 4.2: Variation of $\mathrm{COP_h}$ with source temperature for verification test case of reverse Rankine cycle based configurations.

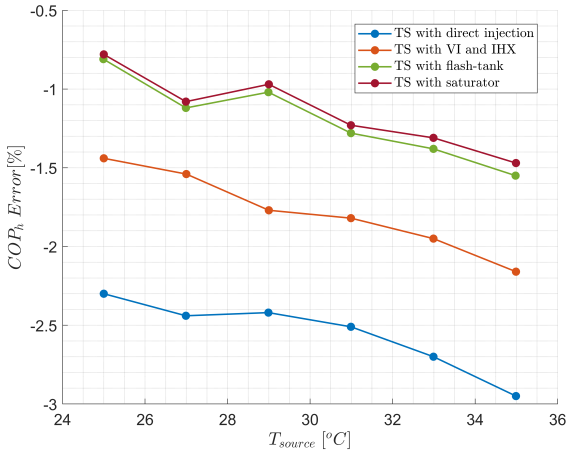

Figure 4.3: Relative error in $\mathrm{COP_h}$ (with respect to reference $\mathrm{COP_h}$) obtained for verification test of reverse Rankine cycle based configurations.

The reason behind the observed difference is due to the uncertainty in the value of compressor isentropic efficiency ($\eta_{\mathrm{is,\,c}}$). For the reference case, $\eta_{\mathrm{is,\,c}}$ is considered a function of compressor's pressure ratio (β_{total}), whereas, in the developed system models a constant value of $\eta_{\mathrm{is,\,c}}$ (= 0.92) is used. This explains why a higher error is obtained for high values of evaporation temperature for all the configurations. With an increase in evaporation temperature, the required β_{total} decreases, thus leading to a higher $\eta_{\mathrm{is,\,c}}$. The specific function used by the authors for $\eta_{\mathrm{is,\,c}}$ is not reported, which makes it difficult to compare the $\eta_{\mathrm{is,\,c}}$ values. Nevertheless, the developed system models can be considered verified given the low relative error obtained and the fact that the general trends of $\mathrm{COP_h}$ are in accordance with the reference case for all the heat pump configurations.

The reference data shown in Figure 4.2 has been extracted using an automated graph data extractor tool [102], since the data given in the paper was in a graphical format. As a result, the $\mathrm{COP_h}$ values shown for the reference case are affected by uncertainties. For the purpose of system verification, this

can be considered acceptable since the difference observed between the results of the reference case and the simulations is mainly caused by the difference in $\eta_{\text{is, c}}$ values.

A reference case was also selected for the system models based on the reverse Brayton cycle [45]. The data for this reference case, provided in Table 4.2, corresponds to transcritical cycle configuration. Thus, the working fluid is in a two-phase region during expansion. Therefore, a simple isenthalpic expansion valve was used instead of a turbine.

Table 4.2: Data of the test case used to verify the reverse Brayton cycle-based models.

Boundary Condition	Value	Unit
Source temperature	0	°C
Sink outlet temperature	45	°C
Low pressure value	3.485	MPa
High pressure value	$9 - 13$	MPa
Temperature increase due to internal recuperation	20	°C
Mechanical efficiency	95	%
Intermediate Pressure	$\sqrt{p_{\text{low}} \cdot p_{\text{high}}}$	MPa
Working fluid	CO_2	-

Also in this case, the $\eta_{\text{is, c}}$ value is not taken constant by the authors but it varies as a function of β_{total}. However, the correlations expressing the relation between $\eta_{\text{is, c}}$ and β_{total} was provided in the paper. So it was possible to implement this relation in the system models. Figure 4.4 shows the variation of COP with respect to the maximum cycle pressure (P_{high}) obtained for the system models, along with the reference results obtained from [45]. Similar to the case of reverse Rankine cycles, solid lines in Figure 4.4 indicate the reference values, whereas the dashed lines represent the values obtained using the system models. The values obtained by the system models agree with the reference values. This is also apparent from Figure 4.5, where the relative error percentages are shown for different heat pump configurations. The average relative error for the two-stage configuration with intercooler and single-stage configuration with recuperator is less than 0.5 %. However, for the case of two-stage configuration with vapor injection and internal heat exchanger, a higher relative error is obtained (maximum deviation -2 % to 1%, as a function of P_{high}).

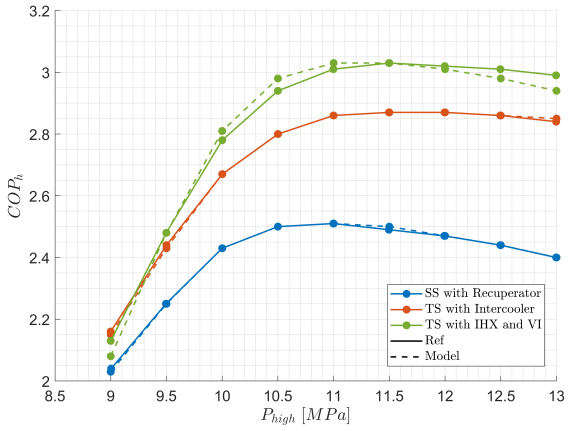

Figure 4.4: Variation of COP_h with compressor outlet pressure for the verification test case of reverse Brayton cycle-based configurations.

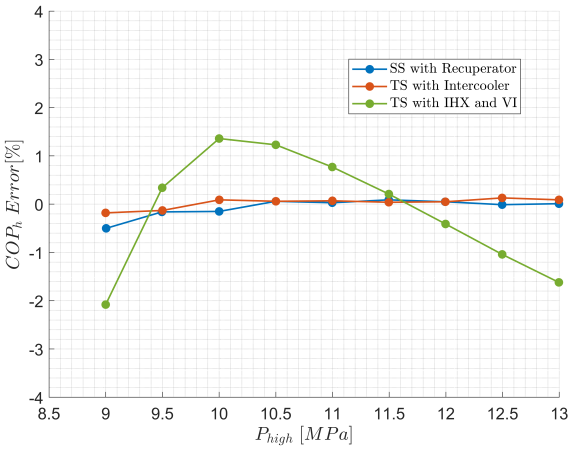

Figure 4.5: Relative error in COP_h (with respect to reference COP_h) obtained for verification test of reverse Brayton cycle based configurations.

A possible reason for the discrepancy observed for this particular configuration is a possible mismatch of the minimum approach temperature in the internal heat exchangers ($\Delta T_{\text{min, HEX}}$), as the value of such a parameter is not provided in [45]. In the system models, a $\Delta T_{\text{min, HEX}}$ of 10 K is used. As for the verification exercise of the reverse Rankine cycle, the reference data shown in Figure 4.4 was obtained using an automated tool to extract numerical data from graphs [102], and thus, are affected by uncertainties. Nevertheless, the reverse Brayton cycle-based models can be considered as verified given the small relative error obtained for the system models.

5

Thermodynamic Performance Analysis

5.1. Reverse Rankine Cycle

The results of the thermodynamic cycle analysis performed for the different heat pump configurations based on the reverse Rankine cycle are presented in this section. The general structure of all the subsections is: firstly, the obtained $\mathrm{COP_h}$ trends are discussed, and then the reason behind such trends is explored by inspecting the underlying thermodynamic cycle on a temperature/specific entropy plane (Ts plane).

5.1.1. Single Stage

The single-stage heat pump configuration does not have any degree of freedom once the sink temperature is fixed. Figure 5.1 shows the process flow diagram of this heat pump concept.Table 5.1 shows the estimated $\mathrm{COP_h}$ for this single-stage heat pump configuration when the sink temperature is varied. If the temperature lift is increased by 150°C, passing form a sink temperature of 150°C to 250°C, the obtained $\mathrm{COP_h}$ decreases by approximately 53 %. This implies that rising the sink temperature, the maximum achievable $\mathrm{COP_h}$ decreases rapidly, as also shown by some of the studies conducted in literature for similar temperature lift values, but at lower temperature levels [74][75].

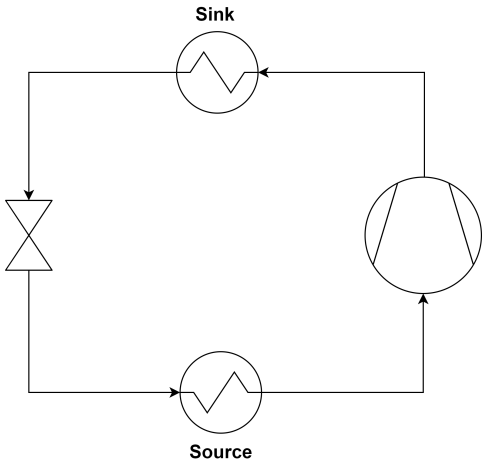

Figure 5.1: Schematic of the single-stage reverse Rankine cycle system.

With an increase in the temperature lift of 100°C, the amount of thermal energy transferred to the sink

also increases by about 18.5 % (relative). However, the required compressor work input increase is around eight times higher (150 % relative increase). As a result of this unbalanced increase in the thermal energy output and the work input, the $\mathrm{COP_h}$ of the heat pump decreases.

Table 5.1: Results obtained for the single-stage reverse Rankine cycle system.

Parameter	Unit	T_{sink} = 150 °C	T_{sink} = 200 °C	T_{sink} = 250 °C
$\mathrm{COP_h}$	-	3.94	2.47	1.87
T_{max}	°C	408.7	631.1	838.4
β_{total}	-	8.81	27.18	66.86
$\dot{Q}_{cond}$	MW	2.6	2.86	3.1
$\dot{Q}_{evap}$	MW	1.98	1.76	1.52
W_{comp}	MW	0.66	1.16	1.66

The pressure difference between the source and sink side depends on the selected T_{source}, T_{sink} and ΔT_{min} since the working fluid needs to undergo evaporation and condensation at the respective temperatures while ensuring a feasible thermal energy exchange within the heat exchangers. Therefore, with an increase in T_{sink}, the required pressure ratio also increases, leading to an increased compressor exit temperature. For the case of T_{sink} = 250°C, the compressor exit temperature reaches higher than 800°C, and the required pressure ratio is around 67, thus making the design of the compressor challenging. However, even for a lower T_{sink} of 200°C, the required pressure ratio is 27. In most of the literature studies, the maximum pressure ratio per stage is limited to around 3.5, considering both technical and economic constraints [103][104]. Therefore, for a feasible implementation of this heat pump configuration, a multi-stage compressor would be required. Regardless, the mechanical problems associated with a compressor exit temperature greater than 600°C would still pose a challenge from both technical and economic viewpoints [103].

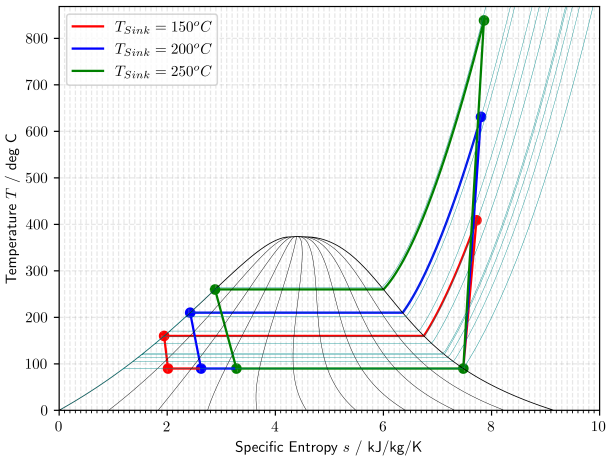

Figure 5.2: Ts diagram highlighting the effect of sink temperature on a single-stage heat pump configuration based on the Reverse Rankine cycle.

Figure 5.2 shows the Ts diagram of the single stage heat pump configuration, using different T_{sink} values. The saturation dome and the iso-quality lines in the figure are shown in “black”, whereas the thin “green” lines indicate the isobars. As the figure shows, the maximum cycle temperature increases with an increase in the T_{sink} value, leading to a higher value of superheating at the condenser inlet. This implies that a large desuperheater would be needed, and depending on the nature of the process stream to be heated, this could lead to increased irreversibilities in the heat exchanger. With an increase in temperature lift, the cycle area also increases. Correlating this observation to the corresponding $\mathrm{COP_h}$ value, it can be argued that an increase in cycle area towards the right side of the saturation dome leads to a lower $\mathrm{COP_h}$ of the heat pump as the increase in compression work becomes orders of magnitude higher than the thermal energy gained at the condenser side.

5.1.2. Two Stage with Direct Injection

p_{intm}, the intermediate pressure level, was identified as the only degree of freedom for this heat pump configuration. Therefore, the effect of p_{intm} on the $\mathrm{COP_h}$ was investigated, for increasing values of T_{sink}. Figure 5.3 shows the schematic of this heat pump configuration.

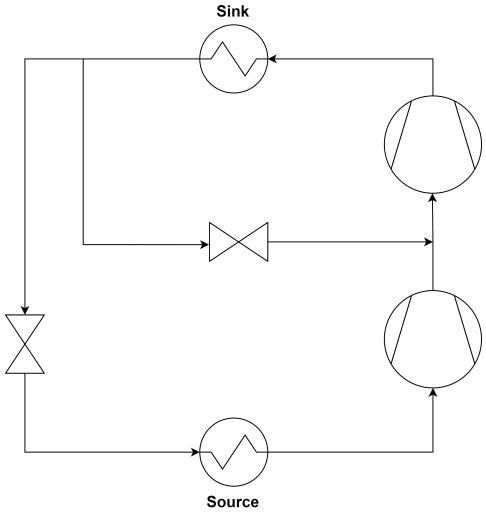

Figure 5.3: Schematic of the two-stage heat pump with direct injection.

To ensure a consistent analysis among the different heat pump configurations, instead of directly varying the p_{intm} value, the pressure ratio split between the two compressors, denoted by P_{frac}, was used as independent variable. In this way, the same values can be used across different heat pump configurations, and some general conclusions could be derived. Equation (5.1) defines P_{frac}, where $\pi_{\text{comp, 1}}$ refers to the pressure ratio of the low-pressure compressor (downstream of the evaporator) and $\pi_{\text{comp, 2}}$ refers to the pressure ratio of the compressor before the condenser inlet, operating at higher pressure.

$$P_{\text{frac}} = \frac{\pi_{\text{comp, 1}}}{\pi_{\text{comp, 1}}} \tag{5.1}$$

Figure 5.4 shows the trends of $\mathrm{COP_h}$ as a function of P_{frac}, for different T_{sink} values. Similar to the case of single-stage heat pump configuration, there is a steep decrease in the $\mathrm{COP_h}$ value with an increase in temperature lift, independent of the value of P_{frac}. As a result of this, the effect of P_{frac} is not identifiable in the chart due to the large variation of $\mathrm{COP_h}$ with T_{sink}. Therefore, a normalized $\mathrm{COP_h}$ value is plotted against P_{frac}in Figure 5.5. In this figure, the value of $\mathrm{COP_h}$ is normalized with the maximum $\mathrm{COP_h}$ value for the that particular T_{sink}.

With an increase in T_{sink} value, the $\mathrm{COP_h}$-P_{frac} curve becomes flatter. However, the value of P_{frac} corresponding to the maximum $\mathrm{COP_h}$ remains independent of T_{sink} value and is equal to 1.0. For the value of P_{frac} higher than the optimal, the decrease in $\mathrm{COP_h}$ is limited. However, for the P_{frac} values lower than the optimal value, the decrease in the $\mathrm{COP_h}$ value is much more prominent. The highest deviation in $\mathrm{COP_h}$, relative to the maximum $\mathrm{COP_h}$ value, ranges from about 4 % to 0.5 % as the T_{sink} value increases from 150° to 250°C. Thus, at higher temperature lift values, the choice of P_{frac} value is not critical for the heat pump performance. In such cases, P_{frac} can be selected based on considerations related to compressor design without as this quantity has a limited influence on the heat pump‘s $\mathrm{COP_h}$ value.

Figure 5.6 and Figure 5.7 show the heat pump Ts diagram for different P_{frac} values at T_{sink} 150°C and 200°C respectively. When the value of P_{frac} is low, the majority of the pressure rise is achieved in the second compressor, which leads to a very high compressor work input and outlet temperature. The main feature of this heat pump configuration is the inter-stage cooling via direct working fluid injection.

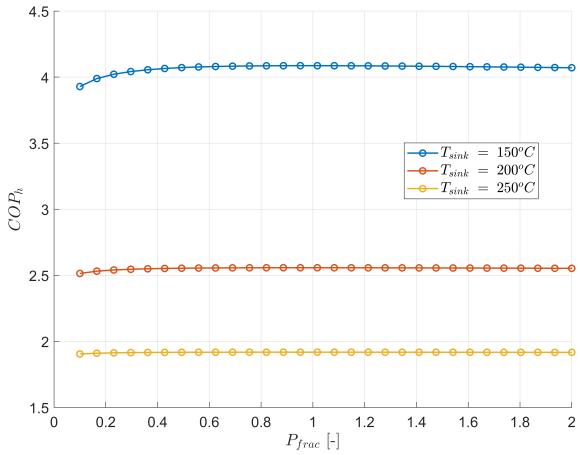

Figure 5.4: Variation of $\mathrm{COP_h}$ with P_{frac}, for two-stage heat pump configuration with direct injection.

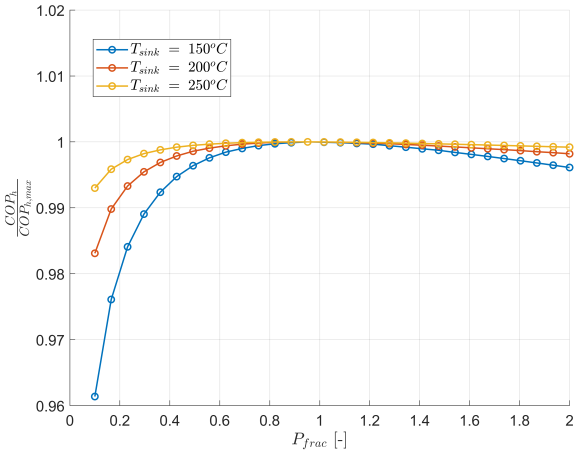

Figure 5.5: Variation of normalized $\mathrm{COP_h}$ (with respect to maximum $\mathrm{COP_h}$) with P_{frac}, for two-stage heat pump configuration with direct injection.

The benefit of working fluid cooling before the second compressor is essentially nullified by having such a low P_{frac} value, and the resulting system resembles more a high-pressure ratio single-stage system, thus featuring a lower $\mathrm{COP_h}$. On the contrary, at high values of P_{frac}, even though the outlet temperature of the first compressor (low-pressure level compressor) increases, the outlet temperature of the second compressor (hence the required work input) remains close to the optimal value, due to the cooling of working fluid via direct injection. As a result, the variation of $\mathrm{COP_h}$ for high values of P_{frac} is much lower as compared to that at low values of P_{frac}.

At the same time, with an increase in T_{sink}, the required overall pressure ratio also increases. Therefore, the pressure ratio of individual compressors also increases, resulting in a decreased influence of the pressure ratio split, as the associated temperature levels are much higher, and the second compressor inlet state is fixed as a saturated vapor.

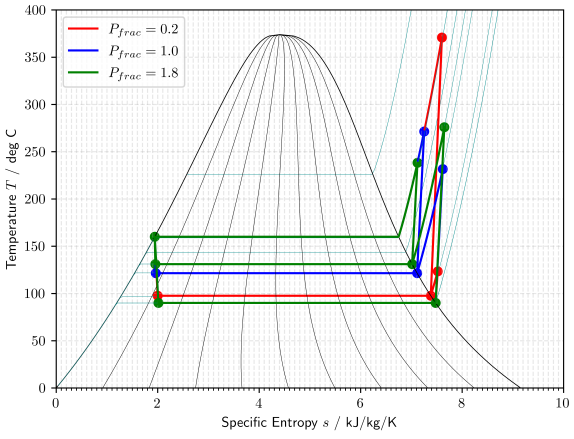

Figure 5.6: Ts diagram showing the effect of P_{frac} with T_{sink} 150 °C on two-stage heat pump configuration with direct injection.

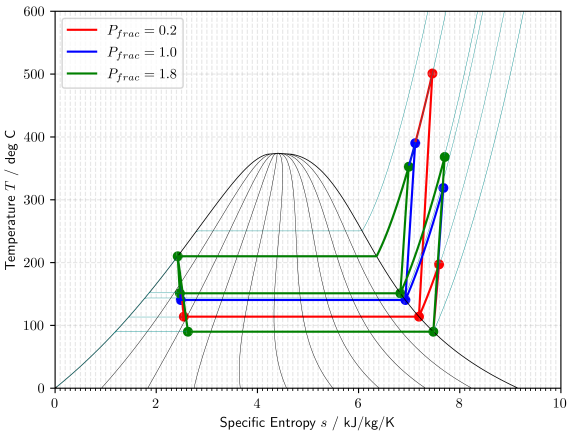

Figure 5.7: Ts diagram showing the effect of P_{frac} with T_{sink} 200 °C on two-stage heat pump configuration with direct injection.

Table 5.2 shows the optimal performance estimated for this heat pump configuration, for different sink temperatures, where α_{inj} represents the fraction of the total mass flow rate injected before the second compressor. With an increase in the T_{sink} value (from 150° to 250°C), the obtained $\mathrm{COP_h}$ decreases by approximately 53 %, becoming similar to that obtained for the single-stage heat pump configuration. However, for this configuration, the values of $\mathrm{COP_h}$ are higher than the ones obtained for the single-stage heat pump. The main reason for the better performance is the cooling of the working fluid before

the second compressor stage, which decreases the total work input. The amount of thermal energy available at the sink also decreases in this case, as the condenser inlet temperature is lower. However, the decrease in the work input is higher than the decrease in the condenser duty (factor of 0.859 vs. 0.89), which results in a $\mathrm{COP_h}$ increase. With an increase in T_{sink} value, the amount of the fluid injected also increases. This is because the thermodynamic state at the second compressor inlet is fixed as a saturated vapor, and a higher amount of low-temperature working fluid is needed to reduce the temperature to the desired level. Another effect of the fixed thermodynamic state at the second compressor inlet is that the value of condenser duty ($\dot{Q}_{\text{cond}}$) remains similar for different T_{sink} values. However, the increase of compression work with an increasingly higher temperature lift, due to the higher pressure ratio, results in a drop of $\mathrm{COP_h}$.

Table 5.2: Results obtained for the two-stage heat pump configuration with direct injection.

Parameter	Unit	T_{sink} = 150 °C	T_{sink} = 200 °C	T_{sink} = 250 °C
$\mathrm{COP_h}$	-	4.09	2.56	1.92
T_{max}	°C	271.43	390	498.3
β_{total}	-	8.81	27.18	66.86
α_{inj}	-	0.1	0.17	0.24
$P_{\text{frac, optim}}$	-	1.0	1.0	1.0
$\dot{Q}_{\text{cond}}$	MW	2.33	2.33	2.30
$\dot{Q}_{\text{evap}}$	MW	1.79	1.46	1.16
$W_{\text{comp, 1}}$	MW	0.26	0.39	0.48
$W_{\text{comp, 2}}$	MW	0.31	0.52	0.72

Figure 5.8 shows the Ts diagram of the optimal configuration of this heat pump concept for different T_{sink} values. Compared with the single-stage heat pump configuration results, for each T_{sink} value, the amount of cycle area on the right side of the saturation dome is reduced. As a result of this, the required compressor work is reduced, without sacrificing significantly $\dot{Q}_{\text{cond}}$, thus the $\mathrm{COP_h}$ increases. Similarly to what was observed for the single-stage heat pump configuration, as the temperature lift increases for a given source temperature, the cycle shifts towards the right, and the maximum temperature increases; as a result, the system $\mathrm{COP_h}$ drops. The required overall pressure ratio is the same as the single-stage heat pump configuration. However, this configuration represents a feasible solution since two compressors are present in the system, and the maximum temperature values are below 500°C.

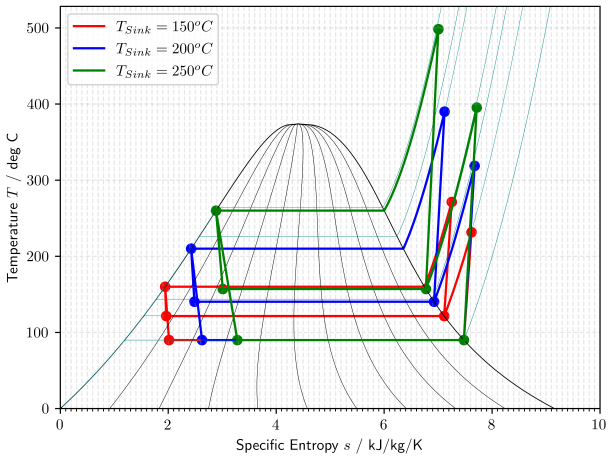

Figure 5.8: Ts diagram showing the effect of sink temperature on two-stage heat pump configuration with direct injection.

5.1.3. Two Stage with Flash-tank

The two-stage heat pump configuration with flash-tank also has one degree of freedom i.e. p_{intm}. Similarly to the previous two-stage heat pump configuration with direct injection, the effect of the p_{intm}

on the $\mathrm{COP_h}$ value was analyzed for this heat pump configuration. Figure 5.9 shows the schematic of this heat pump configuration.

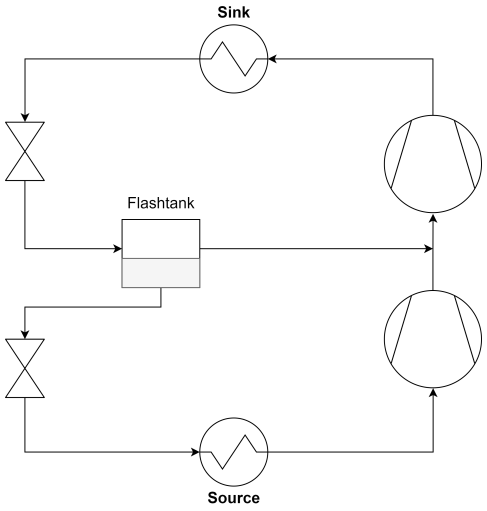

Figure 5.9: Schematic of the two-stage heat pump with flash-tank.

Figure 5.10 shows the variation of this heat pump configuration's $\mathrm{COP_h}$ with P_{frac} for different T_{sink}. Since, the scale of $\mathrm{COP_h}$ is different for different T_{sink} values, normalized $\mathrm{COP_h}$ value is shown in Figure 5.11 to better analyze the trend of $\mathrm{COP_h}$ with P_{frac}. The $\mathrm{COP_h}$ value increases with P_{frac} for all the T_{sink} values and the optimum values lies around the upper limit of P_{frac}. As the T_{sink} value decreases, the $\mathrm{COP_h}$-P_{frac} curve becomes more flat, which is opposite to that obtained for the heat pump configuration with direct injection. However, the dependency of $\mathrm{COP_h}$ with P_{frac}, is much lower than that observed for the previously discussed heat pump configuration. The maximum deviation (with respect to maximum $\mathrm{COP_h}$) ranges from around 1.25 % to 0.2 %, as the T_{sink} value decreases from 250° to 150°C. This is because the thermal energy available at the sink side is almost independent of the P_{frac} value. Therefore, the deviation in $\mathrm{COP_h}$ mainly arises from the required work input difference.

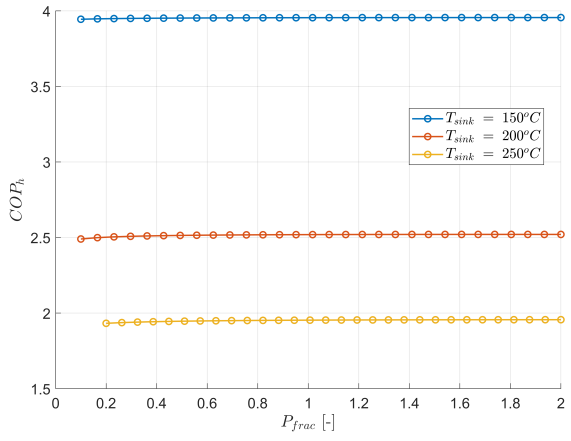

Figure 5.10: Variation of $\mathrm{COP_h}$ with P_{frac}, for two-stage configuration with flash-tank.

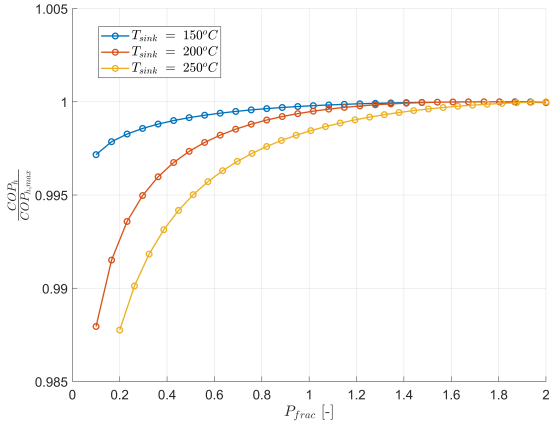

Figure 5.11: Variation of normalized $\mathrm{COP_h}$ (with respect to maximum $\mathrm{COP_h}$) with P_{frac}, for two-stage heat pump configuration with flash-tank.

Figure 5.12 and Figure 5.13 shows the heat pump's Ts diagram for different P_{frac} values at T_{sink} 150°C and 200°C respectively. In this heat pump configuration, the thermodynamic state at the inlet of the second compressor is a superheated vapor since it results from the mixing of the stream coming from the flash-tank, that is at saturated vapor conditions, and the superheated vapor coming from the first compressor. For low T_{sink} value, the deviation in the compressor work with P_{frac} is found to be smaller than that at high T_{sink} value. The main reason behind such a result is the difference in the mass flow

rate through the low-pressure level circuit. For the case of low T_{sink} values, the difference in the mass flow rate between the two circuits (low-pressure and high-pressure circuit) is larger than that at high T_{sink} value, due to increased difference between liquid and vapor enthalpy at lower pressure values. Nevertheless, the overall impact on the COP_{h} is small, as also observed from Figure 5.11.

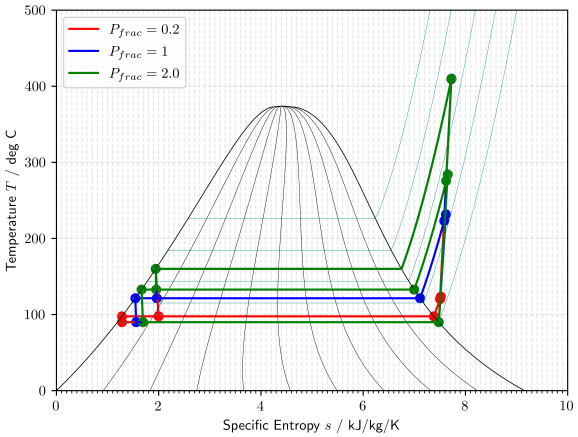

Figure 5.12: Ts diagram showing the effect of P_{frac} with T_{sink} 150 °C on two-stage heat pump configuration with flash-tank.

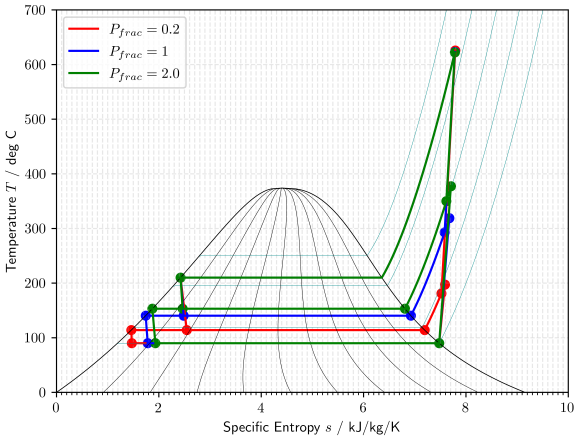

Figure 5.13: Ts diagram showing the effect of P_{frac} with T_{sink} 200 °C on two-stage heat pump configuration with flash-tank.

The P_{frac} value of 1.0 was selected as the optimal value for this heat pump configuration. This was chosen because an equal pressure ratio split helps in reducing the compressor design's complexity, with only limited impact on the COP_{h} value, as apparent from the above results.

Table 5.3 shows the optimal thermodynamic cycle parameters for this heat pump configuration for the different sink temperatures. The relative decrease in COP_{h} due to an increase in the T_{sink} is around 51 %, which is lower than the value found for previously mentioned heat pump configurations. This is mainly because at the highest T_{sink} value, this heat pump configuration performs better than the previously mentioned configurations. However, despite having a better COP_{h} at the highest T_{sink} value, the maximum temperature of the cycle is around 800°C, which indicates that the mechanical complexity of the heat pump design would be very high, especially to achieve a feasible compressor design. For the other T_{sink} values, the COP_{h} values are lower than the two-stage heat pump configuration with direct injection, as the net cooling of the working fluid before the inlet of the second compressor is lower in this configuration as the output of the flash-tank is a saturated vapor.

Table 5.3: Results obtained for the two-stage heat pump configuration with flash-tank.

Parameter	**Unit**	T_{sink} = 150 °C	T_{sink} = 200 °C	T_{sink} = 250 °C
COP_{h}	-	3.95	2.52	1.95
T_{max}	°C	410	623	802.5
β_{total}	-	8.81	27.18	66.86
α_{inj}	-	0.08	0.14	0.23
$P_{\text{frac, optim}}$	-	1.0	1.0	1.0
$\dot{Q}_{\text{cond}}$	MW	2.62	2.85	3.01
$\dot{Q}_{\text{evap}}$	MW	1.99	1.77	1.55
$W_{\text{comp, 1}}$	MW	0.27	0.40	0.49
$W_{\text{comp, 2}}$	MW	0.39	0.73	1.05

Figure 5.14 shows the Ts diagram of optimal two-stage heat pump designs for different T_{sink} values. Compared to the previous two-stage configuration, for each T_{sink} value, the amount of cycle area on the right side of the saturation dome has increased. As a result of this, the compressor work required is increased, without a significant increase in $\dot{Q}_{\text{cond}}$, except for the highest T_{sink} case. The presence of superheated vapor at the second compressor inlet leads to much higher compressor exit temperatures, resulting in higher work input and lower COP_{h} values. Compared to the previous two-stage configuration, a large amount of desuperheating is also needed before/in the condenser for this configuration

as the high pressure compressor‘s outlet temperature levels are much higher. This could also lead to increased irreversibilities in the condenser, depending on the process application that is considered.

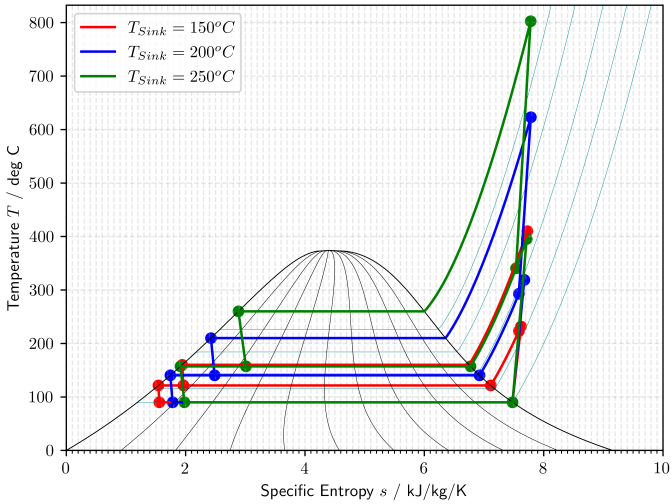

Figure 5.14: Ts diagram showing the effect of sink temperature on two-stage configuration with flash-tank.

5.1.4. Two Stage with Saturator

Like the previously discussed two-stage heat pump configurations, also the two-stage configuration with a saturator has only p_{intm} as the degree of freedom. Figure 5.15 shows the schematic of this heat pump configuration.

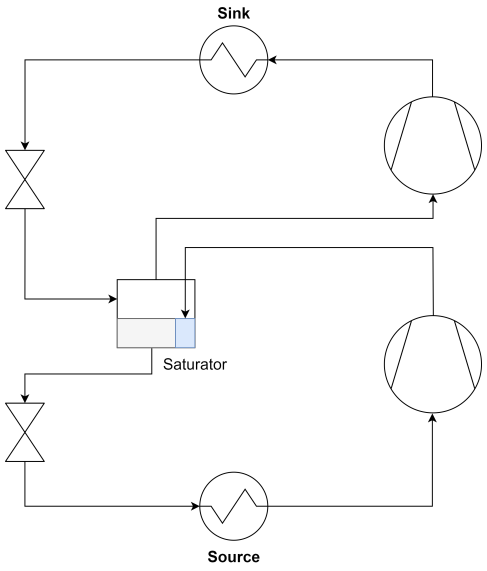

Figure 5.15: Schematic of the two-stage heat pump with saturator.

Figure 5.16 shows the variation of heat pump‘s $\mathrm{COP_h}$ with P_{frac} for different sink temperature levels, while the normalized $\mathrm{COP_h}$ values are shown in Figure 5.17. Similar to the other two-stage heat pump configurations, there is an optimal P_{frac} which maximizes the $\mathrm{COP_h}$ for all T_{sink} values. With an increase in T_{sink}, the optimal P_{frac} shifts towards higher values, varying from 1.08 for T_{sink} 150°C to 1.59 for T_{sink} for 250°C. The $\mathrm{COP_h}$-P_{frac} curve becomes flatter with an increase in T_{sink}. However, the change in curvature of the trend-line is lower than the one observed for the other two-stage configurations. For this heat pump configuration, the maximum deviation in $\mathrm{COP_h}$ (with respect to maximum $\mathrm{COP_h}$) due

to change in P_{frac}, ranges from around 6.5 % to 4 %, as the T_{sink} value increases from 150 to 250°C respectively. The deviation of COP_h with P_{frac} is highest for this configuration, as compared to those previously discussed.

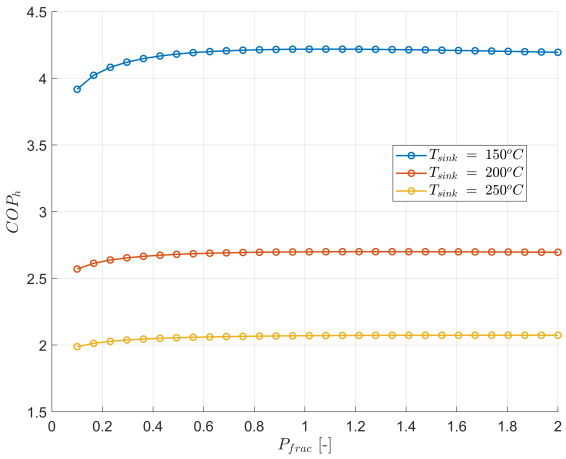

Figure 5.16: Variation of COP_h with P_{frac}, for two-stage heat pump configuration with saturator.

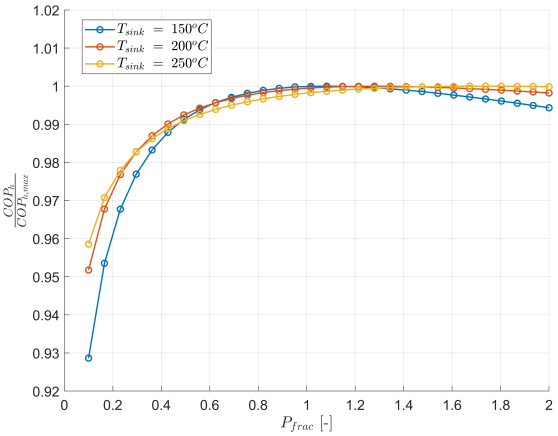

Figure 5.17: Variation of normalized COP_h (with respect to maximum COP_h) with P_{frac}, for two-stage heat pump configuration with saturator.

Figure 5.18 and Figure 5.19 show the heat pump's Ts diagram for different P_{frac} values at T_{sink} 150°C and 200°C respectively. The inlet thermodynamic conditions of the second compressor are those of saturated vapor, regardless of the value of design parameters. Therefore, varying the value of P_{frac} only changes the location of the inlet state point on the saturated vapor line, similarly to what was observed for the two-stage heat pump configuration with direct injection. The value of the mass flow rate through the first compressor is directly influenced by the P_{frac} value since this is a function of the saturator inlet conditions. At very low values of P_{frac}, the inlet temperature of the second compressor is lower but requires a high pressure ratio. Due to this high outlet pressure requirement, the outlet temperature of the second compressor increases (thus also the required total work input). On the contrary, for high values of P_{frac}, the condenser duty decreases because of lower condenser inlet temperatures. With an increase in T_{sink} value, maximum COP_h is achieved at high P_{frac} values, because of higher temperature requirements (Figure 5.19). Nevertheless, the effect of choosing a very low or very high P_{frac} values is similar for different T_{sink} cases.

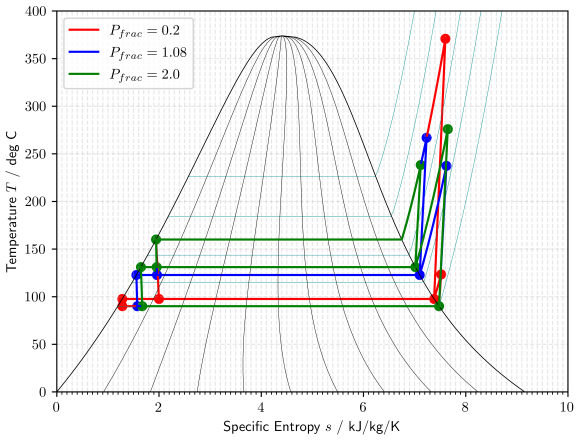

Figure 5.18: Ts diagram showing the effect of P_{frac} with T_{sink} 150 °C on two-stage heat pump configuration with saturator.

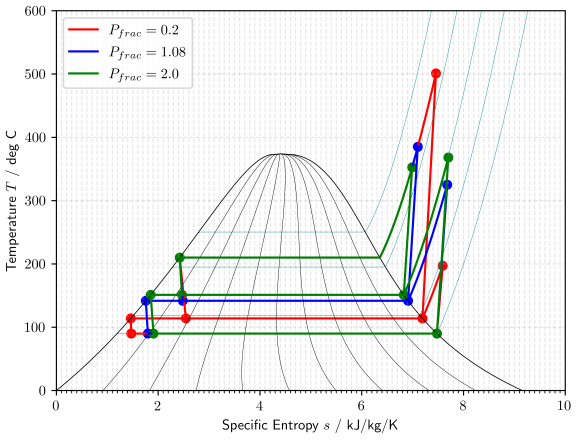

Figure 5.19: Ts diagram showing the effect of P_{frac} with T_{sink} 200 °C on two-stage heat pump configuration with saturator.

Table 5.4 reports the results of the optimization for this heat pump configuration for the different sink temperatures. Instead of α_{inj}, the value of mass flow rate through compressor 1 is reported ($\dot{m}_{\text{comp, 1}}$).

The value of $\dot{m}$ through the second compressor is fixed at 1 kg/s. The $\mathrm{COP_h}$ values obtained for all T_{sink} levels are highest for this heat pump configuration, compared to all the previously mentioned configurations. The inlet state of the second compressor is the same as the one for the case of direct injection. The amount of thermal energy available at the condenser is also similar to that estimated for the configuration with direct vapor injection. However, the amount of thermal energy exchanged in the evaporator is higher for this heat pump as compared to the configuration with direct injection (Table 5.2), resulting in a lower work input. Consequently, this heat pump configuration outperforms the direct injection heat pump configuration. With an increase in T_{sink} from 150 to 250°C, $\mathrm{COP_h}$ drop of about 51 % relative to the maximum $\mathrm{COP_h}$ estimated for the minimum T_{sink} is observed.

Table 5.4: Results obtained for the two-stage heat pump configuration with saturator.

Parameter	Unit	T_{sink} = 150 °C	T_{sink} = 200 °C	T_{sink} = 250 °C
$\mathrm{COP_h}$	-	4.22	2.70	2.07
T_{max}	°C	266.9	376.1	466
β_{total}	-	8.81	27.18	66.86
$\dot{m}_{\text{comp, 1}}$	-	0.84	0.73	0.62
$P_{\text{frac, optim}}$	-	1.08	1.24	1.59
$\dot{Q}_{\text{cond}}$	MW	2.32	2.30	2.22
$\dot{Q}_{\text{evap}}$	MW	1.80	1.49	1.21
$W_{\text{comp, 1}}$	MW	0.25	0.37	0.45
$W_{\text{comp, 2}}$	MW	0.30	0.48	0.63

Figure 5.20 shows the Ts diagram of optimal two-stage heat pump designs for different T_{sink} values, using saturator. Compared with the previous two-stage configuration results, for each T_{sink} value, the amount of cycle area has been increased towards the left inside the saturator dome. This results in a higher $\mathrm{COP_h}$ due to increased evaporator duty at a similar condenser duty value. With an increase in T_{sink} value, the increase in the amount of compressor work input required is higher than the increase in the thermal energy at the condenser side, resulting in a decrease in $\mathrm{COP_h}$ value.

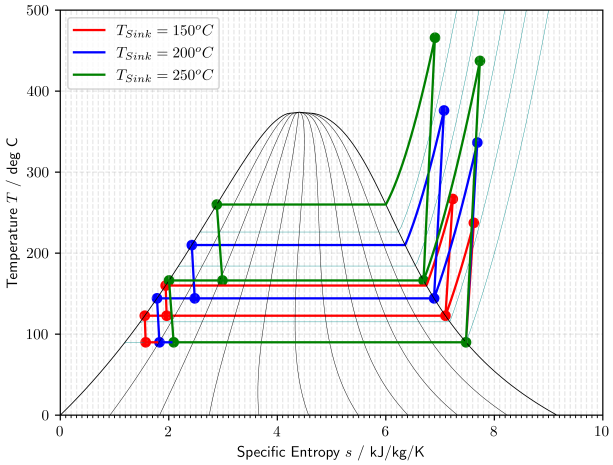

Figure 5.20: Ts diagram showing the effect of sink temperature on two-stage heat pump configuration with saturator.

5.1.5. Two Stage with Internal Heat Exchanger

The last selected configuration for reverse Rankine cycle based heat pump adopts an internal heat exchanger in place of the saturator or the flash tank, as shown in Figure 5.21. This heat pump configuration features only one degree of freedom, i.e., the intermediate pressure level p_{intm}. The parameter P_{frac} was used to analyze its effect on the thermodynamic performance of the heat pump.

Figure 5.22 shows the variation of heat pump's $\mathrm{COP_h}$ with P_{frac} for different temperature levels, while the normalized $\mathrm{COP_h}$ values are shown in Figure 5.23. With an increase in T_{sink} value, the optimal P_{frac}

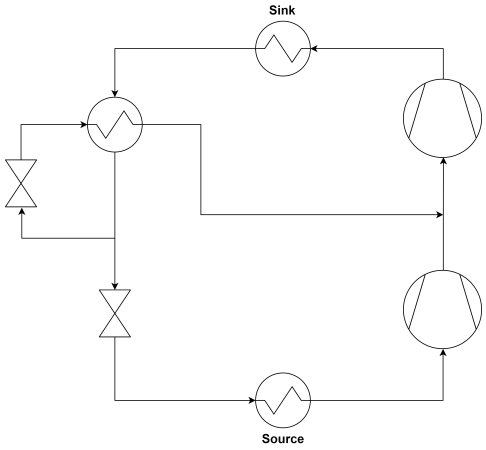

Figure 5.21: Schematic of the two-stage heat pump with internal heat exchanger.

also increases and the $\mathrm{COP_h}$-P_{frac} becomes more flatter, similar to two stage heat pump configuration using direct injection and the configuration using saturator. The optimal P_{frac} is found to shift from 0.95 for T_{sink} 150°C to 1.44 for T_{sink} 250°C. The deviation in $\mathrm{COP_h}$ (with respect to maximum $\mathrm{COP_h}$) with P_{frac} is found to vary from around 6 % to 3.5 % as the T_{sink} value increases from 150 to 250 °C. Similar to the heat pump configuration using saturator, the $\mathrm{COP_h}$ for this heat pump configuration is more sensitive to variations of P_{frac}.

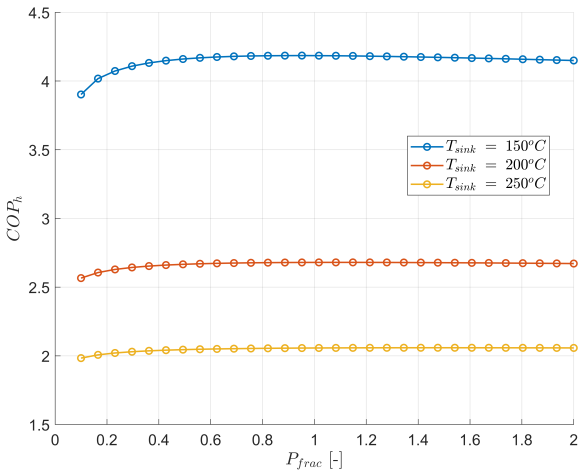

Figure 5.22: Variation of $\mathrm{COP_h}$ with P_{frac}, for two-stage heat pump configuration with internal heat exchanger.

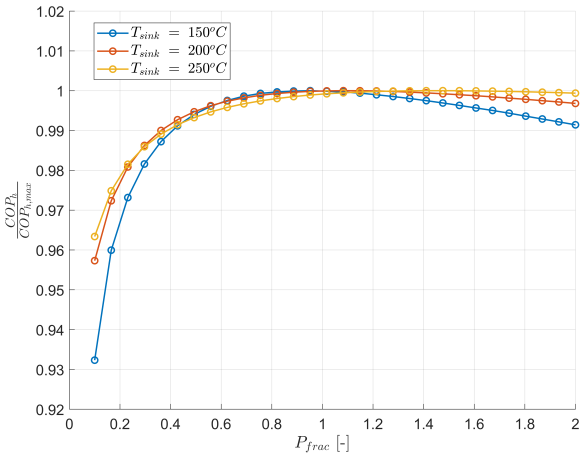

Figure 5.23: Variation of normalized $\mathrm{COP_h}$ (with respect to maximum $\mathrm{COP_h}$) with P_{frac}, for two-stage heat pump configuration with internal heat exchanger.

Figure 5.24 and Figure 5.25 show the heat pump's Ts diagram for different P_{frac} values at T_{sink} 150°C and 200°C respectively. For low values of P_{frac}, the effect of vapor injection becomes negligible as the outlet temperature of the first compressor is relatively low. On the contrary, at high values of P_{frac}, the condenser duty decreases as the maximum temperature at the condenser inlet is reduced. The amount of the vapor injected also increases with the increase in P_{frac}, which leads to a lower first compressor work. However, as P_{frac} continues to increase, this decrease in the first compressor work due to the reduced mass flow rate becomes negligible (with respect to the $\mathrm{COP_h}$ values) as the required pressure ratio for that compressor also starts to increase rapidly.

As T_{sink} increases, higher P_{frac} values are favorable as it allow for an increase in condenser duty which overcomes the increase in compression work. The net effect is a higher $\mathrm{COP_h}$ (Figure 5.25). Table 5.5 summarizes the main features of this heat pump configuration for the different sink temperatures. The $\mathrm{COP_h}$ values obtained for different T_{sink} levels are higher than all the other previously mentioned heat pump concept analyzed above, except for the configuration with the saturator. Nevertheless, the differ-

ence in $\mathrm{COP_h}$ is less than 1 % with respect to the values of $\mathrm{COP_h}$ found for the case with the saturator, regardless of the considered T_{sink}.

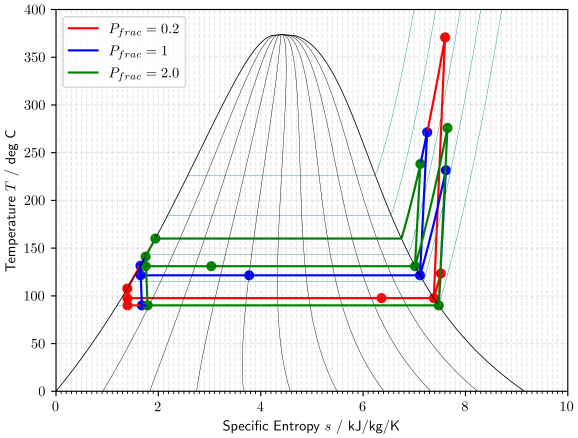

Figure 5.24: Ts diagram showing the effect of P_{frac} with T_{sink} 150 °C on two-stage heat pump configuration with internal heat exchanger.

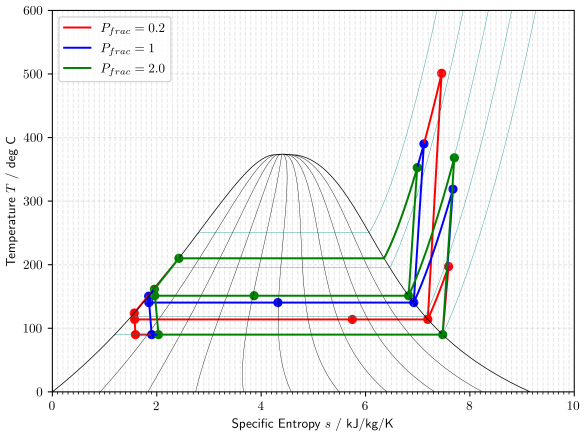

Figure 5.25: Ts diagram showing the effect of P_{frac} with T_{sink} 200 °C on two-stage heat pump configuration with internal heat exchanger.

Figure 5.26 shows the Ts diagram of the optimal design of the heat pump with the internal recuperator for different T_{sink} values, using internal heat exchanger and working fluid injection. The amount of desuperheating and subcooling both increase with T_{sink} value. The resulting vapor quality of the injected vapor is also higher at high T_{sink} values, which requires an increased amount of working fluid to be injected (Table 5.5).

Table 5.5: Results obtained for the two-stage configuration with internal heat exchanger.

Parameter	**Unit**	$\mathrm{T_{sink}}$ = 150 °C	$\mathrm{T_{sink}}$ = 200 °C	$\mathrm{T_{sink}}$ = 250 °C
$\mathrm{COP_h}$	-	4.19	2.68	2.06
T_{max}	°C	274.4	384.4	472.8
β_{total}	-	8.81	27.18	66.86
α_{inj}	-	0.15	0.26	0.37
$P_{\mathrm{frac,\ optim}}$	-	0.95	1.09	1.44
$\dot{Q}_{\mathrm{cond}}$	MW	2.33	2.32	2.24
$\dot{Q}_{\mathrm{evap}}$	MW	1.80	1.5	1.21
$W_{\mathrm{comp,\ 1}}$	MW	0.24	0.36	0.44
$W_{\mathrm{comp,\ 2}}$	MW	0.32	0.50	0.65

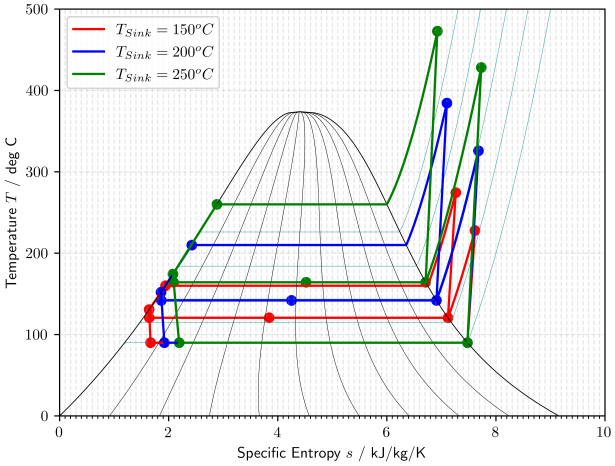

Figure 5.26: Ts diagram showing the effect of sink temperature on two-stage heat pump configuration with internal heat exchanger.

5.2. Reverse Brayton Cycle - Baseline Case

This section provides results for the heat pump configurations based on the reverse Brayton cycle for the case of a constant temperature heat sink, as mentioned earlier in Section 3.5. Since the objective for this baseline analysis was to understand the general $\mathrm{COP_h}$ trends for each heat pump configuration, only one T_{sink} value (=200°C) was considered. Two different working fluids were considered, i.e., $\mathrm{CO_2}$ and air (dry).

5.2.1. Single Stage

The single stage heat pump configuration was found to have two degrees of freedom, namely, the minimum and maximum pressure of the cycle, hereafter referred to as p_{low} and p_{high}. Figure 5.27 shows the schematic of this heat pump configuration. To have a consistent analysis among different configurations, the total pressure ratio of the system (β_{total}) was varied along with p_{low} in the simulations. Regarding the operational limits, the maximum compressor discharge pressure was limited to 250 bar, given the challenges and costs that high pressure equipment entails. In the literature, this maximum pressure limit varies from 140-300 bar, based on techno-economic considerations [48][49]. This limit in the maximum pressure was also considered for all the other heat pump configurations based on the reverse Brayton cycle.

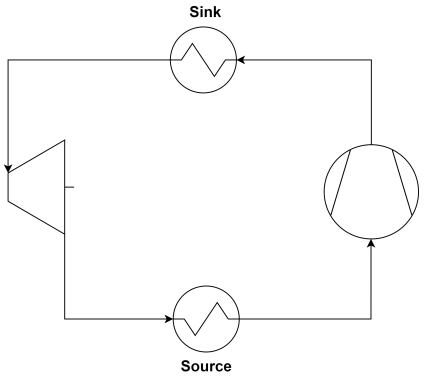

Figure 5.27: Schematic of the single-stage reverse Brayton cycle heat pump.

Figure 5.28 shows the estimated $\mathrm{COP_h}$ as a function of β_{total} at different P_{low} values, using $\mathrm{CO_2}$ as the working fluid and with a T_{sink} of 200°C. With an increase in β_{total}, the value of $\mathrm{COP_h}$ is found to increase, independent of P_{low} value. At low values of β_{total} (<4), the obtained $\mathrm{COP_h}$ is less than 1 and becomes even negative as β_{total} decreases further. The reason behind such $\mathrm{COP_h}$ trends is highlighted in Figure 5.29, which shows the Ts diagram of this heat pump configuration with different β_{total} and a fixed P_{low} of 50 bar. At very low values of β_{total}, the resulting compressor discharge temperature becomes lower than the required T_{sink} value, thus not meeting the design specifications. As the β_{total} value increases, the cycle area increases. Due to the curvature of the isobars of the working fluid, the increase in the thermal energy available at the sink side is higher than the increase in the required work input, which leads to a higher $\mathrm{COP_h}$ value. Therefore, to have a beneficial heat pump operation with this configuration, β_{total} higher than at least 5 is required, depending on P_{low} value. For all P_{low} values, the $\mathrm{COP_h}$ value is found to plateau at very high β_{total} value (>11), implying that, increasing β_{total} further only leads to additional complexity without any gain in $\mathrm{COP_h}$.

For a given β_{total}, the value of $\mathrm{COP_h}$ is found to increase with P_{low} (in range $\mathrm{COP_h} > 0$). But, as the P_{low} values increases, this gain in $\mathrm{COP_h}$ becomes smaller. Figure 5.30 shows the Ts diagram for this heat pump configuration with different P_{low} values, where β_{total} is taken equal to 8. As the P_{low} value increases, the cycle shifts towards the left, towards the critical region. At high values of P_{low}, near the critical region, the curvature of the isobars increases, resembling an “S” shaped curve. As a result, the amount of thermal energy exchange at the sink side increases while limiting the increase in required compressor work input. Once the P_{low} is already high enough to fall near/into the supercritical region,

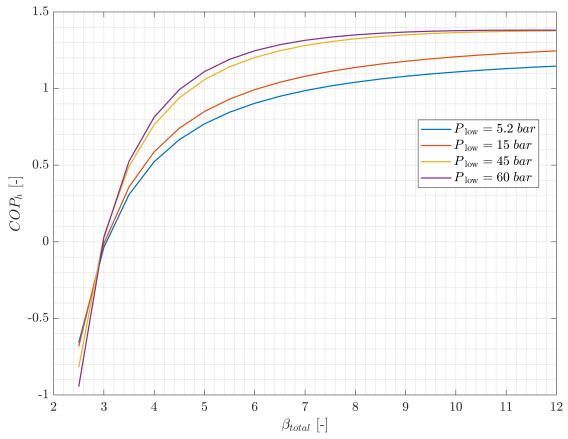

Figure 5.28: Variation of $\mathrm{COP_h}$ with β_{total} at different P_{low} values for the single stage reverse Brayton cycle, using $\mathrm{CO_2}$ as working fluid.

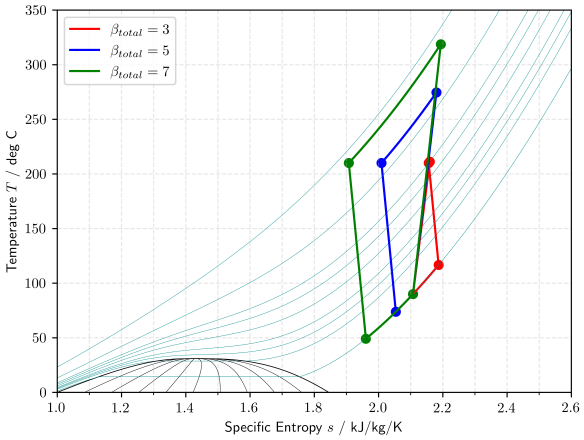

Figure 5.29: Ts diagram showing the effect of β_{total} (with P_{low} 50 bar) on the single-stage reverse Brayton cycle, using $\mathrm{CO_2}$ as working fluid.

the relative change in isobar curvature is limited, and as a result, no major change in the sink capacity is observed. This explains the reason why the $\mathrm{COP_h}$ increase becomes smaller at high P_{low} values, for a given β_{total} . The obtained $\mathrm{COP_h}$ values for this heat pump configuration are smaller than the ones found for the reverse Rankine cycle based heat pump configurations for the same T_{sink} value. Considering an average $\mathrm{COP_h}$ of 2.45 for the reverse Rankine cycle based heat pump configurations, the relative difference in $\mathrm{COP_h}$ is around - 47 %, as the single-stage reverse Brayton cycle based heat pump features a maximum $\mathrm{COP_h}$ of 1.3.

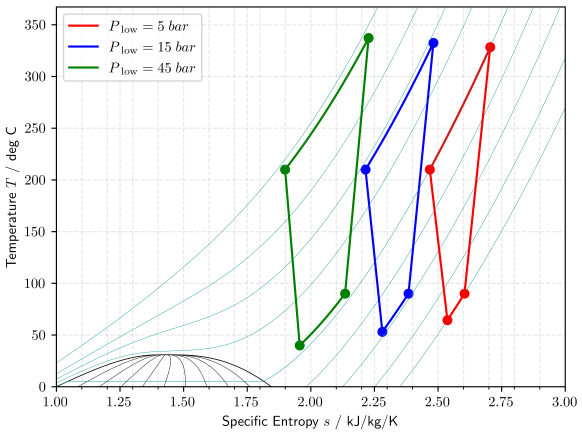

Figure 5.30: Ts diagram showing the effect of P_{low} (with β_{total} = 8) on the single-stage reverse Brayton cycle, using $\mathrm{CO_2}$ as working fluid.

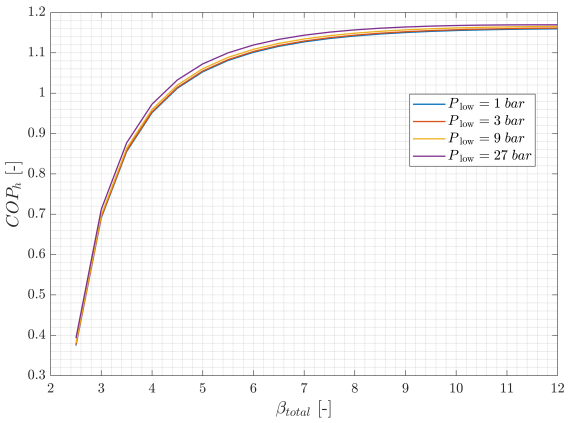

Figure 5.31: Variation of $\mathrm{COP_h}$ with β_{total} at different P_{low} values for the single stage reverse Brayton cycle, using Air as working fluid.

Figure 5.31 shows the trends of $\mathrm{COP_h}$ variation with β_{total} and P_{low}, when using air as the working fluid. The maximum achievable $\mathrm{COP_h}$ is lower than the one found for $\mathrm{CO_2}$. The variation of $\mathrm{COP_h}$ with β_{total} is found to be similar to that of $\mathrm{CO_2}$. With an increase in β_{total}, the value of $\mathrm{COP_h}$ increases, and at very low values of β_{total}, infeasible solutions exist. The reason behind such trends can be explained by Figure 5.32, where Ts diagrams of this heat pump configuration using air as working fluid at different β_{total}, with P_{low} of 20 bar, are presented. At very low values of β_{total}, the resulting turbine exit temperature becomes higher than the selected T_{source} value, resulting in an infeasible thermodynamic cycle. As the β_{total} value increases, the overall cycle area increases. However, due to the curvature of the isobars, the increase in the thermal energy available at the sink side is higher than the increase in the required work input, resulting in an increased $\mathrm{COP_h}$ value.

For the case of air, the effect of P_{low} is small as compared to the results obtained for CO_2. In this case, the maximum deviation of COP_h with a change in P_{low}, at a given β_{total}, is around 1.5 % (relative to the higher value of COP_h). As the P_{low} value increases, no change in the curvature of isobars is observed as the cycle lays in the ideal gas region, as shown by Figure 5.33. This figure shows the heat pump cycle for different P_{low} values, assuming a constant β_{total} of 4. Increasing P_{low}, the cycle shifts towards the left, at higher isobars, but since the isobars are essentially parallel, no change in the COP_h value is obtained.

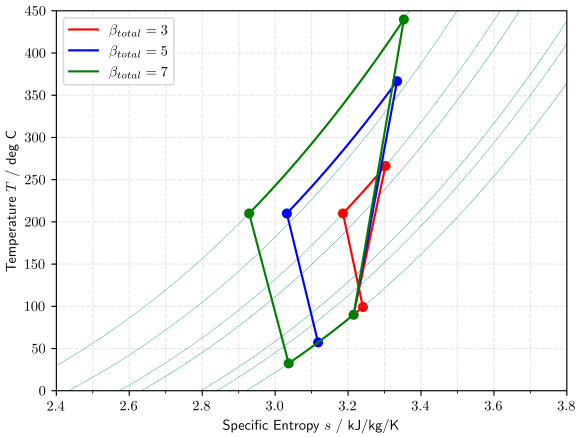

Figure 5.32: Ts diagram showing the effect of β_{total} (with P_{low} 20 bar) on the single-stage reverse Brayton cycle, using Air as working fluid.

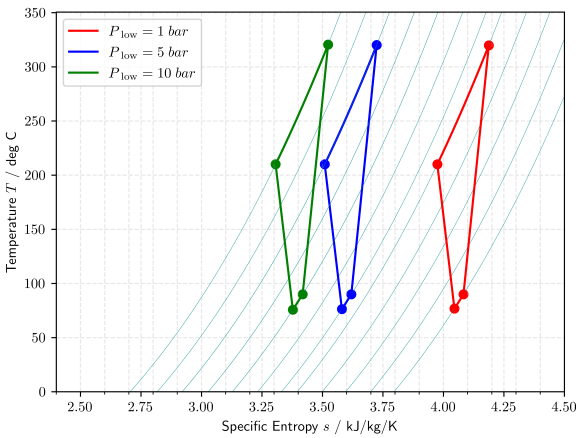

Figure 5.33: Ts diagram showing the effect of P_{low} (with β_{total} = 4) on the single-stage reverse Brayton cycle, using Air as working fluid.

5.2.2. Single Stage with Internal Recuperation

P_{low} and P_{high} are the two degrees of freedom of the single-stage heat pump configuration with internal recuperation. In place of P_{high}, the total pressure ratio β_{total} was varied, in the analysis, in analogy to what was done for the previous heat pump configuration. Figure 5.34 shows the schematic of this heat pump configuration.

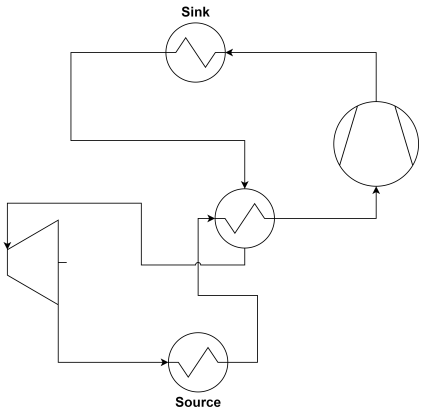

Figure 5.34: Schematic of the single-stage heat pump with internal recuperation.

Figure 5.35 shows the variation of the heat pump COP_h as a function of β_{total}, for different P_{low} values and a T_{sink} of 200°C when using CO_2 as working fluid. With an increase in β_{total}, the COP_h values increase up to a maximum value and then start decreasing. For every P_{low} value, there is an optimal β_{total} maximizing the COP_h and this optimal β_{total} value is found to increase with an increase in the P_{low} value. The COP_h values are higher than the those obtained for the previously analyzed single-stage configuration. This improvement is due to the addition of internal recuperation, which increases the compressor inlet temperature, increasing both the thermal energy exchange at the sink and the

compressor work input, for a constant β_{total}. Nevertheless, the increase in the sink capacity is dominating, leading to an increase in COP_h. The effect of β_{total} on this thermodynamic cycle is illustrated in Figure 5.36, where the Ts diagrams were calculated for a constant P_{low} value of 50 bar. As the value of β_{total} increases, the cycle area expands towards the left, leading to a higher thermal energy exchange at the sink side. Nevertheless, this change is accompanied by higher compression work as the required pressure ratio increases. Up to the "optimal" β_{total} value, the additional compression work is compensated by the increased thermal power transferred to the sink. However, above that value, the increase in compression work is more dominant, resulting in a decrease of COP_h. Also, it is observed that at high β_{total} values, the turbine exit conditions fall into the two-phase region, making the turbine design arguably challenging.

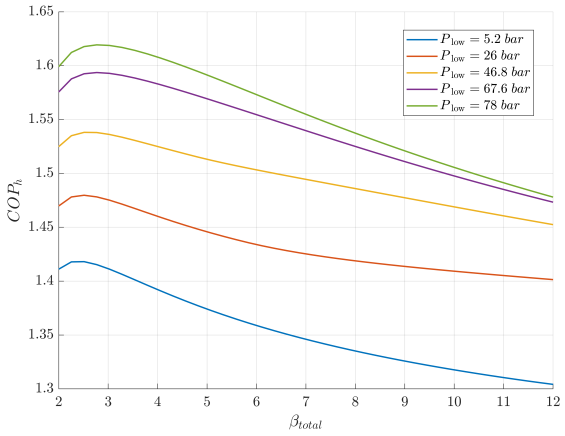

Figure 5.35: Variation of COP_h with β_{total} at different P_{low} values for single stage configuration with internal recuperation, using CO_2 as working fluid.

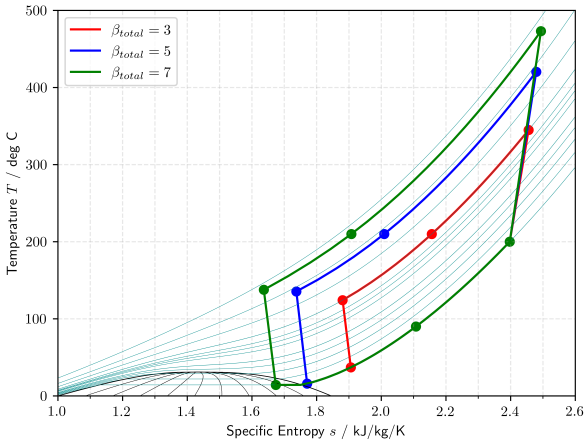

Figure 5.36: Ts diagram showing the effect of β_{total} (with P_{low} 50 bar) on single-stage configuration with internal recuperation, using CO_2 as working fluid.

Compared to the previously mentioned single-stage heat pump configuration, the cycle area is larger for this heat pump configuration (Figure 5.36). The value of COP_h also increases by augmenting P_{low}, at a given β_{total}. To understand the reason, the thermodynamic cycle of this heat pump configuration was plotted in a Ts diagram for different P_{low} values and a constant β_{total} (=4), as shown in Figure 5.37. The curvature of the working fluid isobars starts to change by increasing P_{low}, as now the maximum pressure is higher and falls in the near-critical/critical region. This is beneficial to increase the thermal energy transferred to the sink without a major rise in the compression work. As a result, at high P_{low} values, for a given β_{total}, the cycle area increases, leading to a higher amount of thermal energy exchange at the sink with an only marginal increase in compression work. This can also be explained by the relative decrease in the specific volume of the working fluid at high P_{low} values, which helps in achieving higher sink thermal loads per unit of turbomachinery work [42]. Nevertheless, the COP_h values are still smaller than those obtained for the reverse Rankine cycle based heat pump configurations.

Figure 5.38 shows the variation of the heat pump COP_h for air as a function of β_{total} and P_{low}, with T_{sink} equal to 200°C. The COP_h value decreases monotonically with the increase in β_{total} and thus, the maximum COP_h is found at the lowest β_{total} value. The COP_h values obtained are lower than the ones obtained for CO_2 but are still larger than those obtained for single-stage configuration without recuperation when using air. The effect of β_{total} on the heat pump is apparent from Figure 5.39, which illustrate in the Ts diagram how the thermodynamic cycle changes for different β_{total} values when P_{low} is equal to 20 bar.

With an increase in β_{total}, the cycle area increases, leading to a higher thermal power available at the sink. However, the increase in compression work is larger, as very high compressor discharge temperatures are reached. This results in a lower COP_h value. At high β_{total} values, the amount of thermal power exchanged with the thermal source also increases, as the turbine exit temperature decreases (reaching even temperatures lower than 0°C for high β_{total} values). In this case, the effect of P_{low} is very similar to the one observed for the single-stage configuration. A change in the P_{low}

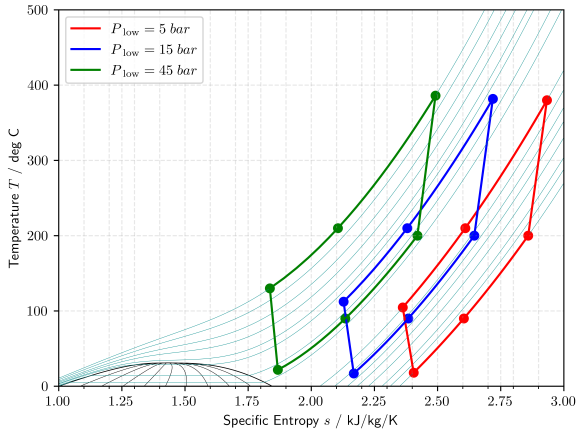

Figure 5.37: Ts diagram showing the effect of P_{low} (with β_{total} = 4) on single-stage configuration with internal recuperation, using CO_2 as working fluid.

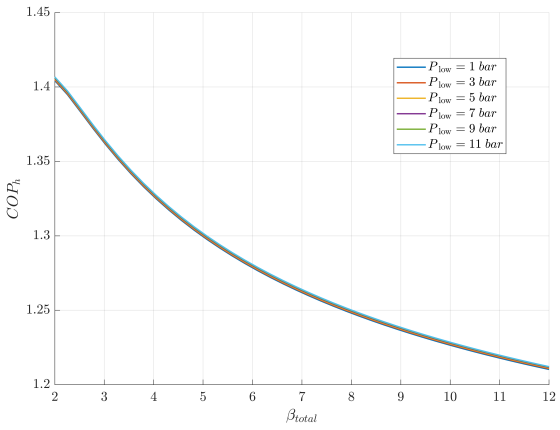

Figure 5.38: Variation of COP_h with β_{total} at different P_{low} values for single stage configuration with internal recuperation, using Air as working fluid.

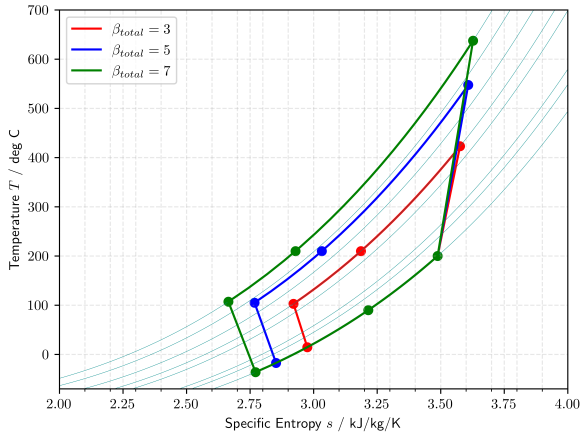

Figure 5.39: Ts diagram showing the effect of β_{total} (with P_{low} 20 bar) on the single-stage configuration with internal recuperation, using Air as working fluid.

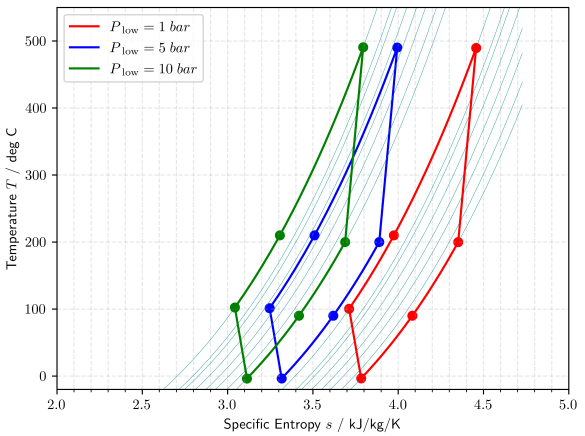

Figure 5.40: Ts diagram showing the effect of P_{low} (with β_{total} = 4) on the single-stage configuration with internal recuperation, using Air as working fluid.

value does not have an impact on the COP_h, as the maximum deviation is less than 0.8% (relative to maximum COP_h). It can be concluded that for an ideal gas the effect of P_{low} is negligible. This holds true also for the other reverse Brayton cycle configurations analyzed in the following. Figure 5.40 shows the Ts diagrams obtained for different P_{low} values and β_{total} equal to 4. The cycle diagram shifts towards the left as the P_{low} increases. However, COP_h values of the various cycles remains essentially the same and much lower than those estimated for CO_2. For these reasons, no further results will be reported for air in the remaining of Section 5.2. For further results related to different heat pump configurations using air as working fluid, see Appendix C.

5.2.3. Two Stage with Intercooling

The two-stage heat pump configuration with intercooling was found to have three degrees of freedom. Compared to the single-stage configurations, the additional degree of freedom, is the intermediate pressure level (p_{intm}). To analyze the effect of p_{intm}, the parameter P_{frac} was varied in the calculations, in analogy to what done for the reverse Rankine cycle based heat pump configurations (Section 5.1). Figure 5.41 shows the schematic of this heat pump configuration. Figure 5.42 shows the variation of COP_h with P_{frac} for different P_{low} values, when β_{total} is taken constant and equal to 4 and CO_2 is the working fluid.

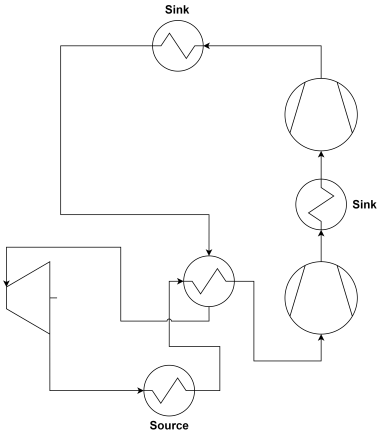

Figure 5.41: Schematic of the two-stage heat pump with intercooling.

As observed for the reverse Rankine cycle two-stage heat pump configuration, the value of $\mathrm{COP_h}$ increases up to an optimal P_{frac} value and, after that, starts to decrease monotonically. This trend is the same regardless the value of P_{low}. However, the $\mathrm{COP_h}$ increases by augmenting P_{low}. To understand the effect of P_{low} on the optimal value of P_{frac}, the values of $\mathrm{COP_h}$ are normalized with respect to maximum $\mathrm{COP_h}$ and are plotted against P_{frac} in Figure 5.43. It can be concluded that the optimal P_{frac} value remains independent of P_{low} and is always around 1.1 for this heat pump configuration.

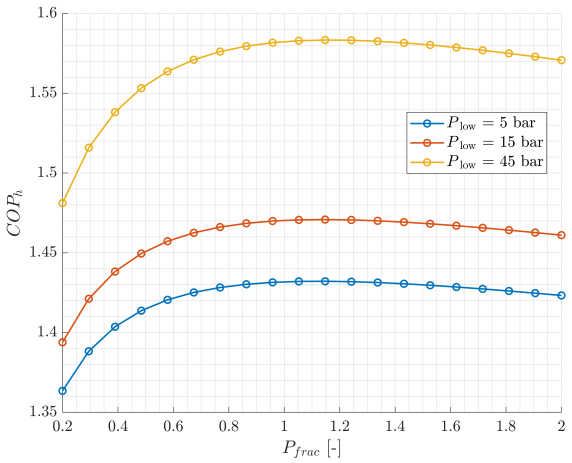

Figure 5.42: Variation of $\mathrm{COP_h}$ with P_{frac} at different P_{low} values (with β_{total} = 4) for the two-stage configuration with intercooling, using $\mathrm{CO_2}$ as working fluid.

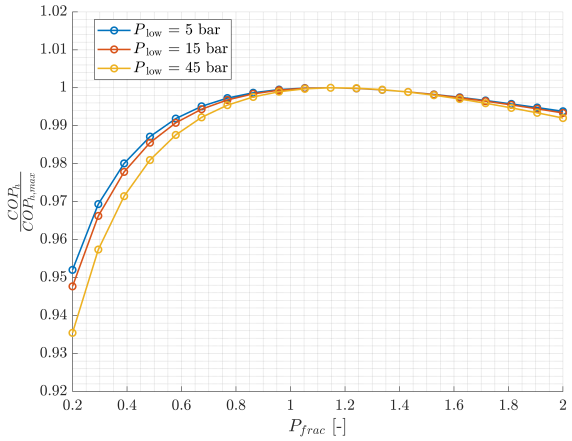

Figure 5.43: Variation of normalized $\mathrm{COP_h}$ (with respect to maximum $\mathrm{COP_h}$) with P_{frac} at different P_{low} values (with β_{total} = 4) for the two-stage configuration with intercooling, using $\mathrm{CO_2}$ as working fluid.

Figure 5.44 and Figure 5.45 shows the Ts diagram of thermodynamic cycle for different P_{frac} values assuming P_{low} equal to 15 bar or 45 bar and β_{total} equal to 4. As the P_{frac} value increases, the thermal power exchanged with the low-pressure sink increases while the thermal power available at the high-pressure sink decreases. Similar behavior is also observed for the power input of the two compressors. An increase in P_{frac} leads to higher power input for low-pressure compressor while this decreases for the high-pressure compressor. For both the P_{low} values, similar behavior is observed.

No results are reported for the case of air. However, the overall trend of $\mathrm{COP_h}$ variation with P_{frac} is same as observed for $\mathrm{CO_2}$.

Figure 5.46 shows the variation of the heat pump $\mathrm{COP_h}$ as a function of β_{total} and P_{low}, when T_{sink} equal to 200°C and P_{frac} equal to 1.0 and $\mathrm{CO_2}$ is the working fluid. The obtained trends show an optimal β_{total} value for which the $\mathrm{COP_h}$ is maximized. For low values of P_{low}, this optimal β_{total} is close to 2.5, but as the P_{low} values rises up to 60 bar, this value increases to around 4.2. The values of $\mathrm{COP_h}$

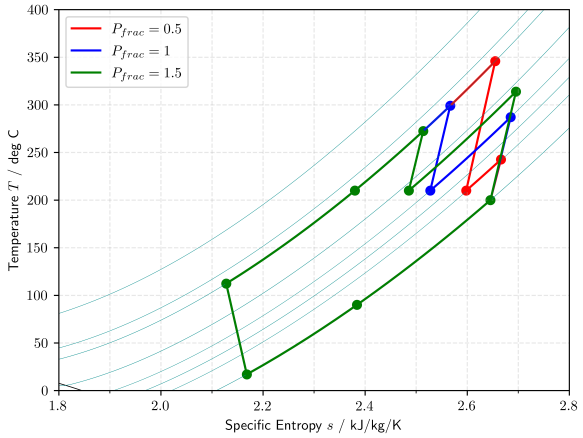

Figure 5.44: Ts diagram showing the effect of P_{frac} (with P_{low} = 15 bar and β_{total} = 4) on the two-stage configuration with intercooling, using CO_2 as working fluid.

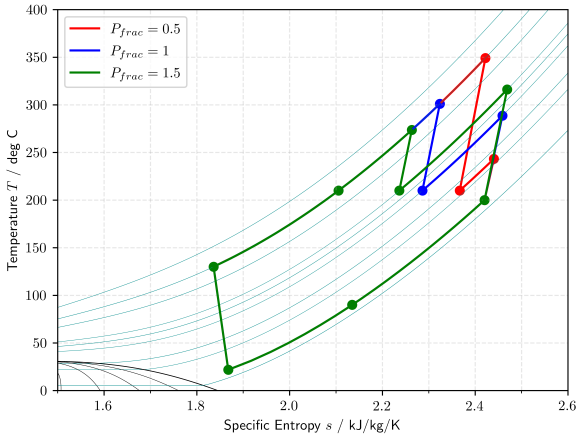

Figure 5.45: Ts diagram showing the effect of P_{frac} (with P_{low} = 45 bar and β_{total} = 4) on the two-stage configuration with intercooling, using CO_2 as working fluid.

for this configuration are higher than those obtained for the single-stage heat pump with recuperation. Comparing the maximum COP_h estimated for single-stage configuration with recuperation, at P_{low} of 60 bar, the relative increase in COP_h is around 4.5 %. The effect of β_{total} is illustrated by Figure 5.47, which shows in the Ts diagrams how the thermodynamic cycle changes by varying β_{total} for the case of P_{low} equal to 50 bar. The cycle area increases with an increase in β_{total}, leading to a higher thermal energy available at the sink and a higher compression work. In correspondence of the optimal β_{total} value, the increase in thermal power transferred to the sink prevails over that in the compression power due to the S-shaped trend of the isobars. As the β_{total} is further increased, the compression work rises substantially, leading to a decrease in COP_h. For high β_{total} values, the turbine exit temperature tends to decrease, promoting thermal recuperation from the heat pump source. However, for very high β_{total} values, the turbine exit conditions fall into the two-phase region, complicating the design of the machine. The maximum β_{total} depends on the value of P_{low} for a given T_{source} and T_{sink}.

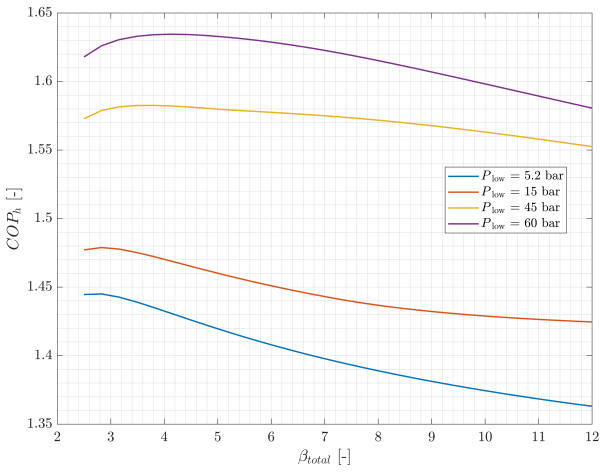

Figure 5.46: Variation of COP_h with β_{total} at different P_{low} values for the two-stage configuration with intercooling (with P_{frac} = 1), using CO_2 as working fluid.

The higher COP_h opbtained with respect to the single stage recuperated configuration can be explained by comparing Figure 5.36 and Figure 5.47. The compression work reduces by cooling the working fluid before the second compressor. The cooling of working fluid is exploited to transfer thermal energy to the heat pump sink, increasing the overall heat pump capacity. However, the overall thermal power transferred to the sink is still lower than that obtained for a single stage heat pump with internal recuperation. Nevertheless, the decrease in compression work is prevailing, which leads to a higher COP_h

value for the two-stage heat pump configuration with intercooling. The effect of P_{low} on the COP_h is the same as for other configurations. For any given β_{total}, higher P_{low} value leads to higher COP_h. Figure 5.48 shows in a Ts diagram, the changes in the thermodynamic cycle for different P_{low} values and a constant β_{total} (=4).

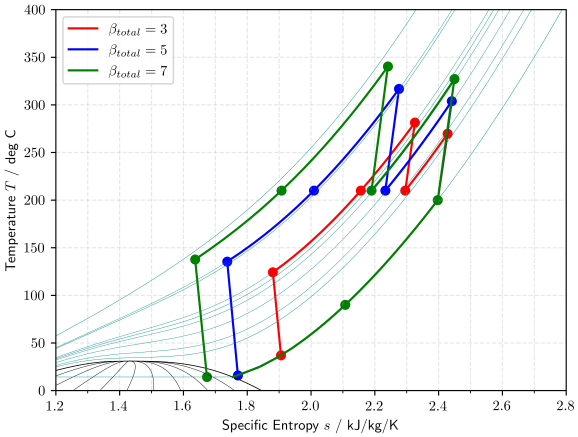

Figure 5.47: Ts diagram showing the effect of β_{total} (with P_{low} = 50 bar and P_{frac} = 1) on the two-stage configuration with intercooling, using CO_2 as working fluid.

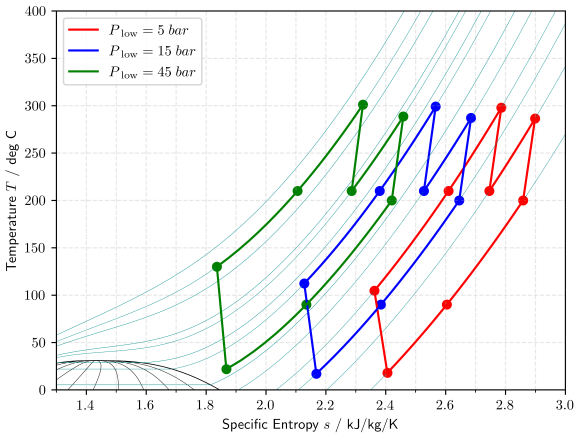

Figure 5.48: Ts diagram showing the effect of P_{low} (with β_{total} = 4 and P_{frac} = 1) on the two-stage configuration with intercooling, using CO_2 as working fluid.

5.2.4. Two Stage with Internal Recuperation and Intercooling

This heat pump configuration has three pressure levels that can be optimized, namely, P_{low}, p_{intm} and P_{high}. In analogy to the case of two-stage heat pump configuration with intercooling, the thermodynamic cycle parameters which have been varied in the analysis are P_{frac}, P_{low} and β_{total}. Figure 5.49 shows the schematic of this heat pump configuration.

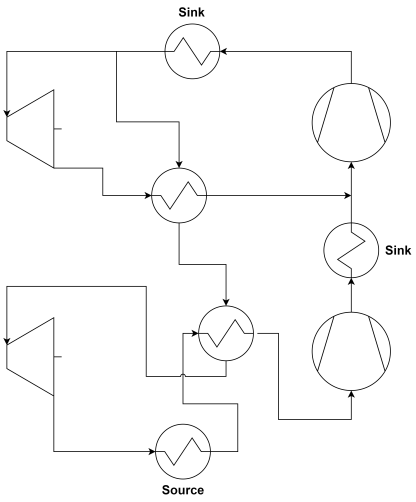

Figure 5.49: Schematic of the two-stage heat pump with internal heat recuperation and intercooling.

Figure 5.50 shows the variation of COP_h with P_{frac} for different values of P_{low}, while β_{total} is taken constant and equal to 4. There is an optimal P_{frac} value which maximizes the COP_h value. The COP_h values rapidly drop for P_{frac} values lower than the optimal one. On the contrary, the decrease in COP_h is more gradual for larger values of P_{frac}.Figure 5.51 shows the variation of the COP_h once normalized with respect to the maximum value with P_{frac} and P_{low}. The optimal P_{frac} value is found to be independent of the P_{low} value. However, with an increase in P_{low} value, the COP_h-P_{frac} curve becomes more flat, reducing the sensitivity of COP_h to a change in P_{frac}. The optimal P_{frac} value is around 1.3 for this heat

pump configuration.

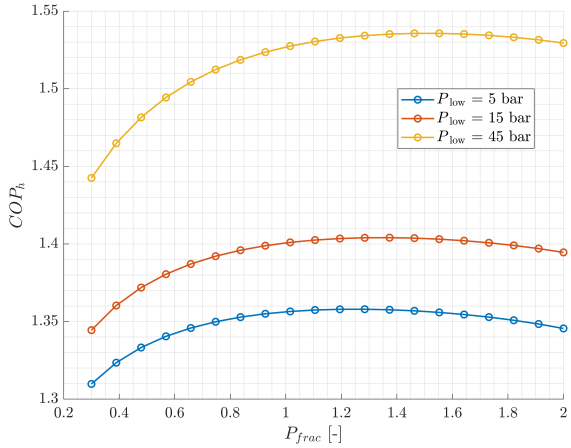

Figure 5.50: Variation of $\mathrm{COP_h}$ as a function of P_{frac} and P_{low} values (with β_{total} = 4) for the two-stage configuration with internal recuperation and intercooling, using $\mathrm{CO_2}$ as working fluid.

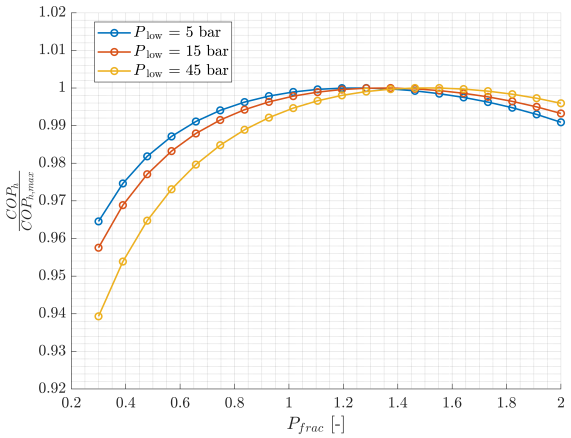

Figure 5.51: Variation of normalized $\mathrm{COP_h}$ (with respect to maximum $\mathrm{COP_h}$) as a function of P_{frac} and P_{low} (with β_{total} = 4) for the two-stage configuration with internal recuperation and intercooling, using $\mathrm{CO_2}$ as working fluid.

Figure 5.52 and Figure 5.53 represent the thermodynamic cycle for this heat pump configuration in the Ts diagram for different P_{frac} values. The charts differ for the assumed P_{low} value, which is, respectively, 15 bar and 45 bar. With an increase in P_{frac}, the thermal power exchanged in the low-pressure sink and the power consumed by the first compressor increase. In contrast, the opposite trend is observed for the high-pressure sink and the second compression stage. Thus, the optimal P_{frac} value is that allowing for the best trade-off between the increase in thermal power exchanged at the two sinks and the overall compression work. This trade-off seems to be insensitive to the value of P_{low}.

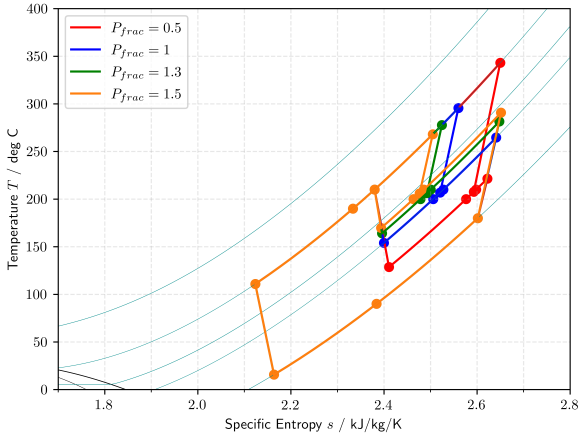

Figure 5.52: Ts diagram showing the effect of P_{frac} (with P_{low} = 15 bar and β_{total} = 4) on the two-stage configuration with internal recuperation and intercooling, using $\mathrm{CO_2}$ as working fluid.

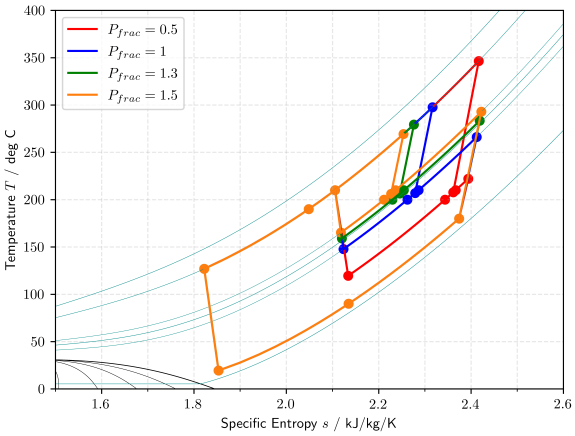

Figure 5.53: Ts diagram showing the effect of P_{frac} (with P_{low} = 45 bar and β_{total} = 4) on the two-stage configuration with internal recuperation and intercooling, using $\mathrm{CO_2}$ as working fluid.

Figure 5.54 shows the variation of the heat pump $\mathrm{COP_h}$ as a function of β_{total} and P_{low}, when T_{sink} and P_{frac} are equal to 200°C and 1.3, respectively, using $\mathrm{CO_2}$ as working fluid. There is an optimal β_{total} value whereby the $\mathrm{COP_h}$ value is maximized. For low values of P_{low}, this optimal β_{total} is very close to 5, but as the P_{low} values is raised to 60 bar, the optimal value shifts to around 6. The values of $\mathrm{COP_h}$ for this configuration are lower than those obtained for the two-stage heat pump configuration with intercooling. The maximum $\mathrm{COP_h}$ is lower by about 1.8 %. Figure 5.55 illustrates the effect of β_{total} on thermodynamic cycle, where Ts diagram for different β_{total} values, while P_{low} and P_{frac} are taken equal to 50 bar and 1.3, respectively, is shown. The cycle area increases with an increase in

β_{total}, leading to a higher thermal power exchanged at the sinks and compression power. An increase in the β_{total} value also increases the thermal energy recuperated from the thermal source as the turbine exit temperature decreases. However, at very high β_{total} values, the turbine exit conditions fall into the two-phase region, possibly hindering the reliability and feasibility of the expander. As mentioned earlier, the maximum feasible value of β_{total} depends on the value of P_{low} for a given T_{source} and T_{sink}.

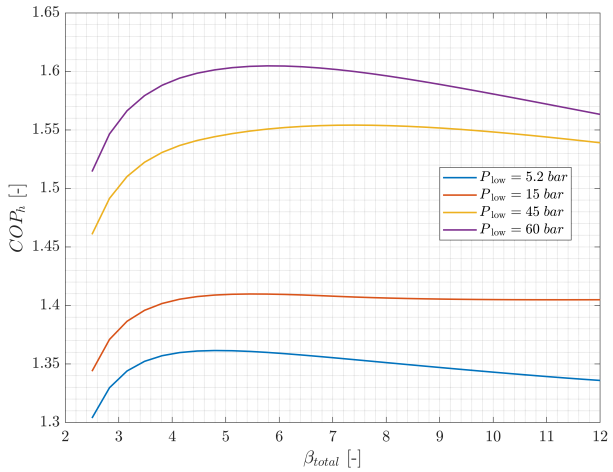

Figure 5.54: Variation of COP_h with β_{total} at different P_{low} values (with P_{frac} = 1.3) for two-stage configuration with internal recuperation and intercooling, using CO_2 as working fluid.

The reason for the decrease in maximum COP_h, under similar pressure levels, with respect to the two-stage heat pump configuration with intercooling, can be explained by comparing Figure 5.48 and Figure 5.56. For the case of the current configuration, lower compression work is required, as the working fluid is cooled further in this case. However, this leads to a lower sink duty due to reduced compressor discharge temperature. This decrease in thermal power transferred to the sink is higher than the decrease in the compression work, which results in an overall decrease in COP_h for this configuration. The variation of COP_h with P_{low}, for a given β_{total}, is similar to that observed for other configurations. For any given β_{total} values, increasing P_{low} results in an increased COP_h value. Figure 5.56 shows the thermodynamic cycle of this heat pump configuration in the Ts diagram for different P_{low} values at constant β_{total} (= 4). As apparent from the figure, for high P_{low} values, the thermal power exchanged with the sink increases substantially at the cost of a marginal increase in compression work due to the “S”-shaped characteristics of the isobars at high-pressure levels.

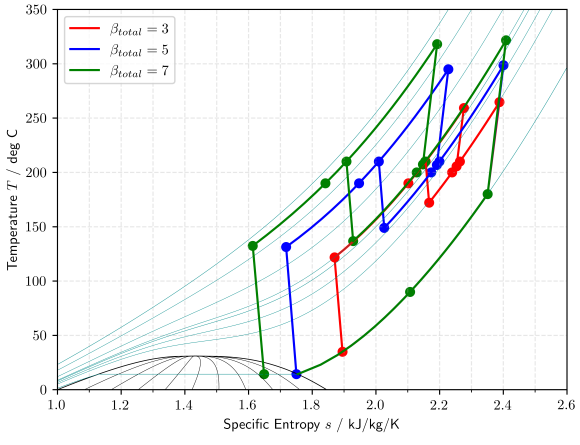

Figure 5.55: Ts diagram showing the effect of β_{total} (with P_{low} = 50 bar and P_{frac} = 1.3) on two-stage configuration with internal recuperation and intercooling, using CO_2 as working fluid.

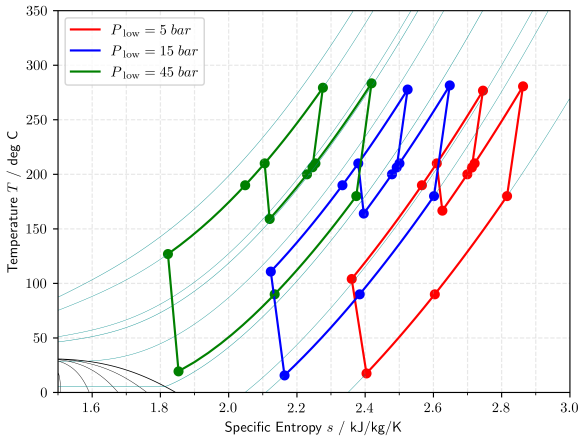

Figure 5.56: Ts diagram showing the effect of P_{low} (with β_{total} = 4 and P_{frac} = 1.3) on two-stage configuration with internal recuperation and intercooling, using CO_2 as working fluid.

5.3. Reverse Brayton Cycle - Sensible Heat Sink Case

This section provides the results of the thermodynamic cycle analysis performed for the heat pump configurations based on the reverse Brayton cycle for the sensible heat sink case, namely when the stream in the cold side of the thermal sink undergoes a temperature increase. In this scenario, the temperature of the working fluid is specified at the outlet of the thermal sink and not at the inlet, as explained earlier (Section 3.5).

5.3.1. Single Stage

This heat pump configuration has two degrees of freedom, namely, the minimum pressure (P_{low}) and the temperature drop over the heat exchanger which represents the thermal sink of the heat pump (ΔT_{sink}). In an actual industrial application, this second parameter will depend on the requirements of the process stream to be heated. However, for current investigations, this parameter was varied to evaluate the minimum required temperature drop to get a $\mathrm{COP_h}$ comparable to that of reverse Rankine cycle based heat pumps.

Figure 5.57 shows the $\mathrm{COP_h}$ variation of this heat pump configuration as a function of P_{low}, for different T_{sink} values, using $\mathrm{CO_2}$ as working fluid. The values of $\mathrm{COP_h}$ obtained for this case are higher than those obtained in the previous section for the constant temperature thermal sink, because the maximum temperature of the cycle is lower and thus, the required pressure ratio and the work input are lower. Compared to baseline case, the maximum $\mathrm{COP_h}$ has been increased (relative) by around 71 % for the same T_{sink} of 200°C and P_{low} of 60 bar.

At higher T_{sink} values, a lower $\mathrm{COP_h}$ value is observed, as for the reverse Rankine cycle based heat pumps. With an increase in P_{low}, $\mathrm{COP_h}$ is found to increase for all the T_{sink} values. However, this increase occurs only up to a certain value of P_{low}, after which $\mathrm{COP_h}$ starts to decrease. Therefore, there is an optimal P_{low} value for every T_{sink} value. At the same time, this optimal P_{low} value falls always in a relatively high pressure range (>100 bar) for all the T_{sink} values. This high P_{low} value can lead to excessively high maximum cycle pressures. An upper limit of 250 bar was then set for this quantity, in analogy to what done earlier in Section 5.2. Figure 5.58 shows the variation of the required β_{total} to achieve the prescribed temperature in the thermal sink as a function P_{low} and for different T_{sink} values, using $\mathrm{CO_2}$ as working fluid. In this figure, the maximum allowed β_{total} is also represented with a black dashed curve. Except for T_{sink} of 150°C, the optimal P_{low} value leads to a β_{total} and, then, maximum operating pressure in excess of 250 bar. Therefore, for this heat pump configuration, the maximum achievable $\mathrm{COP_h}$ is limited by the maximum feasible β_{total}.

Another important parameter influenced by P_{low}, which affects the feasibility of the heat pump, is the minimum temperature (T_{min}) achieved by the working fluid at the inlet of the heat exchanger. To have a feasible heat pump design, this minimum temperature needs to be higher than the saturation temperature of the working fluid. This condition is necessary to ensure that the working fluid always remains in the vapor phase. Figure 5.59 shows the variation of T_{min} with P_{low}, for different T_{sink} values, using $\mathrm{CO_2}$ as working fluid. This figure reports the minimum allowed temperature as a black dashed line. This limiting line reaches a constant value as P_{low} becomes higher than the critical pressure value (73.77 bar). T_{min} becomes, indeed, equal to the critical temperature (30.98°C). A combination of low P_{low} and T_{sink} values can indeed result in a two-phase state (blue curve in Figure 5.59). However, for high values of such variables, this condition is not reached. Therefore, in terms of maximum achievable $\mathrm{COP_h}$, the limit on T_{min} is not critical for this heat pump configuration.

The effect of P_{low} on the heat pump thermodynamic cycle characteristics is highlighted in Figure 5.60, which shows in a Ts diagram how the thermodynamic cycle changes by varying P_{low} when T_{sink} is 200°C and ΔT_{sink} is equal to 100 K. As the P_{low} value increases, the cycle diagram moves closer to the critical region. Due to the characteristics of the isobars in the critical region, an increased thermal energy exchange at the sink side is achieved a significant increase in the compression work. However, as P_{low} is increased further, the associated isobars move far away from the critical region. As a result, the $\mathrm{COP_h}$ value diminishes. It follows that for every T_{sink} value an optimal P_{low} value exists. But, as

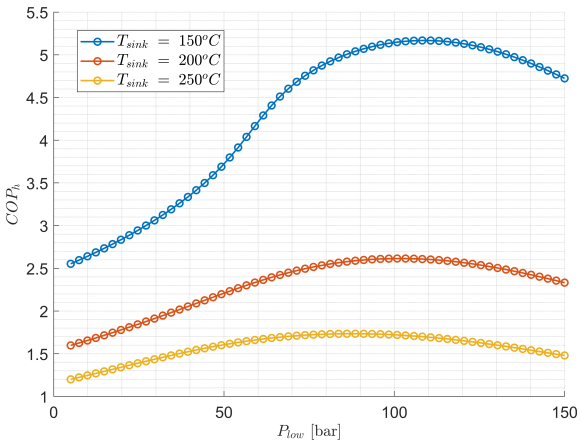

Figure 5.57: Variation of $\mathrm{COP_h}$ as a function of P_{low} and T_{sink} (ΔT_{sink} = 100 °C) for the single-stage heat pump configuration, using $\mathrm{CO_2}$ as working fluid.

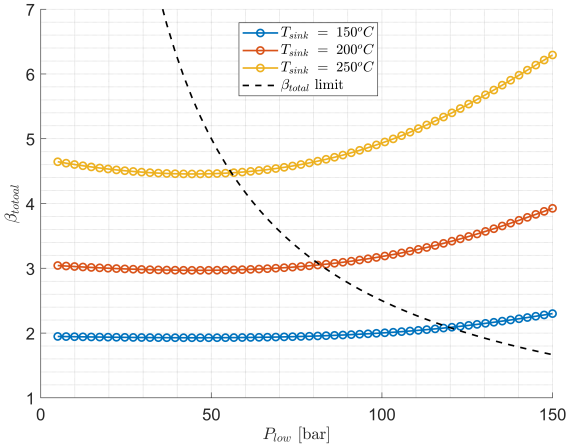

Figure 5.58: Variation of β_{total} as a function of P_{low} and T_{sink} (ΔT_{sink} = 100 °C) for the single-stage heat pump configuration, using $\mathrm{CO_2}$ as working fluid.

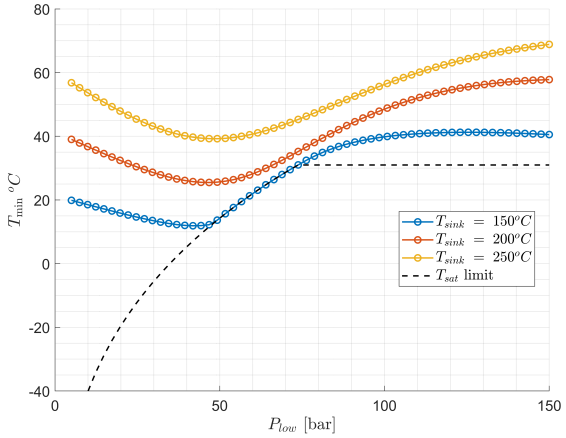

Figure 5.59: Variation of T_{min} as a function of P_{low} and T_{sink} (ΔT_{sink} = 100 °C) for the single-stage heat pump configuration, using $\mathrm{CO_2}$ as working fluid.

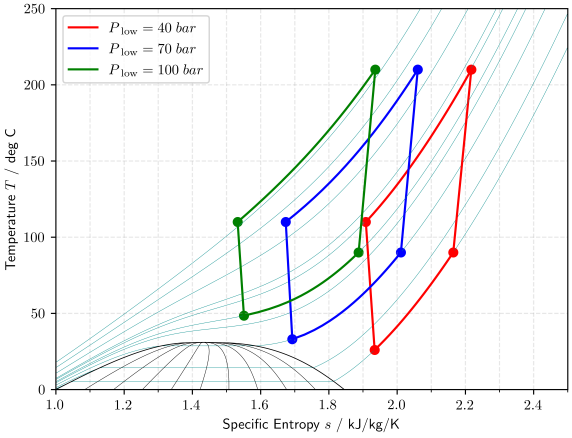

Figure 5.60: Ts diagram showing the effect of P_{low} (T_{sink} = 200 °C and ΔT_{sink} = 100 °C) on the single-stage heat pump configuration, using $\mathrm{CO_2}$ as working fluid.

found previously, for T_{sink} greater than 150°C, the value of P_{low} must be limited to prevent a excessively high maximum pressure of the thermodynamic cycle.

Figure 5.61 shows the variation of $\mathrm{COP_h}$ with ΔT_{sink}, for different T_{sink} values and $\mathrm{CO_2}$ as working fluid. For this analysis, the P_{low} is kept constant at a value of 100 bar. With an increase in ΔT_{sink}, the $\mathrm{COP_h}$ value is found to increase approximately in a linear trend, independently from the value of T_{sink}. However, with an increase in T_{sink} value, the slope of the curve decreases, implying a smaller increase in $\mathrm{COP_h}$. At high P_{low} values, an increase in ΔT_{sink} results in better utilization of the characteristics of isobars in the critical region, which leads to an increased $\mathrm{COP_h}$ value. Figure 5.62 highlights this effect, where the thermodynamic cycle corresponding to this heat pump configuration is plotted in the Ts diagram for different ΔT_{sink} values and P_{low} equal to 100 bar and T_{sink} equal to 200°C.

The required pressure ratio is independent from the ΔT_{sink} value for this particular heat pump configuration. However, the T_{min} value is influenced by ΔT_{sink}. Figure 5.63 shows the variation of T_{min} with ΔT_{sink} values, for different T_{sink} values and a constant P_{low} of 100 bar. The black dashed line in this figure again highlights the critical temperature limit. As the ΔT_{sink} value increase, T_{min} value is found to decrease. This is because with an increase in ΔT_{sink}, the turbine inlet temperature decreases, resulting in a decreased exit temperature for a similar expansion ratio. This is also shown in Figure 5.62, when

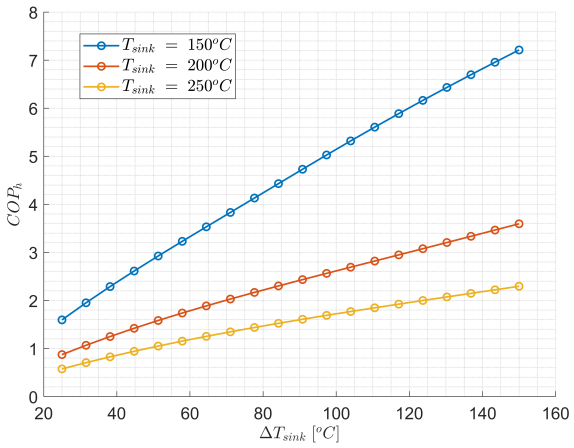

Figure 5.61: Variation of $\mathrm{COP_h}$ as a function of ΔT_{sink} and T_{sink} (P_{low} = 100 bar) for the single-stage heat pump configuration, using $\mathrm{CO_2}$ as working fluid.

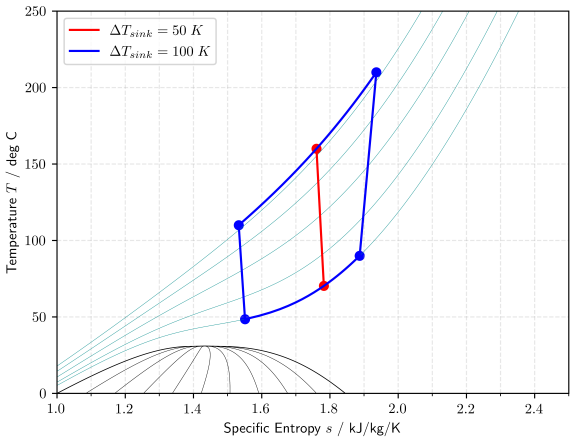

Figure 5.62: Ts diagram showing the effect of ΔT_{sink} (T_{sink} = 200 °C and P_{low} = 100 bar) on the single-stage heat pump configuration, using $\mathrm{CO_2}$ as working fluid.

T_{sink} is equal to 150°C and ΔT_{sink} is higher than 115°C, the turbine outlet state is in the two phase region.

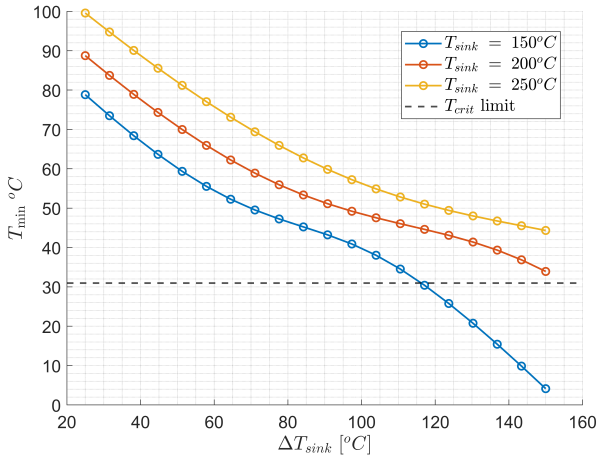

Figure 5.63: Variation of T_{min} as function of ΔT_{sink} and T_{sink} (P_{low} = 100 bar) for the single-stage heat pump configuration, using $\mathrm{CO_2}$ as working fluid.

Figure 5.64 shows the trend of $\mathrm{COP_h}$ with P_{low} when air is the working fluid, assuming ΔT_{sink} 50 K and T_{sink} 200°C. For a given T_{sink} value, the variation in $\mathrm{COP_h}$ with P_{low} value is smaller than the one observed for $\mathrm{CO_2}$, as observed before for the case of a constant temperature thermal sink. Figure 5.65 shows the variation of $\mathrm{COP_h}$ with P_{low} when the value of the former is normalized with respect to the maximum $\mathrm{COP_h}$ achievable by this heat pump configuration. The maximum deviation in $\mathrm{COP_h}$ due to P_{low} varies from about 6 % to 2.5 % as the value of T_{sink} values increase from 150 to 250°C. Similar to the case of $\mathrm{CO_2}$, there is an optimal P_{low} value. However, in this case, the relative deviation is small, arguably of the same order of magnitude of the model uncertainty. The choice of high P_{low} then is not justified. Anyway, the optimal P_{low} value decreases as the value of T_{sink} increases. Figure 5.66 shows the effect of P_{low} on the heat pump's thermodynamic cycle with fixed values of T_{sink} and ΔT_{sink} (200°C and 100°C, respectively). As the isobars are almost parallel, the cycle characteristics remain almost identical with an increase in P_{low}.

For the case of air, the T_{min} value is not critical. This is not the case for the required β_{total}. In this regard, Figure 5.67 shows the effect of P_{low} on β_{total}. For simplicity, a maximum pressure limit similar to the one used for $\mathrm{CO_2}$ was assumed as highlighted in this figure (250 bar). Similarly to what observed for the variation of $\mathrm{COP_h}$, the deviation in β_{total} with P_{low} is small (relative deviation < 5 %). Nevertheless,

at high T_{sink} values, higher β_{total} values are required, implying that a lower value of maximum P_{low} can be used, before the maximum pressure limit is reached.

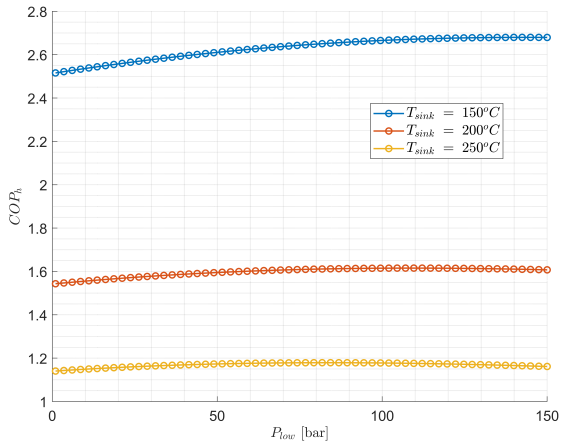

Figure 5.64: Variation of $\mathrm{COP_h}$ as a function of P_{low} and T_{sink} (ΔT_{sink} = 100 °C) for the single-stage heat pump configuration, using Air as working fluid.

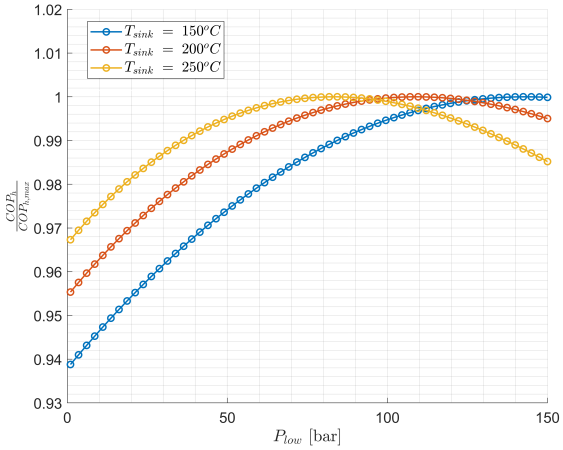

Figure 5.65: Variation of normalized $\mathrm{COP_h}$ as a function of P_{low} and T_{sink} (ΔT_{sink} = 100 °C) for the single-stage heat pump configuration, using Air as working fluid.

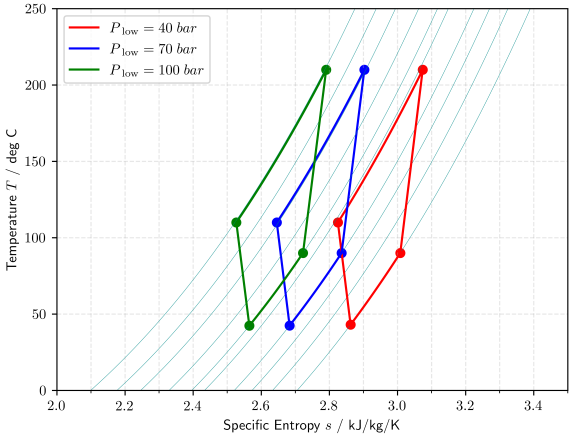

Figure 5.66: Ts diagram showing the effect of P_{low} (T_{sink} = 200 °C and ΔT_{sink} = 100 °C) on the single-stage heat pump configuration, using Air as working fluid.

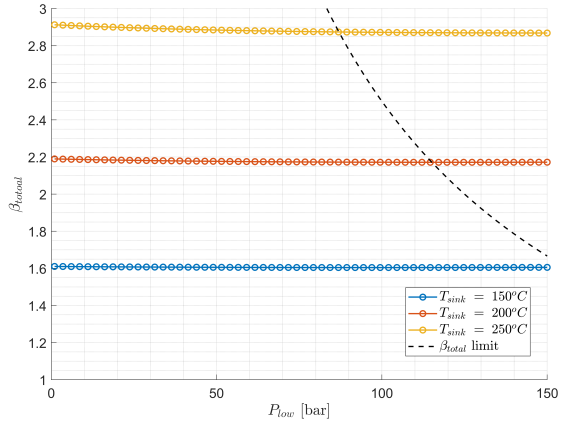

Figure 5.67: Variation of β_{total} as a function of P_{low} and T_{sink} (ΔT_{sink} = 100 °C) for the single-stage heat pump configuration, using Air as working fluid.

Figure 5.68 shows the change in $\mathrm{COP_h}$ due to a variation in ΔT_{sink}, for fixed values of T_{sink} and P_{low} (200°C and 80 bar respectively). By augmenting ΔT_{sink}, an increase in $\mathrm{COP_h}$ is obtained. The found relation is similar to the one observed earlier for $\mathrm{CO_2}$. The value of T_{sink} influences the increase of $\mathrm{COP_h}$ as a function of ΔT_{sink}. Notably, with increased T_{sink} values, this change in $\mathrm{COP_h}$ per degree of ΔT_{sink} increase is found to decrease. The variation of the thermodynamic cycle of the heat pump occurring by changing ΔT_{sink} is shown in Figure 5.69, for constant P_{low} and T_{sink} values. As the value of ΔT_{sink} increases, both the required work input and the sink capacity increase. However, the increase in sink capacity is higher, leading to an increase in $\mathrm{COP_h}$. The obtained $\mathrm{COP_h}$ values are lower than the ones obtained for $\mathrm{CO_2}$ but are higher than those obtained for the case of a constant temperature thermal sink.

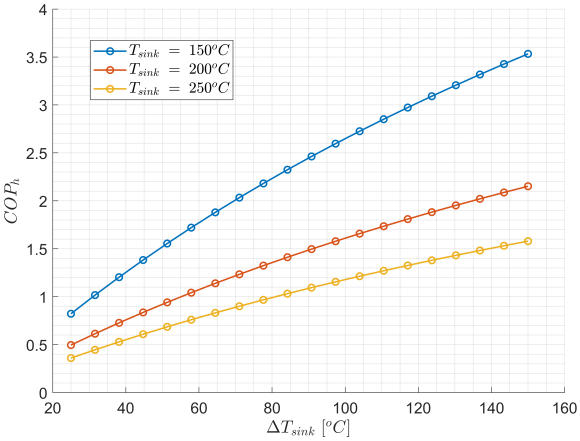

Figure 5.68: Variation of $\mathrm{COP_h}$ as a function of ΔT_{sink} and T_{sink} (P_{low} = 80 bar) for the single-stage heat pump configuration, using Air as working fluid.

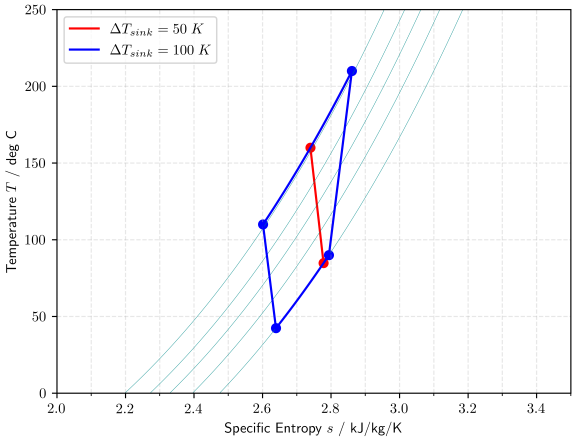

Figure 5.69: Ts diagram showing the effect of ΔT_{sink} (T_{sink} = 200 °C and P_{low} = 80 bar) on the single-stage heat pump configuration, using Air as working fluid.

5.3.2. Single Stage with Internal Recuperation

This heat pump configuration has two degrees of freedom, namely, P_{low} and ΔT_{sink}. Figure 5.70, Figure 5.71 and Figure 5.72 shows the effect of P_{low} on $\mathrm{COP_h}$, β_{total} and T_{min} respectively for a fixed ΔT_{sink} of 50 K, a T_{sink} of 200°C, and $\mathrm{CO_2}$ as working fluid. In this case, the value of ΔT_{sink} cannot be chosen independently. To prevent that temperature profiles of the two streams of the recuperator intersect each other, the sink outlet temperature must be at least 110°C to allow for a feasible temperature difference in this heat exchanger. Similarly, the maximum allowed ΔT_{sink} for other T_{sink} was also selected.

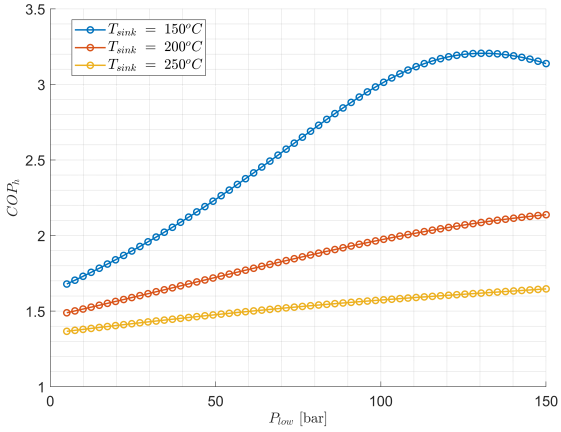

Figure 5.70: Variation of $\mathrm{COP_h}$ as a function P_{low} and T_{sink} (ΔT_{sink} = 50 °C) for the single-stage heat pump configuration with internal recuperation, using $\mathrm{CO_2}$ as working fluid, for the case of sensible heat sink.

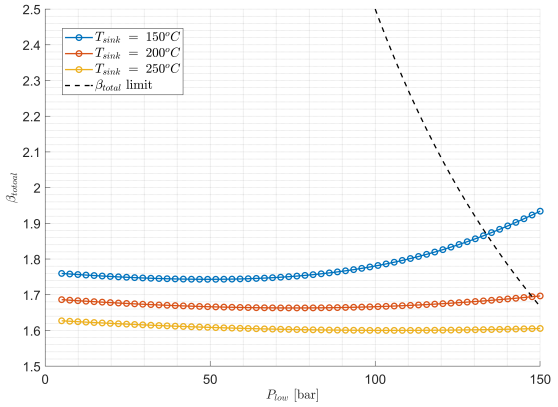

Figure 5.71: Variation of β_{total} as a function of P_{low} and T_{sink} (with ΔT_{sink} = 50 °C) for the single-stage heat pump configuration with internal recuperation, using $\mathrm{CO_2}$ as working fluid, for the case of sensible heat sink.

Contrary to the previous configuration, an optimal P_{low} value is found only for a T_{sink} of 150°C. For the other T_{sink} values, $\mathrm{COP_h}$ is found to increase monotonically with P_{low}, for the considered range of this parameter. Figure 5.71 explains the reason of such a trend. For this configuration, the required β_{total} is lower than in the single-stage configuration. Moreover, in this case, as T_{sink} increases, the required β_{total} decreases. Since, for a fixed ΔT_{sink}, the compressor inlet temperature also increases with T_{sink}, due to the internal recuperator. As a result, the required pressure ratio decreases since the compressor outlet temperature is fixed. The lower β_{total} value imply that higher P_{low} values are feasible, resulting in higher $\mathrm{COP_h}$. Figure 5.73 confirms this analysis, the heat pump thermodynamic cycle is plotted in the

Ts diagram for different P_{low} values.

Regarding T_{min}, Figure 5.72 shows the variation of this quantity with P_{low} for a ΔT_{sink} of 50 K. Note that the values of T_{min} are higher than those reported in the previous section for the non-recuperated configuration, as the ΔT_{sink} was taken equal to100 K. Nevertheless, in this case, because the turbine inlet temperature will be reduced further due to internal recuperation, it can be expected that the source inlet temperature will also be lower. At the same time, in this case, the required expansion ratio is also considerably lower, which helps maintain a high enough temperature at the source inlet, as also apparent from Figure 5.73. However, a combination of high ΔT_{sink} and low P_{low} can still lead to a T_{min} value lower than the saturation/critical temperature, though this does not occur for the thermodynamic cycle exhibiting the maximum COP_h. The maximum allowed ΔT_{sink} and β_{total} are the actual limiting conditions determining the maximum COP_h of the system.

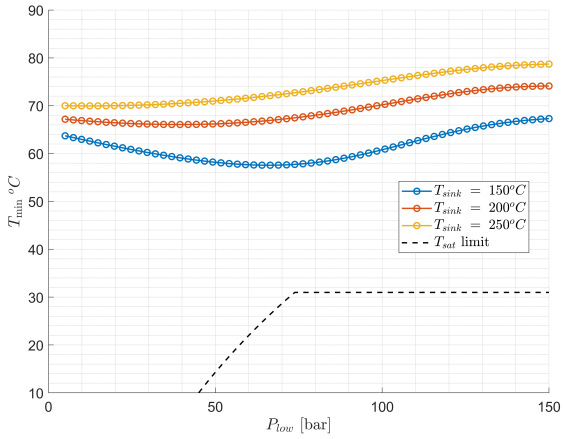

Figure 5.72: Variation of T_{min} as a function of P_{low} and T_{sink} (with ΔT_{sink} = 50 °C) for the single-stage heat pump configuration with internal recuperation, using CO_2 as working fluid.

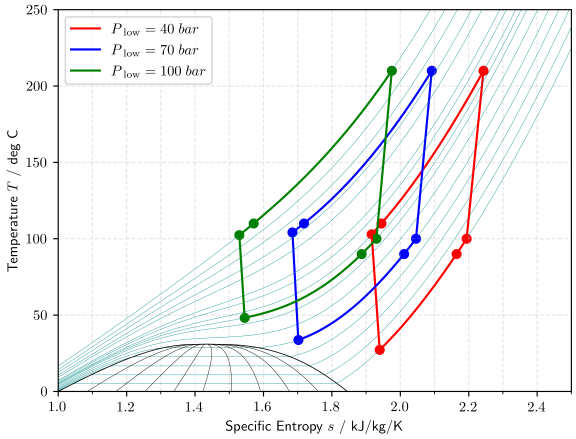

Figure 5.73: Ts diagram showing the effect of P_{low} (with T_{sink} = 200 °C and ΔT_{sink} = 100 °C) on the single-stage heat pump configuration with internal recuperation, using CO_2 as working fluid.

Figure 5.74 shows the variation of COP_h with ΔT_{sink} for CO_2 when T_{sink} and P_{low} are taken equal to 200°C and 100 bar, respectively. For this heat pump configuration, ΔT_{sink} also affects the required β_{total} since the compressor inlet temperature is directly influenced by the value of ΔT_{sink}. The effect of ΔT_{sink} on β_{total} and T_{min} is shown in Figure 5.75 and Figure 5.76 respectively, using the T_{sink} and P_{low} equal to 200°C and 100 bar, respectively. The different limits of ΔT_{sink} for each T_{sink} are visible in all the figures. As observed for the other configurations, a higher value of ΔT_{sink} leads to a higher COP_h value, but the relative increase of this parameter depends ont the value of T_{sink}. In this case, the limit on the maximum operating pressure has a direct impact on the maximum feasible ΔT_{sink}, limiting the maximum COP_h of the system.

At high values of ΔT_{sink}, the T_{min} value also reduces. However, at high P_{low}, this is not a limiting factor, as explained earlier. Actually, the limit on the maximum operating pressure is more stringent for this configuration than that concerning T_{min}. Figure 5.77 illustrates how the thermodynamic cycle varies with ΔT_{sink} given P_{low} equal to 100 bar and T_{sink} 200°C. With an increase in ΔT_{sink}, the cycle area increases. Due to the lower temperature of the working fluid at the thermal sink outlet, the compressor inlet temperature decreases, leading to lower internal recuperation. As a result, the required compression work increases. Nevertheless, since the amount of thermal energy transferred to the thermal sink is also increased, the net effect is positive for the COP_h. This effect is even more prominent for high P_{low} values due to the slope of CO_2 isobars near the critical region, as also shown by Figure 5.73.

Figure 5.78 shows the trend of COP_h variation with P_{low} for the case of air as working fluid, assuming ΔT_{sink} 50 K and T_{sink} 200°C. Similarly to the previous single-stage heat pump configuration, the variation of COP_h with P_{low} is smaller than the one observed for CO_2 for all T_{sink} values. Figure 5.79 shows the variation with P_{low} of COP_h when normalized with the respect to its maximum value. The maximum

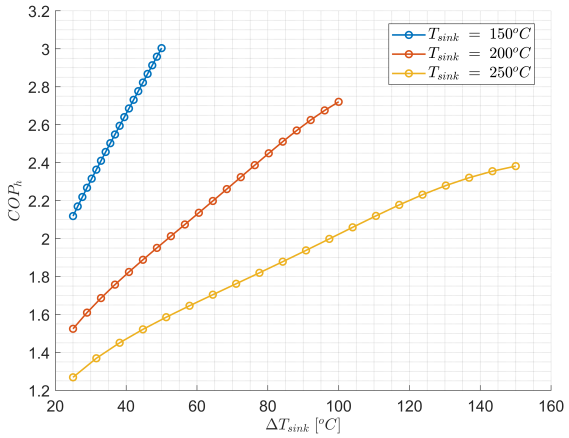

Figure 5.74: Variation of $\mathrm{COP_h}$ with ΔT_{sink} at different values of T_{sink} (with P_{low} = 100 bar) for single-stage heat pump configuration with internal recuperation, using $\mathrm{CO_2}$ as working fluid.

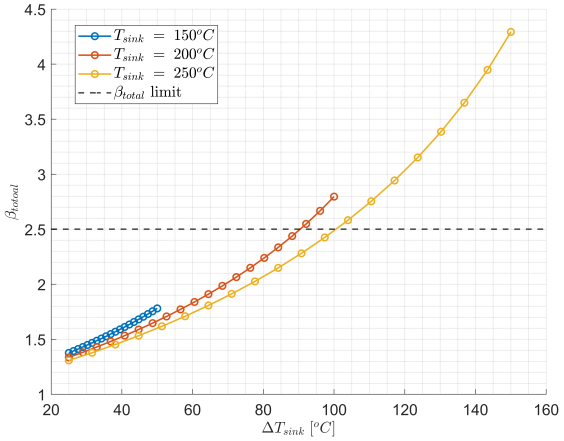

Figure 5.75: Variation of β_{total} with ΔT_{sink} at different values of T_{sink} (with P_{low} = 100 bar) for single-stage heat pump configuration with internal recuperation, using $\mathrm{CO_2}$ as working fluid.

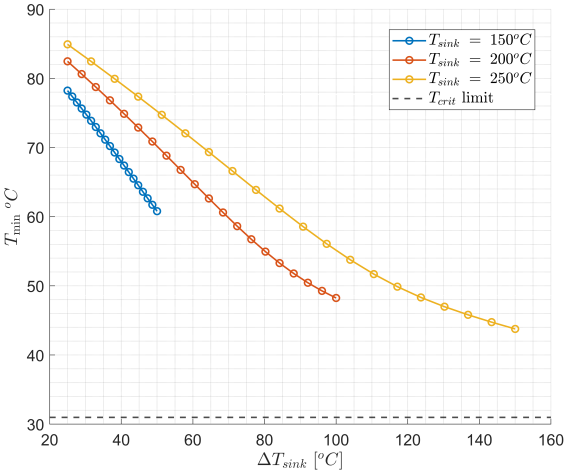

Figure 5.76: Variation of T_{min} as a function of ΔT_{sink} and T_{sink} (with P_{low} = 100 bar) for the single-stage heat pump configuration with internal recuperation, using $\mathrm{CO_2}$ as working fluid.

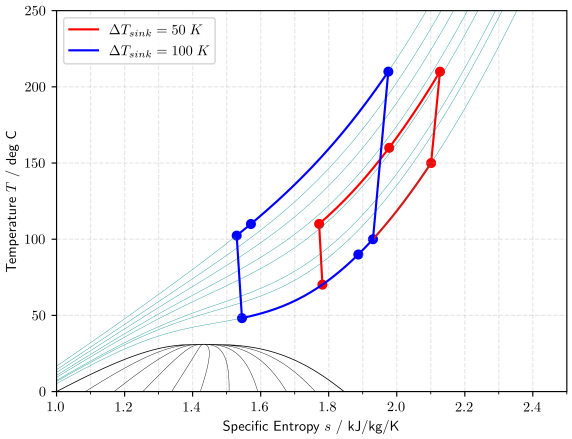

Figure 5.77: Ts diagram showing the effect of ΔT_{sink} (with T_{sink} = 200 °C and P_{low} = 100 bar) on the single-stage heat pump configuration with internal recuperation, using $\mathrm{CO_2}$ as working fluid.

deviation of $\mathrm{COP_h}$ due to P_{low} varies from about 5.2 % to 0.8 % as the value of T_{sink} values increases from 150 to 250°C. The optimal P_{low} maximizing the $\mathrm{COP_h}$ is found to be towards the upper end of the range shown. Figure 5.80 shows the shape of thermodynamic cycle on a Ts diagram, for different P_{low} values and T_{sink} and ΔT_{sink} assumed equal to 200°C and 100°C, respectively. As for the other single-stage heat pump configuration, no change in cycle characteristic is observed with a change in P_{low} value, as the associated isobars' characteristics do not change with the operating pressure level.

Figure 5.81 shows the variation of β_{total} with P_{low} for the case of air. As for $\mathrm{COP_h}$, the deviation of β_{total} with P_{low} is small (relative deviation < 0.4 %). Thus, the P_{low} value does not affect the β_{total} of the system, as also apparent from Figure 5.80. With an increase in P_{low}, the cycle just shifts to the left in the Ts diagram. Since the slope of isobar curves remains essentially constant, β_{total} changes marginally.

The change in $\mathrm{COP_h}$ due to change in ΔT_{sink} is shown in Figure 5.82, where T_{sink} and P_{low} are fixed (200°C and 80 bar respectively). An increase in $\mathrm{COP_h}$ is obtained with an increase in ΔT_{sink}, as ob-

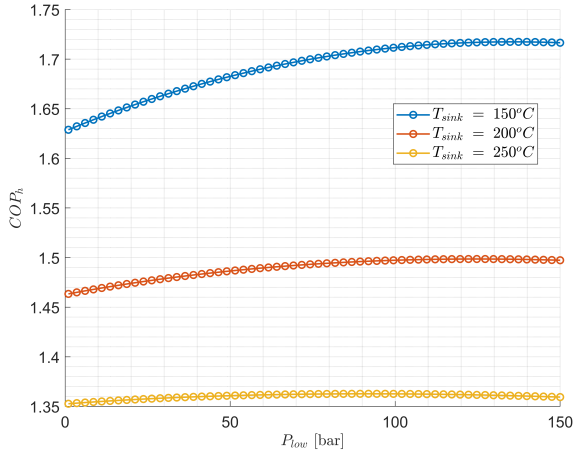

Figure 5.78: Variation of $\mathrm{COP_h}$ as a function of P_{low} and T_{sink} (with ΔT_{sink} = 50 °C) for the single-stage heat pump configuration with internal recuperation, using Air as working fluid, for the case of sensible heat sink.

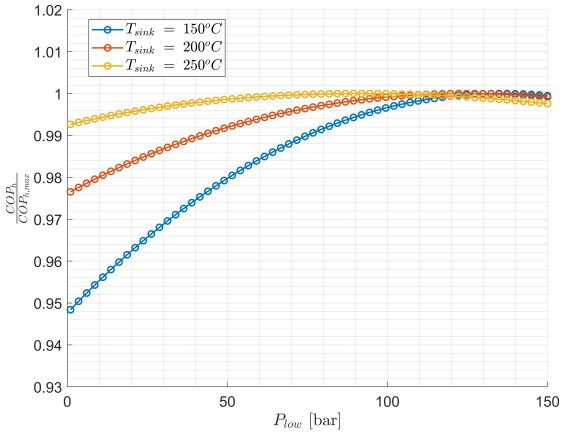

Figure 5.79: Variation of normalized $\mathrm{COP_h}$ as a function of P_{low} and T_{sink} (with ΔT_{sink} = 50 °C) for the single-stage heat pump configuration with internal recuperation, using Air as working fluid, for the case of sensible heat sink.

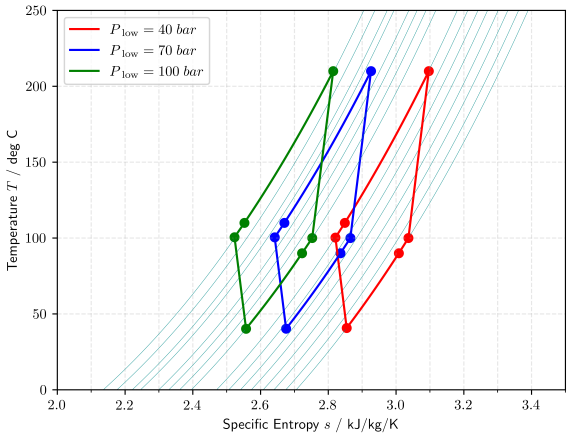

Figure 5.80: Ts diagram showing the effect of P_{low} (with T_{sink} = 200 °C and ΔT_{sink} = 100 °C) on the single-stage heat pump configuration with internal recuperation, using Air as working fluid.

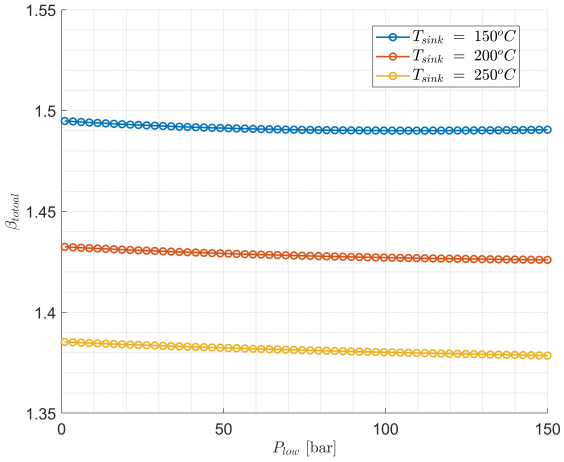

Figure 5.81: Variation of β_{total} as a function of P_{low} and T_{sink} (with ΔT_{sink} = 50 °C) for the single-stage heat pump configuration with internal recuperation, using Air as working fluid.

served earlier for $\mathrm{CO_2}$. For the case of air as well, the required β_{total} is found to increase with ΔT_{sink} (Figure 5.83). However, since the values of β_{total} are lower than in the case of $\mathrm{CO_2}$, the maximum pressure of the cycle does not reach the imposed limit, regardless of the value of ΔT_{sink}, if P_{low} is equal to 80 bar. Since the variation of β_{total} with P_{low} is found to be small, it can be concluded that for the case of air, the maximum ΔT_{sink} is not limited by the maximum pressure constraint. The effect of ΔT_{sink} on the heat pump thermodynamic cycle is shown in Figure 5.84, via the means of the Ts diagram. The increase in the sink capacity is higher than the required work input, independently of P_{low}, which leads to an increased $\mathrm{COP_h}$ as the value of ΔT_{sink} increases.

5.3.3. Two Stage with Intercooling

Alike the previously discussed configurations, for the sensible sink scenario, two degrees of freedom were obtained for the two-stage configuration with intercooling. For this case also, the minimum outlet temperature of the sink needs to be at least 110°C to allow for internal recuperation since the selected

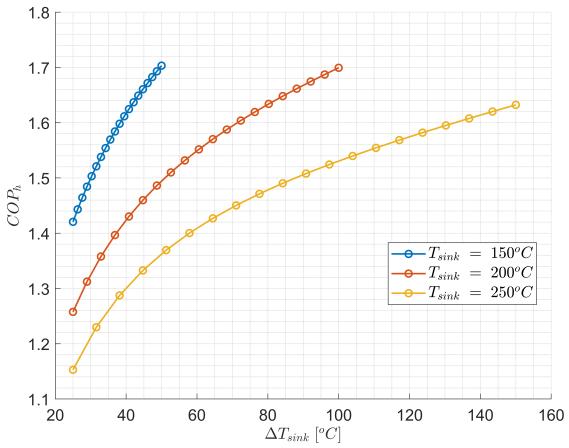

Figure 5.82: Variation of $\mathrm{COP_h}$ as a function of ΔT_{sink} and T_{sink} (with P_{low} = 80 bar) for the single-stage heat pump configuration with internal recuperation, using Air as working fluid.

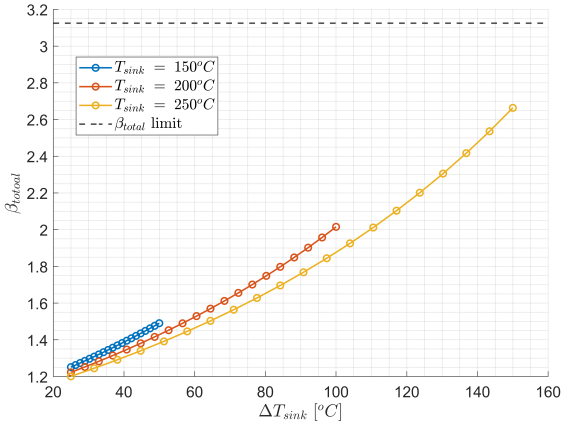

Figure 5.83: Variation of β_{total} as a function of ΔT_{sink} and T_{sink} (with P_{low} = 80 bar) for the single-stage heat pump configuration with internal recuperation, using Air as working fluid.

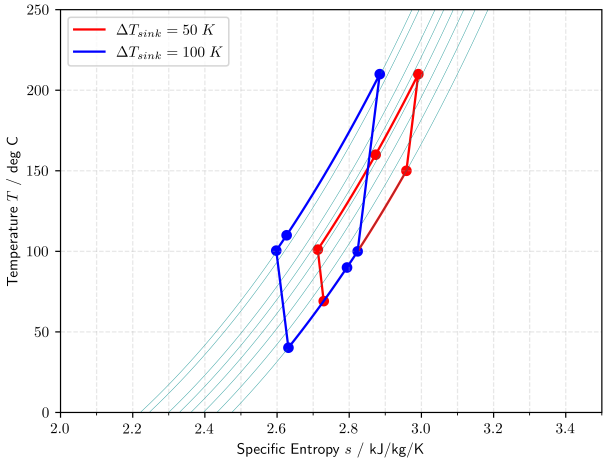

Figure 5.84: Ts diagram showing the effect of ΔT_{sink} (with T_{sink} = 200 °C and P_{low} = 80 bar) on the single-stage heat pump configuration with internal recuperation, using Air as working fluid.

source temperature is 100°C.

With an increase in P_{low}, from 5 to 150 bar, the $\mathrm{COP_h}$ keeps increasing for the T_{sink} values of 200 and 250°C. For the case of T_{sink} 150°C, the $\mathrm{COP_h}$ is maximized when P_{low} is equal to 110 bar, as shown in Figure 5.85 for a fixed ΔT_{sink} of 50°C. Figure 5.86 shows the variation of β_{total} with P_{low}, for the same value of ΔT_{sink}. The required β_{total} also increases with an increase in P_{low} value, leading to maximum cycle pressure in the excess of 250 bar, the limit considered in this work. It follows that the maximum $\mathrm{COP_h}$ of this heat pump configuration is limited by the constraint on the maximum cycle pressure. The value of β_{total} depends also on T_{sink} value. At higher T_{sink} values, the increases in β_{total} with P_{low} becomes lower. The effect of P_{low} on the thermodynamic cycle of this heat pump configuration is shown in Figure 5.87, which illustrates the thermodynamic process in the Ts diagram for different P_{low} values, and a fixed T_{sink} and ΔT_{sink} value of 200°C and 100°C respectively. Higher pressure values are required at the second heat exchanger that works as thermal sink of the system, as the working fluid is cooled before entering the second compressor.

Figure 5.88 shows the variation of T_{min} with P_{low}, for different T_{sink} values while ΔT_{sink} is taken equal to 50°C and T_{sink} 200°C. In Figure 5.88, all T_{min} value remains above the saturation/critical limit, as relative low value of ΔT_{sink} (=50°C) is used. However, for low P_{low} and high ΔT_{sink} values, the minimum

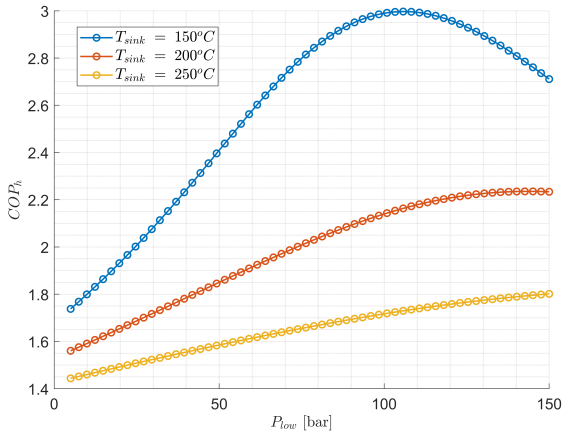

Figure 5.85: Variation of $\mathrm{COP_h}$ as a function of P_{low} and T_{sink}(with ΔT_{sink} = 50 °C) for the two-stage heat pump configuration with intercooling, using $\mathrm{CO_2}$ as working fluid, for the case of sensible heat sink.

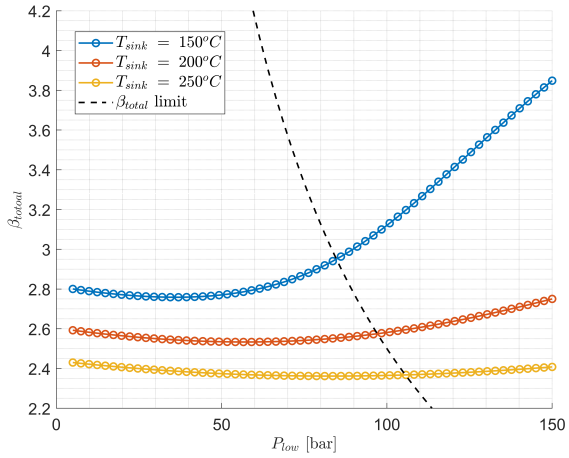

Figure 5.86: Variation of β_{total} as a function of P_{low} and T_{sink}(with ΔT_{sink} = 50 °C) for the two-stage heat pump configuration with intercooling, using $\mathrm{CO_2}$ as working fluid, for the case of sensible heat sink.

temperature level does fall below the saturation curve, as shown by Figure 5.87. Thus, the value of P_{low} becomes more critical for the combination of low T_{sink} and high ΔT_{sink} values. Since this choice of parameters does not lead to high $\mathrm{COP_h}$ values, the improvement of the heat pump performance does not pass through the development of a two-phase expander.

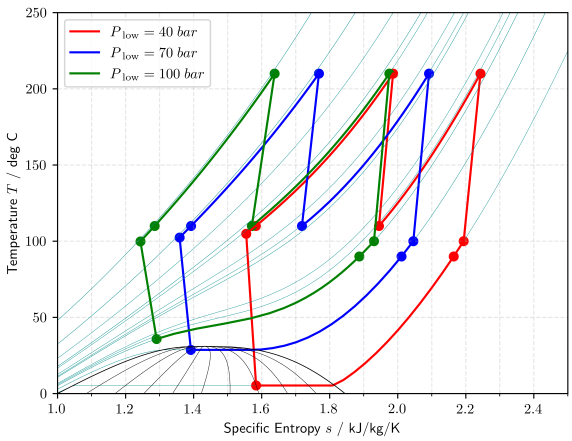

Figure 5.87: Ts diagram showing the effect of P_{low} (with T_{sink} = 200 °C and ΔT_{sink} = 100 °C) on the two-stage heat pump configuration with intercooling, using $\mathrm{CO_2}$ as working fluid.

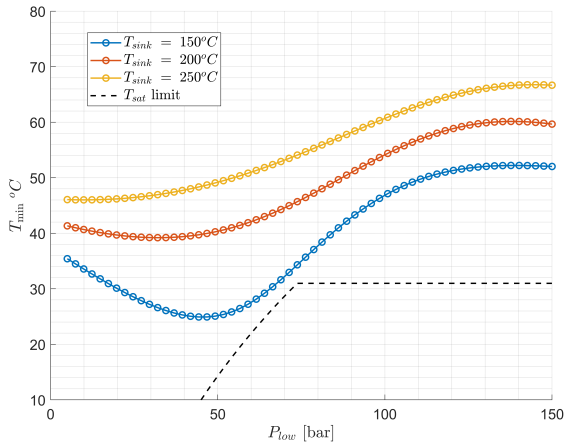

Figure 5.88: Variation of T_{min} as a function of P_{low} and T_{sink}(with ΔT_{sink} = 50 °C) for the two-stage heat pump configuration with intercooling, using $\mathrm{CO_2}$ as working fluid.

Figure 5.89 shows the variation of $\mathrm{COP_h}$ with ΔT_{sink} for a fixed P_{low} of 100 bar. The effect of ΔT_{sink} on the $\mathrm{COP_h}$ is similar to the one obtained for the single-stage heat pump with internal recuperation. However, for this configuration, an optimal ΔT_{sink} value is found for T_{sink} of 200 and 250°C. Nevertheless, the maximum feasible $\mathrm{COP_h}$, for all the T_{sink} values, is lower than the one obtained for a single stage heat pump with internal recuperation. Figure 5.90 shows the reason thereof by showing the variation of the β_{total} with ΔT_{sink} (with fixed P_{low} of 100 bar). Similarly to the case of a single stage with recuperation, the value of ΔT_{sink} also affects the required β_{total} for this heat pump configuration. Additionally, in this case, due to the cooling of the working fluid before the second compressor, the compressor inlet temperature is reduced further with an increase in ΔT_{sink}. As a result, the required β_{total} is higher for this configuration and the resulting maximum $\mathrm{COP_h}$ is lower.

Figure 5.91 shows the effect of ΔT_{sink} on the thermodynamic cycle characteristics by the means of a Ts

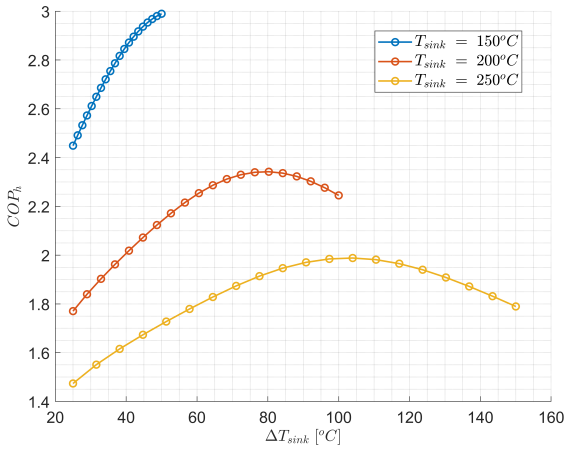

Figure 5.89: Variation of $\mathrm{COP_h}$ as a function of ΔT_{sink} and T_{sink}(with P_{low} = 100 bar) for the two-stage heat pump configuration with intercooling, using $\mathrm{CO_2}$ as working fluid.

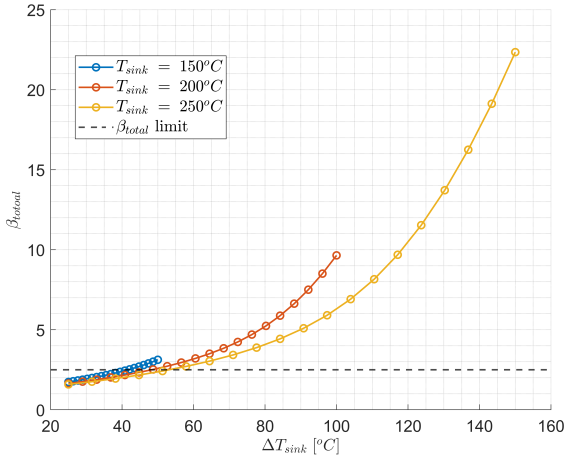

Figure 5.90: Variation of β_{total} as a function of ΔT_{sink} and T_{sink}(with P_{low} = 100 bar) for the two-stage heat pump configuration with intercooling, using $\mathrm{CO_2}$ as working fluid.

diagram, where P_{low} and T_{sink} are taken equal to 100 bar and 200°C respectively. As the ΔT_{sink} value increases, the inlet temperature of the turbine is reduced. This effect combined with an increase in the expansion ratio (due to the larger β_{total}) leads to a lower T_{min} value for this heat pump configuration. The similar trend is also confirmed by Figure 5.92, where the variation of T_{min} with ΔT_{sink} is shown, assuming P_{low} value of 100 bar.

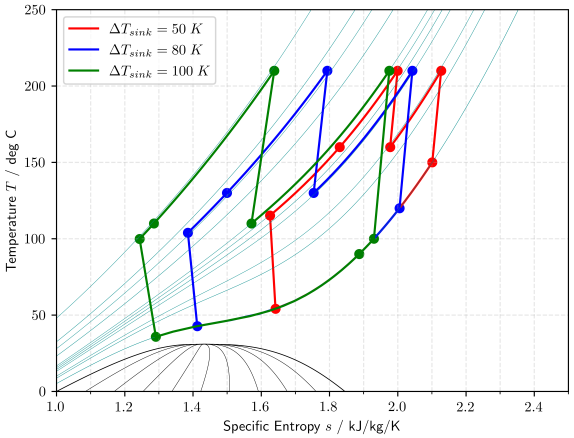

Figure 5.91: Ts diagram showing the effect of ΔT_{sink} (with T_{sink} = 200 °C and P_{low} = 100 bar) on the two-stage heat pump configuration with intercooling, using $\mathrm{CO_2}$ as working fluid.

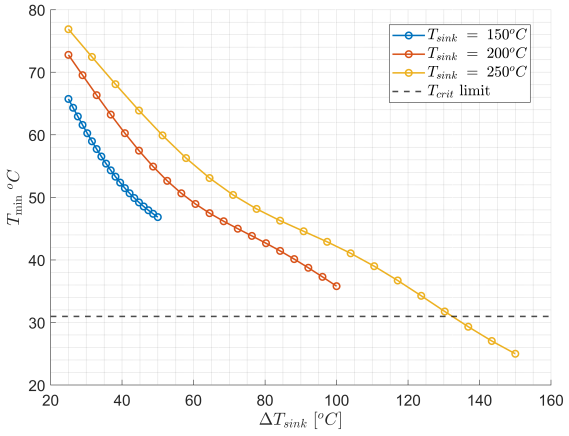

Figure 5.92: Variation of T_{min} as a function of ΔT_{sink} and T_{sink}(with P_{low} = 100 bar) for the two-stage heat pump configuration with intercooling, using $\mathrm{CO_2}$ as working fluid.

Figure 5.93 shows the trend of $\mathrm{COP_h}$ variation with P_{low} for the case of air, assuming a ΔT_{sink} of 50 K and T_{sink} of 200°C. The maximum deviation in $\mathrm{COP_h}$ with P_{low} ranges from about 4.5 % to less than 1 %, as the value of T_{sink} increase from 150 to 250 °C, see Figure 5.94, where the normalized $\mathrm{COP_h}$ values (with respect to the maximum $\mathrm{COP_h}$) are shown as a function of P_{low}. Differently from what observed before for $\mathrm{CO_2}$, The maximum feasible $\mathrm{COP_h}$ is higher for this configuration than the single-stage configuration with internal recuperation. However, the required β_{total} in this case is higher. Similarly to the case of $\mathrm{CO_2}$, due to the cooling of the working fluid between the two compressors, the required pressure ratio is increased as the compressor outlet temperature is fixed for both compressors. However, the increase in the thermal power transferred to the thermal sink dominates in this case, compared to the increase in the compression work, leading to a higher $\mathrm{COP_h}$ value. Concerning P_{low}, similarly to other configurations, no change in the cycle characteristic is observed with this parameter for air.

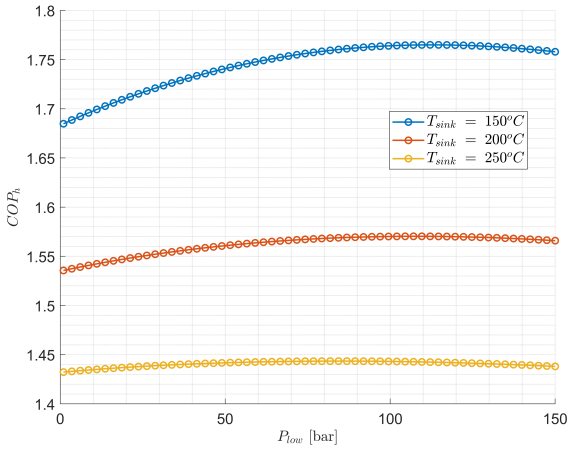

Figure 5.93: Variation of $\mathrm{COP_h}$ with P_{low} at different values of T_{sink}(with ΔT_{sink} = 50 °C) for two-stage heat pump configuration with intercooling, based on reverse Brayton cycle, using Air as working fluid, for the sensible heat sink case.

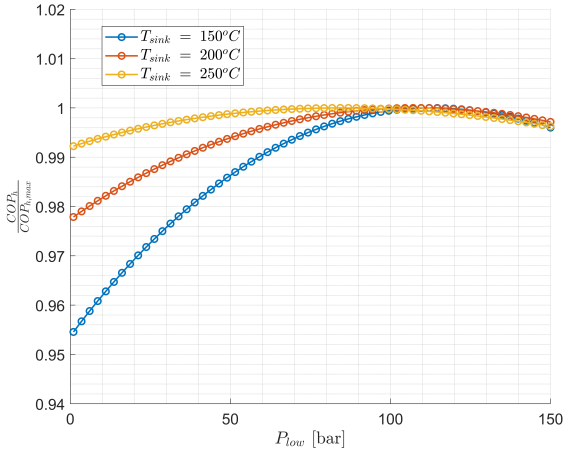

Figure 5.94: Variation of normalized $\mathrm{COP_h}$ with P_{low} at different values of T_{sink}(with ΔT_{sink} = 50 °C) for two-stage heat pump configuration with intercooling, based on reverse Brayton cycle, using Air as working fluid, for the sensible heat sink case.

Regarding the other key parameters of this heat pump configuration, namely β_{total} and ΔT_{sink}, the trend observed earlier for $\mathrm{CO_2}$ is also found for air. An increase in $\mathrm{COP_h}$ and β_{total} is obtained by augmenting ΔT_{sink}. At the same time, β_{total} is found to be the limiting factor for the maximum allowed ΔT_{sink} value and thus also the maximum $\mathrm{COP_h}$.

5.3.4. Two Stage with Internal Recuperation and Intercooling

The design of this two-stage heat pump configuration has two degrees of freedom as well i.e. P_{low} and ΔT_{sink}. Compared to previous concept, the minimum sink outlet temperature is higher, 130°C, to allow for internal recuperation. This higher temperature limit is due to an additional internal heat exchanger (Figure 5.49). Thus, for the case of T_{sink} 150°C, the maximum allowed ΔT_{sink} becomes 30°C, whereas for 200 and 250°C T_{sink}, the maximum limit is at 80 and 130°C respectively.

Figure 5.95 shows the effect of P_{low} on $\mathrm{COP_h}$, for different T_{sink} values. The value of ΔT_{sink} was fixed at 50°C, and due to this reason, the curve for T_{sink} 150°C value is not shown here. As for all the previous configurations, an increase in P_{low} has a positive impact on the $\mathrm{COP_h}$ value. For the case of T_{sink} of 200°C, an optimal P_{low} value of around 115 bar is found. However, for T_{sink} of 250°C, the $\mathrm{COP_h}$ value increases monotonically with P_{low}, for the given P_{low} range of 5-150 bar. The range of $\mathrm{COP_h}$ values obtained for this heat pump configuration is lower than the one obtained for the two-stage heat pump with intercooling. The reason thereof can be explained by Figure 5.96, where the variation of β_{total} with P_{low}, along with the maximum feasible β_{total} resulting from the limit on the maximum pressure, are shown. The required β_{total} for this configuration is the highest among all the considered configurations (for the sensible heat sink scenario) for a given T_{sink} and ΔT_{sink}. It follows that the maximum allowed P_{low} is lower, as the β_{total} limit is reached earlier. Consequently, the maximum feasible $\mathrm{COP_h}$ is limited to lower values.

The reason for such large required β_{total} is highlighted in Figure 5.97, where the thermodynamic cycle of this heat pump configuration is plotted in Ts diagram for different P_{low} values and fixed T_{sink} of 200°C and ΔT_{sink} of 50°C. With an increase in P_{low}, the cycle area increases, and the amount of of thermal power transferred to the sink also increases. Compared to the previously discussed configurations with internal recuperation, the temperature at the first compressor inlet is the lowest among the analyzed configurations, since there are two internal recuperators. It follows that the required pressure ratio increases. Additionally, the gain due to extra cooling before the second compressor does not compensate for the additional increase in the required pressure ratio in the first compressor stage. As

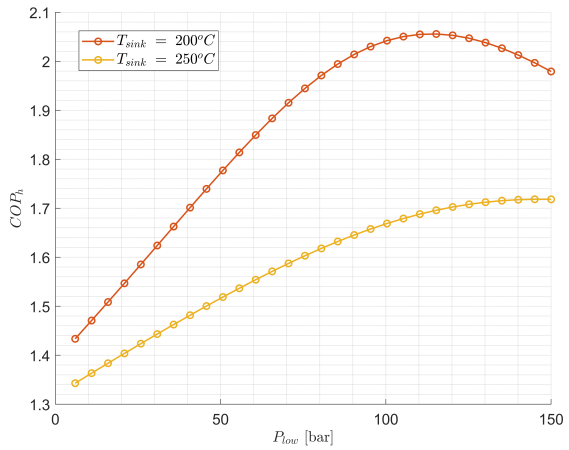

Figure 5.95: Variation of $\mathrm{COP_h}$ as a function of P_{low} and T_{sink}(with ΔT_{sink} = 50 °C) for the two-stage heat pump configuration with internal recuperation and intercooling, using $\mathrm{CO_2}$ as working fluid, for the case of sensible heat sink.

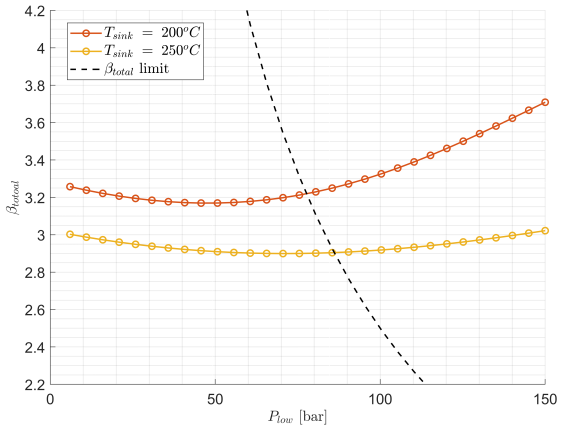

Figure 5.96: Variation of β_{total} as a function of P_{low} and T_{sink}(with ΔT_{sink} = 50 °C) for the two-stage heat pump configuration with internal recuperation and intercooling, using $\mathrm{CO_2}$ as working fluid, for the case of sensible heat sink.

a result, the required pressure ratio is higher for this case. At high values of P_{low}, this effect becomes even more important, as for a same temperature state, the value of specific enthalpy decreases with an increase in pressure, for $\mathrm{CO_2}$. The larger increase in compression work leads to lower $\mathrm{COP_h}$ gain compared to the two-stage configuration with intercooling.

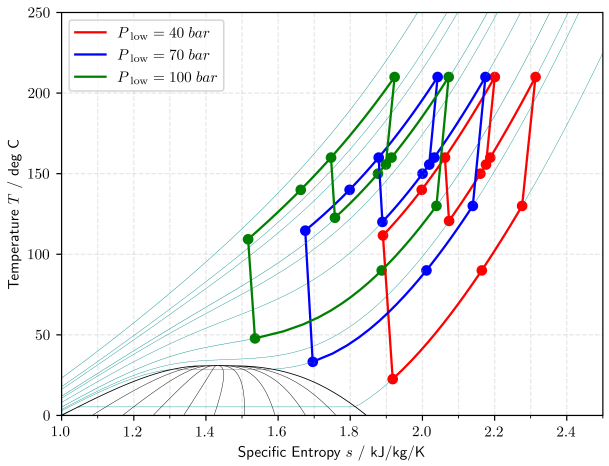

Figure 5.97: Ts diagram showing the effect of P_{low} (with T_{sink} = 200 °C and ΔT_{sink} = 50 °C) on the two-stage heat pump configuration with internal recuperation and intercooling, using $\mathrm{CO_2}$ as working fluid.

The overall range of T_{min} values obtained for this heat pump configuration is lower than those obtained for the previously discussed two-stage heat pump configuration. This is because of two factors: the turbine inlet temperature is lower due to the additional recuperator and the larger expansion ratio. This is also visible in Figure 5.97, which illustrates the thermodynamic cycle of the heat pump at hand for different P_{low} values.

Figure 5.98 shows the variation of $\mathrm{COP_h}$ with ΔT_{sink} for fixed P_{low} of 100 bar. The effect of ΔT_{sink} on the $\mathrm{COP_h}$ is similar to the one observed for the two-stage configuration with intercooling. However, the values of $\mathrm{COP_h}$ are lower in this case, as discussed earlier. Furthermore, the maximum allowed value for ΔT_{sink} in this case is lower, as shown by Figure 5.99, where the variation of β_{total} with ΔT_{sink} is shown (with fixed P_{low} of 100 bar). Similarly to the case of the previous two-stage configuration, the value of ΔT_{sink} also affects the required β_{total}. However, since there is an additional internal heat exchanger for this configuration, the compressor inlet temperature is reduced further if ΔT_{sink} is increased. As

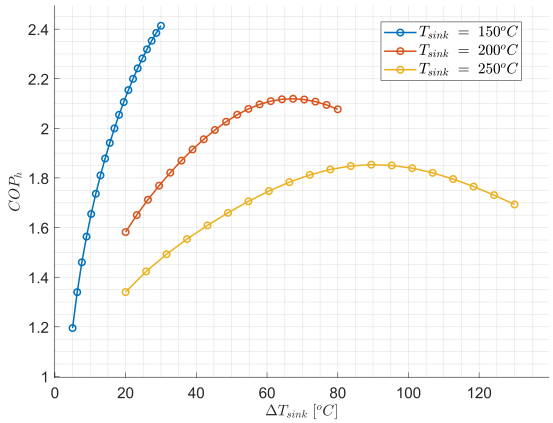

Figure 5.98: Variation of $\mathrm{COP_h}$ with ΔT_{sink} at different values of T_{sink}(with P_{low} = 100 bar) for two-stage heat pump configuration with internal recuperation and intercooling, using $\mathrm{CO_2}$ as working fluid.

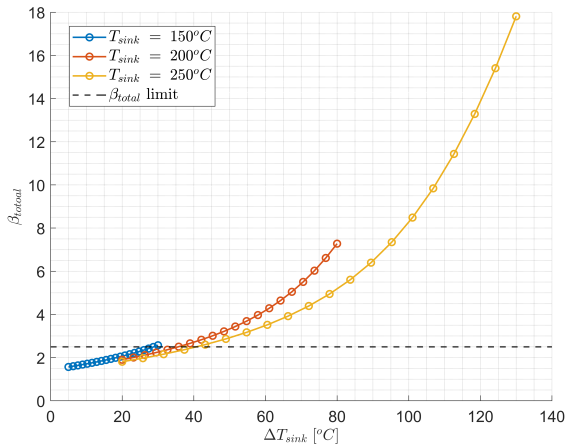

Figure 5.99: Variation of β_{total} as a function of ΔT_{sink} and T_{sink}(with P_{low} = 100 bar) for the two-stage heat pump configuration with internal recuperation and intercooling, using $\mathrm{CO_2}$ as working fluid.

a result, the required β_{total} is higher for this configuration, and the maximum feasible ΔT_{sink} is lower, resulting in a lower maximum feasible $\mathrm{COP_h}$. Figure 5.100 shows the effect of ΔT_{sink} on this heat pump configuration's thermodynamic characteristics through the means of Ts diagram at fixed P_{low} and T_{sink} of 100 bar and 200°C respectively. As the ΔT_{sink} value increases, the inlet temperature of turbines is reduced. This combined with an increased expansion ratio (due to increased β_{total}) leads to a lower T_{min} value for this heat pump configuration. The similar trend is also confirmed by Figure 5.101, where the variation of T_{min} with ΔT_{sink} is shown at fixed P_{low} of 100 bar.

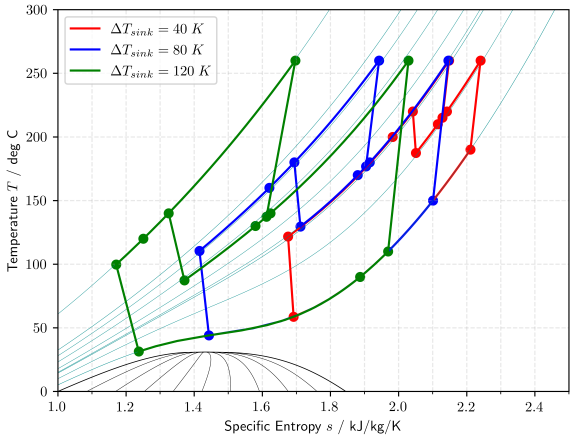

Figure 5.100: Ts diagram showing the effect of ΔT_{sink} (with T_{sink} = 250 °C and P_{low} = 100 bar) on the two-stage heat pump configuration with internal recuperation and intercooling, using $\mathrm{CO_2}$ as working fluid.

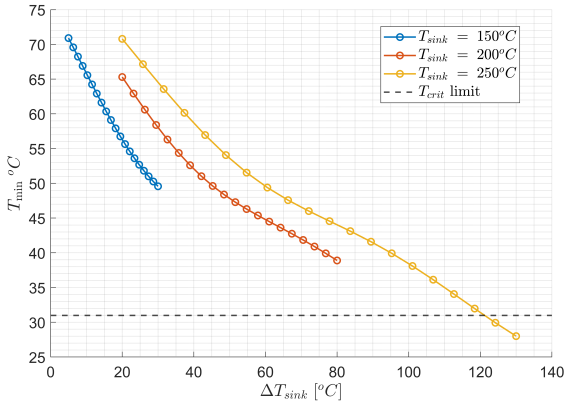

Figure 5.101: Variation of T_{min} as a function of ΔT_{sink} and T_{sink}(with P_{low} = 100 bar) for the two-stage heat pump configuration with internal recuperation and intercooling, using $\mathrm{CO_2}$ as working fluid.

For the case of air, the results are similar to those presented for the previous heat pump configurations and thus are not reported here (Appendix C).

5.4. Optimal Cycle Configurations

For all the cases, the best-performing heat pump configuration was selected from both the categories (reverse Rankine cycle based and reverse Brayton cycle based) . Figure 5.102 and Figure 5.103 shows an overview of the $\mathrm{COP_h}$ obtained, with T_{source} = 100 °C and T_{sink} = 200 °C, for the different heat pump configurations based on reverse Rankine cycle and reverse Brayton cycle respectively. For the reverse Brayton cycle-based heat pump configurations, $\mathrm{CO_2}$ is selected as the working fluid because higher $\mathrm{COP_h}$ values were obtained as compared to air (Section 5.3). In Figure 5.103, the results are shown for three different P_{low} values because the heat pump performance is dependent strongly on the selected pressure level (as discussed earlier in Section 5.3). To facilitate an easy comparison between the two heat pump concepts, the maximum $\mathrm{COP_h}$ value obtained using the reverse Rankine cycle based heat pump configurations is highlighted by the dashed line in Figure 5.103.

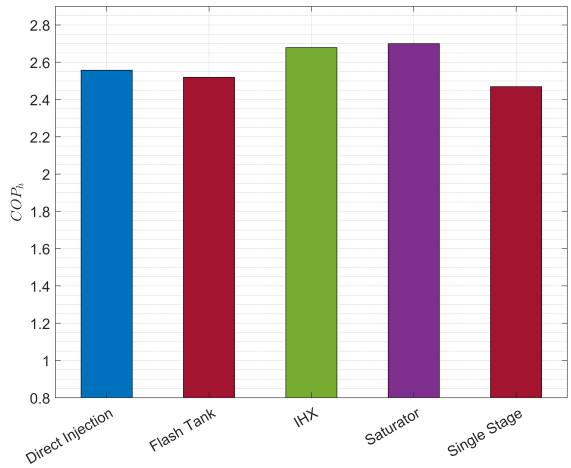

Figure 5.102: Performance comparison of different configurations based on reverse Rankine cycle for T_{source} = 100 °C and T_{sink} = 200 °C.

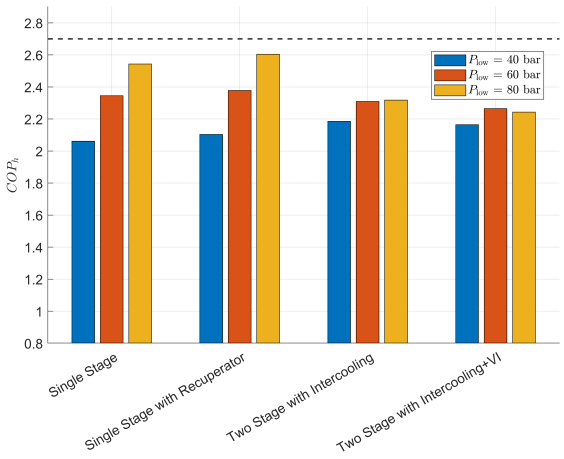

Figure 5.103: Performance comparison of different configurations based on reverse Brayton cycle (under sensible heat sink case) for T_{source} = 100 °C, T_{sink} = 200 °C and ΔT_{sink} = 100 °C.

For reverse Rankine cycle based heat pump configurations, the two-stage configuration with a saturator provided the highest $\mathrm{COP_h}$ under the given boundary conditions. However, from a practical integration viewpoint, a drawback was found. For this configuration, it is impossible to control the degree of superheating at the inlet of the second compressor. This is because the inlet thermodynamic state is fixed by the outlet conditions of the saturator, which, by definition, is a saturated vapor state. For a feasible compressor design, often in practice, a certain degree of superheating is used at the inlet to avoid having any issues with the occurrence of two-phase flow within the compressor [104]. The same conclusion was also found when performing the initial compressor design for the test cases selected in this chapter (discussed further in Section 6.2). Therefore, for all the case studies, the two-stage heat pump configuration with an internal heat exchanger and vapor injection was selected for the reverse Rankine cycle category. The difference in $\mathrm{COP_h}$ between the two configurations is around 1%; therefore, by selecting the heat pump with the internal heat exhchanger, the drop in $\mathrm{COP_h}$ is very small. The control of superheating at the second compressor inlet is achieved by regulating the amount of working fluid injected through the valve upstream the internal heat exchanger.

For the reverse Brayton cycle-based heat pump configurations, the only constraint is related to the maximum operating pressure level, which was selected as 250 bar (as discussed earlier in Section 5.2). Thus, for this heat pump concept, the single-stage heat pump configuration with a recuperator was selected for the different case studies.

6

Practical Integration - Case Studies

The final phase of the project involved a comparison between the reverse Rankine cycle and reverse Brayton cycle based heat pump configurations for a few industrial test cases, to assess the actual implications of the integration in an industrial process of the two heat pump concepts. Along with a thermodynamic cycle analysis, the conceptual design of the turbomachinery components was also performed for each test case. This section provides detail about the selected case studies and the results obtained with the different heat pump configurations for each of them.

6.1. Selected Case Studies

Three different case studies were selected for this analysis. The first case study reflects a hypothetical application based on the industrial potential identified from literature for the high-temperature heat pump systems. The other two cases were chosen to represent a specific industrial processes.

6.1.1. Case 1

The first case study was formulated using the information gathered from literature regarding the industrial potential of high-temperature heat pump systems, see Section 1.1 (Figure 1.5). The use of heat pump units in industry is envisaged for small thermal capacity applications (<5 MW) and in terms of temperature levels, sink temperatures greater than 150 °C guarantee the coverage of a large share of industrial processes. Based on these observations, a hypothetical case scenario was constructed, whose main specifications are summarized in Table 6.1. Similar to the methodology used for the thermodynamic analysis, both sink and source heat exchangers are modeled considering only one stream (working fluid).

Table 6.1: Specifications of the case study 1.

Variable	Value	Units
T_{source}	100	°C
T_{sink}	200	°C
Sink capacity ($\dot{Q}_{\text{sink}}$)	1	MW
$\Delta T_{\text{min, HEX}}$	10	K

6.1.2. Case 2

The second case study concerns a spray drying process in the food industries. In this process, heated air is used to dry the liquid food that is sprayed as atomized liquid in the drying chamber [105]. Within the food industry, spray drying processes usually are characterized by high energy and temperature level requirements compared to other processes [106]. Due to this high temperature and energy requirements, combined with high thermal energy demand, this process can be considered promising for heat pump implementation. In light of this, a spray drying process associated with milk production was selected, using the data provided in [26]. Table 6.2 provides the case specifications, where q refers to the absolute humidity of the air flow. The required thermal capacity is fixed as the inlet, and outlet temperatures of the air stream to be heated are known, along with the respective mass flow rate. On the source side, only the inlet temperature is known. The source stream outlet temperature will be determined by the coupling with the thermodynamic cycle of the heat pump.

Table 6.2: Specifications of the case study 2 (spray drying process).

Variable	Value	Units
Source T_{in}	50	°C
Source T_{out}	-	-
Source $\dot{m}$	64.3	kg/s
Source Stream	*Moist Air* (q_{in} =28.88 g/kg)	-
Sink T_{in}	64	°C
Sink T_{out}	210	°C
Sink $\dot{m}$	54.9	kg/s
Sink Stream	*Moist Air* (q_{in} = 6.43 g/kg)	-
$\Delta T_{\text{min, HEX}}$	7.5	K

6.1.3. Case 3

The final case study is related to the alumina production process. Bayer process is usually the most commonly used method to refine the bauxite to alumina [107]. This process has a high energy demand since the energy is needed for pre-heating the bauxite and the digestion of the slurry generated in the bauxite reduction process [108]. As a result, high amounts of waste thermal energy at different temperature levels are available, which makes the process suitable for a potential heat pump implementation. The data provided in [26] and summarized in Table 6.3 were used for this case study. The exhaust air from the calciner stage is used as the thermal energy source for the heat pump. The data of the stream to be heated is not available, but it is assumed that its specific heat capacity can be modeled as constant (the fluid could be a molten salt or thermal oil) [108][109].

Table 6.3: Specifications of the case study 3 (alumina production process).

Variable	Value	Units
Source T_{in}	110	°C
Source T_{out} (max)	60	°C
Sink T_{in}	140	°C
Sink T_{out}	280	°C
Sink capacity ($\dot{Q}_{\text{sink}}$)	50	MW
$\Delta T_{\text{min, HEX}}$	7.5	K

6.2. Case 1

6.2.1. Reverse Rankine cycle based configuration

The design of the two-stage heat pump configuration with an internal heat exchanger and working fluid injection has only one degree of freedom, namely, p_{intm}. Following the methodology adopted in Section 5.1, P_{frac}, the ratio between the compression ratios of the two heat pump compressors, was varied to get the optimal p_{intm} value.

The optimal P_{frac} is equal to 1.1 in this case. Table 6.4 shows the corresponding performance of the system. The value of COP_h reported here is lower than the value shown earlier in Section 5.1. This is because, in this case, a degree of superheating of 11 K was added before the inlet of both compressors. After simulating the system model, the specifications for the compressor design were also obtained, see Table 6.5. Using these design requirements, the conceptual design was performed for both compressors of the heat pump.

Table 6.4: Case 1 - main characteristics at the design point of the two-stage configuration adopting an internal heat exchanger and vapor injection (reverse Rankine cycle based).

Variable	Value	Units
COP_h	2.64	-
Q_{source}	641	kW
β_{total}	27.19	-
$P_{\text{frac, optim}}$	1.1	-
$\dot{m}_{\text{comp 1}}$	0.31	kg/s
$\dot{m}_{\text{comp 2}}$	0.42	kg/s

Table 6.5: Case 1 - compressor design requirements for the two-stage configuration adopting an internal heat exchanger and vapor injection (reverse Rankine cycle based).

Variable	Compressor 1	Compressor 2
$P_{t,in}$	0.702 bar	3.84 bar
$T_{t,in}$	101^oC	153.1^oC
β_{total}	5.47	4.97
$\dot{m}$	0.31 kg/s	0.42 kg/s

Before performing the optimization of the compressor design, a manual exploration of the design space was conducted for both heat pump compressors. The selected value for the degree of superheating was also decided based on this initial design investigation. The results of this manual design investigation are added in Appendix D, and only the design optimization results are provided here. The main outcomes of the preliminary design investigation were: both compressors require at least two stages to comply with the prescribed compression ratio. If only one stage is adopted, the maximum peripheral speed at the impeller outlet (U_2) exceeds the value of 700 m/s, whatever is the chosen set of design variables. This range of U_2 values is well beyond the mechanically feasible condition [103]. With a twin stage design, the definition of the velocity triangle at the outlet of the stage is critical, as the angle of the relative speed at the impeller outlet (β_2) becomes positive (indicating forward swept blades). The forward swept blades are undesirable as the maximum efficiency operating points fall in the unstable region [90]. Depending on κ, the split of the compression ratio between the two stages, this critical condition occurs at the outlet either of the first stage or the second stage. Therefore, in the design optimization, constraints on the maximum β_2, U_2, and RPM were imposed to guarantee the feasibility of the twin stage compressor design.

The compressor immediately after the thermal source of the heat pump is called as first compressor (or compressor 1), while the other compressor (before the inlet of the thermal sink) is referred to as the second compressor (or compressor 2).

Table 6.6 shows the design constraints for the first compressor. Their values were obtained after a few iterative attempts based on preliminary results of the optimization. Therefore, the value of maximum power on the design speed line was also determined based on these initial runs. The optimization was performed using the NSGA-II algorithm. The Latin hypercube sampling method was used to get the initial population, where ten individuals were used for every design variable. This resulted in 160 evaluations per population (10x16 design variables). Table 6.7 shows the optimization results for the first compressor design.

Table 6.6: Constraints values selected for the design of compressor 1 design of Case 1, for the two-stage configuration adopting an internal heat exchanger and vapor injection (reverse Rankine cycle based).

Constraint Variable	Type of Constraint	Value
β_2	Maximum Value	-6^o
U_2	Maximum Value	590 m/s
RPM	Maximum Value	100e3
W_{el}	Maximum Value	250 kW
AR	Minimum Value	0.24
AR	Maximum Value	1.5
M_4	Maximum Value	0.7
Choke Margin	Minimum Value	1.05
$\Delta\beta_{total}$	Maximum Value	20 %

Table 6.7: Compressor 1 design optimization results for two-stage configuration adopting an internal heat exchanger and vapor injection (reverse Rankine cycle based).

Parameter	Value
Number of function evaluations	13760
Number of generations	86
Number of Logical Processors Used	8
Total Time Taken [hr]	72.3
Average Time per Generation [min]	50.4

The convergence of the optimization run is presented in Appendix D. Figure 6.1 shows the obtained Pareto front for the compressor 1 design. Fourteen non-dominated design options were obtained for this compressor. The chosen optimal conceptual design represents a trade-off between the operating range and the total-to-total compressor efficiency value. The associated design variables of this solution are listed in Table 6.8. The value of κ is greater than 1. As per the findings reported in [88], having $\kappa > 1$ helps enhancing the efficiency of both the stages without penalizing the operating range of the compressor. The value of the isentropic loading coefficient (ψ_{is}) for the first stage is found close to the upper limit, which can be explained by the need to comply wit the stringent constraint on the RPM of the machine. The second impeller is found to have a more negative backsweep angle than the first stage. The reason behind such a trend is related to the size of the two machines. A higher value of the relative clearance gap is obtained for the second impeller because of the reduced blade height. This reduction in blade height is a consequence to the reduced volumetric flow rate in the second impeller. The net effect of this larger relative clearance gap is a decrease in efficiency. To counteract this decrease in efficiency, the meridional velocity component is decreased at the second impeller exit such that the blade span at the impeller outlet increases. Having a more negative backsweep angle helps in achieving this desired effect [88].

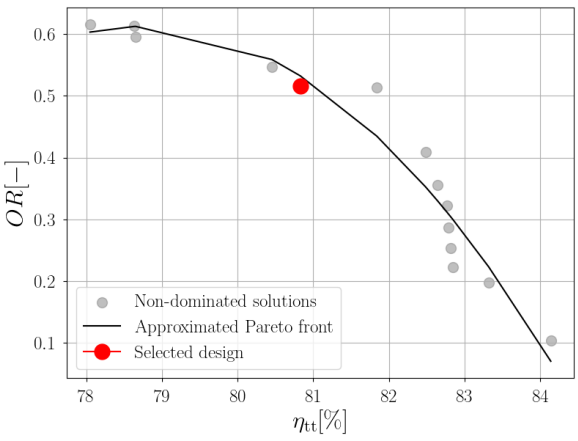

Figure 6.1: Pareto front obtained for the design of compressor 1 of the reverse Rankine cycle based configuration, under Case 1 conditions.

Table 6.8: Design variables corresponding to the selected optimal design point for compressor 1 (from Pareto front) of reverse Rankine cycle-based configuration, under Case 1 conditions.

Variable	Stage 1	Stage 2
$\beta_{\text{tt, target}}$	2.68	2.04
kRPM	97	97
ϕ_{t1}	0.169	0.094
$\psi_{\text{is}} - \psi$	$0.95 - 0.81$	$0.92 - 0.81$
α_2	66.1°	63.7°
k	0.86	0.96
$N_{\text{bl}} - N_{\text{split}}$	$19 - 0$	$24 - 12$
R_3/R_2	1.64	1.79
$R_{\text{r,pinch}}$	0.44	0.18
$H_{\text{r,pinch}}$	0.05	0.31

Figure 6.2 shows the meridional flow path of the individual stages of the optimal design for compressor 1. The average axial and radial dimensions of both stages are similar, but the impeller shape factor is different. Therefore, the axial width of the diffuser is also different for the two stages.

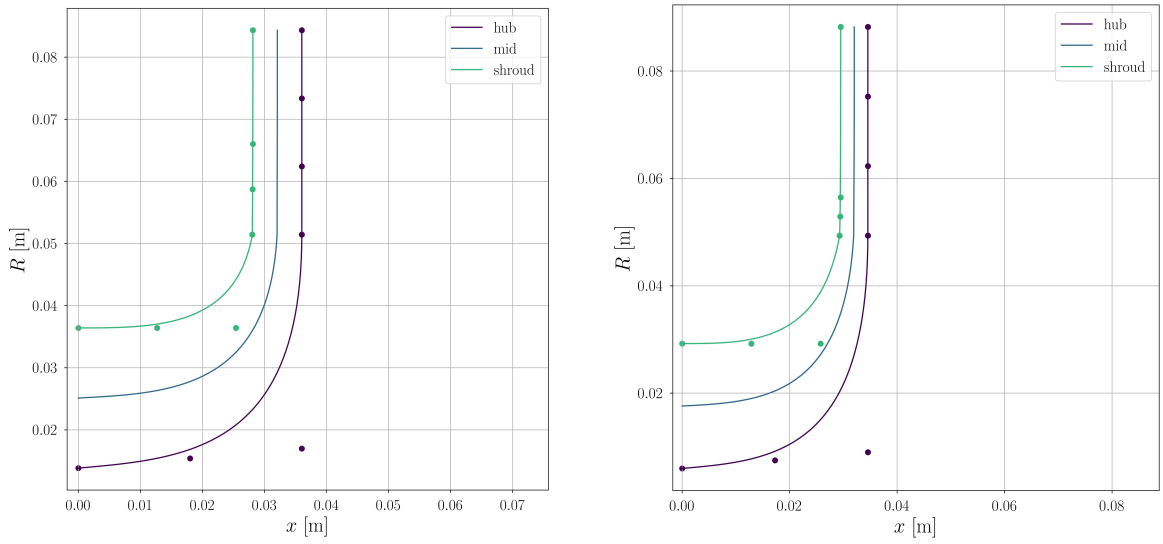

(a) Stage 1 **(b)** Stage 2

Figure 6.2: Meridional flow path obtained for optimized design of compressor 1, for reverse Rankine cycle based configuration, under Case 1 conditions.

Finally, the operating maps were also obtained for this optimized design. Figure 6.3a and Figure 6.3b shows the maps of the total pressure ratio (β_{tt}) and total-to-total efficiency (η_{tt}). The nominal RPM value was found to be 97E+03 (Table 6.8). At the design point, the η_{tt} for the whole machine is around 84 %, and the required power is 130 kW. With an increase in RPM, the speed lines tend to change their slope, which is expected per the reference designs shown in literature [90].

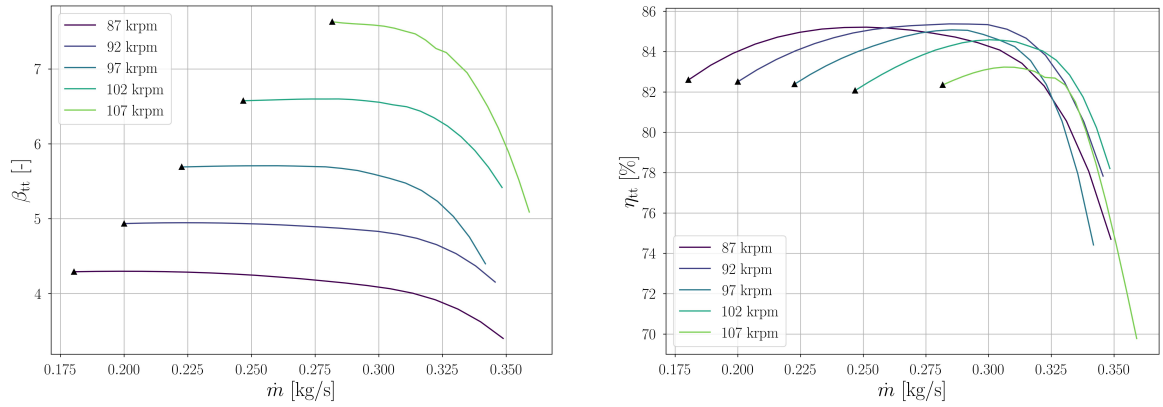

(a) β_{tt} vs $\dot{m}$ **(b)** η_{tt} vs $\dot{m}$

Figure 6.3: Operating maps obtained for the optimized design of compressor 1, of the reverse Rankine cycle based configuration, under Case 1 conditions.

For the design of compressor 2, the same procedure adopted previously for compressor 1 was followed. Table 6.9 shows the constraints considered while solving the related optimization problem. Compared to compressor 1, the constraint on maximum RPM had to be relaxed because of the higher operating pressure of this compressor. The initialization method based on Latin hypercube was used for the optimization algorithm. Table 6.10 shows the results of the optimization for the second compressor.

Table 6.9: Constraint values selected for the design of compressor 2 of Case 2 - two-stage configuration adopting an internal heat exchanger and vapor injection (reverse Rankine cycle based).

Constraint Variable	Type of Constraint	Value
β_2	Maximum Value	-5^o
U_2	Maximum Value	600 m/s
RPM	Maximum Value	115e3
W_{el}	Maximum Value	450 kW
AR	Minimum Value	0.24
AR	Maximum Value	1.5
M_4	Maximum Value	0.7
Choke Margin	Minimum Value	1.05
$\Delta\beta_{total}$	Maximum Value	20 %

Table 6.10: Compressor 2 design optimization results for two-stage configuration adopting an internal heat exchanger and vapor injection (reverse Rankine cycle based).

Parameter	Value
Number of function evaluations	21600
Number of generations	135
Number of Logical Processors Used	12
Total Time Taken [hr]	150.7
Average Time per Generation [min]	67

The convergence of the optimization run is presented in Appendix D. Figure 6.4 shows the obtained Pareto front for the design of compressor 2. Fourteen non-dominated design options were obtained. The value of operating range (OR) is higher for this compressor than for compressor 1. However, the values of efficiency are lower. Like compressor 1, the optimal conceptual design was chosen as a trade-off between the operating range and the total-to-total compressor efficiency, see Figure 6.4. Table 6.11 shows the associated design variables of the chosen optimal solution. Similar values are observed for the design variables of the two stages, as for the first compressor. In this case, however, the value of β_2 is very close to the lower bound set in the optimization and less negative than in the first impeller. The reason thereof is the value of κ, which is about 1.1, whereas, for compressor 1, instead of 1.3 as in compressor 1. It results that the backsweep has to be minimized to ensure that the maximum U_2 value remains in the feasible range.

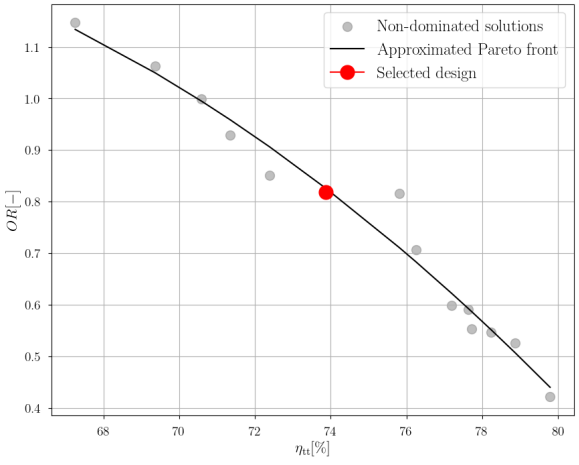

Figure 6.4: Pareto front obtained for the design of compressor 2 of the reverse Rankine cycle based configuration, under Case 1 conditions.

Table 6.11: Design variables corresponding to the selected optimal design point for compressor 2 (from Pareto front) of the reverse Rankine cycle-based configuration, under Case 1 conditions.

Variable	Stage 1	Stage 2
$\beta_{\text{tt, target}}$	2.34	2.12
kRPM	114	114
ϕ_{t1}	0.072	0.029
$\psi_{\text{is}} - \psi$	$0.92 - 0.83$	$0.96 - 0.86$
α_2	$67.2°$	$71.9°$
k	0.65	0.79
$N_{\text{bl}} - N_{\text{split}}$	$25 - 0$	$26 - 13$
R_3/R_2	1.49	1.53
$R_{\text{r,pinch}}$	0.91	0.98
$H_{\text{r,pinch}}$	0.95	0.99

The nominal RPM value was found to be 114E+03 (Table 6.11) for this compressor design. At the design point, the η_{tt} for the whole machine is around 78 %, and the required power is found to be 210 kW. Figure 6.5a and Figure 6.5b shows the operating maps of the total pressure ratio (β_{tt}) and total-to-total efficiency (η_{tt}). In this case, the speed line associated with the highest RPM was found to have numerical errors. Because of this only part of the speed line is shown in the operating maps. The reason behind this is expected to be related to the numerical errors associated with the solution of implicit empirical models.

Figure 6.6 shows the meridional channel of the individual stages for the optimal design of compressor 2. The average axial and radial dimensions of the second stage are found to be higher. Further, the impeller shape factor is different for both stages. As a result, the axial width of the diffuser is also

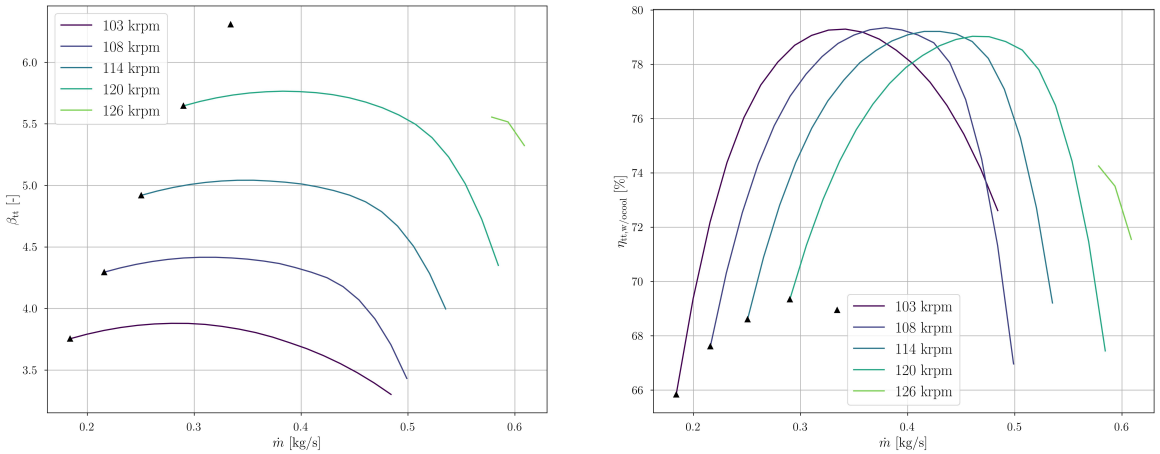

(a) β_{tt} vs $\dot{m}$

(b) η_{tt} vs $\dot{m}$

Figure 6.5: Operating maps obtained for the optimized design of compressor 2 of the reverse Rankine cycle based configuration, under Case 1 conditions.

different for the two stages. It is smaller in the second stage than in the first stage. At the design point, volute, diffuser, and friction losses were highest in magnitude (in order) for the first stage. Whereas for the second stage, the percentage of diffuser loss was almost twice as large as that in the first compressor, followed by friction and volute losses.

Finally, a preliminary investigation was done for both compressor designs to check the feasibility of the required electric motor design. For this purpose, the maps reported in [110][111] and reproduced in Figure 6.7 were used. In both charts, the required RPM and power for compressors 1 and 2 are highlighted in red and blue, respectively. As these points represent the design conditions, only a qualitative assessment is possible. Further, note that the location of the points representing the selected compressor designs on the map is approximated. However, this is considered sufficient for this work, as the main objective is to assess the feasibility of an electric motor directly connected to the compressor impellers based on the existing machines.

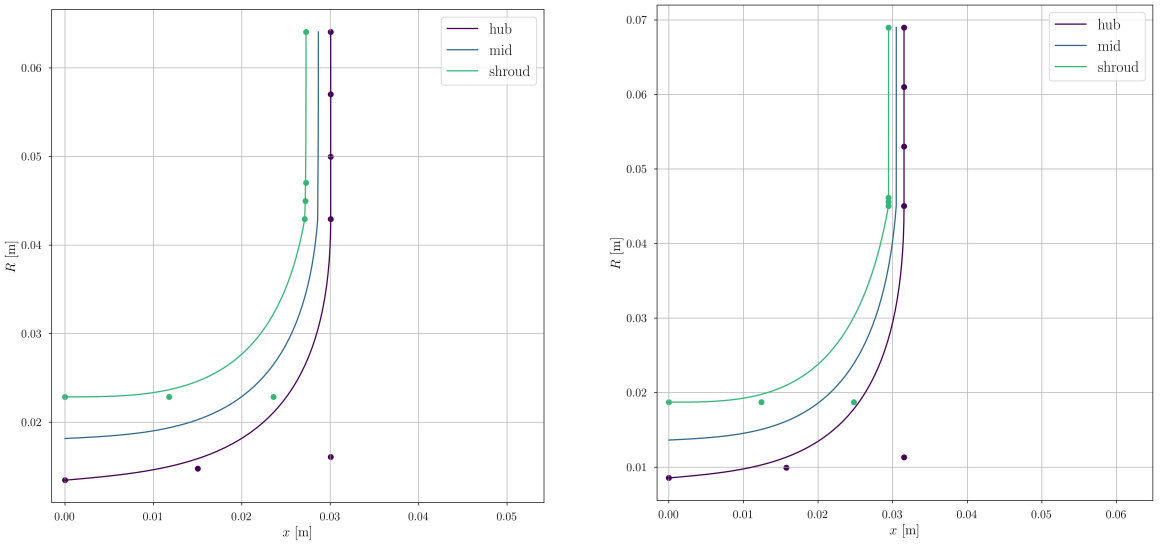

(a) Stage 1

(b) Stage 2

Figure 6.6: Meridional flow path obtained for the optimized design of compressor 2 of the reverse Rankine cycle based configuration, under Case 1 conditions.

The scales of the y-axis in both figures is logarithmic. Therefore, the difference between the design points of the two compressors is small on the map. For compressor 1, the design point is within the feasible design region, and there are existing machines with similar characteristics. However, the design point of compressor 2 is farther away from the region covered by commercial products (the limit of this region is shown as a solid black line in the figure). Nevertheless, the combination of rotational speed and power required for compressor 2 is still within the vicinity of the feasible region, and given the latest advancements in the motor designs for high RPM and high power [112], it can be expected that machines with these characteristics will become available in the near future. However, dedicated investigations must be carried out to confirm the mechanical feasibility of such an electric motor.

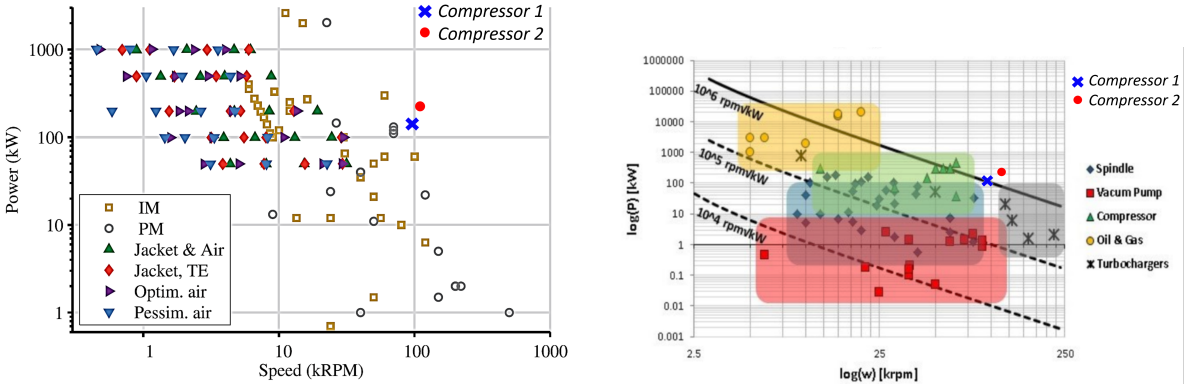

(a) Study 1 [110] **(b)** Study 2 [111]

Figure 6.7: Electric motor requirements for both the compressors of Case 1, superimposed on the feasibility limits of electric motors obtained from the literature.

6.2.2. Reverse Brayton cycle based configuration

The design of the CO_2 single-stage heat pump with internal recuperation has two degrees of freedom, i.e., P_{low} and ΔT_{sink}. For the value of ΔT_{sink}, the limiting value depends on the temperature of the thermal source and the minimum temperature difference in the recuperator. This resulted in a ΔT_{sink} of 100 °C. Using this value of ΔT_{sink}, the variation of COP_{h} and β_{total}, as a function of P_{low}, was analyzed to check the maximum feasible pressure in the thermal source. Figure 6.8 shows the obtained results. In this figure, the dashed black line indicates the maximum allowed value of β_{total} for a given P_{low} value, based on the maximum operating pressure limit of 250 bar.

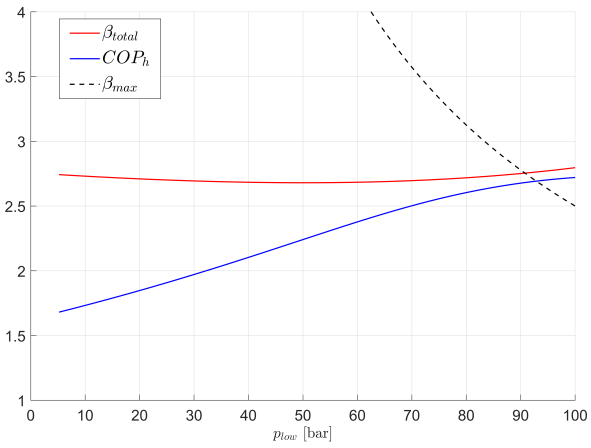

Figure 6.8: Variation of COP_{h} and β_{total} with P_{low}, for the CO_2 single stage configuration with internal recuperation, under the operating conditions of case 1.

Table 6.12: Case 1 - Main characteristics of single-stage configuration with internal recuperation.

Variable	Value	Units
COP_{h}	2.68	-
Q_{source}	661	kW
β_{total}	2.75	-
P_{low}	90	bar
$\dot{m}$	5.84	kg/s
$T_{\text{t, comp in}}$	100	°C
$T_{\text{t, turb in}}$	103.2	°C

Based on the trends shown in Figure 6.8, the optimal value of P_{low} was found to be 90 bar. The characteristics of this heat pump configuration, which results from assuming ΔT_{sink} 100°C and P_{low} 90 bar, are shown in Table 6.12. The value of COP_h is higher for this configuration than for the reverse Rankine cycle based heat pump configuration. However, the relative increase in COP_h is only about 1.4 %. This result is in contrast with those reported in Section 5.3. The main reason is the thermodynamic loss associated with the 10°C of superheating imposed at the inlet of both compressors of the steam heat pump, which leads to a decrease in COP_h value.

Compared to the case of the reverse Rankine cycle, the design requirements of the compressor of this heat pump concept are less stringent as the required compression ratio (β_{total}) is lower, and the operating mass flow rate is higher. Due to the lower β_{total}, a single-stage machine was found to be feasible. Table 6.13 shows the design constraints accounted in the optimization of the single stage CO_2 compressor. Table 6.14 shows the results of the optimization. The convergence of the optimization algorithm is discussed in Appendix D. Figure 6.9 shows the Pareto front.

Table 6.13: Constraints values selected for the design of the compressor of the Case 1 for CO_2 single stage configuration with internal recuperation.

Constraint Variable	Type of Constraint	Value
β_2	Maximum Value	-10^o
U_2	Maximum Value	550m/s
RPM	Maximum Value	100e3
W_{el}	Maximum Value	700 kW
AR	Minimum Value	0.24
AR	Maximum Value	1.5
M_4	Maximum Value	0.7
Choke Margin	Minimum Value	1.05
$\Delta\beta_{total}$	Maximum Value	5 %

Table 6.14: Compressor design optimization results for the CO_2 single stage configuration with internal recuperation.

Parameter	Value
Number of function evaluations	3840
Number of generations	48
Number of Logical Processors Used	4
Total Time Taken [hr]	14.2
Average Time per Generation [min]	17.7

35 non-dominated design options were obtained for this compressor. Though the optimization algorithm did not achieve full convergence with respect to the applied tolerances. Therefore, the solutions on the Pareto front may be still sub-optimal.

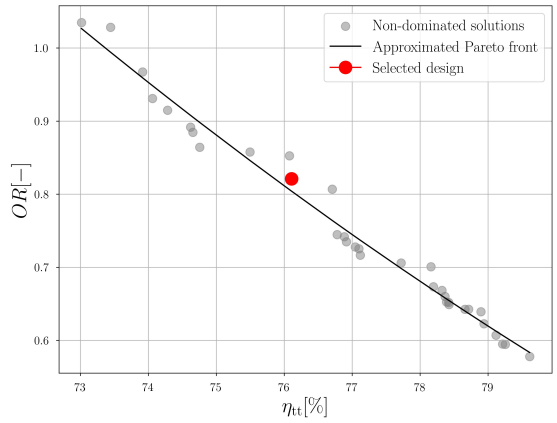

Figure 6.9: Pareto front obtained for the design of compressor of the reverse Brayton cycle based configuration, under Case 1 conditions.

Table 6.15: Design variables corresponding to the selected optimal design point for the compressor (from Pareto front) of the reverse Brayton cycle-based configuration, under Case 1 conditions.

Variable	Value
$\beta_{\text{tt, target}}$	2.75
kRPM	92.3
ϕ_{t1}	0.022
$\psi_{\text{is}} - \psi$	$0.85 - 0.68$
α_2	72◦
k	0.93
$N_{\text{bl}} - N_{\text{split}}$	$12 - 0$
R_3/R_2	1.34
$R_{\text{r,pinch}}$	0.915
$H_{\text{r,pinch}}$	0.802

Table 6.15 shows the design variables associated with the chosen optimal design. Notice, very low value of swallowing capacity of the compressor. This is because of the constraint applied on the maximum RPM value. Further, no splitter blades were needed for this design. As a result of low β_{total} and the characteristics of CO_2 as working fluid, the maximum U_2 value, in this case, was found well below the limit of 550 m/s (around 380 m/s). At the nominal operating conditions, the main losses, in order

of relevance, are clearance, leakage, diffuser, and friction losses. Figure 6.10 shows the meridional channel obtained for the optimal design of this compressor. The axial and radial dimensions are lower than those of the H_2O compressors, despite the higher mass flow rate. This is because the volumetric flow rate is lower for this case due to the higher density of CO_2. The compactness of the machine also explains why the leakage losses are higher for this design, as compared to the H_2O compressors. The design point RPM value was found to be 92E+03 (Table 6.15). At the design point, the η_{tt} for the whole machine is around 80 %, OR is equal to 0.76, and the required power is 480 kW.

Figure 6.11a and Figure 6.11b shows the operating maps of the total pressure ratio (β_{tt}) and total-to-total efficiency (η_{tt}), obtained for the optimized design. The triangle and square symbols in these figures represent the stall/surge and choking limit, respectively. These symbols were not present for the case of H_2O compressors because, in the case of the twin stage configuration, the final operating map is obtained based on the operating maps of the individual stages. Therefore, for example, if one of the stages does not have feasible operating points in a certain range of values for mass flow rate, then those operating points will not even be considered for the other stage. As a result, it is possible that the true limits of individual stages are not shown, but since the stages operation is coupled, the final operating range is dictated by the individual operating maps of both stages.

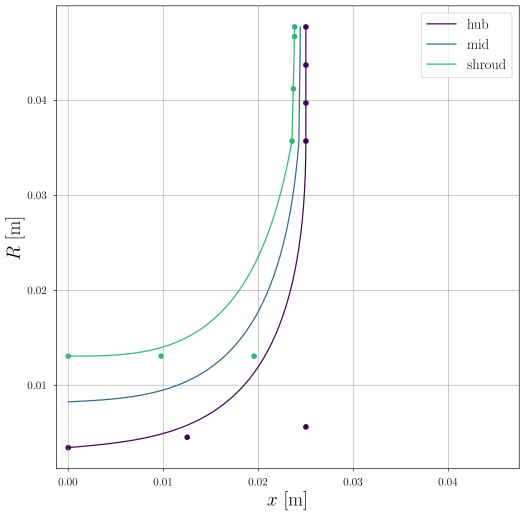

Figure 6.10: Meridional flow path obtained for the optimized compressor design of the reverse Byaton cycle based configuration, under Case 1 conditions.

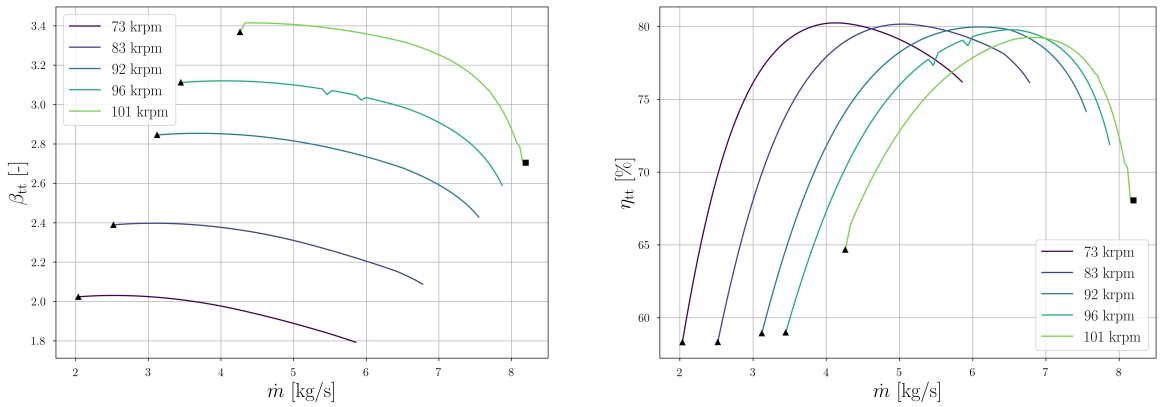

(a) β_{tt} vs $\dot{m}$ **(b)** η_{tt} vs $\dot{m}$

Figure 6.11: Operating maps obtained for the optimized compressor design of the reverse Brayton cycle based configuration, under Case 1 conditions.

As for the case of H_2O compressors, the feasibility of electric motor design was also investigated for this CO_2 compressor. Figure 6.12 shows the design point of the CO_2 compressor superimposed on the feasible design maps of electric motors, obtained from the literature. For this compressor design, the required electric motor characteristics are further away from the feasible region than the H_2O compressors. This is mainly because of the high power required. However, one study in the literature was found mentioning feasible commercial CO_2 compressors up to 40 MW, but no information about the RPM or maximum pressure value was provided [113]. Therefore, to loosen the requirements of the electric motor, the possibility to couple the compressor and turbine on the same shaft was considered, such that the turbine can supply a part of the required compressor power. As a result, a lower power requirement would be needed for the electric motor, facilitating its design. However, such a configuration has also drawbacks, mainly related to the system startup and matching of the operating range of both compressor and turbine. The investigation of such issues was out of the scope of the current project. Nevertheless, it was investigated the design of the turbine if this has to operate at the same rotational speed of the compressor.

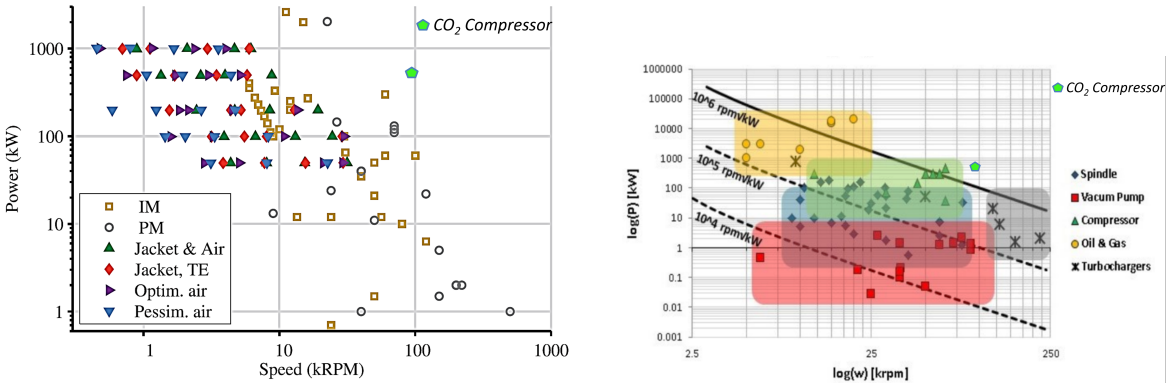

(a) Study 1 [110] **(b)** Study 2 [111]

Figure 6.12: Electric motor requirements for CO_2 compressor of Case 1, superimposed on the feasibility limits of electric motors obtained from the literature.

More in detail, two conceptual designs were obtained for the turbine. In the first design (design 1), no constraint on RPM was imposed, and the duty coefficients were optimized for maximum efficiency. Whereas for the second design (design 2), the duty coefficients were optimized to match the RPM of the compressor. Some of the geometrical parameters of the turbine were not optimized but their values was defined based on the reference designs provided in literature for CO_2 and similar operating conditions [114][115]. These selected values are provided in Appendix D. To design the diffuser geometry, guidelines provided in literature guaranteeing the minimization of the fluid-dynamic losses were followed [116][117].

The main characteristics of the two turbine designs are shown in Table 6.16 and Table 6.17. Observing the characteristics of the two design options, it can be concluded that the relative difference in efficiency value is small (<1 %). Given the associated uncertainties with the empirical loss and fluid model, this difference cannot be considered significant. Therefore, in this case, it is possible to arrange the compressor and turbine on the same shaft without any penalty on turbine performance, at least at the design point. The full operating map needs to be investigated to assess the penalty in efficiency that may occur in off-design conditions. Further, comparing the dimensions of the two machines, the design of the mechanical coupling between the compressor and turbine may be not trivial, with the result that the complexity and cost of the overall assembly may considerably increase.

The meridional channel of the two design solutions is shown in Figure 6.13 and Figure 6.14 respectively. Design 1 has a smaller radial extension for the diffuser and impeller blades than design 2. However, the axial dimension of the impeller section is higher for the case of Design 1. The diffuser design is also very similar for both the solutions because of the similar design inputs. Nevertheless, the diffuser for design 2 is found to be longer as compared to design 1.

Table 6.16: Design variables corresponding to the optimized turbine design of reverse Brayton cycle-based configuration, under Case 1 conditions (with no constraint on RPM).

Variable	Value	Units
β_{tt}	2.79	-
η_{tt}	0.845	-
kRPM	114.9	-
W_{out}	161.5	kW
ϕ_2	0.311	-
ψ	0.719	-
χ	0.58	-
α_2	67.4	°
β_3	−52.7	°
N_{rotor}	10	-
N_{stator}	12	-

Table 6.17: Design variables corresponding to the optimized turbine design of reverse Brayton cycle-based configuration, under Case 1 conditions (with turbine and compressor on the same shaft).

Variable	Value	Units
β_{tt}	2.78	-
η_{tt}	0.838	-
kRPM	94.3	-
W_{out}	160.3	kW
ϕ_2	0.283	-
ψ	0.739	-
χ	0.567	-
α_2	69.7	°
β_3	−52.7	°
N_{rotor}	11	-
N_{stator}	6	-

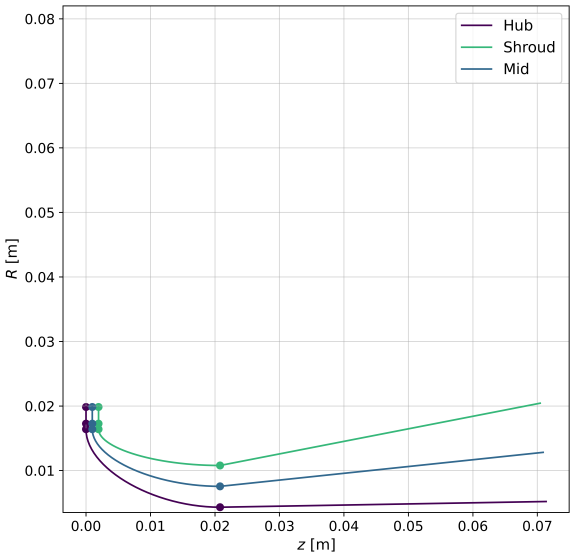

Figure 6.13: Meridional flow path corresponding to the optimal turbine design, for the reverse Byaton cycle based configuration, under Case 1 conditions (with no constraint on RPM).

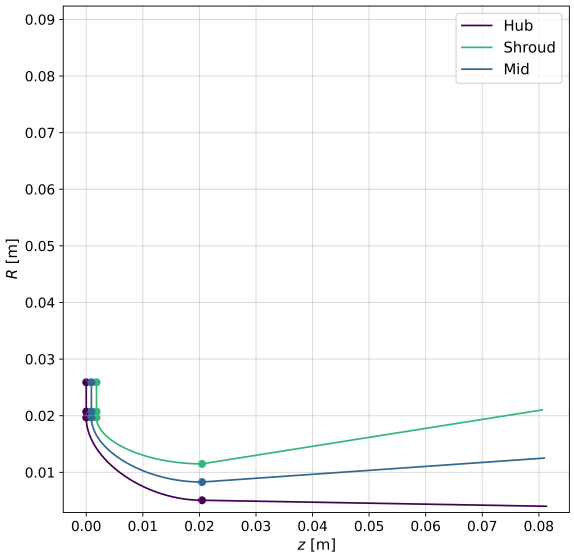

Figure 6.14: Meridional flow path corresponding to the optimal turbine design, for the reverse Byaton cycle based configuration, under Case 1 conditions (with turbine and compressor on the same shaft).

6.3. Case 2 - Spray drying process

This case study considers the use of a heat pump to provide the required thermal input of a spray drying process in a milk production plant. In this case, both the waste thermal energy source and the stream to be heated are moist air, with different values of specific humidity. Therefore, in the thermal source side heat as the moist air is cooled down and the temperature decreases below the dew point, some of the water vapor condenses.

6.3.1. Reverse Rankine cycle based configuration

The model of the two-stage heat pump configuration adopting an internal heat exchanger and vapor injection had to be modified. Mainly because, the evaporation and condensation temperature must be selected based on the process stream conditions and the assumed minimum temperature differences

in the heat exchangers. The modified heat pump system model is shown in Figure 6.15 and the values used to make the system of equations well-posed are listed in Table 6.18. The degrees of freedom associated with the design of the heat pump are highlighted in red in this table, following the nomenclature discussed earlier in Section 3.4. To simplify the analysis, the value of P_{frac} was taken equal to 1, to fix P_{intm}.

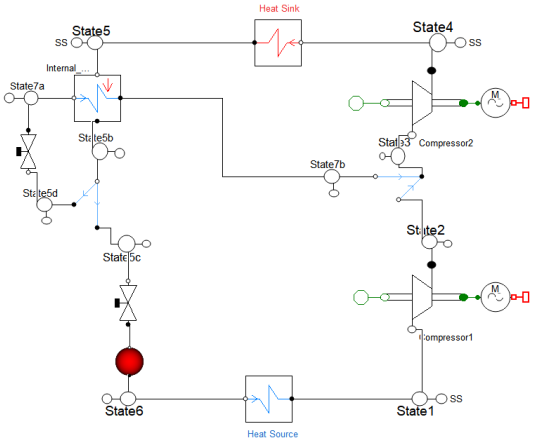

Figure 6.15: Schematic of the two-stage heat pump adopting an internal heat exchanger and vapor injection, selected for Case 2.

Table 6.18: Additional equations to close the mathematical model of the heat pump.

State/Components	Imposed Constraints
1	$x = 1, T = T_1$
1b	$T_{1b} = T_1 + \Delta T_{suph}$
2	$p_2 = p_{intm}$
3	$T_3 = T_{7b} + \Delta T_{suph}$
4	None
4b	$x = 1, T_{4b}$
4c	$x = 0$
5	$T_5 = T_{4c} - \Delta T_{subc}$
5b	$T_{5b} = T_{7b} + \Delta T$
6	$X = X_{ref}$
7b	$p_{7b} = p_{intm}$
Compressor	$\eta_{is,c}$, η_m , η_{motor}

To understand the requirements of the process, an exemplary temperature-heat diagram is shown in Figure 6.16 for this process, where the x-axis represents the transferred thermal energy and the y-axis represents the temperature level. Concerning the condensation temperature (T_{4b} or T_{cond}), the value of ΔT_{min} is the governing factor, along with the process stream requirements. In the sink, the pinch point occurs in correspondence of the starting of steam condensation. Using the information about the pinch point location, the minimum required condensation temperature can be calculated based on simple energy balances over the desuperheater and the condenser. Notably, it results that the expression for the condensing temperature reads as shown in Equation (6.1).

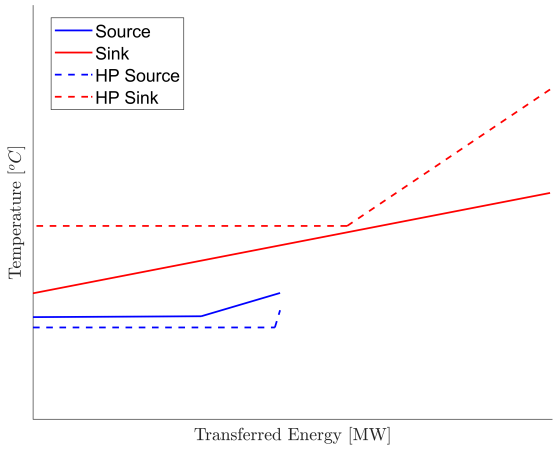

Figure 6.16: An exemplary Temperature-heat diagram for a reverse Rankine cycle-based heat pump when integrated with process of Case 2.

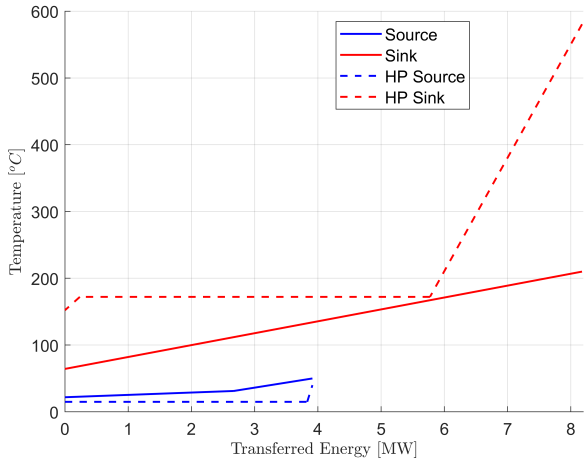

Figure 6.17: Temperature-heat diagram corresponding to optimized thermodynamic cycle found for the reverse Rankine cycle based heat pump integration when integrated with the process of Case 2.

$$T' = T_{\text{sink, out}} - \left(\frac{\left(T_{\text{sink, out}} - T_{\text{sink, in}}\right)}{\dot{Q}_{\text{sink}}} \cdot \dot{Q}_{\text{desup}}\right)$$
$$T_{\text{cond}} = T' + \Delta T_{\text{min}} \tag{6.1}$$

A similar procedure cannot be followed to determine the evaporation temperature, as the thermal source capacity is not given and the outlet temperature for waste heat stream is also not specified. Selecting a high evaporation temperature is desired, as it would decrease the required pressure ratio. However, this can lead to an infeasible outlet temperature of the source stream. For example, selecting the highest possible evaporation temperature ($T_{\text{source, in}}$ - ΔT_{min}) of 42.5 °C, the thermal power recovered from the thermal source of the heat pump is around 4.3 MW. To achieve this value, the moist air which represents source stream needs to be cooled to around 15 °C, which is infeasible. An example of a possible feasible solution is shown in Figure 6.17, where the evaporation temperature is 15 ° and the degree of superheating is set as 25 °C at the inlet of the first compressor and 10 °C at the inlet of the second compressor, along with degree of subcooling as 20 °C. For this set of thermodynamic cycle parameters, the required total pressure ratio is around 490, which is infeasible for a two-stage heat pump system (considering a maximum of two stages per compressor). As can be observed from the figure, there is a mismatch between the the temperature profile of two streams at the sink side, which results in higher irreversibilities thus lowering the overall thermodynamic performance.

Considering the obtained preliminary results, it was concluded that the reverse Rankine cycle based heat pump is not suited to this process. The temperature of the waste thermal energy source is too low, leading to very low saturation pressure values. This, combined with the high condenser pressure, results in a very high pressure ratio.

6.3.2. Reverse Brayton cycle based configuration

Also for the single-stage heat pump configuration with internal recuperation, a different model setup was used with respect to what documented in Chapter 5. Notably, P_{low} along with β_{total} (pressure ratio of the cycle) and the turbine outlet temperature (T_6) were selected as the degrees of freedom of the design of the thermodynamic cycle. This is also similar to the model setup used in the literature for a similar test case [26].

Before optimizing the thermodynamic cycle, the effect of each degree of freedom on the $\mathrm{COP_h}$ was investigated. Figure 6.18 shows the effect of β_{total} and P_{low} on the heat pump $\mathrm{COP_h}$, the temperature of the working fluid at the outlet of the thermal source (T_1) and at the outlet of the thermal sink (T_4). In these figures, the limiting values of these temperatures are also indicated. For T_1, this temperature must be lower than the source inlet temperature (by at least ΔT_{min}), whereas, for T_4, this temperature must be higher than the sink stream outlet temperature (by at least ΔT_{min}). As can be observed from the figure, the limiting value for β_{total}, for a fixed P_{low}, is governed by T_1. Therefore, the maximum feasible $\mathrm{COP_h}$ is also dictated by this limit. Also, with an increase in P_{low}, the maximum feasible β_{total} decreases.

Figure 6.19 shows the effect of the minimum temperature of the cycle (T_6) on $\mathrm{COP_h}$ and T_1, for different β_{total} values. In this case, the value of T_1 is again found to be the parameter limiting the performance of the cycle. For a given T_6, the maximum allowed value of β_{total} depends on T_1. Based on this information, the optimization was carried out to maximize the $\mathrm{COP_h}$ while enforcing the assumed ΔT_{min} in all the heat exchangers.

The optimization was carried out using the NSGA-II algorithm, of the *Pymoo* library, a *Python* optimization library. For each design variable, ten individuals were selected for the initial population. Therefore, a total of 30 evaluations were performed per generation. Table 6.19 shows the optimized heat pump parameters and Table 6.20 shows the corresponding main heat pump characteristics.

The obtained temperature-heat diagram for this heat pump configuration is shown in Figure 6.20. The smaller mismatch between the temperature profiles of the cold and hot streams for both the heat exchangers, implies lower irreversibilities associated with the heat transfer. No compressor design was performed for this configuration since a comparison with the compressors of the reverse Rankine cycle-based heat pump was infeasible for this case. Nevertheless, observing the design requirements for the compressor (based on Table 6.19), it is expected that a feasible compressor design for this configuration can be obtained using a single-stage compressor.

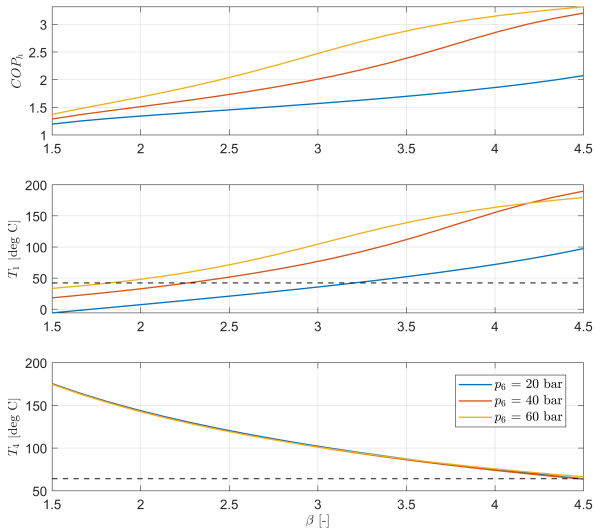

Figure 6.18: Effect of β_{total} and P_{low} on COP_h, T_1 and T_4 of the single-stage configuration with internal recuperation, under case 2 conditions.

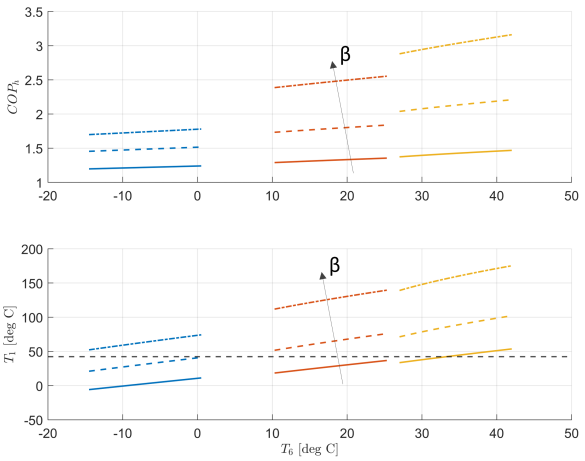

Figure 6.19: Effect of β_{total} and T_{min} on the COP_h and T_1 of the single-stage configuration with internal recuperation, under case 2 conditions.

Table 6.19: Optimal values of the design parameters obtained for the single-stage heat pump configuration with internal recuperation, for Case 2.

Cycle Parameter	Value	Units
P_{low}	30.5	bar
T_6	−4.94	°C
β_{total}	2.69	-

Table 6.20: Case 2 - Main characteristics of the optimized single-stage heat pump configuration with internal recuperation.

Variable	Value	Units
COP_h	1.66	-
Q_{source}	3.68	MW
$\dot{m}$	65.9	kg/s

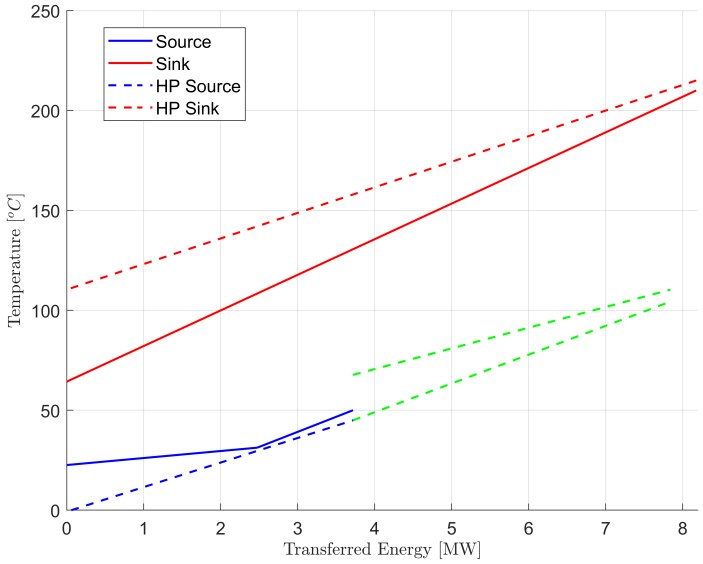

Figure 6.20: Temperature-heat diagram corresponding to optimal cycle parameters found for the reverse Brayton cycle-based heat pump when integrated with the process of Case 2.

6.4. Case 3 - Alumina production

6.4.1. Reverse Rankine cycle based configuration

For this case, the model setup of the two-stage heat pump configuration with an internal heat exchanger and vapor injection is similar to the one presented for Case 2 in Figure 6.15 and Table 6.18. Firstly, the effect of P_{frac} was analyzed. Figure 6.21 shows the variation of the COP_h and maximum temperature of the cycle (T_{max}) with P_{frac} and for different evaporation temperatures (T_{eva}). The highest COP_h is found at very low values of P_{frac}. However, for this re-partition of the pressure ratio between the two compressors, T_{max} value becomes greater than 600 °C, which is not desired given the costs and the technical complexity of systems operating at such high temperature levels. Therefore, it was decided to assume the P_{frac} equal to 1.0, as it will also help to reduce the compressor design complexity.

The condensation temperature is calculated as in Case 2, using Equation (6.1). The only difference is that, in this case, the mass flow rate of the stream to be heated is not provided; instead, the thermal power to be delivered to the sink is given. So the same method can be followed. For the selection of T_{eva}, again a trade-off between the process requirements and the required pressure ratio (β_{total}) needs to be found. The minimum value for the source outlet temperature is provided in this case (= 60°C). Considering this maximum value as the target for the cycle design, T_{eva} is then 52.5 °C (60°C - ΔT_{min}). Using this value of T_{eva}, combined with a degree of superheating 10 ° at the inlet of two compressors, respectively, and a subcooling of 20 °, the required β_{total} is around 250, which is infeasible, assuming a twin stage configuration for both the compressors.

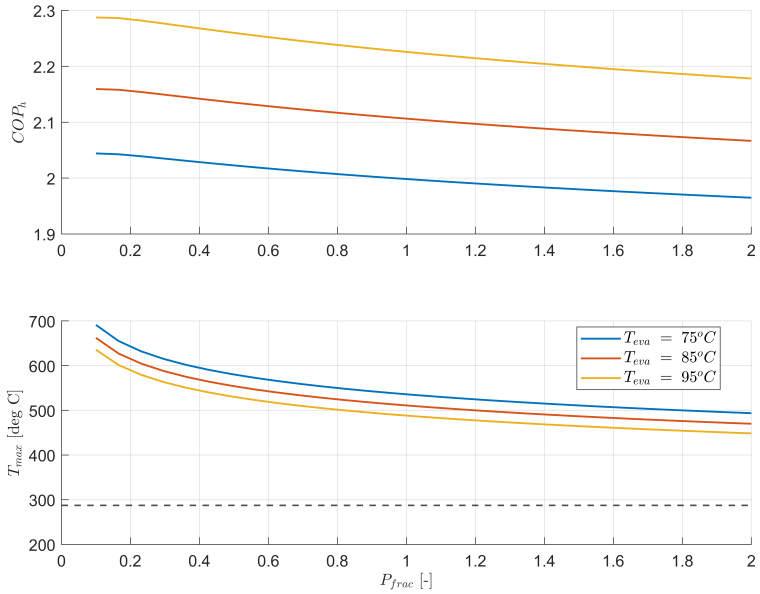

Figure 6.21: Effect of P_{frac} and T_{evap} on cycle characteristics of two-stage configuration adopting an internal heat exchanger and vapor injection, under Case 3 conditions.

To find a feasible solution, it is assumed that the stream representing the thermal energy source of the heat pump is cooled to a higher temperature. However, this choice can lead to a lower thermal power recuperated by the heat pump and then a lower power delivered to the sink. Since no information about the waste heat stream is given, it is assumed that the required thermal power at the sink can be met by adjusting the waste thermal energy stream mass flow rate. Using this approach, a feasible solution is found using T_{eva} of 85 °, with a degree of superheating of 11 ° the inlet of both compressors and 20 ° subcooling. The temperature-heat diagram for this scenario is shown in Figure 6.22.

As can be observed from Figure 6.22, there is a large mismatch between the temperature profile of the two streams in the heat exchanger corresponding to the thermal sink, which implies higher irreversibilities associated with heat transfer and thus a lower thermodynamic performance. Table 6.21

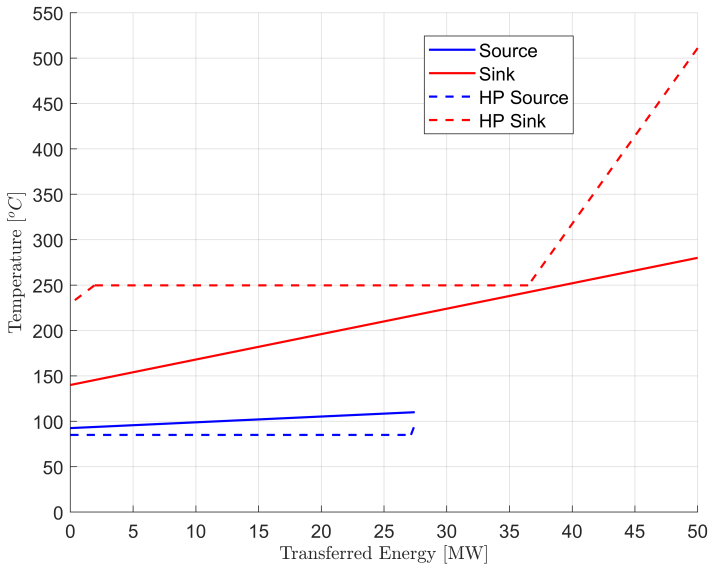

Figure 6.22: Temperature-heat diagram corresponding to the optimized cycle of the reverse Rankine cycle based heat pump when integrated with the process of Case 3.

provides the main characteristics for this heat pump configuration, using the temperature values mentioned above. Due to the large thermal power delivered to the sink, the required mass flow rate of the working fluid is higher compared to previous case studies. The corresponding design requirements of both compressors are shown in Table 6.22.

Table 6.21: Case 3 - Main characteristics at the design point of the two-stage configuration adopting an internal heat exchanger and vapor injection.

Variable	Value	Units
$\mathrm{COP_h}$	2.11	-
Q_{source}	27.45	MW
β_{total}	68.35	-
P_{frac}	1.0	-
$\dot{m}_{\text{comp 1}}$	13.68	kg/s
$\dot{m}_{\text{comp 2}}$	20.14	kg/s

Table 6.22: Case 3 - compressor design requirements for the two-stage configuration adopting an internal heat exchanger and vapor injection.

Variable	Compressor 1	Compressor 2
$P_{t,in}$	0.579 bar	4.78 bar
$T_{t,in}$	96 °C	161.2^oC
β_{total}	8.27	8.27
$\dot{m}$	13.68 kg/s	20.14 kg/s

As a next step, the preliminary design of both the compressors was performed. The adopted methodology is similar to the one discussed earlier for case 1. However, the designs obtained for both the compressors showed numerical issues related with some of the loss models used in *TurboSim*, as this design tool is not validated for this scale of machines. Due to this reason, the results related to the design of the two compressors are not shown here. During the Project, the *TurboSim* was repeatedly updated, as a result of which some of these observed issues have been resolved. However, given the planned project timeline, it was not possible to re-run the optimizations for this case as the associated computational time is very high.

6.4.2. Reverse Brayton cycle based configuration

The model setup for this test case was similar to the one described for case 2. Similarly, the heat pump parameters were optimized to maximize the COP, while ensuring the prescribed ΔT_{min} in all the heat exchangers. Table 6.23 shows the values of the optimized variables and Table 6.24 shows the corresponding main characteristics of the heat pump.

Table 6.23: Optimized cycle parameters for the single stage configuration with internal recuperation, under Case 3 conditions.

Cycle Parameter	Value	Units
P_{low}	60	bar
T_6	31.15	°C
β_{total}	3.35	-

Table 6.24: Main characteristics of the optimized single-stage configuration with internal recuperation, under Case 3 conditions.

Variable	Value	Units
COP_h	1.97	-
Q_{source}	26.95	MW
$\dot{m}$	259	kg/s
$T_{\text{t, comp in}}$	123.4	°C
$T_{\text{t, turb in}}$	140	°C

As for the case of the reverse Rankine cycle based heat pump configuration, the required mass flow rate is much higher due to larger sink capacity. The value of COP_h obtained for this heat pump configuration is lower than that obtained for the H_2O heat pump. However, this heat pump configuration allows the waste thermal energy source to be cooled to its required temperature, and no assumptions are needed with respect to the mass flow rate of this stream. Therefore, the comparison between the two configurations is inconsistent for this case because, for the case of reverse Rankine cycle-based heat pump configuration, it is assumed that a temperature drop of around 20 °C is compatible with the required thermal power at the sink, whereas, for this heat pump configuration, the same thermal power at the sink is obtained with a temperature drop of 50 °C. The obtained temperature-heat diagram for this heat pump configuration is shown in Figure 6.23. The temperature profile of the two streams in the heat exchanger representing the thermal sink show a good match for this case, and the pinch point occurs at the high-temperature side of the thermal source. This implies that the outlet temperature of the waste heat stream could be further reduced without any negative impact on the heat pump thermodynamic performance.

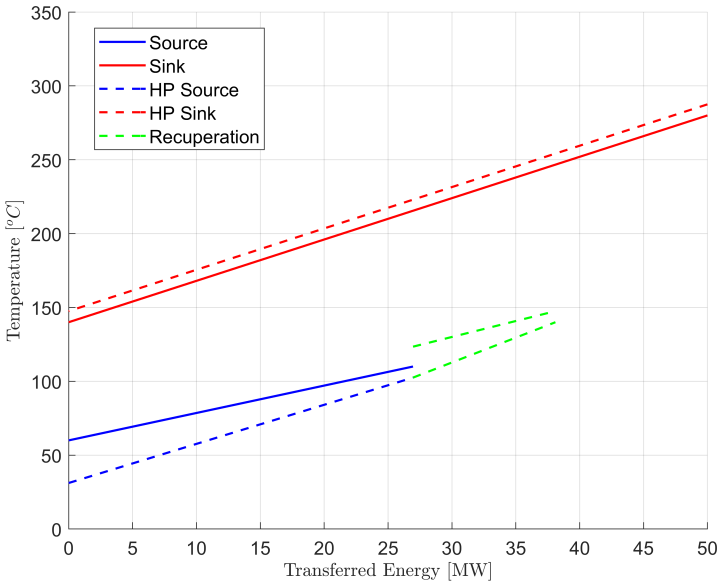

Figure 6.23: Temperature-heat diagram corresponding to the optimized cycle parameters found for the reverse Brayton cycle based heat pump integration under Case 3 conditions.

Regarding the preliminary design of the compressor, Table 6.25 shows the constraints considered in the optimization.Table 6.26 shows the corresponding results.

Table 6.25: Constraints values selected for the design of the compressor of Case 3 for the single stage configuration with internal recuperation.

Constraint Variable	Type of Constraint	Value
β_2	Maximum Value	-10^o
U_2	Maximum Value	550 m/s
RPM	Maximum Value	100e3
W_{el}	Maximum Value	40 MW
AR	Minimum Value	0.24
AR	Maximum Value	1.5
M_4	Maximum Value	0.7
Choke Margin	Minimum Value	1.05
$\Delta\beta_{total}$	Maximum Value	5 %

Table 6.26: Compressor design optimization results for the single stage configuration with internal recuperation, under conditions of Case 3

Parameter	Value
Number of function evaluations	6000
Number of generations	75
Number of Logical Processors Used	4
Total Time Taken [hr]	19.97
Average Time per Generation [min]	16

The convergence of the optimization algorithm is also documented in Appendix D. Figure 6.24 shows the obtained Pareto front for the compressor design. 48 non-dominated design solutions were obtained as a result of the optimization. The chosen solution represents a trade-off between the operating range and the total-to-total efficiency of the machine. Table 6.27 shows the main characteristics of the selected solution. The value of β_2 is very close to the limit value. At the same time, the swallowing capacity and the working coefficient values are close to their upper limit.

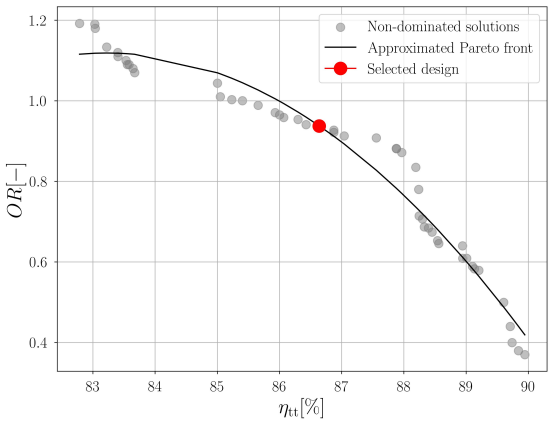

Figure 6.24: Pareto front obtained for the design of compressor of the reverse Brayton cycle based configuration, under Case 3 conditions.

Table 6.27: Design variables corresponding to the selected optimal design for the compressor of the reverse Brayton cycle based configuration, under Case 3 conditions.

Variable	Value
$\beta_{\text{tt, target}}$	3.35
kRPM	15
ϕ_{t1}	0.033
$\psi_{\text{is}} - \psi$	$0.85 - 0.69$
α_2	70.1^o
k	0.965
$N_{\text{bl}} - N_{\text{split}}$	$12 - 0$
R_3/R_2	1.7
$R_{\text{r,pinch}}$	0.34
$H_{\text{r,pinch}}$	0.58

Figure 6.25 shows the meridional channel of the compressor. The axial and radial dimensions are lower than those of the H_2O compressors, despite the higher mass flow rate. This is because the volumetric flow rate is lower due to the higher density of CO_2. At the design point, diffuser losses were found to be the highest, followed by friction and clearance losses. Due to the large scale of the machine, the leakage and recirculation losses become small as the relative clearance values decrease. For this compressor design, the design point RPM value was found to be 15E+03 (Table 6.27), while the η_{tt} for the whole machine is around 89.3 %, and the required power is about 28.3 MW.

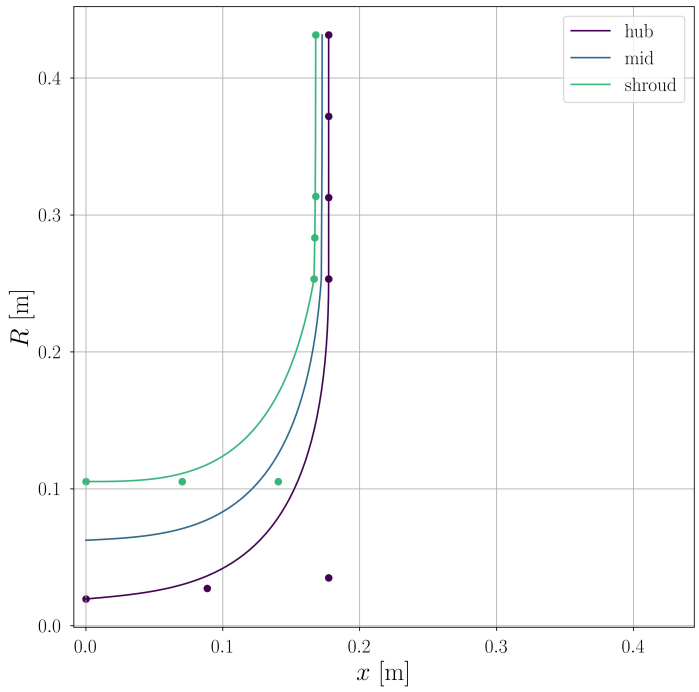

Figure 6.25: Meridional flow path obtained for the optimized compressor design of the reverse Byaton cycle based configuration, under Case 3 conditions.

Figure 6.26a and Figure 6.26b shows the operating maps for the total pressure ratio (β_{tt}) and total-to-total efficiency (η_{tt}), obtained for the selected optimal solution. Contrary to the case of the H_2O compressors, no numerical errors were observed for any of the speed lines.

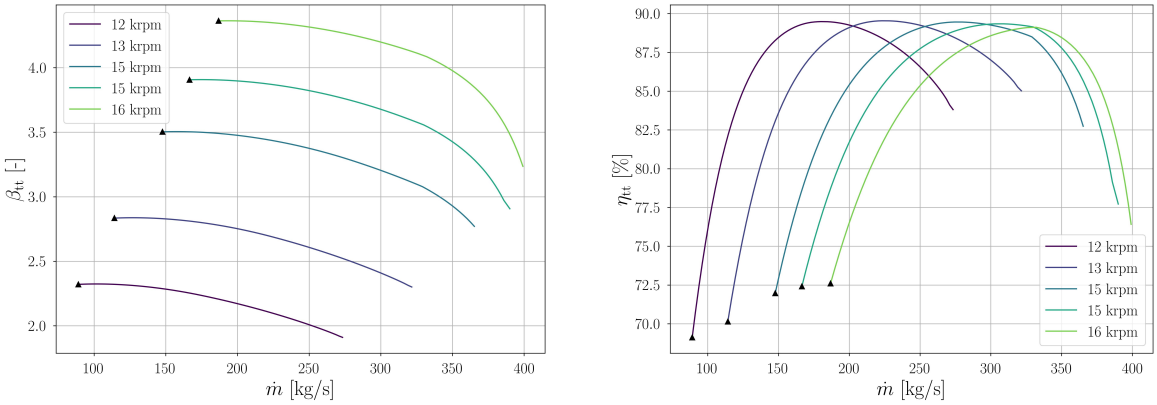

(a) β_{tt} vs $\dot{m}$ **(b)** η_{tt} vs $\dot{m}$

Figure 6.26: Operating maps obtained for the optimized compressor design of the reverse Byaton cycle based configuration, under Case 3 conditions.

For the obtained conceptual design of CO_2 compressor, the feasibility of the required electric motor design was also investigated, using a similar approach as for Case 1. Figure 6.27 shows the design point obtained for this test case, superimposed on the electric motor design maps obtained from literature [111]. The required electric motor characteristics are in the feasible design region and fall in the category of the machines typically found in oil and gas industries.

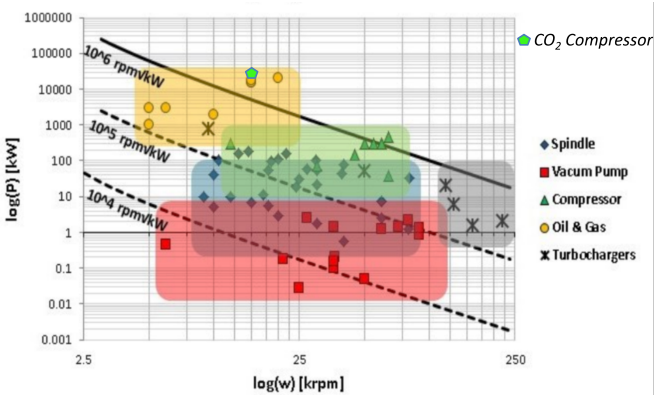

Figure 6.27: Electric motor requirements of the CO_2 compressor of Case 3, superimposed on the feasibility limits of electric motors obtained from literature [111].

A conceptual design of the turbine was also obtained for this case. As for Case 1, only duty coefficients were optimized, while the remaining geometrical parameters were selected based on reference designs presented in literature [114]. Table 6.28 shows the main results of the preliminary design of the turbine, based on the specifications in Table 6.23 and Table 6.24. The geometrical parameters used for this case are similar to that of the turbine of Case 1 and are listed in Appendix D.

The meridional channel resulting from the preliminary design is shown in Figure 6.28. As for the compressor, large dimensions (> 0.1 m) are also obtained for the turbine due to the high mass flow rate of this application.

Table 6.28: Design variables corresponding to the optimized turbine design of the reverse Brayton cycle based configuration, under Case 3 conditions

Variable	Value	Units
β_{tt}	3.37	-
η_{tt}	0.835	-
kRPM	10.3	-
W_{out}	12.3	MW
ϕ_2	0.237	-
ψ	0.7191	-
χ	0.59	-
α_2	72	°
β_3	-52.7	°
N_{rotor}	11	-
N_{stator}	8	-

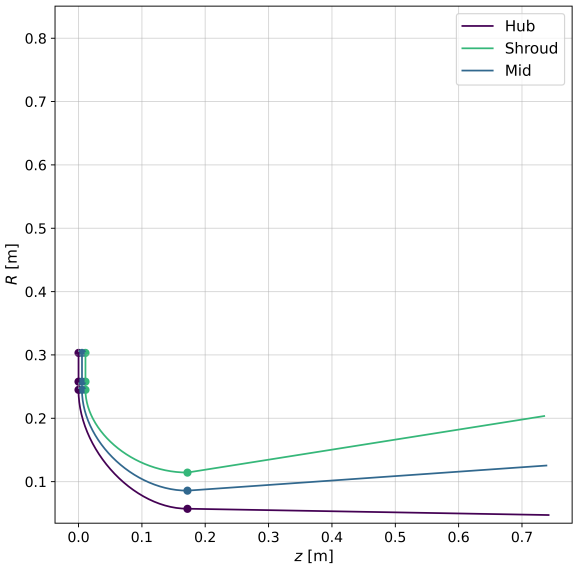

Figure 6.28: Meridional flow path obtained for the optimized turbine design, for the reverse Byaton cycle based configuration, under Case 3 conditions.

7

Discussion

7.1. Characteristics of the heat pump based on the reverse Rankine and Brayton cycle

The first phase of the project was focused on the thermodynamic cycle analysis of different heat pump configurations based on the reverse Rankine cycle and the reverse Brayton cycle. For all the T_{sink} values considered, using a similar modeling setup for both the heat pump types, the reverse Rankine cycle based heat pump configurations (assuming no superheating and subcooling) outperformed those based on the CO_2 reverse Brayton cycle in terms of maximum COP_h. For a T_{sink} of 200°C, with T_{source} at 100°C, the relative decrease in maximum COP_h for the CO_2 reverse Brayton cycle based configurations was found to be around 30 %. When considering air as working fluid, this difference was even higher (around 40 %). The reverse Brayton cycle based heat pump configurations showed lower COP_h because of higher compressor outlet temperatures. In reality, such high temperature levels are not required if the stream to be heat does not undergo a phase change. Therefore, higher COP_h values were obtained for the reverse Brayton cycle based heat pump configurations when considering the sensible heat sink model setup. In this scenario, the difference in the maximum COP_h was reduced to about 2 % for T_{sink} of 200°C. Whereas, fora T_{sink} of 150 and 250°C, a higher COP_h value was obtained for the reverse Brayton cycle based heat pump configurations, using ΔT_{sink} of 100 and 150°C respectively. The increase in COP_h was found to be around 7 % and 11 % for the two temperature levels, respectively. Thus, for the cases involving a high-temperature heat source and high-temperature lift at the sink side (ΔT_{sink} > 100°C), the CO_2 reverse Brayton cycle based heat pump can provide higher thermodynamic performance as compared to the H_2O reverse Rankine cycle based heat pump. Under this sensible sink scenario, improvements in COP_h values were also found when using air as the working fluid. However, the increase was smaller than the one observed for CO_2. This is because of the inherent characteristics of the working fluid. For the case of air, by decreasing the compressor outlet temperature, the magnitude of the decrease in the available sink capacity dominates with respect to the decrease in the compressor work. Therefore, the COP increase is lower.

The two heat pumps concepts imply also different component design requirements. As the value of T_{sink} increases, the increase in the required pressure ratio for the H_2O reverse Rankine cycle based heat pump is higher than that for the reverse Rankine cycle based system. Therefore, for a H_2O reverse Rankine cycle based heat pump system, at high-temperature lift values, more compression stages would be needed to maintain the peripheral speed with the acceptable limits. For the case of the CO_2 reverse Brayton cycle based heat pump, competitive COP_h values are only obtained at high operating pressure values (> 60 bar). Such high-pressure values impose additional constraints on the mechanical design of the individual components. For example, thicker walls need to be considered to contain the high-pressure working fluid. However, high operating pressures can also bring some advantages. For example, a higher value of velocity can be considered in the heat exchangers because, at high-pressure

values, the acceptable limits for the pressure drop become higher for the case of CO_2 [44].

7.2. Process Integration

In the initial thermodynamic cycle analysis, no superheating was considered for the reverse Rankine cycle systems. However, when performing the conceptual design of the compressors for case study 1, a certain degree of superheating (11°C) was found as necessary to prevent the condensation of the vapour at the inlet for the impeller. As a result of this additional superheating, the value of COP_h decreased to a value lower than that calculated for the reverse Brayton cycle system. This indicates that the best configuration for a high-temperature heat pump system is process-dependent, and the process parameters must be included in the model to make an accurate comparison. For both case studies 2 and 3, higher COP_h values were obtained for the reverse Rankine cycle based heat pump. However, the required pressure ratio for the H_2O heat pump was very high compared to that of CO_2 reverse Brayton cycle systems, to the point that the design of the two compressors becomes infeasible (considering a twin stage arrangement for both the compressors). Therefore, despite the high COP_h, the reverse Rankine cycle based heat pump does not arguably represent a valid technological option for processes requiring a combination of low source temperatures, i.e., less than 70°C and T_{sink} higher than 200°C.

In both the selected case studies the stream being heated undergo a large temperature increase. In such a scenario, the reverse Brayton cycle based system always guarantees in the heat exchanger representing the thermal sink of the heat pump a better match between the temperature profiles of the working fluid and the process stream. On the contrary, in the case of the reverse Rankine cycle based heat pump, the temperature-heat diagrams for case 2 and case 3 show that the heat transfer between the process stream and steam occurs under a large temperature difference, which entail higher thermodynamic losses and a lower overall thermodynamic performance. Reverse Rankine cycle based systems would achieve a better thermodynamic performance in those processes involving steam generation. Therefore, both the reverse Brayton and the reverse Rankine cycles are valid options to supply the thermal energy requested by different industrial sectors, depending on the specific process type. The temperature-heat diagrams obtained for the reverse Brayton cycle based heat pump also showed that the heat transfer between CO_2 and the process streams representing either the source or sink of the heat pump is still affected by significant differences in the thermal capacities of the involved fluids (in both cases 1 and 2) though, the temperature differences between the process streams and CO_2 are definitively smaller than in the reverse Rankine cycle based heat pump. This is because the process data used for the case studies have been optimized considering only the process requirements. Thus, to increase the overall effectiveness of the heat pump integration, the process parameters also need to be reevaluated, as they are based on conventional design practice where the energy supply is provided by the combustion of fossil fuels. The minimum required pinch point temperature difference is an example of such a process parameter.

The feasibility of the electric motors was also qualitatively assessed for the cases where the preliminary design of the compressors was performed . For both the low (1 MW) and high (50 MW) thermal capacity heat pumps, the motor characteristics required for the H_2O compressors were found to be unconventional except for compressor 1 of the reverse Rankine cycle based 1 MW heat pump. Nevertheless, given the recent ongoing developments in the design of high-speed and high-power electric motors [112] and considering the required combination of nominal power/rotational speed existing machines, the electric motors are not expected to be a hard limitation for the feasibility of steam high-temperature heat pumps. However, they require technological developments. A similar consideration applies to the CO_2 compressor of the 1MW heat pump, especially if the turbine and compressor are mounted on the same shaft, a solution which lowers the required power of the electric motor making its design requirements similar to those of commercially available machines. For the case of the large capacity heat pump, the required motor characteristics were found to be similar to the machines typically found in oil and gas industries. Therefore, the electrical motor design is not limiting for CO_2 reverse Brayton cycle based system for large capacities.

7.3. Uncertainties in Turbomachinery Design

The preliminary design of the turbomachines of all the case studies was performed using a methodology based on scaling analysis. As mentioned earlier, the program used in this work was *TurboSim*, a tool developed by the propulsion and power group for the preliminary design of radial machines which has been verified and validated against experimental data. However, given the type of applications considered in this project, it is possible to identify three primary sources of uncertainties associated with the preliminary design of compressors.

The first source of uncertainty concerns the semi-empirical models used to predict the losses and the stall/surge limits. The validation of the code has been performed against a very different application with smaller pressure ratios and smaller capacities (around 50-100 kW). As a result, the selected parameters of the different correlations may be inaccurate for the current case. A suitable test case, representative of the conditions simulated in this project, needs to be selected to quantify this uncertainty.

The second source of uncertainty is related to the simplifications in the compressor model adopted to reduce the computational cost of the design optimization. In the “optimization” mode, only the design speed line is considered to estimate the operating range of the compressor.

The final source of uncertainty is related to working fluid modeling. The program uses the thermodynamic library developed by NIST to estimate the thermodynamic properties of the working fluid, as also the system models of the heat pump. The working fluid properties obtained using this program are intrinsically affected by uncertainties as the equation of state of a fluid always entails a certain level of approximation. Nevertheless, the equations of state for $\mathrm{CO_2}$ and especially $\mathrm{H_2O}$ implemented in the thermodynamic library are characterized by a high level of accuracy as they represent the industrial standard for these fluids.

For the preliminary design of the turbine, similar considerations do apply. An additional source of uncertainty in this case concerns the design of the diffuser. In the current project, the values chosen for the design parameters of the diffuser were selected based on general guidelines presented in the literature for minimizing the losses in supercritical $\mathrm{CO_2}$ diffusers [116][117]. Commonly the design of the diffuser strongly depends on space limitations specific of the application. Nevertheless, the obtained geometry does not differ significantly from other designs reported in the literature for similar conditions [114][115]. Regarding turbine design optimization, only the duty coefficients were optimized, which implies that the explored design space is limited. Therefore, the geometry obtained in this project represents only an initial estimate for the optimal design of the diffuser.

8

Conclusions and Recommendations

8.1. Conclusions

This thesis focused on investigating the thermodynamic performance and feasibility of high-temperature heat pump systems based on the reverse Rankine cycle and the reverse Brayton cycle. Several different configurations were selected for both the reverse Rankine cycle and the Brayton cycle based systems based on previous works in the literature. The effect of individual design parameters on the heat pump thermodynamic characteristics was analyzed for each of the selected configurations. Once the optimal heat pump configuration for both heat pump concepts was obtained, three case studies were conducted to analyze the practical implications of the integration of the two technologies in industrial processes and the design specifications of turbomachinery components of such heat pump systems. These selected case studies represent exemplary industrial applications identified from the literature which, however, are representative of the expected market for high-temperature heat pumps.

The conclusions obtained for each of the research questions, based on the performed investigations, are given as follows:

> "What are the effects of the cycle parameters and working fluid choice on the thermodynamic performance of reverse Brayton cycle and reverse Rankine cycle based high-temperature heat pump systems, for a given temperature lift/industrial process?"

To answer this question, a steady-state 0D modeling approach was followed. Three different values of temperature lifts were considered 50°, 100°, and 150°C, with a fixed source temperature of 100°C. For reverse Rankine cycle based configurations (using H_2O), the pressure ratio split between the two compression stages (for two-stage configurations) was identified as the only design parameter. The optimal value of this parameter was found to be in the range of 1 to 1.3, depending on specific configuration and temperature lift value. Two-stage heat pump configuration using a saturator was found to have the highest thermodynamic performance at all temperature lift values. For all the reverse Brayton cycle based heat pump configurations, when using CO_2 as the working fluid, maximum COP_h was found only near the critical region of the state diagram. Within reverse Brayton cycle based heat pump systems, a single-stage heat pump configuration with a recuperator was found to have the highest thermodynamic performance at all temperature lift values, except for the lowest temperature lift value. Because at low temperature lift values, the maximum temperature drop in the sink heat exchanger is limited by the minimum temperature required for feasible recuperation. High values of minimum pressure in the cycle (> 60 bar) and high values of temperature drop in the sink heat exchanger (> 100 °C) were found to be required conditions for the reverse Brayton cycle based heat pump to have COP_h similar or higher than the reverse Rankine cycle based heat pump. When using air as a working fluid, the COP_h values

obtained were lower than the CO_2, with relative differences in maximum COP_h ranging from 27 % to 48 %, depending on the temperature lift value.

> "What are the technological challenges associated with the development of reverse Rankine cycle and reverse Brayton cycle based heat pumps and with their integration in an actual industrial process?"

To obtain the preliminary design of the turbomachinery components required for the different heat pump systems, a design method based on scaling law was used, where semi-empirical models were used for the estimation of loss and operating range of the machines. Concerning the design of the steam compressors, it was concluded that for the values of backsweep angle, maximum peripheral speed, and rotational speed are the critical constraints limiting the feasible design range. For the case of CO_2 compressors, due to the lower speed of sound of this fluid with respect to steam, the limit on the maximum peripheral speed was not found to be critical. With respect to the optimization routine, due to the non linearity of the design problem and the number of design variables (16 for a twin-stage configuration), the evolutionary algorithm (NSGA-II) was selected for the compressor design optimizations. In contrast, a gradient-based algorithm ($\mathrm{Nelder-Mead}$ method) was found to be sufficient for the turbine design optimization since only duty coefficients were optimized.

For all the case studies, both the reverse Brayton cycle and Rankine cycle based heat pump showed comparable values for COP_h. For cases 2 and 3, that refer to specific industrial applications, the COP_h value was found to be higher for the reverse Rankine cycle based heat pump. However, due to the low temperature of the available waste thermal energy source, the required pressure ratio for the reverse Rankine cycle became very high (>200). Thus, for case 2, the reverse Rankine cycle based heat pump was concluded to be infeasible, whereas for case 3, a feasible solution was possible after making some assumptions about the thermal capacity of the waste heat stream (required pressure ratio of 68.4). In terms of component design, for the low capacity heat pump (case 1, 1 MW), feasible turbomachinery designs were obtained for both heat pump concepts, but the design requirements of the electric motor too demanding with respect to what is achieved by electric machines presently commercially available. For the large thermal capacity case (case 3, 50 MW), the required speed and power of the electric motor of the CO_2 heat pump fell in the typical range of characteristics of machines for the oil and gas industry. The results obtained from the performed case studies indicate that the process heating supply up to 250 °C, with a capacity less than 10 MW, is technically feasible, based on existing technologies and ongoing research developments. Therefore, this demonstrates the high potential for these heat pump systems to cover large proportions of process heating demands.

The comparison between the reverse Rankine cycle and the Brayton cycle based heat pump, revealed that both solutions are promising technologies for decarbonizing the industrial process heating supply. Nevertheless, the best solution is case dependent. The reverse Brayton cycle based heat pump offers a relatively simpler construction complexity due to the single-stage configuration and is suitable for high-temperature requirements (>200 °C). However, its COP_h value was found to be smaller than that of the reverse Rankine cycle based heat pump (except for Case 1). On the other hand, despite the higher COP_h value, the reverse Rankine cycle based heat pump was found to be infeasible where the available source temperatures are low (< 70°C) and the required condensation temperatures are higher than 200 °C, as in Case 2 and 3.

8.2. Recommendations

With respect to future research, two main directions have been identified: the first is related to the modeling methodology, including the turbomachinery design methods, while the second is related to the additional aspects to be investigated to demonstrate further the potential of heat pump systems in the decarbonization of industrial process heating supply. The following subsections provide details about both research directions in the form of research actions.

8.2.1. Modeling Methodology

- ***Pinch point temperature difference*:** A constant value of pinch point temperature difference was used for all the different heat exchangers, independently of the operating conditions and the working fluid. This assumption may be inadequate. For example, a smaller temperature difference is usually considered when one of the streams of the heat exchanger has a constant temperature with respect to the case where both the stream undergo a temperature variation, for an approximately equal mean temperature difference.

- ***Validation case for* TurboSim:** The validation tests performed for *TurboSim* considered a very different application (much smaller capacity and temperature levels). As a result, some of the parameters used in the different semi-empirical models might not be valid for the applications considered in this project. Performing a validation test using an application similar to the ones considered in this project will be beneficial in quantifying the uncertainties associated with the obtained design solutions.

- ***Turbine design optimization*:** In the preliminary design of the turbine (for reverse Brayton cycle based system), only non-dimensional duty coefficients were optimized. This limits the extent of the design space explored, as the non-dimensional geometric parameters also affect the performance. Therefore, by including these additional design parameters (non-dimensional geometrical parameters) as optimization variables, an expanded design space can be explored, leading to better-performing designs. However, such an optimization would also have a higher computational cost.

- ***Turbine operating maps*:** Only design point performance was considered while optimizing the turbine design, as the operating map feature was not available in *TurboSim* and the development of such a routine was outside the scope of the project. Nevertheless, implementing a turbine map estimation routine is recommended to gain further insight into the feasible operation range of the heat pump system. This is crucial especially if the coupling of compressor and turbine on the same shaft is considered.

- ***Electric motor consideration*:** The feasibility of the electric motor required to drive the compressors was investigated by comparing the required power and speed of the electric motor with those of commercially available machines. However, the data found was based on studies conducted in 2015/2016. Therefore, to get a better understanding of the design feasibility of the electrical machines, a model-based design approach can be used. The level of complexity of the model can be tailored per the requirements, but such an approach can provide helpful insights into the type of limitations encountered and possible ways to address them.

8.2.2. Demonstrating Heat Pump Potential

- ***Heat pump inclusive process optimization***: The data used for the case studies was derived from the available process information, and thus, the different process parameters, such as minimum approach temperatures, have been defined based on conventional combustion-based systems. For this reason, the heat pump estimated potential would be lower, as the data represents a system layout that is optimized without considering any heat pump system. Therefore, a re-evaluation of process parameters and system layout optimization are recommended to get a more representative value of the industrial potential of the heat pump systems.

- ***Use of Mixtures for reverse Rankine cycle based systems***: The reverse Rankine cycle based system configuration (two-stage with saturator) showed higher performance but very high-pressure ratio requirements especially if the waste heat stream features low temperatures. To further enhance the performance potential of reverse Rankine cycle based systems, a working fluid comprising a mixture of different compounds can be considered. Such a mixture can help increasing the evaporation pressure for low-temperature thermal sources and the composition can be tailored to better match the temperature profiles in the heat exchangers.

- ***Other possible configurations***: The set of configurations selected for the two cycle types in this project only represents a subset of different possible configurations for a potential heat pump system. Therefore, for a specific application, other process-specific configurations may be worth of investigation.
- ***Economic considerations***: All the analyses conducted in this project were limited to the evaluation of the thermodynamic performance of the different heat pump systems for different operating conditions. However, such an analysis is insufficient to demonstrate the potential of the technology among the manufacturers and the industrial users. A preliminary investigation of the economic competitiveness of these systems is thus recommended.

Bibliography

[1] Robert de Boer, Andrew Marina, Benjamin Zühlsdorf, Cordin Arpagaus, Michael Bantle, Veronika Wilk, Brian Elmegaard, José Corberán, and Jessica Benson. Strengthening industrial heat pump innovation: Decarbonizing industrial heat. *High Temperature Heat Pump Symposium*, 2020.

[2] UN Environment. The Emissions Gap Report 2017: A UN Environment Synthesis report. Technical report, 2017. URL https://wedocs.unep.org/bitstream/handle/20.500.11822/22070/EGR_2017.pdf.

[3] Eurostat. Energy database, 2018. URL http://ec.europa.eu/eurostat/web/energy/data/database.

[4] Yoann Jovet, Frédéric Lefèvre, Alexis Laurent, and Marc Clausse. Combined energetic, economic and climate change assessment of heat pumps for industrial waste heat recovery. *Applied Energy*, 313:118854, 2022. doi: https://doi.org/10.1016/j.apenergy.2022.118854.

[5] Matthias Bendig, François Maréchal, and Daniel Favrat. Defining "waste heat" for industrial processes. *Applied Thermal Engineering*, 61(1):134–142, 2013. doi: https://doi.org/10.1016/j.applthermaleng.2013.03.020.

[6] Sarah Brueckner, Laia Miró, Luisa F. Cabeza, Martin Pehnt, and Eberhard Laevemann. Methods to estimate the industrial waste heat potential of regions – a categorization and literature review. *Renewable and Sustainable Energy Reviews*, 38:164–171, 2014. ISSN 1364-0321. doi: https://doi.org/10.1016/j.rser.2014.04.078. URL https://www.sciencedirect.com/science/article/pii/S1364032114003165.

[7] George Kosmadakis. Estimating the potential of industrial (high-temperature) heat pumps for exploiting waste heat in eu industries. *Applied Thermal Engineering*, 156:287–298, 2019. doi: https://doi.org/10.1016/j.applthermaleng.2019.04.082.

[8] Cordin Arpagaus, Frédéric Bless, Michael Uhlmann, Jürg Schiffmann, and Stefan S. Bertsch. High temperature heat pumps: Market overview, state of the art, research status, refrigerants, and application potentials. *Energy*, 152:985–1010, 2018. ISSN 03605442. doi: 10.1016/j.energy.2018.03.166.

[9] Anton Kiss and Carlos Ferreira. *Heat Pumps in Chemical Process Industry*. 09 2016. ISBN 978-1-4987-1895-0. doi: 10.1201/9781315371030.

[10] Europian Commision. Clean energy for all europeans. 2019.

[11] Europian Commision. A clean planet for all. a european long-term strategic vision for a prosperous, modern, competitive and climate neutral economy. 2018.

[12] Clemens Forman, Ibrahim Muritala, Robert Pardemann, and Bernd Meyer. Estimating the global waste heat potential. *Renewable and Sustainable Energy Reviews*, 57:1568–1579, 05 2016. doi: 10.1016/j.rser.2015.12.192.

[13] Stefan Wolf, Jochen Lambauer, Markus Blesl, Ulrich Fahl, and Alfred Voß. Industrial heat pumps in germany: Potentials, technological development and market barriers. In *Proceedings of the ECEEE*, pages 543–550, 2012.

[14] G.P. Hammond and J.B. Norman. Heat recovery opportunities in uk industry. *Applied Energy*, 116:387–397, 2014. ISSN 0306-2619. doi: https://doi.org/10.1016/j.apenergy.2013.11.008. URL https://www.sciencedirect.com/science/article/pii/S030626191300901X.

[15] Martin Pehnt, Jan Bödeker, Marlene Arens, Eberhard Jochem, and Farikha Idrissova. Industrial waste heat–tapping into a neglected efficiency potential. In *Proceedings of ECEEE*, 2011.

[16] Michael Papapetrou, George Kosmadakis, Andrea Cipollina, Umberto La Commare, and Giorgio Micale. Industrial waste heat: Estimation of the technically available resource in the eu per industrial sector, temperature level and country. *Applied Thermal Engineering*, 138:207–216, 2018. ISSN 1359-4311. doi: https://doi.org/10.1016/j.applthermaleng.2018.04.043. URL https://www.sciencedirect.com/science/article/pii/S1359431117347919.

[17] Michael Papapetrou, George Kosmadakis, Andrea Cipollina, Umberto Commare, and Giorgio Micale. Industrial waste heat: Estimation of the technically available resource in the eu per industrial sector, temperature level and country. *Applied Thermal Engineering*, 138, 04 2018. doi: 10.1016/j.applthermaleng.2018.04.043.

[18] A. Marina, S. Spoelstra, H.A. Zondag, and A.K. Wemmers. An estimation of the european industrial heat pump market potential. *Renewable and Sustainable Energy Reviews*, 139: 110545, 2021. ISSN 1364-0321. doi: https://doi.org/10.1016/j.rser.2020.110545. URL https://www.sciencedirect.com/science/article/pii/S1364032120308297.

[19] F. Schlosser, M. Jesper, J. Vogelsang, T.G. Walmsley, C. Arpagaus, and J. Hesselbach. Large-scale heat pumps: Applications, performance, economic feasibility and industrial integration. *Renewable and Sustainable Energy Reviews*, 133:110219, 2020. ISSN 1364-0321. doi: https://doi.org/10.1016/j.rser.2020.110219.

[20] Cordin Arpagaus, Frédéric Bless, Michael Uhlmann, Jürg Schiffmann, and Stefan Bertsch. High temperature heat pumps: Market overview, state of the art, research status, refrigerants, and application potentials. 08 2018.

[21] Dennis van de Bor and C. Ferreira. Quick selection of industrial heat pump types including the impact of thermodynamic losses. *Energy*, 53:312–322, 05 2013. doi: 10.1016/j.energy.2013.02.065.

[22] Di Wu, Jiatong Jiang, Bin Hu, and R.Z. Wang. Experimental investigation on the performance of a very high temperature heat pump with water refrigerant. *Energy*, 190:116427, 10 2019. doi: 10.1016/j.energy.2019.116427.

[23] Institute for sustainable process technology (ispt). encore - next generation compression heat pump, 2020. URL https://ispt.eu/projects/encore/.

[24] Dryficiency project, 2020. URL https://dryficiency.eu/.

[25] Sintef. Heatup project. URL https://www.sintef.no/projectweb/heatup/.

[26] B. Zuhlsdorf, F. Buhler, M. Bantle, and B. Elmegaard. Analysis of technologies and potentials for heat pump based process heat supply above 150 deg c. *Energy Conversion and Management*, 2, 2019. ISSN 2590-1745. doi: https://doi.org/10.1016/j.ecmx.2019.100011.

[27] XueTao Cheng and Xingang Liang. Entransy and entropy analyses of heat pump systems. 58: 4696–4702, 12 2013. doi: 10.1007/s11434-013-6096-4.

[28] Opeyemi Bamigbetan, Trygve Eikevik, Petter Nekså, and Michael Bantle. Review of vapour compression heat pumps for high temperature heating using natural working fluids. *International Journal of Refrigeration*, 80, 04 2017. doi: 10.1016/j.ijrefrig.2017.04.021.

[29] HJ Laue et al. Annex 35 iea. application of industrial heat pumps, final report, part 1, 2014.

[30] Choyu Watanabe. Pioneering industrial heat pump technology in japan, 2013.

[31] Mattias Nilssona, Nes Harald Risla, and Konstantinos Kontomaris. Measured performance of a novel high temperature heat pump with hfo-1336mzz(z) as the working fluid. *12th IEA Heat Pump Conference*, 2017.

[32] K Ochsner. High temperature heat pumps for waste heat recovery. *8th EHPA European Heat Pump Forum*, 2015.

[33] F Zauner. Hochtemperatur-wärmepumpen zur energetischen nutzung industrieller (niedertemperatur-) abwärme, ochsner energie technik gmbh. *Highlights der Energieforschung 2016: Die Rolle der Wärmepumpe im zukünftigen Energiesystem, Wien*, 2016.

[34] JK Jensen, WB Markussen, L Reinholdt, and B Elmegaard. On the development of high temperature ammonia-water hybrid absorption- compression heat pumps. *International Journal of Referigeration*, 2015.

[35] HJ Laue et al. Application of industrial heat pumps, final report, part 1, 2014.

[36] Stefan Wolf, U Fahl, M Blesl, A Voß, and R Jakobs. Analyse des potenzials von industriewärmepumpen in deutschland. *Forschungsbericht. Stuttgart: Univeritat Stuttgart*, 2014.

[37] M Blesl, S Wolf, and U Fahl. Large scale application of heat pumps. *7th EHPA European Heat Pump Forum, Berlin*, 2014.

[38] Friotherm AG. Uniturbo 50fy e centrifugal compressor for large scale refrigeration plants and heat pumps, brochure g008-05, 2005.

[39] L Wojtan. Industrielle abwärmerückgewinnung auf hohem temper- aturniveau. *News aus der Wärempumpen-Forschung, HTI Burgdorf*, 2016.

[40] EMERSON. Neatpump: The high temperature ammonia heat pump, brochure dv143-en-1209, 2012.

[41] ECN. Nationale energieverkenning 2017, 2017.

[42] G Angelino and C Invernizzi. Prospects for real-gas reversed brayton cycle heat pumps. *International Journal of Refrigeration*, 18(4):272–280, 1995. ISSN 0140-7007. doi: https://doi.org/10.1016/0140-7007(95)00005-V.

[43] Limei Gai, Petar Sabev Varbanov, Timothy Gordon Walmsley, and Jiří Jaromír Klemeš. Critical analysis of process integration options for joule-cycle and conventional heat pumps. *Energies*, 13(3), 2020. ISSN 1996-1073. URL https://www.mdpi.com/1996-1073/13/3/635.

[44] Man-Hoe Kim, Jostein Pettersen, and Clark W Bullard. Fundamental process and system design issues in co2 vapor compression systems. *Progress in Energy and Combustion Science*, 30(2): 119–174, 2004. ISSN 0360-1285. doi: https://doi.org/10.1016/j.pecs.2003.09.002.

[45] Xuetao Liu, Yusheng Hu, Qifan Wang, Liang Yao, and Minxia Li. Energetic, environmental and economic comparative analyses of modified transcritical co2 heat pump system to replace r134a system for home heating. *Energy*, 229:120544, 2021. ISSN 0360-5442. doi: https://doi.org/10.1016/j.energy.2021.120544.

[46] R. Huang, Bin Hu, R.Z. Wang, Trygve Magne Eikevik, and T.S. Ge. Thermodynamic and economic analysis of two-stage co2 heat pump with reverse brayton cycle. *International Journal of Refrigeration*, 2022. ISSN 0140-7007. doi: https://doi.org/10.1016/j.ijrefrig.2022.07.001.

[47] Monica C. Guzik and Thomas M. Tomsik. An active broad area cooling model of a cryogenic propellant tank with a single stage reverse turbo-brayton cycle cryocooler. 2011.

[48] Benjamin Monje, David Sánchez, Mark Savill, P. Pilidis, and Tatiana Sanchez. A design strategy for supercritical co2 compressors. *Proceedings of the ASME Turbo Expo*, 3, 06 2014. doi: 10.1115/GT2014-25151.

[49] Philipp Vinnemeier, Manfred Wirsum, Damien Malpiece, and Roberto Bove. Integration of heat pumps into thermal plants for creation of large-scale electricity storage capacities. *Applied Energy*, 184:506–522, 2016. ISSN 0306-2619. doi: https://doi.org/10.1016/j.apenergy.2016.10.045.

[50] *CO2 Research Rig for Advanced Compressors (CORA)*, Turbo Expo: Power for Land, Sea, and Air, 06 2015. URL https://doi.org/10.1115/GT2015-42501.

[51] Merja A Heikkinen, Markku J Lampinen, and Margarete Tamasy-Bano. Thermodynamic analysis and optimization of the brayton process in a heat recovery system of paper machines. *Heat Recovery Systems and CHP*, 13(2):123–131, 1993.

[52] V Kousidis, B Zühlsdorf, F Bühler, and B Elmegaard. Integration and optimization of a reversed brayton cycle coupled with renewables and thermal storage in an oil refinery. In *2nd Symposium on High-Temperature Heat Pumps*, pages 235–241. SINTEF, 2019.

[53] Pau Farres-Antunez, Joshua D. McTigue, and Alexander J. White. A pumped thermal energy storage cycle with capacity for concentrated solar power integration. In *2019 Offshore Energy and Storage Summit (OSES)*, pages 1–10, 2019. doi: 10.1109/OSES.2019.8867222.

[54] Victorino Franco, J. Blázquez, J. Ipus, Jia Yan Law, Luis Moreno-Ramírez, and A. Conde. Magnetocaloric effect: From materials research to refrigeration devices. *Progress in Materials Science*, 93, 11 2017. doi: 10.1016/j.pmatsci.2017.10.005.

[55] Andrej Kitanovski and P.W. Egolf. Thermodynamics of magnetic refrigeration. *International Journal of Refrigeration*, 29:3–21, 01 2006. doi: 10.1016/j.ijrefrig.2005.04.007.

[56] Cristina Baglivo, Paolo Congedo, and Pasquale Donno. Analysis of thermodynamic cycles of heat pumps and magnetic refrigerators using mathematical models. *Energies*, 14, 02 2021. doi: 10.3390/en14040909.

[57] Paulo Trevizoli, Theo Christiaanse, Premakumara Govindappa, Iman Niknia, Reed Teyber, Jader Barbosa Jr, and Andrew Rowe. Magnetic heat pumps: An overview of design principles and challenges. *Science and Technology for the Built Environment*, 22:00–00, 03 2016. doi: 10.1080/23744731.2016.1171632.

[58] Carl Zimm, Andre Boeder, Bryant Mueller, Kyle Rule, and Steven Russek. The evolution of magnetocaloric heat-pump devices. *MRS Bulletin*, 43:274–279, 04 2018. doi: 10.1557/mrs.2018.71.

[59] Andrej Kitanovski, Uros Plaznik, Jaka Tušek, and A. Poredoš. New thermodynamic cycles for magnetic refrigeration. *International Journal of Refrigeration*, 37:28–35, 01 2014. doi: 10.1016/j.ijrefrig.2013.05.014.

[60] Bingfeng Yu, Qingqing Gao, Bo Zhang, Xiangzhao Meng, and Zhenhua Chen. Review on research of room temperature magnetic refrigeration. *International Journal of Refrigeration-revue Internationale Du Froid*, 26:622–636, 2003.

[61] Andrej Kitanovski, Uros Plaznik, Urban Tomc, and Alojz Poredoš. Present and future caloric refrigeration and heat-pump technologies. *International Journal of Refrigeration*, 39, 06 2015. doi: 10.1016/j.ijrefrig.2015.06.008.

[62] S.B Riffat and Xiaoli Ma. Thermoelectrics: a review of present and potential applications. *Applied Thermal Engineering*, 23(8):913–935, 2003. ISSN 1359-4311. doi: https://doi.org/10.1016/S1359-4311(03)00012-7.

[63] Gennadiy Kozhemyakin, Y Krutov, A Oleinikova, and S Skipidarov. Efficiency of a thermoelectric heat pump. 06 2010.

[64] James Lincicome. A study on the application of thermoelectric heat pumps for heating applications. 05 2007.

[65] Fankai Meng, Lingen Chen, and Fengrui Sun. Effects of heat reservoir temperatures on the performance of thermoelectric heat pump driven by thermoelectric generator. *International Journal of Low-Carbon Technologies*, 5(4):273–282, 09 2010.

[66] Saima Sophie Siouane, Slavisa Jovanovic, and Philippe Poure. A novel identification method of thermal resistances of thermoelectric modules combining electrical characterization under constant temperature and heat flow conditions. *Transactions on Environment and Electrical Engineering*, 1:44, 11 2016. doi: 10.22149/teee.v1i4.72.

[67] Zhenyuan Xu and Ruzhu Wang. Absorption heat pump for waste heat reuse: current states and future development. *Frontiers in Energy*, 11, 11 2017. doi: 10.1007/s11708-017-0507-1.

[68] Min Wang. Highly efficient absorption heat pump and refrigeration systems based on ionic liquids : Fundamentals & applications. 2019.

[69] K.E. Herold, R. Radermacher, and S.A. Klein. *Absorption Chillers and Heat Pumps*. CRC Press, 2016. ISBN 9781498714341. URL https://books.google.nl/books?id=fNlkjgEACAAJ.

[70] João M.S. Dias and Vítor A.F. Costa. Adsorption heat pumps for heating applications: A review of current state, literature gaps and development challenges. *Renewable and Sustainable Energy Reviews*, 98:317–327, 2018. ISSN 1364-0321. doi: https://doi.org/10.1016/j.rser.2018.09.026.

[71] Hasan Demir, Moghtada Mobedi, and Semra Ülkü. A review on adsorption heat pump: Problems and solutions. *Renewable and Sustainable Energy Reviews*, 12(9):2381–2403, 2008. ISSN 1364-0321. doi: https://doi.org/10.1016/j.rser.2007.06.005.

[72] Francis Meunier. Adsorption heat powered heat pumps. *Applied Thermal Engineering*, 61(2):830–836, 2013. ISSN 1359-4311. doi: https://doi.org/10.1016/j.applthermaleng.2013.04.050.

[73] Joana M. Pinheiro, Sérgio Salústio, João Rocha, Anabela A. Valente, and Carlos M. Silva. Adsorption heat pumps for heating applications. *Renewable and Sustainable Energy Reviews*, 119:109528, 2020. ISSN 1364-0321. doi: https://doi.org/10.1016/j.rser.2019.109528.

[74] Xing-Qi Cao, Wei-Wei Yang, Fu Zhou, and Ya-Ling He. Performance analysis of different high-temperature heat pump systems for low-grade waste heat recovery. *Applied Thermal Engineering*, 71(1):291–300, 2014. ISSN 1359-4311. doi: https://doi.org/10.1016/j.applthermaleng.2014.06.049.

[75] Carlos Mateu-Royo, Cordin Arpagaus, Adrián Mota-Babiloni, Joaquín Navarro-Esbrí, and Stefan S. Bertsch. Advanced high temperature heat pump configurations using low gwp refrigerants for industrial waste heat recovery: A comprehensive study. *Energy Conversion and Management*, 229:113752, 2021. ISSN 0196-8904. doi: https://doi.org/10.1016/j.enconman.2020.113752.

[76] Seon Tae Kim, Robert Hegner, Göksel Özuylasi, Panagiotis Stathopoulos, and Eberhard Nicke. Performance analysis of high temperature heat pump cycle for industrial process. 2021. URL https://elib.dlr.de/146568/.

[77] P. Colonna. Modeling and simulation of power and propulsion applications, 2021.

[78] John E. Gray and Stephen R. Addison. Generalized extensivity, generalized superposition and the principle of parsimony. *Journal of the Washington Academy of Sciences*, 103:9–26, 2017. ISSN 00430439, 25732110. URL https://www.jstor.org/stable/90013589.

[79] Francesco Casella, Michael Sielemann, and Luca Savoldelli. Steady-state initialization of object-oriented thermo-fluid models by homotopy methods. 06 2011. doi: 10.3384/ecp1106386.

[80] Zhaoyong Liu, Li Zhao, Xuezheng Zhao, and Hailong Li. The occurrence of pinch point and its effects on the performance of high temperature heat pump. *Applied Energy*, 97:869–875, 2012. ISSN 0306-2619. doi: https://doi.org/10.1016/j.apenergy.2011.12.061.

[81] You-Rong Li, Jian-Ning Wang, and Mei-Tang Du. Influence of coupled pinch point temperature difference and evaporation temperature on performance of organic rankine cycle. *Energy*, 42(1): 503–509, 2012. ISSN 0360-5442. doi: https://doi.org/10.1016/j.energy.2012.03.018.

[82] Jianhui Qi, Thomas Reddell, Kan Qin, Kamel Hooman, and Ingo H. J. Jahn. Supercritical co2 radial turbine design performance as a function of turbine size parameters. *Journal of Turbomachinery*, 139(8), 2017. ISSN 0889-504X. URL https://doi.org/10.1115/1.4035920.

[83] Benjamin Zuhlsdorf, Christian Schlemminger, Michael Bantle, Kjetil Evenmo, and Brian Elmegaard. Design recommendations for r-718 heat pumps in high temperature applications. In *Proceedings of the 13th IIR Gustav Lorentzen Conference, Valencia, 2018*. IIR, 2018.

[84] Paul De Larminat, D Arnou, P Le Sausse, F Clunet, and JL Peureux. A high temperature heat pump using water vapor as working fluid. In *Hangzhou, China: Proc. 11th IIR Gustav Lorentzen Conf*, 2014.

[85] Ian H. Bell, Jorrit Wronski, Sylvain Quoilin, and Vincent Lemort. Pure and pseudo-pure fluid thermophysical property evaluation and the open-source thermophysical property library coolprop. *Industrial & Engineering Chemistry Research*, 53(6):2498–2508, 2014. URL http://pubs.acs.org/doi/abs/10.1021/ie4033999.

[86] Rene Van den Braembussche. *Design and Analysis of Centrifugal Compressors*. ASME Press, 2020. ISBN 9781119424093. URL https://doi.org/10.1115/1.861VAN.

[87] Andrea Giuffre, Piero Colonna, and Matteo Pini. The effect of size and working fluid on the multi-objective design of high-speed centrifugal compressors. *International Journal of Refrigeration*, 2022. ISSN 0140-7007. doi: https://doi.org/10.1016/j.ijrefrig.2022.06.023.

[88] Andrea Giuffre, Piero Colonna, and Matteo Pini. Design optimization of a high-speed twin-stage compressor for next-gen aircraft environmental control system. *Proceedings of ASME Turbo Expo 2022*, 2022.

[89] E. W. Lemmon, I.H. Bell, M. L. Huber, and M. O. McLinden. NIST Standard Reference Database 23: Reference Fluid Thermodynamic and Transport Properties-REFPROP, Version 10.0, National Institute of Standards and Technology, 2018. URL https://www.nist.gov/srd/refprop.

[90] M. Casey and C. Robinson. *Radial Flow Turbocompressors: Design, Analysis, and Applications*. Cambridge University Press, 2021. ISBN 9781108271462. URL https://books.google.nl/books?id=6hYwEAAAQBAJ.

[91] John D. Stanitz. One-dimensional compressible flow in vaneless diffusers of radial- and mixed-flow centrifugal compressors, including effects of friction, heat transfer and area change. 1952.

[92] C. Freeman and N. A. Cumpsty. Method for the prediction of supersonic compressor blade performance. *Journal of Propulsion and Power*, 8:199–208, 1992. URL https://doi.org/10.2514/3.23461.

[93] Hiromi Kobayashi, Hideo Nishida, Takeo Takagi, and Yasuo Fukushima. A study on the rotating stall of centrifugal compressors. II - Effect of vaneless diffuser inlet shape on rotating stall. *JSME Transactions*, 56:2646–2651, 1990.

[94] Michele Marconcini, Alessandro Bianchini, Matteo Checcucci, Giovanni Ferrara, Andrea Arnone, Lorenzo Ferrari, Davide Biliotti, and Dante Tommaso Rubino. A Three-Dimensional Time-Accurate Computational Fluid Dynamics Simulation of the Flow Field Inside a Vaneless Diffuser During Rotating Stall Conditions. *Journal of Turbomachinery*, 139(2), 2016. URL https://doi.org/10.1115/1.4034633.

[95] Julian Blank and Kalyanmoy Deb. Pymoo: Multi-objective optimization in python. *IEEE Access*, 8:89497–89509, 2020. doi: 10.1109/ACCESS.2020.2990567.

[96] K. Deb, A. Pratap, S. Agarwal, and T. Meyarivan. A fast and elitist multiobjective genetic algorithm: Nsga-ii. *IEEE Transactions on Evolutionary Computation*, 6(2):182–197, 2002. doi: 10.1109/4235.996017.

[97] Ronald H. Aungier. *Turbine Aerodynamics: Axial-Flow and Radial-Flow Turbine Design and Analysis*. ASME Press, 2006. ISBN 0791802418. URL https://doi.org/10.1115/1.802418.

[98] M. Pinni. Turbomachinery- radial turbines, 2021.

[99] *Performance Prediction for High Pressure-Ratio Radial Inflow Turbines*, volume Volume 6: Turbo Expo 2007, Parts A and B of *Turbo Expo: Power for Land, Sea, and Air*, 2007. doi: 10.1115/GT2007-27057. URL https://doi.org/10.1115/GT2007-27057.

[100] A Whitfield and Alias Noor. Design and performance of vaneless volutes for radial inflow turbines: Part 1: Non-dimensional conceptual design considerations. *Proceedings of The Institution of Mechanical Engineers Part A-journal of Power and Energy - PROC INST MECH ENG A-J POWER*, 208:199–211, 1994. doi: 10.1243/PIME_PROC_1994_208_035_02.

[101] S. Singer and J. Nelder. Nelder-Mead algorithm. *Scholarpedia*, 4:2928, 2009. doi: 10.4249/scholarpedia.2928.

[102] Ankit Rohatgi. Webplotdigitizer: Version 4.5, 2021. URL https://automeris.io/WebPlotDigitizer.

[103] Milan N. Šarevski and Vasko N. Šarevski. Thermal characteristics of high-temperature r718 heat pumps with turbo compressor thermal vapor recompression. *Applied Thermal Engineering*, 117:355–365, 2017. ISSN 1359-4311. doi: https://doi.org/10.1016/j.applthermaleng.2017.02.035.

[104] M.N. Šarevski and V.N. Šarevski. Characteristics of water vapor turbocompressors applied in refrigeration and heat pump systems. *International Journal of Refrigeration*, 35:1484–1496, 2012. ISSN 0140-7007. doi: https://doi.org/10.1016/j.ijrefrig.2012.03.014.

[105] R Paul Singh and Dennis R Heldman. *Introduction to food engineering*. Gulf Professional Publishing, 2001.

[106] Martin Atkins, Michael Walmsley, and James Neale. Integrating heat recovery from milk powder spray dryer exhausts in the dairy industry. *Applied Thermal Engineering*, 31, 09 2011. doi: 10.1016/j.applthermaleng.2011.03.006.

[107] J. Metson. 2 - production of alumina. In *Fundamentals of Aluminium Metallurgy*. Woodhead Publishing, 2011. ISBN 978-1-84569-654-2. doi: https://doi.org/10.1533/9780857090256.1.23.

[108] Gu Songqing and Yin Zhonglin. Preheaters and digesters in the bayer digestion process. In *Essential Readings in Light Metals*, pages 356–361. Springer, 2016.

[109] Reiner Wischnewski, Cleto Maues de Azevedo, Emerson LS Moraes, and Arthur Barros Monteiro. Alunorte global energy efficiency. In *Light Metals 2011*, pages 179–184. Springer, 2011.

[110] Martin van der Geest, Henk Polinder, Jan Abraham Ferreira, and Markus Christmann. Power density limits and design trends of high-speed permanent magnet synchronous machines. *IEEE Transactions on Transportation Electrification*, 1(3):266–276, 2015. doi: 10.1109/TTE.2015.2475751.

[111] Robert Abebe, Mauro Di Nardo, David Gerada, Giovanni Lo Calzo, Luca Papini, and Chris Gerada. High speed drives review: Machines, converters and applications. In *IECON 2016 - 42nd Annual Conference of the IEEE Industrial Electronics Society*, pages 1675–1679, 2016. doi: 10.1109/IECON.2016.7793721.

[112] Paolo Bertoldi. *Energy Efficiency in Motor Systems Proceedings of the 11th international Conference EEMODS'19: Proceedings of the 11th international Conference EEMODS'19*. 01 2021. ISBN 978-3-030-69798-3. doi: 10.1007/978-3-030-69799-0.

[113] Vipluv Aga, Enrico Conte, Richard Carroni, Bertrand Burcker, and Mathieu Ramond. Supercritical co2-based heat pump cycle for electrical energy storage for utility scale dispatchable renewable energy power plants. In *Proc: 5th Int. Symp.—Supercritical CO2 Power Cycles (San Antonio, United States)*, 2016.

[114] Jianhui Qi, Thomas Reddell, Kan Qin, Kamel Hooman, and Ingo H. J. Jahn. Supercritical CO2 Radial Turbine Design Performance as a Function of Turbine Size Parameters. *Journal of Turbomachinery*, 139(8), 2017. URL https://doi.org/10.1115/1.4035920.

[115] Kehan Zhou, Jiangfeng Wang, Jiaxi Xia, Yumin Guo, Pan Zhao, and Yiping Dai. Design and performance analysis of a supercritical co2 radial inflow turbine. *Applied Thermal Engineering*, 167:114757, 2020. doi: https://doi.org/10.1016/j.applthermaleng.2019.114757.

[116] Joshua A. Keep and Ingo H. J. Jahn. Design of an Annular-Radial Diffuser for Operation With a Supercritical CO2 Radial Inflow Turbine. *Journal of Engineering for Gas Turbines and Power*, 141(8), 2019. URL https://doi.org/10.1115/1.4043431.

[117] B. Monje, D. Sánchez, R. Chacartegui, T. Sánchez, M. Savill, and P. Pilidis. Aerodynamic analysis of conical diffusers operating with air and supercritical carbon dioxide. *International Journal of Heat and Fluid Flow*, 44:542–553, 2013. doi: https://doi.org/10.1016/j.ijheatfluidflow.2013.08.010.

[118] Jahar Sarkar and Souvik Bhattacharyya. Assessment of blends of co2 with butane and isobutane as working fluids for heat pump applications. *International Journal of Thermal Sciences*, 48(7):1460–1465, 2009. ISSN 1290-0729. doi: https://doi.org/10.1016/j.ijthermalsci.2008.12.002. URL https://www.sciencedirect.com/science/article/pii/S1290072908002846.

[119] K Kontmaris. A zero-odp, low gwp working fluid for hpexp temperature heating and power generation from low temperature heat: Dr-2. In *Proceedings of the International Symposium on New Refrigerants and Environmental Technology 2012, JRAIA, 11*, pages 212–217, 2012.

[120] Damien Bobelin and Ali Bourig. Experimental results of a newly developed very high temperature industrial heat pump (140 c) equipped with scroll compressors and working with a new blend refrigerant. 2012.

[121] Chieko Kondou and Shigeru Koyama. Thermodynamic assessment of high-temperature heat pumps using low-gwp hfo refrigerants for heat recovery. *International Journal of Refrigeration*, 53:126–141, 2014. ISSN 0140-7007. doi: https://doi.org/10.1016/j.ijrefrig.2014.09.018. URL https://www.sciencedirect.com/science/article/pii/S0140700714002576.

[122] Marwan Chamoun, Romuald Rulliere, Philippe Haberschill, and Jean-Louis Peureux. Experimental and numerical investigations of a new high temperature heat pump for industrial heat recovery using water as refrigerant. *International Journal of Refrigeration*, 44:177–188, 2014. ISSN 0140-7007. doi: https://doi.org/10.1016/j.ijrefrig.2014.04.019. URL https://www.sciencedirect.com/science/article/pii/S0140700714000954.

[123] P De Larminat, D Arnou, P Le Sausse, F Clunet, and JL Peureux. A high temperature heat pump using water vapor as working fluid. In *11th Iir Gustav Lorentzen Conference on Natural Refrigerants (2014)*, pages 857–864, 2014.

[124] I Tolstorebrov, M Bantle, A Hafner, B Kuz, and TM Eikevik. Energy efficiency by vapor compression in superheated steam drying systems. In *11th IIR Gustav Lorentzen Conference on Natural Refrigerants, Hangzhou, China*, 2014.

[125] S Fukuda, C Kondou, N Takata, and S Koyama. Low gwp refrigerants r1234ze(e) and r1234ze(z) for high temperature heat pumps. In *International Journal of Refrigeration*, 2014.

[126] Martin Glosli Bergland. Optimizing the compression/absorption heat pump system at high temperatures. Master's thesis, NTNU, 2015.

[127] T Fleckl, M Hartl, F Helminger, and K. Pfaffl Kontomaris. Performance testing of a lab-scale high temperature heat pump with hfo-1336mzz-z as the working fluid. In *European Heat Pump Summit, Nuremberg*, 2015.

[128] Florian Reißner. Development of a novel high temperature heat pump system. 2015.

[129] Opeyemi Bamigbetan, Petter Nekså, Trygve Eikevik, and Michael Bantle. Evaluation of natural working fluids for the development of high temperature heat pumps. 08 2016.

[130] Xiaokun Wu, Ziwen Xing, Zhilong He, Xiaolin Wang, and Wenqing Chen. Performance evaluation of a capacity-regulated high temperature heat pump for waste heat recovery in dyeing industry. *Applied thermal engineering*, 93:1193–1201, 2016.

[131] F Helminger, M Hartl, T Fleckl, and K Pfaff Kontomaris. Hochtemperatur warmepumpen messergebnisse einer laboranlage mit hfo-1336mzz-z bis 160 c kondensationstemperatur. In *14. Symposium Energieinnovation, TU Graz*, 2016.

[132] R Noack. Entwicklung einer hochtemperatur-w€armepumpe für nutztem- peraturen über 120 c. In *Deutsche Kälte- und Klimatagung, Kassel*, 2016.

[133] V Wilk, M Hartl, T Fleckl, E Widhalm, F Ramler, G Adelberger, and K Ochsner. Hochtemperaturwärmepumpe für industrieanwendungen: Prüfstandmessungen und systemsimulation, iv. 18. *Deutsche Kälte-und Klimatagung 2016, Kassel, 16.-18. November 2016, Kurzfassungen*, 2016.

[134] M Huanga, X Lianga, and R Zhuanga. Experimental investigate on the performance of high temperature heat pump using scroll compressor. In *12th IEA Heat Pump Conference*, 2017.

[135] Yan Zhang, Yufeng Zhang, Xiaohui Yu, Jing Guo, Na Deng, Shengming Dong, Zhonglu He, and Xuelian Ma. Analysis of a high temperature heat pump using by-5 as refrigerant. *Applied Thermal Engineering*, 127:1461–1468, 2017. ISSN 1359-4311. doi: https://doi.org/10.1016/j.applthermaleng.2017.08.072. URL https://www.sciencedirect.com/science/article/pii/S1359431117337134.

A

Additional Literature Data

Table A.1: Material properties of Gadolinium (Gd), derived from [56]

Parameter	Value	Units
External electronic configuration	$4f^7\ 5d^1\ 6s^2$	
Quantum number of spins (N_S)	3.5	
Quantum orbital number (J_O)	0	
Quantum number of the total angular momentum (J_A)	3.5	
Landè factor (g)	2	
Mass (m)	1	kg
Molar mass (M)	157.25	g/mol
Number of moles (n)	6.36	mol
Avogadro number (N_A)	6.02 X 1023	
Number of atoms in 1kg of Gadolinium (N_g)	3.83 X 1024	atoms/kg
Bohr magneton (μ_B)	9.27 X 10-24	J/T
Boltzmann constant (k)	1.38 X 10-23	J/K
Curie constant (C)	501.23	JK/T^2
Curie Temperature (T_C)	294.4	K

Table A.2: Overview of the studies found related to vapor compression cycle based high temperature heat pump

Author	Type of System	Refrigerant	Maximum Sink Temperature [^{o}C]	Temperature lift [^{o}C]	COP	Reference
Sarkar J. and Bhattacharyya S. (2009)	Single stage with internal heat exchanger	Multiple considered: R114,R600, R744	125	95	1.44-3.16	[118]
Kontmaris K. (2012)	With superheating and undercooling	DR-2	155	75	3.08	[119]
Bobelin D. and Bourig A. (2012)	With superheating and undercooling	Multiple considered: ECO3, R245fa, R717, R1234ze, R236fa, R365mfc	140	75	2-4	[120]
Kondou C. and Koyama S. (2014)	Different configurations: triple tandem cycle, two-stage extraction cycle, three-stage extraction cycle, and cascade cycle	Multiple Considered: R717, R365mfc, R1234ze(E) and R1234ze(Z)	160	80	4.3-4.94	[121]
Chamoun M. et. al. (2014)	Twin screw compressor with water injection and a biphasic flow.	Water	145	41	5.9	[122]
Larminat P. de et. al. (2014)	Two-stage centrifugal compressor	Water	130	40	5.5	[123]
Tolstorebrov I. et. al. (2014)	Heat pump assisted superheated steam dryer using radial compressor	Water	180	90	3.31	[124]
Fakuda S. et. al. (2014)	Single stage with twin rotary compressor	R1234ze(Z)	125	30	6.6	[125]
Bergland M.G. (2015)	Hybrid system using an internal water-ammonia absorption circuit (CAHP cycle)	Ammonia-water	171.8	121.5	2.08	[126]
Fleckl T. et. al. (2015)	Single stage with piston compressor	R1336mzz(Z)	150	70	2.4	[127]
Reißner F. et. al. (2015)	Single stage with internal heat exchanger and piston compressor	LG6	140	60	3.2	[128]
Bamigbetan O. et. al. (2016)	Double compression-double throttling with flash intercooling; Cascade system	Ammonia; Hydrocarbons	150	110	3.6-3.95	[129]
Wu X. et. al. (2016)	HTHP system for dyeing process	R245fa	95	65	4.2	[130]
Helminger F. et. al. (2016)	Single stage with internal heat exchanger and piston compressor	R1336mzz(Z)	156	47	2.7	[131]
Noack R. (2016)	Single stage with piston compressor	HT125	140	70	1.7	[132]
Wilk et. al. (2016)	Single stage with injection and screw compressor	R245fa	130	70	2.3	[133]
Huang M. et. al. (2017)	Single stage with scroll compressor	R245fa	120	50	5.1	[134]
Zhang Y. et. al. (2017)	Single stage with flash tank and scroll compressor	BY-5	130	50	2.2	[135]

B

Additional System Modeling Data

The following subsections describe the details of modeling of individual components required to obtain the system model of HP based on the reverse Rankine cycle and reverse Brayton cycle.

B.1. Thermal Source/Sink

The thermal source and thermal sink are modeled as only one fluid heat exchanger. At this stage no additional information about the source and sink streams is available. As a result, adopting this modeling choice allows one to compute the available heating and cooling capacities, without any additional information about the corresponding streams.

The relevant phenomenon thus for this case only becomes the mass, momentum, and energy conservation. It is assumed that the component is thermally insulated, thus component can be modeled as an adiabatic system. In reality, there will be some thermal energy exchange with the environment in the form of heat loss. However, at this stage of modeling, this assumption can be considered valid as no information is available about the geometry of the heat exchangers. Further, the assumption does not hinder the primary objective of the system model, as it still allows for consistent performance comparison among the different HP configurations.

Thus, using the simplifications, the corresponding required equations are shown as follows, where P represent pressure, $\dot{Q}$ represents the amount of thermal power available and h represents specific enthalpy [J/kg]. The stations "node_{in}" and "node_{out}" represent the inlet and the outlet connecting node of the components as also depicted in Figure B.1.

For this stage of modeling, both ΔP_{source} and ΔP_{sink} were considered zero, representing an ideal situation where no pressure losses are encountered. This was done as no information about the actual component design specifications was available at this stage of modeling.

Heat Source	Heat Sink	
$\dot{m}_{\text{node}_{\text{in}}} = \dot{m}_{\text{node}_{\text{out}}}$	$\dot{m}_{\text{node}_{\text{in}}} = \dot{m}_{\text{node}_{\text{out}}}$	(B.2)
$P_{\text{node}_{\text{out}}} = P_{\text{node}_{\text{in}}} - \Delta P_{\text{source}}$	$P_{\text{node}_{\text{out}}} = P_{\text{node}_{\text{in}}} - \Delta P_{\text{sink}}$	(B.3)
$\dot{Q}_{\text{source}} = \dot{m}_{\text{node}_{\text{in}}} \cdot \left(h_{\text{node}_{\text{out}}} - h_{\text{node}_{\text{in}}}\right)$	$\dot{Q}_{\text{sink}} = \dot{m}_{\text{node}_{\text{in}}} \cdot \left(h_{\text{node}_{\text{in}}} - h_{\text{node}_{\text{out}}}\right)$	(B.4)

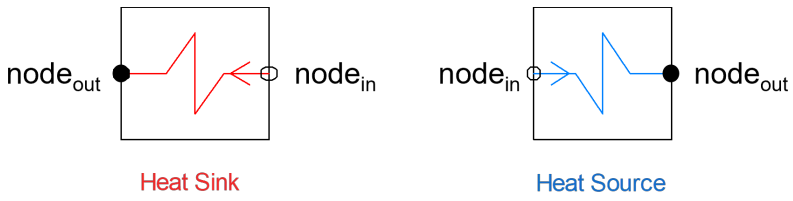

Figure B.1: Schematic of heat source and heat sink component model, indicating the inlet and outlet connecting nodes

B.2. Compressor Modeling

To develop the 0D compressor model, several assumptions are made to allow the modeling at this stage where no specific information about compressor type is available. It is assumed that the compressor is perfectly thermally insulated. This implies that the system can be considered adiabatic and no heat leakage losses are present. Further, it is also assumed that isentropic efficiency ($\eta_{\text{is, comp}}$) can be considered a constant irrespective of the pressure ratio (π). In reality, $\eta_{\text{is, comp}}$ is a function of the operating π and is dependent on the compressor design, however, for the current model purpose, no specific information about compressor design, assuming a constant $\eta_{\text{is, comp}}$ allows a consistent comparison among different HP configurations.

Using the above-mentioned assumptions, the required conservation equations for the compressor can be derived. Similar to the case of heat sink and source, the compressor component also has two fluid nodes (inlet and outlet), as shown in Figure B.2. In terms of mass conservation, the equation is trivial i.e. inlet mass flow rate is equal to the outlet mass flow rate. In terms of momentum and energy conservation, firstly the outlet state of the compressor needs to be defined. Using the assumption of $\eta_{\text{is, comp}}$, the outlet state can be written in terms of isentropic outlet state (state achieved using isentropic conditions $s_{\text{node}_{\text{in}}} = s_{\text{node}_{\text{out}}}$), as shown in Equation (B.5). In Equation (B.5), subscript "is" represents the isentropic state and the symbol "s" represents the specific entropy [J/kg K] of the particular state.

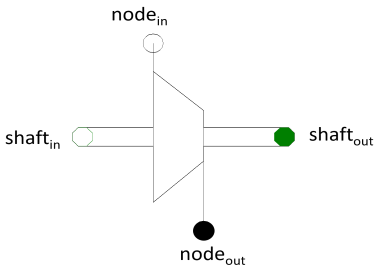

Figure B.2: Schematic of compressor model, indicating mechanical and fluid connectors.

$$
\begin{aligned}
h_{\text{node}_{\text{out}}} &= h_{\text{node}_{\text{in}}} + \frac{\left(h_{\text{node}_{\text{out, is}}} - h_{\text{node}_{\text{in}}}\right)}{\eta_{\text{is, comp}}}\,, \\
h_{\text{node}_{\text{out, is}}} &= \mathrm{f}\left(P_{\text{node}_{\text{out}}}, s_{\text{node}_{\text{in}}}\right)\,, \\
s_{\text{node}_{\text{in}}} &= \mathrm{f}\left(P_{\text{node}_{\text{in}}}, T_{\text{node}_{\text{in}}}\right)
\end{aligned}
\tag{B.5}
$$

Using, this outlet state, the required compressor power can also be implemented, as shown in Equation (B.6), where $\eta_{\text{m, comp}}$ represents the mechanical efficiency of the connecting shafts and thus depicts the mechanical losses associated with power transmission.

$$
W_{\text{comp}} = \frac{\dot{m}_{\text{node}_{\text{in}}}\left(h_{\text{node}_{\text{out}}} - h_{\text{node}_{\text{in}}}\right)}{\eta_{\text{m, comp}}} \tag{B.6}
$$

Thus, once the inlet state is given and the outlet pressure or temperature is specified, the outlet state can be fully computed. Alternatively, if the compressor power is given along with one of the inlet or outlet states, the other remaining state can be fully defined.

Further, as can be observed, in addition to the fluid connectors, two additional connectors have also

been implemented in the compressor model (shown in green color). These additional connectors represent the mechanical connectors (called ”shaft”) and allow for the compressor to be connected to an external power source (for example motor). An additional energy balance equation is included for these connectors to have a completely defined system. This equation is shown in Equation (B.7), where ω and M represents the rotational speed and moment respectively.

$$\left(M_{\text{shaft}_{\text{in}}} \cdot \omega_{\text{shaft}_{\text{in}}}\right) - \left(\omega_{\text{shaft}_{\text{out}}} \cdot M_{\text{shaft}_{\text{out}}}\right) = W_{\text{comp}} \tag{B.7}$$

B.3. Turbine Modeling

For the reverse Brayton cycle-based HP configurations, the turbine is used as the expansion device. Thus, a representative model of the turbine is also required. The 0D modeling approach for the turbine is very similar to the one presented for the compressor in Appendix B.2. The underlying assumptions and simplifications are the same, except in this case the efficiency values are different. For the case of the turbine, the isentropic efficiency and the mechanical efficiency values are thus represented by $\eta_{\text{is, turb}}$ and $\eta_{\text{m, turb}}$ respectively.

The mass conservation equation remains the same as that of compressor. However, the outlet state equation needs to be modified as the underlying phenomenon is an expansion in this case, instead of compression. The modified equations for the outlet state and the model schematic for the turbine are shown in Equation (B.8) and Figure B.3.

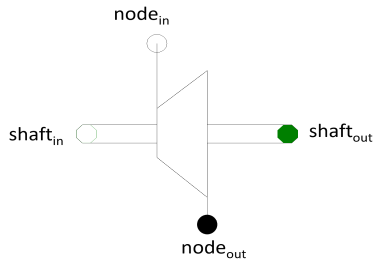

Figure B.3: Schematic of turbine model, indicating mechanical and fluid connectors.

$$\begin{aligned} h_{\text{node}_{\text{out}}} &= h_{\text{node}_{\text{in}}} - \eta_{\text{is, turb}} \cdot \left(h_{\text{node}_{\text{in}} - h_{\text{node}_{\text{out, is}}}}\right) , \\ h_{\text{node}_{\text{out, is}}} &= \mathrm{f}\left(P_{\text{node}_{\text{out}}}, s_{\text{node}_{\text{in}}}\right) , \\ s_{\text{node}_{\text{in}}} &= \mathrm{f}\left(P_{\text{node}_{\text{in}}}, T_{\text{node}_{\text{in}}}\right) \end{aligned} \tag{B.8}$$

Similar to the case of the compressor, once the inlet state is given and one of the outlet state quantities (P or T) is known, the complete outlet state and power achievable can be computed. Alternatively, for a given power and one state, the other state can be fully derived.

For this case, the achievable work can be computed as shown in Equation (B.9). For the turbine model, there are additional shaft connectors are also present, as was the case for the compressor model. Thus, the corresponding shaft power balance equation is the same for the turbine as the one shown in Equation (B.7).

$$W_{\text{turb}} = \frac{\dot{m}_{\text{node}_{\text{in}}} \left(h_{\text{node}_{\text{in}}} - h_{\text{node}_{\text{out}}}\right)}{\eta_{\text{m, turb}}} \tag{B.9}$$

B.4. Expansion Valve Modeling

For the heat pump systems based on the reverse Rankine cycle, an expansion valve is used as the expansion device instead of a turbine. For the modeling of the expansion valve, the assumption of

a perfectly insulated component is also made, making the system adiabatic. The expansion valve is usually modeled as a "*isenthalpic*" device. This implies that the specific enthalpy of the fluid remains constant as it passes through the valve.

Using these assumptions and simplifications, the corresponding conservation equations for the valve can be written as shown in the following equations. Equation (B.10) , Equation (B.11) and Equation (B.12) represent the mass, energy and momentum conservation respectively. In Equation (B.12) ΔP_{valve} represents the pressure loss due to the friction in the valve. Since no valve-specific information is available at this point, this factor is assumed to be zero, thus representing the ideal situation.

$$\dot{m}_{\text{node}_{\text{in}}} = \dot{m}_{\text{node}_{\text{out}}} \tag{B.10}$$

$$h_{\text{node}_{\text{in}}} = h_{\text{node}_{\text{out}}} \tag{B.11}$$

$$P_{\text{node}_{\text{out}}} = P_{\text{node}_{\text{in}}} - \Delta P_{\text{valve}} \tag{B.12}$$

B.5. Internal Heat Exchanger Modeling

The 0D modeling of IHX is different than the earlier mentioned models for heat source and sink. The main difference lies in terms of the fluid arrangement. For the case of IHX, two fluids have to be considered and both the fluid would be the same refrigerant (but with different flow rates and state values) as it is an internal heat exchanger. Thus, for the case of IHX four fluid connectors were implemented (two per fluid stream), as shown in Figure B.4.

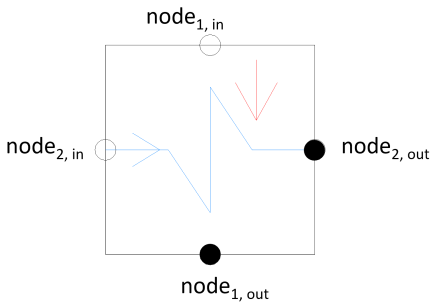

Figure B.4: Schematic of internal heat exchanger model, indicating the inlet and outlet connecting nodes for both hot and cold streams (1 and 2 respectively)

In terms of the relevant phenomenon and the simplifications, a similar approach is taken for the heat source and heat sink models. However, in this case, the conservation equations need to be written for both the fluid streams. Thus, the corresponding mass conservation can be represented as shown in Equation (B.13), where subscripts 1 and 2 represent the hot and cold fluid streams respectively.

$$\begin{aligned} \dot{m}_{\text{node}_{1,\text{ in}}} &= \dot{m}_{\text{node}_{1,\text{ out}}} \\ \dot{m}_{\text{node}_{2,\text{ in}}} &= \dot{m}_{\text{node}_{2,\text{ out}}} \end{aligned} \tag{B.13}$$

Similarly, the energy balance, in this case, required two different equations, as shown in Equation (B.14).

$$\begin{aligned} \dot{Q}_{\text{IHX}} &= \dot{m}_{\text{node}_{1,\text{ in}}} \cdot \left(h_{\text{node}_{1,\text{ in}}} - h_{\text{node}_{1,\text{ out}}} \right) \\ \dot{Q}_{\text{IHX}} &= \dot{m}_{\text{node}_{2,\text{ in}}} \cdot \left(h_{\text{node}_{2,\text{ out}}} - h_{\text{node}_{2,\text{ in}}} \right) \end{aligned} \tag{B.14}$$

Finally, in terms of momentum balance, the conservation equations are computed as shown in Equation (B.15), where ΔP_1 and ΔP_2 represent the pressure losses in the hot and cold streams respectively.

$$\begin{aligned} P_{\text{node}_{1,\,\text{out}}} &= P_{\text{node}_{1,\,\text{in}}} - \Delta P_1 \\ P_{\text{node}_{2,\,\text{out}}} &= P_{\text{node}_{2,\,\text{in}}} - \Delta P_2 \end{aligned} \tag{B.15}$$

B.6. Flash tank

This component is used to separate the liquid fraction of the stream. Therefore, it is also known as a vapor-liquid separator. There are two outputs from this component, one is saturated vapor and the other is a saturated liquid stream. Thus, the energy balance for this component can be written as shown in Equation (B.16), where $h_{\text{sat, v}}$ and $h_{\text{sat, l}}$ represent the specific enthalpy of the saturated vapor and liquid respectively, at the inlet pressure conditions.

$$\begin{aligned} h_{\text{node}_{1,\,\text{out}}} &= h_{\text{sat, v}}\,, \\ h_{\text{node}_{2,\,\text{out}}} &= h_{\text{sat, l}}\,, \\ \left(\dot{m}_{\text{node}_{\text{in}}} \cdot h_{\text{node}_{\text{in}}}\right) &= \left(\dot{m}_{\text{node}_{2,\,\text{out}}} \cdot h_{\text{node}_{2,\,\text{out}}}\right) + \left(\dot{m}_{\text{node}_{1,\,\text{out}}} \cdot h_{\text{node}_{1,\,\text{out}}}\right) \end{aligned} \tag{B.16}$$

The mass balance for this component can be written as shown in Equation (B.17), since there is no accumulation, the inlet mass flow rate is equal to the sum of the two outlet nodes‘ mass flow rate.

$$\dot{m}_{\text{node}_{\text{in}}} = \dot{m}_{\text{node}_{1,\,\text{out}}} + \dot{m}_{\text{node}_{2,\,\text{out}}} \tag{B.17}$$

It was assumed that no pressure losses are present within the component, therefore the momentum balance is trivial and can be written as shown in Equation (B.18).

$$\begin{aligned} P_{\text{node}_{1,\,\text{out}}} &= P_{\text{node}_{\text{in}}} \\ P_{\text{node}_{2,\,\text{out}}} &= P_{\text{node}_{\text{in}}} \end{aligned} \tag{B.18}$$

B.7. System Verification Tests

Table B.1: Summary of additional system verification tests performed

Test Description	Quantification	Result
Overall energy balance ($\dot{Q}_{\text{sink}} = \dot{Q}_{\text{source}} + W_{\text{comp}}$)	$\mathrm{O}(10^{-11})$	*Pass*
Increasing $\eta_{\text{is, c}}$ leads to a linear increase in $\mathrm{COP_h}$	${R^2}_{\text{avg}} = 0.998$	*Pass*
Increasing $\eta_{\text{is, t}}$ leads to a linear increase in $\mathrm{COP_h}$	${R^2}_{\text{avg}} = 0.996$	*Pass*
Increasing $\dot{m}$ leads to a linear increase in $\dot{Q}_{\text{source/sink}}$	${R^2}_{\text{avg}} = 1.0$	*Pass*
Increasing $\dot{m}$ leads to a constant $\mathrm{COP_h}$	Machine Precision	*Pass*
Decreasing ΔT_{min} leads to a linear increase in $\dot{Q}_{\text{source/sink}}$	${R^2}_{\text{avg}} = 1.0$	*Pass*
Decreasing ΔT_{min} leads to an increase in $\mathrm{COP_h}$	Linear, ${R^2}_{\text{avg}} = 0.99$	*Pass*

C

Additional Thermodynamic Cycle Data

Two Stage with Intercooling - using Air

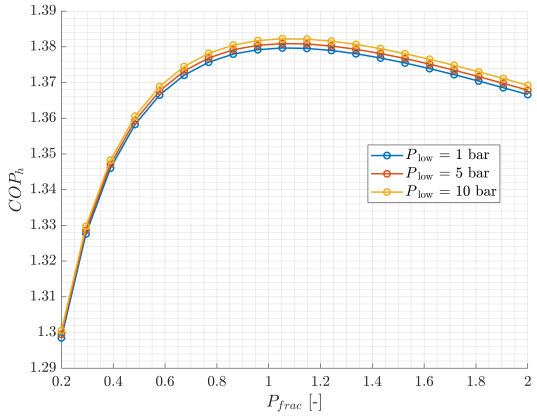

Figure C.1: Variation of $\mathrm{COP_h}$ with P_{frac} at different P_{low} values (with β_{total} = 4) for the two-stage configuration with intercooling, using Air as working fluid (under baseline case).

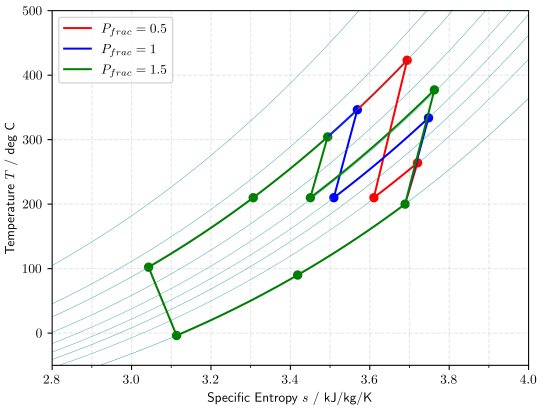

Figure C.2: Ts diagram showing the effect of P_{frac} (with P_{low} = 10 bar and β_{total} = 4) on the two-stage configuration with intercooling, using Air as working fluid (under baseline case).

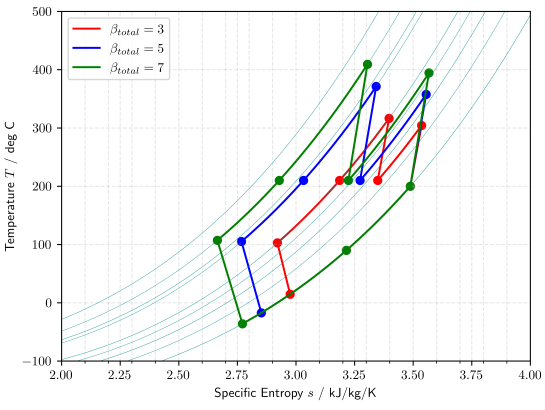

Figure C.3: Ts diagram showing the effect of β_{total} (with P_{low} 20 bar and P_{frac} = 1) on the two-stage configuration with intercooling, using Air as working fluid (under baseline case).

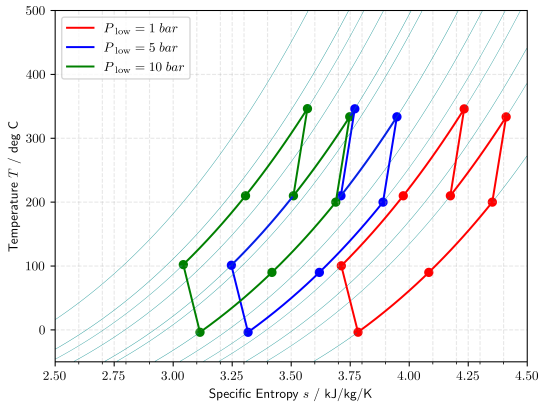

Figure C.4: Ts diagram showing the effect of P_{low} (with β_{total} = 4 and P_{frac} = 1) on the two-stage configuration with intercooling, using Air as working fluid (under baseline case).

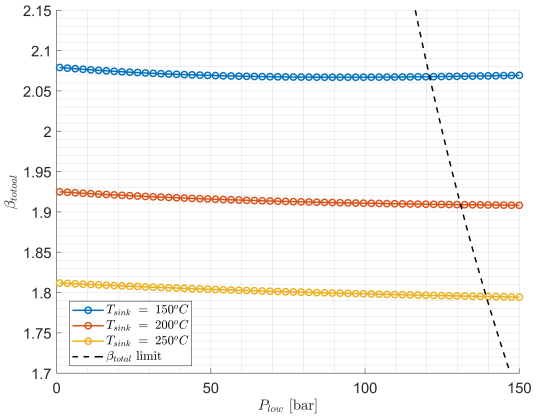

Figure C.5: Variation of β_{total} with P_{low} at different values of T_{sink}(with ΔT_{sink} = 50 °C) for the two-stage configuration with intercooling, using Air as working fluid (under sensible heat sink scenario).

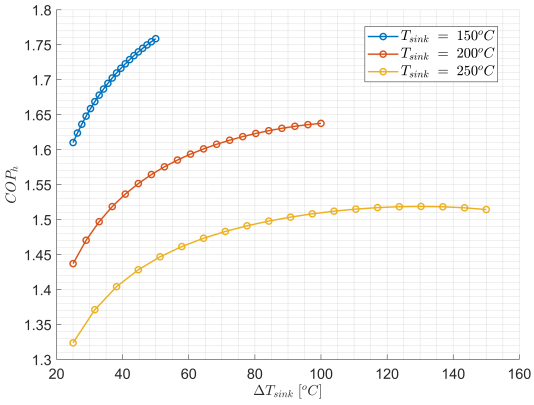

Figure C.6: Variation of $\mathrm{COP_h}$ with ΔT_{sink} at different values of T_{sink}(with P_{low} = 80 bar) for the two-stage configuration with intercooling, using Air as working fluid (under sensible heat sink scenario).

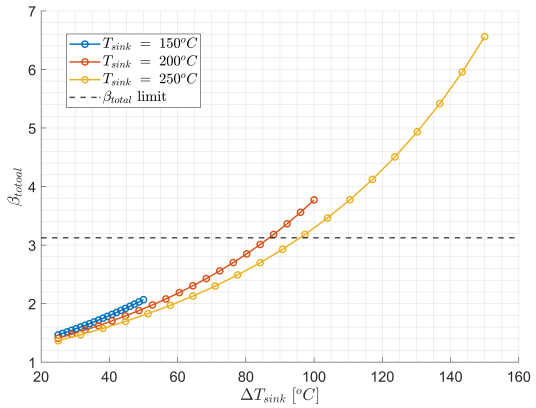

Figure C.7: Variation of β_{total} with ΔT_{sink} at different values of T_{sink}(with P_{low} = 80 bar) for the two-stage configuration with intercooling, using Air as working fluid (under sensible heat sink scenario).

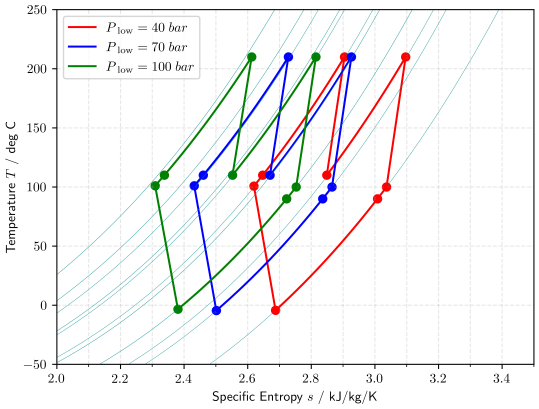

Figure C.8: Ts diagram showing the effect of P_{low} (with T_{sink} = 200 °C and ΔT_{sink} = 100 °C) on the two-stage configuration with intercooling, using Air as working fluid (under sensible heat sink scenario).

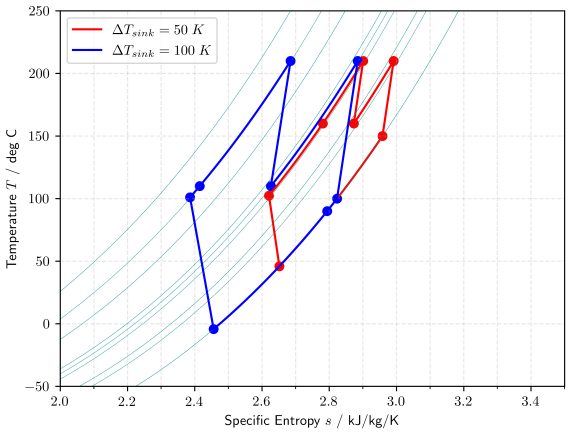

Figure C.9: Ts diagram showing the effect of ΔT_{sink} (with T_{sink} = 200 °C and P_{low} = 80 bar) on the two-stage configuration with intercooling, using Air as working fluid (under sensible heat sink scenario).

Two Stage with Internal Recuperation and Intercooling - using Air

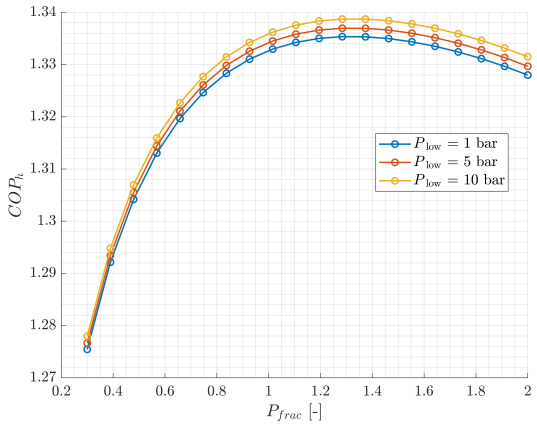

Figure C.10: Variation of $\mathrm{COP_h}$ with P_{frac} at different P_{low} values (with β_{total} = 4) for the two-stage configuration with internal recuperation and intercooling, using Air as working fluid (under baseline case).

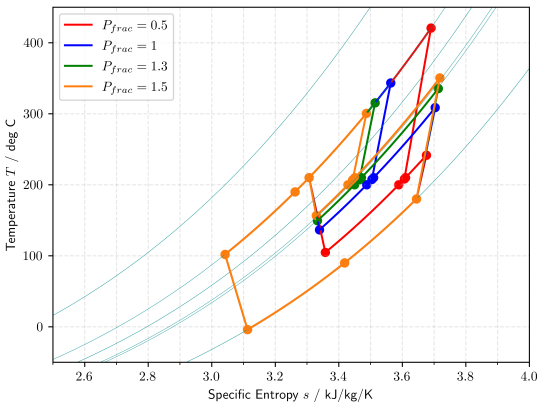

Figure C.11: Ts diagram showing the effect of P_{frac} (with P_{low} = 10 bar and β_{total} = 4) on the two-stage configuration with internal recuperation and intercooling, using Air as working fluid (under baseline case).

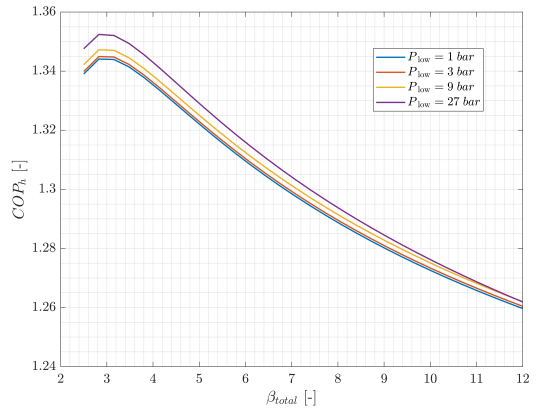

Figure C.12: Variation of $\mathrm{COP_h}$ with β_{total} at different P_{low} values (with P_{frac} = 1.3) for the two-stage configuration with internal recuperation and intercooling, using Air as working fluid (under baseline case).

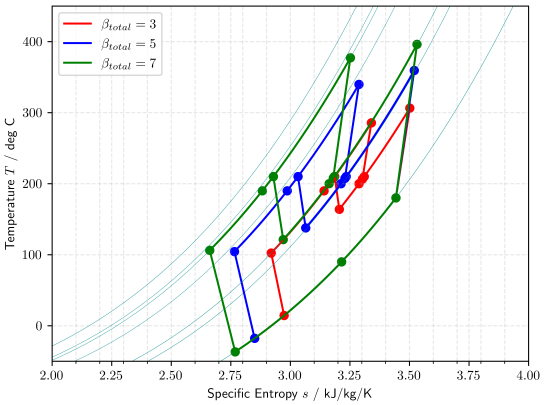

Figure C.13: Ts diagram showing the effect of β_{total} (with P_{low} 20 bar and P_{frac} = 1.3) on the two-stage configuration with internal recuperation and intercooling, using Air as working fluid (under baseline case).

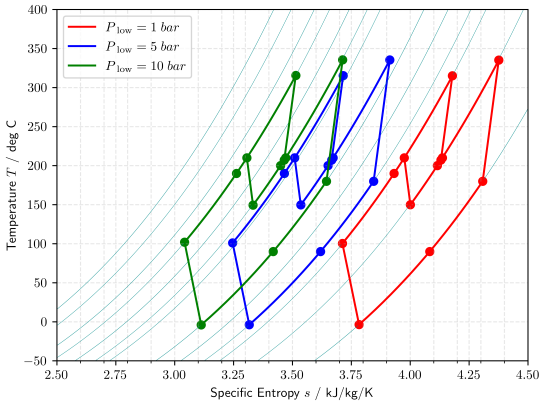

Figure C.14: Ts diagram showing the effect of P_{low} (with β_{total} = 4 and P_{frac} = 1.3) on two-stage configuration with internal recuperation and intercooling, using Air as working fluid (under baseline case).

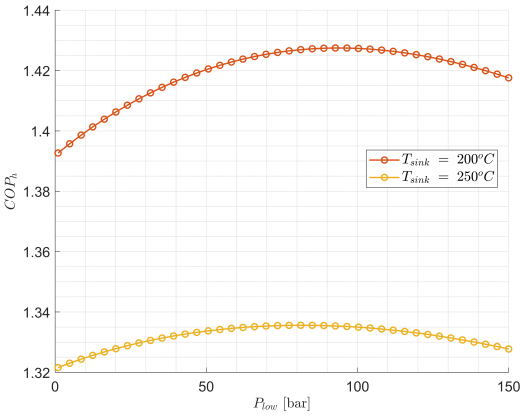

Figure C.15: Variation of $\mathrm{COP_h}$ with P_{low} at different values of T_{sink}(with ΔT_{sink} = 50 °C) for the two-stage heat pump configuration with internal recuperation and intercooling, using Air as working fluid (under sensible heat sink scenario).

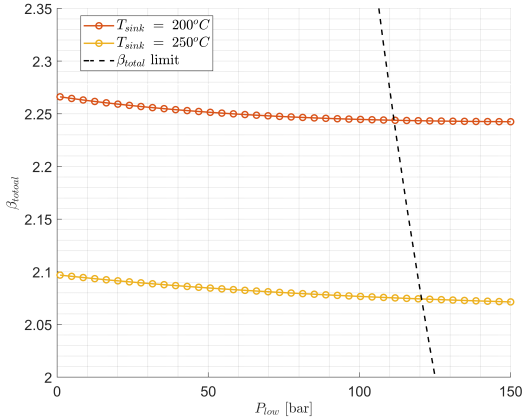

Figure C.16: Variation of β_{total} with P_{low} at different values of T_{sink}(with ΔT_{sink} = 50 °C) for the two-stage heat pump configuration with internal recuperation and intercooling, using Air as working fluid (under sensible heat sink scenario).

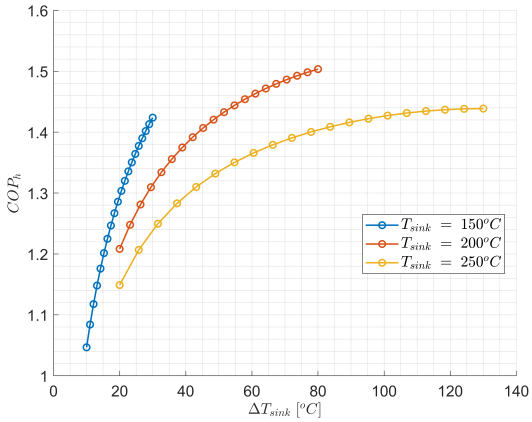

Figure C.17: Variation of $\mathrm{COP_h}$ with ΔT_{sink} at different values of T_{sink}(with P_{low} = 80 bar) for the two-stage heat pump configuration with internal recuperation and intercooling, using Air as working fluid (under sensible heat sink scenario).

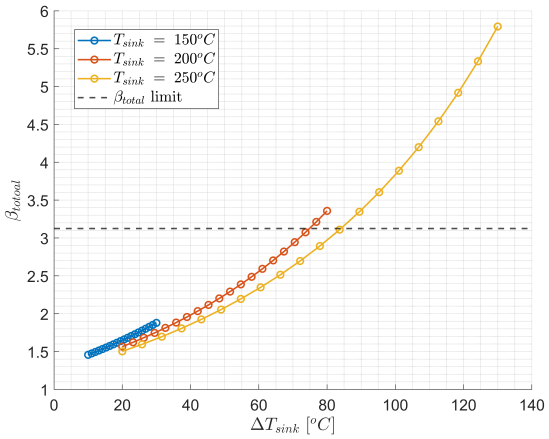

Figure C.18: Variation of β_{total} with ΔT_{sink} at different values of T_{sink}(with P_{low} = 80 bar) for the two-stage heat pump configuration with internal recuperation and intercooling, using Air as working fluid (under sensible heat sink scenario).

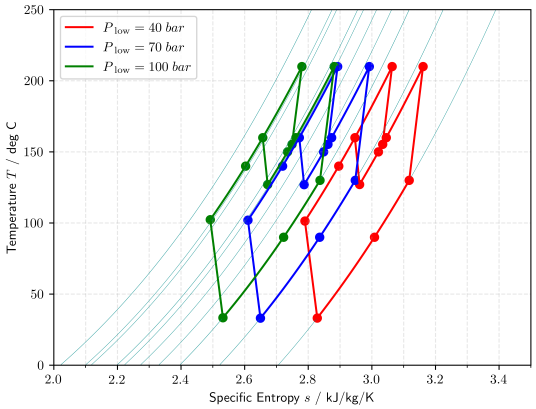

Figure C.19: Ts diagram showing the effect of P_{low} (with T_{sink} = 200 °C and ΔT_{sink} = 50 °C) on the two-stage heat pump configuration with internal recuperation and intercooling, using Air as working fluid (under sensible heat sink scenario).

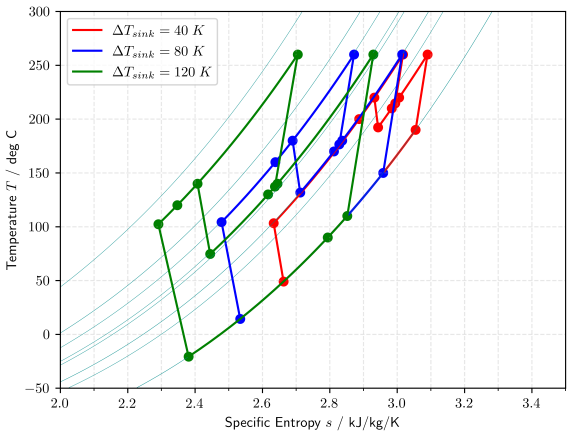

Figure C.20: Ts diagram showing the effect of ΔT_{sink} (with T_{sink} = 250 °C and P_{low} = 80 bar) on the two-stage heat pump configuration with internal recuperation and intercooling, using Air as working fluid (under sensible heat sink scenario).

D

Additional Turbomachinery Design Data

D.1. Compressor

Manual Design Exploration

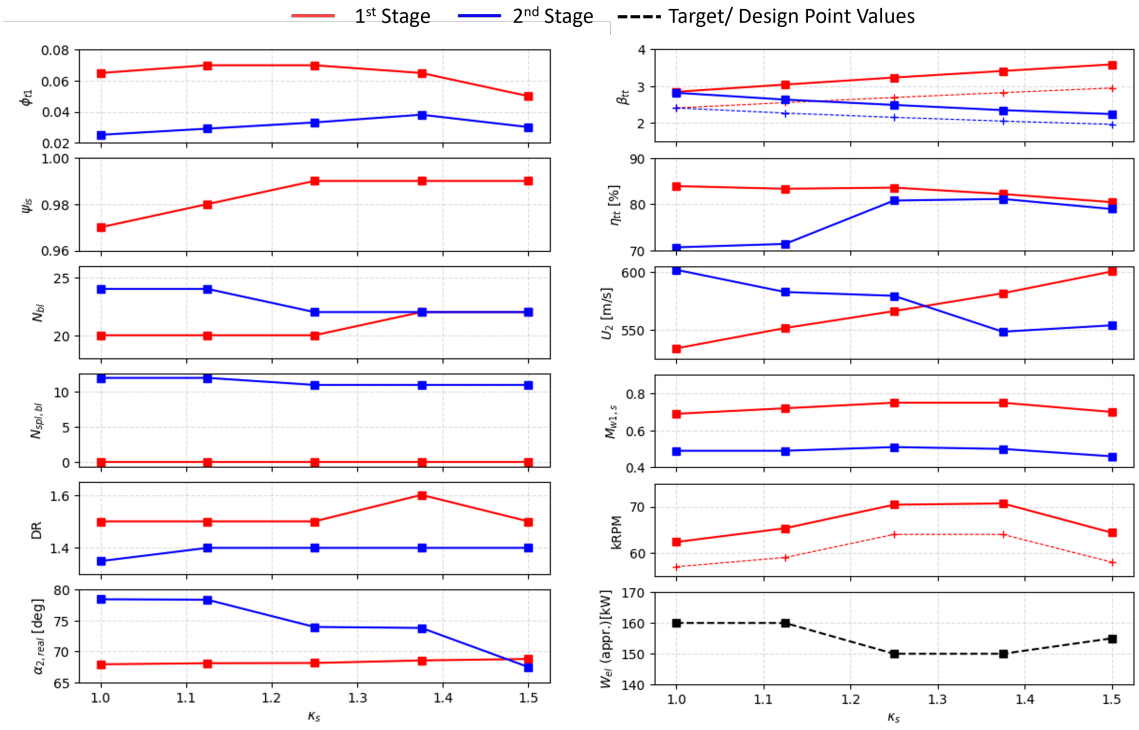

Figure D.1: Manual design exploration for compressor 1 design, based on reverse Rankine cycle based configuration, under Case 1 conditions.

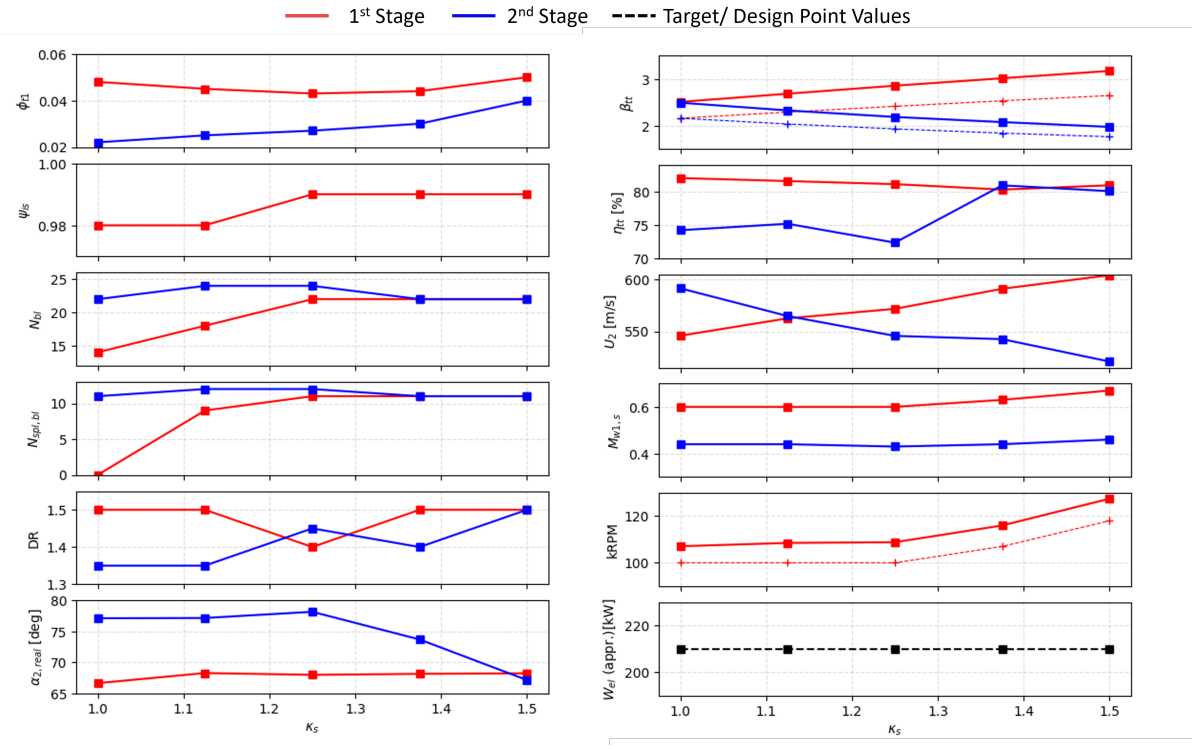

Figure D.2: Manual design exploration for compressor 2 design, based on reverse Rankine cycle based configuration, under Case 1 conditions.

Algorithm Selection

Table D.1: Combined overview of the required characteristics and possible solutions for Optimizer

Characterstic	Compressor Design Optimization Case	Possible Promising Solutions
Objective Function Structure	Multi-Objective	Only multi-objective algorithms
Constraints	Non-Linear Constraints	Only Constrained Optimization Algorithms (SQP, Newton, GA, PSO, EA, NM, interior-point etc.)
Model Structure	Non-Linear	Non-Linear Programming Algorithms
Nature of Design Space	Unknown	Robust Stochastic Algorithms would be preferred (GA, EA, Surrogate Based) or a robust Pattern search
Optimum Nature	Global Optimum	EA, GA, Hybrid Strategy, Dividing Rectangles Method, Global Pattern Search (PSO)
Use of Gradient Information	No Gradient information Available	Only gradient-free Global Methods (EA, GA, Pattern Search, Dividing Rectangles)
Use of Model	Direct Preferred (for better accuracy)	For Direct : Not a constraining factor For Model Based : Kriging or Support Vector Machine Model with Adaptive infill strategy

Optimization Convergence Plots

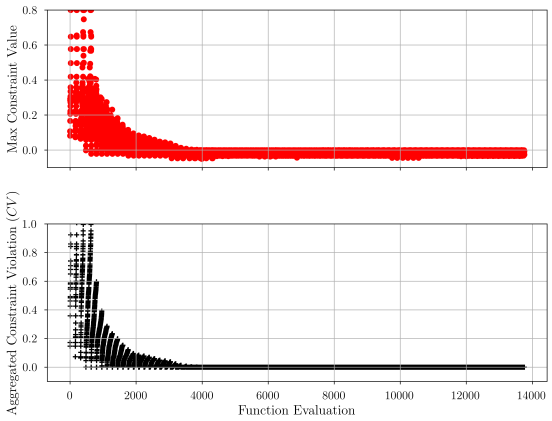

Figure D.3: Constraint convergence trends obtained for compressor 1 design, based on reverse Rankine cycle based configuration, under Case 1 conditions.

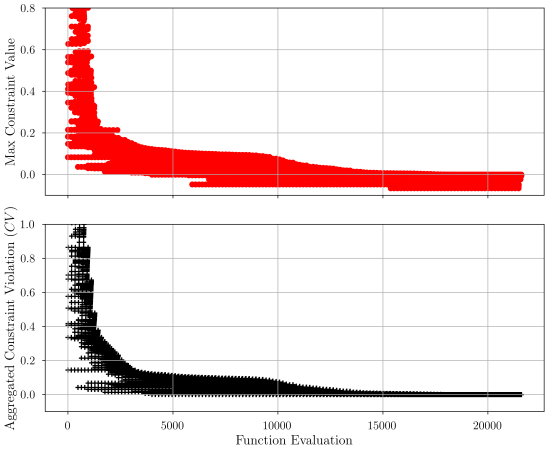

Figure D.4: Constraint convergence trends obtained for compressor 2 design, based on reverse Rankine cycle based configuration, under Case 1 conditions.

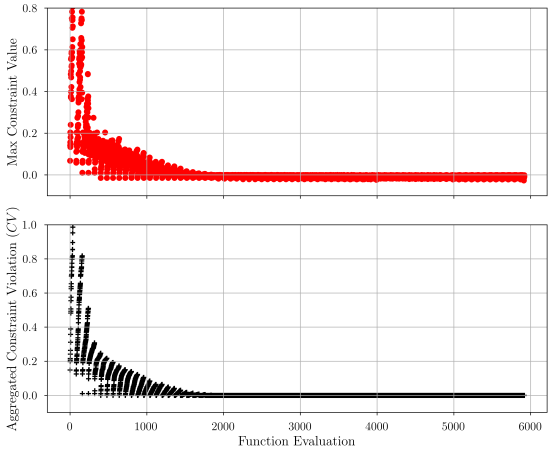

Figure D.5: Constraint convergence trends obtained for compressor design, based on reverse Brayton cycle based configuration, under Case 1 conditions.

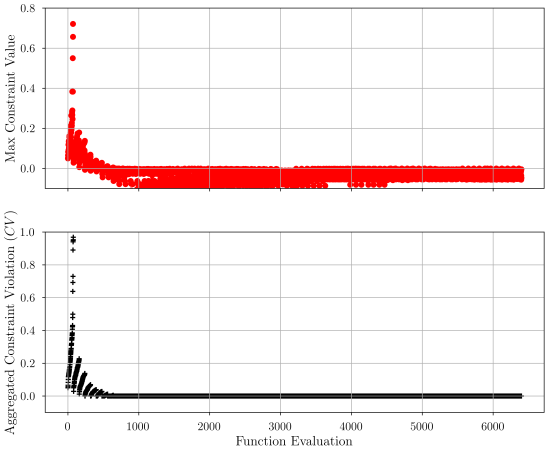

Figure D.6: Constraint convergence trends obtained for compressor design, based on reverse Brayton cycle based configuration, under Case 3 conditions.

D.2. Turbine

Table D.2: Selected values of geometrical design parameters to obtain the optimized turbine designs of reverse Brayton cycle-based configuration

Variable	Case 1 (Fix RPM)	Case 1 (Max Efficiency)	Case 3
$R_{h,r}/R_{t,r}$	0.44	0.4	0.5
R_3/R_2	0.42	0.46	0.35
R_1/R_0	0.8	0.87	0.85
Radius Ratio Radial Gap	0.95	0.95	0.95
V_{m3}/V_{m2}	1.0	1.0	1.0
Diffuser Area Ratio	4	4	4
Cant Angle	4°	6°	4°
Divergence Angle	5°	5°	5°